

AD-A186 750

ONE FILE COPY

(2)

Bulletin 57
(Part 3 of 4 Parts)

THE SHOCK AND VIBRATION BULLETIN

Part 3

Isolation and Damping,
Vibration Test Criteria, and
Vibration Analysis and Test

JANUARY 1987

DTIC
ELECTED
NOV 19 1987
S E D
G D

A Publication of
**THE SHOCK AND VIBRATION
INFORMATION CENTER**
Naval Research Laboratory, Washington, D.C.



Office of
**The Under Secretary of Defense
for Research and Engineering**

Approved for public release; distribution unlimited.

87 10 28 030

SYMPOSIUM MANAGEMENT

THE SHOCK AND VIBRATION INFORMATION CENTER

J. Gordan Showalter, Acting Director
Rudolph H. Volin, P.E. ed.
Elizabeth A. McLaughlin
Mary K. Gobbett
Ann Grant

Bulletin Production

Publications Branch, Technical Information Division,
Naval Research Laboratory

Bulletin 57
(Part 3 of 4 Parts)

THE SHOCK AND VIBRATION BULLETIN

JANUARY 1987

A Publication of
**THE SHOCK AND VIBRATION
INFORMATION CENTER**
Naval Research Laboratory, Washington, D.C.

The 57th Symposium on Shock and Vibration was held in New Orleans, Louisiana, October 14-16, 1986. The Defense Nuclear Agency, Washington, DC and the U.S. Army Engineer Waterways Experiment Station, Vicksburg, Mississippi were the hosts.



Accession For	
NTIS	CRA&I
DTIC	TAB
Unannounced	
Justification	
By _____	
Distribution/	
Availability Codes	
Dist	Avail and/or Special
A-1	

Office of
The Under Secretary of Defense
for Research and Engineering

CONTENTS

PAPERS APPEARING IN PART 3

<u>Isolation and Damping</u>	
ON FREE DECAY/DAMPING TESTS.....	1
L. K. H. Lu, R. Perez, K. B. Schneider, Westinghouse Electric Corporation, Sunnyvale, CA	
RESPONSE OF A SEQUENTIAL DAMPER TO SHOCK INPUTS.....	9
S. Rakheja and S. Sankar, Concordia University, Montreal, Quebec, Canada	
LIQUID-SPRING DESIGN METHODOLOGY FOR SHOCK ISOLATION SYSTEM APPLICATIONS.....	17
M. L. Winiarz, the BDM Corporation, Albuquerque, NM	
DESIGN AND TEST OF A SPACECRAFT INSTRUMENT SHOCK ISOLATOR.....	29
D. Schiff, N. Jones and S. Fox, Assurance Technology Corporation, Carlisle, MA	
DYNAMIC ANALYSIS OF A STRUCTURE WITH SLIDING BASE.....	47
T.C. Liauw and Y.K. Cheung, University of Hong Kong, Hong Kong, and Q. L. Tian, Chinese Academy of Sciences, Peking, China	
A MODAL CONTROL BASED LIMITING PERFORMANCE FORMULATION FOR SHOCK EXCITED SYSTEMS.....	57
W. D. Pilkey, University of Virginia, Charlottesville, VA, and Y. Narkis, State of Israel Armament Development Authority, Haifa, Israel	
ANALYTICAL STUDY OF THE EFFECT OF EARLY WARNING ON OPTIMAL SHOCK ISOLATION.....	67
W. D. Pilkey, University of Virginia, Charlottesville, VA, and Y. Narkis, State of Israel Armament Development Authority, Haifa, Israel	
<u>Vibration Test Criteria</u>	
TECOM'S RESEARCH EFFORTS IN THE DYNAMIC ENVIRONMENTS.....	73
J. A. Robinson, U.S. Army Combat Systems Test Activity, Aberdeen Proving Ground, MD	
THE DEVELOPMENT OF LABORATORY VIBRATION TEST SCHEDULES -- PHILOSOPHIES AND TECHNIQUES.....	89
R. D. Baily, U.S. Army Combat Systems Test Activity, Aberdeen Proving Ground, MD	
LABORATORY VIBRATION TEST SCHEDULES DEVELOPED BEYOND MIL-STD-810D.....	103
R. D. Baily, U.S. Army Combat Systems Test Activity, Aberdeen Proving Ground, MD	
A PROPOSED TECHNIQUE FOR GROUND PACKAGED VEHICLE LOOSE CARGO VIBRATION SIMULATION.....	107
W. H. Connon, III, U.S. Army Combat Systems Test Activity, Aberdeen Proving Ground, MD	

ANALYSIS OF SHOCK AND VIBRATION ENVIRONMENTS FOR CARGO ON C9B TRANSPORT AIRCRAFT	133
T. J. Baca, J. W. Doggett and C. A. Davidson, Sandia National Laboratories, Albuquerque, NM	
COMPREHENSIVE INFLIGHT VIBRATION AND ACOUSTIC TESTING	147
P. G. Boids, Air Force Wright Aeronautical Laboratories Wright-Patterson Air Force Base, OH	

Vibration Analysis and Test

EVALUATION OF VIBRATION SPECIFICATIONS FOR ACOUSTIC ENVIRONMENTS	155
L. T. Nguyen and G. J. Zeronian, Northrop Corporation, Hawthorne, CA	
FATIGUE EFFECTS OF A SWEPT SINE TEST	159
A. E. Galef, TRW, Redondo Beach, CA	
STATISTICAL MEASURES OF CLIPPED RANDOM SIGNALS	165
T. L. Paez and D. O. Smallwood, Sandia National Laboratories, Albuquerque, NM	
FULLY TURBULENT INTERNAL FLOW EXCITATION OF PIPE SYSTEMS	179
J. M. Cuschieri, E. J. Richards and S. E. Dunn, Florida Atlantic University, Boca Raton, FL	
THE EFFECTS OF ROTOR UNBALANCE ON THE VERTICAL RESPONSE OF A SOFT-MOUNTED BLOCK	187
B. M. Antkowiak, The Charles Stark Draper Laboratory, Cambridge, MA, F. C. Nelson, Tufts University, Medford, MA, and M. Nabavi-Noori, Worcester Polytechnic Institute, Worcester, MA	
INVESTIGATION OF VIBRATION PROBLEMS WITH HETERODYNE HOLOGRAPHIC INTERFEROMETER	193
R. A. McLaughlin, Texas A & I University, Kingsville, TX	

PAPERS APPEARING IN PART 4

Structural Dynamics

QUALIFICATION BY ANALYSIS OF IUS PLUME DEFLECTORS	
R. F. Hain, Boeing Aerospace Company, Seattle, WA	
ANALYSIS OF REINFORCED CONCRETE STRUCTURES UNDER THE EFFECTS OF LOCALIZED DETONATIONS	
T. Kruthammer, University of Minnesota, Minneapolis, MN	
REINFORCED CONCRETE ARCHES UNDER BLAST AND SHOCK ENVIRONMENTS	
T. Kruthammer, University of Minnesota, Minneapolis, MN	
DYNAMIC STRESS AT CRITICAL LOCATIONS OF A STRUCTURE AS A CRITERION FOR MATHEMATICAL MODEL MODIFICATION	
C. Ip and C. A. Vickery, Jr., TRW, Inc., Norton Air Force Base, CA, and D. I. G. Jones, Air Force Wright Aeronautical Laboratories Wright-Patterson Air Force Base, OH	
OPTIMIZED STRUCTURE DESIGN USING REANALYSIS TECHNIQUES	
F. H. Chu, T. E. Pollak and J. C. Reuben RCA/Astro Electronics, Princeton, NJ	
RELIABILITY OF STRUCTURES WITH STIFFNESS AND STRENGTH DEGRADATION	
F. C. Chang and F. D. Ju, the University of New Mexico, Albuquerque, NM	
A NEW LOOK AT THE USE OF LINEAR METHODS TO PREDICT AIRCRAFT DYNAMIC RESPONSE TO TAXI OVER BOMB-DAMAGED AND REPAIRED AIRFIELDS	
J. J. Olsen, Air Force Wright Aeronautical Laboratories Wright-Patterson Air Force Base, OH	
FREQUENCY RESPONSE FUNCTIONS OF A NONLINEAR SYSTEM	
D. A. Dederman, T. L. Paez, D. L. Gregory, and R. G. Coleman, Sandia National Laboratories, Albuquerque, NM	

SYSTEM CHARACTERIZATION IN NONLINEAR RANDOM VIBRATION
T. L. Paez and D. L. Gregory, Sandia National Laboratories, Albuquerque, NM

**AN INTERACTIVE-Graphics METHOD FOR DYNAMIC SYSTEM MODELLING,
APPLYING CONSISTENCY RULES**
M. D. C. Dyne, Institute of Sound and Vibration Research, Southampton, England

**DYNAMIC RESPONSE OF A GEARED TRAIN OF ROTORS SUBJECTED TO
RANDOM SUPPORT EXCITATIONS**
S. V. Neriya, R. B. Bhat, and T. S. Sankar, Concordia University, Montreal, Canada

THE DYNAMICS OF AN OSCILLATING FOUR-BAR LINKAGE
P. Tchong, NASA Langley Research Center, Hampton, VA

Modal Test and Analysis

MIC CENTAUR G PRIME MODAL TEST
M. Trubert, Jet Propulsion Laboratory, Pasadena, CA
A. Cutler, General Dynamics Space System Division
San Diego, CA, R. Miller, NASA Lewis Research Center
Cleveland, OH, D. Page, General Dynamics Convair Division
San Diego, CA, and C. Englehardt, Structural Dynamics
Research Corporation, San Diego, CA

PAPERS APPEARING IN PART 1

Welcome

WELCOME
Dr. Robert W. Whalir, Ph.D., P.E., Technical Director, U.S. Army
Waterways Experiment Station, Vicksburg, MS

Keynote Address

ICBM MODERNIZATION: A SHOCK AND VIBRATION PERSPECTIVE
Eugene Sevin, Assistant Deputy Undersecretary, Offensive and Space Systems, Office of the
Undersecretary of Defense Research and Engineering, The Pentagon, Washington, DC

Invited Papers

RESEARCH AND DEVELOPMENT
Bob O. Benn, Assistant Director, Research and Development
Directorate (Military Programs), U.S. Army Corps of Engineers, Washington, DC

NDI FROM A MANAGER'S POINT OF VIEW
Robert Lehnes, Deputy Project Manager, Systems and
Engineering, Mobile Subscriber Equipment, U.S. Army
Communications-Electronics Command, Ft. Monmouth, NJ

DYNAMIC TESTING — SEVEN YEARS LATER
Allen J. Curtis, Hughes Aircraft Company, El Segundo, CA

Nondevelopment Items Workshop

**GUIDELINES FOR QUALIFYING NON-DEVELOPMENT EQUIPMENT
TO SHOCK AND VIBRATION**
C. J. Beck, Jr., Boeing Aerospace Company, Seattle, WA

**MAJOR ACCOMPLISHMENTS OF THE AIR FORCE WEAPONS LABORATORY'S
SURVIVABILITY UTILITIES PROGRAM**
Lt. L. T. Nichols and Capt. G. C. Laventure, Jr., Air
Force Weapons Laboratory, Kirtland Air Force Base, NM

**A CASE HISTORY OF THE QUALIFICATION PROGRAM CONDUCTED BY THE
U.S. ARMY OF THE GERMAN 120MM TANK MAIN ARMAMENT SYSTEM
FOR THE M1A1 ABRAMS TANK**
H. L. Bernstein, Office of the Project Manager, Tank Main Armament Systems, Dover, NJ

DERIVATION OF EQUIPMENT VIBRATION REQUIREMENTS FOR AV-8B
T. H. Beier, McDonnell Douglas Corporation, St. Louis, MO

Pyrotechnic Shock Workshop

DESIGNING ELECTRONICS FOR PYROTECHNIC SHOCK*
H. Luhrs, TRW, Redondo Beach, CA

ZEROSHIFT OF PIEZOELECTRIC ACCELEROMETERS IN PYROSHOCK MEASUREMENTS*
A. Chu, Endevco Corporation, San Juan Capistrano, CA

*This paper was presented in the Pyrotechnic Shock Workshop at the 57th Shock and Vibration Symposium.

PAPERS APPEARING IN PART 2

Instrumentation

AN INTEGRATION TEST FOR ACCELEROMETER EVALUATION

E. C. Hansen, David Taylor Naval Ship Research and Development Center, Portsmouth, VA

SPECTRAL DENSITY ESTIMATES OF COARSELY QUANTIZED RANDOM VIBRATION DATA

T. J. Baca, Sandia National Laboratories, Albuquerque, NM

A QUANTITATIVE METHOD FOR EVALUATING SENSOR LAYOUTS

T. F. Chwastyk, Naval Sea Systems Command, Washington, DC

and D. G. Rapp, Westinghouse Electric Corporation, West Mifflin, PA

Shock Analysis

A SUMMARY OF EXPERIMENTAL RESULTS ON SQUARE PLATES STIFFENED PANELS SUBJECTED TO AIR-BLAST LOADING

R. Houlston and J. E. Slater, Defence Research Establishment, Suffield, Ralston, Alberta, Canada

IN-STRUCTURE SHOCK IN A PROTOTYPE BLAST SHELTER

S. C. Woodson and S. C. Kiger, U.S. Army Engineer Waterways Experiment Station, Vicksburg, MS

RESPONSE OF NONREINFORCED MASONRY WALLS TO CONVENTIONAL WEAPONS

J. C. Ray, R. E. Walker and W. L. Huff, U.S. Army Engineer Waterways Experiment Station, Vicksburg, MS

RETARDED POTENTIAL TECHNIQUE APPLIED FOR SHOCK WAVE LOADING OF DOUBLY SYMMETRIC SUBMERGED STRUCTURES

W. W. Webbon, Martin Marietta Baltimore Aerospace, Baltimore, MD, and M. Tamm, Naval Research Laboratory, Washington, DC

Shock Testing

HIGH-VELOCITY REVERSE BALLISTIC ROCKET SLED TESTING AT SANDIA NATIONAL LABORATORIES

R. D. M. Tachau, Sandia National Laboratories, Albuquerque, NM

MECHANICAL IMPACT: THEORETICAL SIMULATION CORRELATION

G. L. Ferguson, Sandia National Laboratories, Albuquerque, NM, and L. C. Mixon and F. W. Shearer, Holloman Air Force Base, NM

MEASUREMENT, DATA ANALYSIS, AND PREDICTION OF PYROTECHNIC SHOCK FROM PIN-PULLERS AND SEPARATION JOINTS

M. J. Evans and V. H. Neubert, The Pennsylvania State University, University Park, PA, and L. J. Bement, NASA, Langley Research Center, Hampton, VA

FACILITIES FOR SHOCK TESTING OF NUCLEAR SHELTER EQUIPMENT IN SWITZERLAND

P. Hunziker, NC-Laboratory Spiez, Spiez, Switzerland

SHOCK TESTS OF CONCRETE ANCHOR BOLTS FOR SHOCK RESISTANT APPLICATIONS IN PROTECTIVE STRUCTURES

P. Hunziker, NC-Laboratory Spiez, Spiez, Switzerland

MICROCOMPUTERS IN SHOCK TESTING OF WATER SATURATED SANDS

W. A. Charlie, H. Hassen and D. O. Doehring, Colorado State University, Fort Collins, CO, and M. E. Hubert, Applied Research Associates, Inc., South Royalton, VT

SHOCK INDUCED POREWATER PRESSURE INCREASES IN WATER SATURATED SOILS

W. A. Charlie, T. E. Bretz and D. J. Allard, Colorado State University, Fort Collins, CO, and G. E. Veyera, California Research and Technology, Inc., Albuquerque, NM

SESSION CHAIRMEN AND COCHAIRMEN

<u>Date</u>	<u>Session Title</u>	<u>Chairmen</u>	<u>CoChairmen</u>
Tuesday 14 October, A.M.	Opening Session	Dr. Don A. Linger, Defense Nuclear Agency, Washington, DC	Dr. Sam Kiger, U.S. Army Engineer Waterways Experiment Station, Vicksburg, MS
Tuesday 14 October, P.M.	Instrumentation	Mr. Richard P. Joyce, IIT Research Institute, Chicago, IL	Mr. W. Scott Walton U.S. Army Combat Systems Test Activity, Aberdeen Proving Ground, MD
Tuesday 14 October, P.M.	Shock Analysis	Mr. James D. Cooper, Defense Nuclear Agency, Washington, DC	Mr. William J. Flathau, JAYCOR, Vicksburg, MS
Wednesday 15 October, A.M.	Plenary A	Rudolph H. Volin, P.E., Shock and Vibration Information Center, Naval Research Laboratory, Washington, DC	
Wednesday 15 October, A.M.	Nondevelopment Items Workshop, Session I, Methods	Mr. James W. Daniel, U.S. Army Missile Command, Redstone Arsenal, AL	Mr. Paul Hahn, Martin Marietta Orlando Aerospace, Orlando, FL
Wednesday 15 October, A.M.	Structural Dynamics I	Mr. Stanley Barrett, Martin Marietta Denver Aerospace, Denver, CO	Mr. W. Paul Dunn, The Aerospace Corporation, El Segundo, CA
Wednesday 15 October, A.M.	Isolation and Damping	Dr. Paul N. Sonnenburg, Physicon, Inc., Huntsville, AL	Matthew Kluesener, P.E., University of Dayton Research Institute, Dayton, OH
Wednesday 15 October, P.M.	Nondevelopment Items Workshop, Session II, Case Histories	Mr. Howard Camp, Jr., U.S. Army Communications- Electronics Command, Ft. Monmouth, NJ	Edgar K. Stewart, P.E., U.S. Army Armament Command, Dover NJ
Wednesday 15 October, P.M.	Structural Dynamics II	Dr. John L. Gubser, McDonnell Douglas Astronautics, St. Louis, MO	C. Allen Ross, Ph.D., P.E., Air Force Engineering Services Center, Tyndall Air Force Base, FL

Wednesday 15 October, P.M.	Shock Testing	Mr. David Coltharp, U.S. Army Engineer Waterways Experiment Station, Vicksburg, MS	Mr. Steve Tanner, Naval Weapons Center, China Lake, CA
Thursday 16 October, A.M.	Plenary B	Mr. Jerome Pearson, Air Force Wright Aeronautical Laboratories, Wright-Patterson Air Force Base, OH	
Thursday 16 October, A.M.	Vibration Test Criteria	Mr. Tommy Dobson, 6585 Test Group, Holloman Air Force Base, NM	Mr. Edward Szymkowiak, Westinghouse Electric Corporation, Baltimore, MD
Thursday 16 October, A.M.	Modal Test and Analysis	Richard Stroud, Ph.D., P.E., Synergistic Technology, Cupertino, CA	Connor D. Johnson, Ph.D., P.E. CSA Engineering, Inc. Palo Alto, CA
Thursday 16 October, P.M.	Vibration Analysis and Test	Mr. Frederick Anderson, U.S. Army Missile Command, Redstone Arsenal, AL	Mr. David Bond, Northrop Advanced Systems Division, Pico Rivera, CA
Thursday 16 October, P.M.	Short Discussion Topics	Mr. William Wassmann, Naval Surface Weapons Center, Silver Spring, MD	

ISOLATION AND DAMPING

ON FREE DECAY DAMPING TESTS

L. K. H. Lu, R. Perez, K. B. Schneider
Westinghouse Electric Corporation
Sunnyvale, California

Measuring logarithmic acceleration response to a transient input is a relatively simple method used to estimate an average damping coefficient. The method is not limited by either high modal density or high damping values. However, the time decay curve obtained from these tests can be difficult to interpret because of either the presence of beating or of multiple decay slopes.

In this paper, the results of both predicting response of, and testing a simple rectangular plate with constrained layer damping treatment on one half of the plate are presented. The predicted results are based on both Statistical Energy Analysis (SEA) and Finite Element Analysis (FEA). It is found that simple SEA equations predict the dual slopes found in the time transient responses reasonably well.

INTRODUCTION

The knowledge of approximate average damping levels in various frequency bands is necessary if frequency response functions are to be predicted or the efficacy of a damping treatment verified. For simple structures, analytical approaches such as the modal strain energy method (1) can be used to predict the damping levels of structures treated by a damping layer, on a mode by mode basis. When structures becomes complex, such as marine propulsion system, analytical solutions become difficult or impractical. In such cases, experimental techniques are particularly well suited to obtaining estimates of composite damping levels.

When modes are reasonably well spaced, several experimental techniques are available for damping estimation. Among, them, the poly-reference method (2) is suitable for extracting modal parameters despite some modal overlapping. However, techniques based on fitting individual modes cease to be practical at higher modal densities,

due to excessive modal overlapping. One alternative is a simple transient decay approach which can provide approximate average damping levels in frequency bands. However, the time decay curve obtained from these tests can be somewhat difficult to interpret because of either the presence of beating or of multiple decay rates. Reference (3) suggests procedures to include the effect of beating in the damping estimation. However, the presence of dual slopes appears not to have been investigated previously.

In this paper, tests and calculations of a simple rectangular plate with one half of the plate covered by constrained layer damping material are presented. The experimental results were compared to estimates based on Finite Element Analysis (FEA) and Statistical Energy Analysis (SEA) (4) methods. It was found that the dual slopes observed in the transient responses are in agreement with FEA results. Further, the nature of dual slope behavior can be explained by application of the SEA power balance principle. This knowledge can aid the interpretation of decay rate damping test results.

TEST SPECIMEN

A long rectangular steel plate of .125" thickness was used in the investigation. One half of the plate was covered with 0.05" thickness DYAD 606 visco-elastic material and .0625" thickness steel face plate. The specimen was suspended by elastic cord to simulate a free-free condition. Transient response history due to hammer impact was processed by a GENRAD model 2515 signal analyzer. The test set-up is shown in Figure 1.

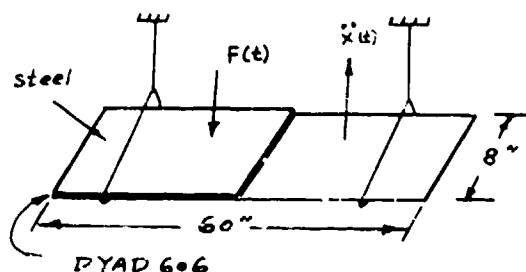


Figure 1: Test specimen

The material properties of DYAD 606 as a function of ambient temperature and frequency are shown in Figure 2.

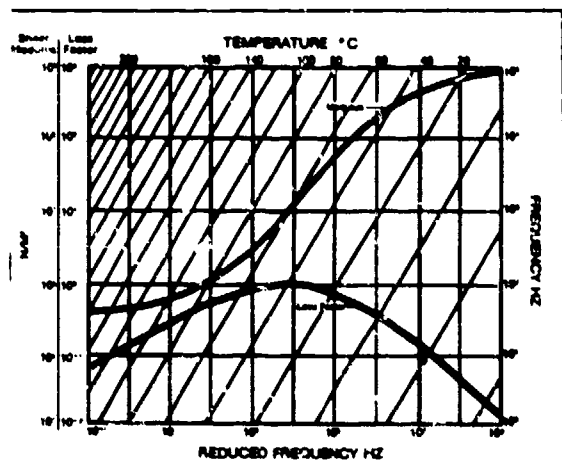


Figure 2: Damping Material Properties

To estimate damping levels by FEA, the specimen is modeled by 150 QUADA plate elements plus 50 brick elements for the viscoelastic material. The modal strain energy approach (1) is used to calculate the modal damping. Figure 3 shows the mode by mode natural frequencies and damping values estimated from the FEA model of the plate. To estimate decay rates resulting from a hammer blow, an analytical impulse with frequency content judged to be adequate up to 1500 Hz is applied to the damped side of the plate. The response is then calculated using the NASTRAN computer program.

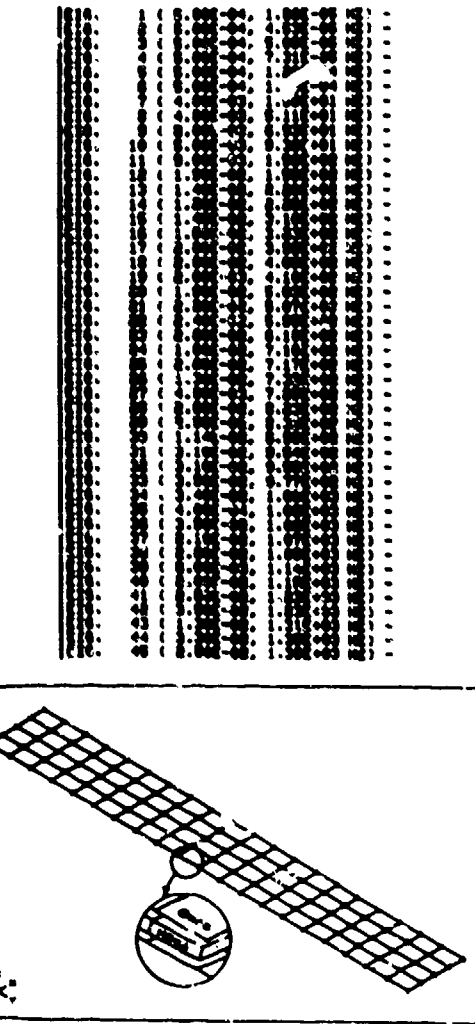


Figure 3: FEA Model and corresponding modal frequencies and damping ratios

RESULTS AND DISCUSSION

Shown in Figure 4 are FEA-calculated transient responses of the test specimen due to impact on the damped side. Responses at several locations are shown in Figures 4A through 4D. Figures 4E and 4F are the RMS responses of 16 modes on the damped and undamped sides, respectively. Also shown are the transient decay slopes obtained by the SEA model presented in Appendix 1.

Equation (6) of Appendix 1 is the closed form solution of a two energy block SEA system. Despite the simplification of including only two bending mode energy blocks, the results agree well with the solution obtained by step-by-step numerical integration using the commercially available SEAM computer code (5), shown in Figure 5.

The material loss factors used in the SEA model were obtained by calculating the modal strain energy of the viscoelastic material. Only the damped half plate was considered in the FEA model. Because of possible variation of DYAD 606 from its nominal values, upper and lower limits of loss factors ($\eta = 0.1$ to $\eta = 0.15$) were used.

Presented in Figure 6 is a typical experimental transient decay plot with the accelerometer on the excited side. Dual slopes can clearly be identified. Also plotted in this figure are the slopes calculated by SEA equation (6), showing good agreement with the test data.

CONCLUSIONS

In this study, the impulse response of a structure is compared to SEA and FEA calculations from an energy transmission point of view. As discussed in Appendix 1, the first slope of the acceleration time decay curve on the excited side is related to the rate of energy flow from the impacted structure to its surroundings. The second slope of the decay curve is related to the average damping value of the total structure.

The responses predicted by the SEA equations of a laboratory specimen agree quite well with those calculated by the FEA method.

ACKNOWLEDGMENT

The authors would like to thank Dr. R.G. DeJong for his helpful discussion on the interpretation of SEA equations and to Mr. J.F. Jakovich for his work on FEA model preparation. The encouragement and support from Mr. P.C. Warner and Mr. W.J. Hawkins were essential to the completion of this work.

REFERENCES

- (1) Johnson, C.D. et.al., "Design and Analysis of Damped Structure using Finite Element Techniques," ASME Paper No. 85-DET-T3T.
- (2) Volt, H. et.al., "A multi-input Modal Estimation Algorithm for Mini-computers," SAE Paper No. 820194. 1982.
- (3) Liang, Z. "A Possible Extrc of Impulse Test and the way of Its Improving," 3rd International Modal Analysis Conference, Florida, 1985.
- (4) Manning, J.E. and Lee, K. "Predicting Mechanical Shock Transmission," The Shock & Vibration Bulletin No. 37, 1968.
- (5) "CC/SEAM User's Manual," Cambridge Collaborative, Inc., Cambridge, Ma. 1985.

APPENDIX 1: TRANSIENT SEA MODEL

When a structure is subjected to a shock loading, the frequency content of the response is usually very broad due to the broad input spectrum of impulsive excitation. Traditional analytical techniques used to calculate this type of response are limited by the high modal density of the structure within the frequency range of interest. Statistical Energy Analysis (SEA) offers a means of simplifying the problem by calculating the average and standard deviation of frequency-band response in high modal density structures.

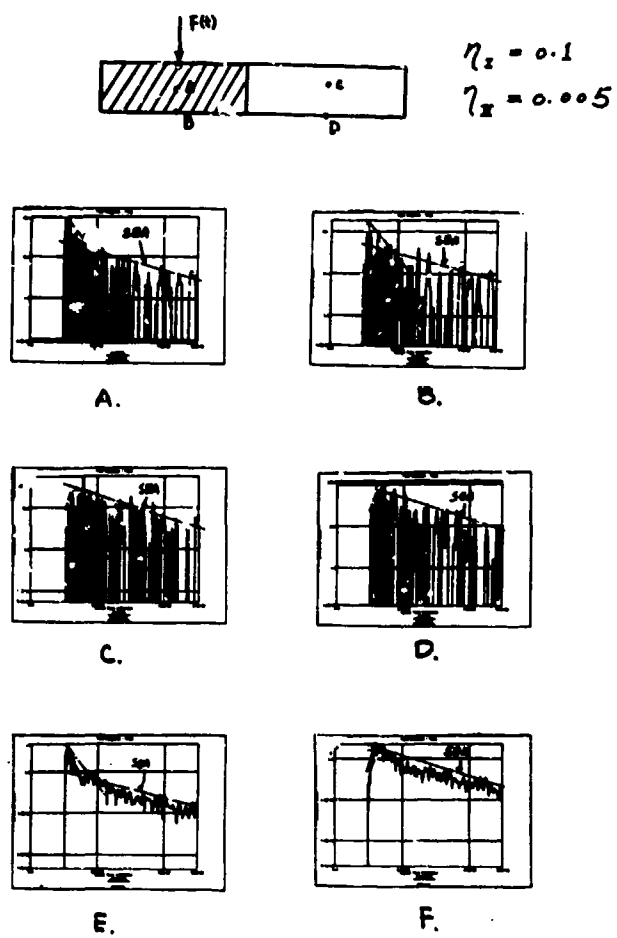


Figure 4: Comparison of decay curve obtained by SEA and FEA methods.

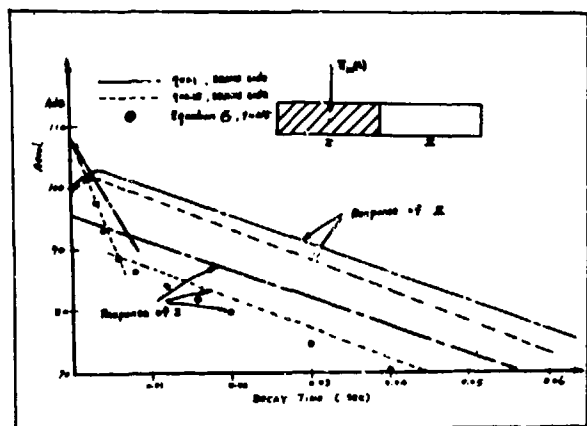


Figure 5: Decay Curves Derived by SEA Concept.

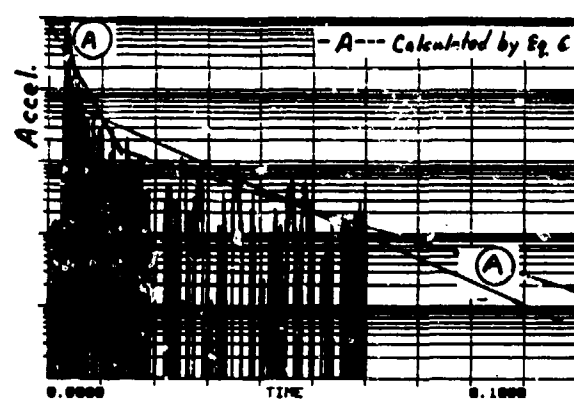


Figure 6: Comparison of Slopes Calculated by SEA and Test data.

The plate specimen in Figure 1 is modeled by a two-block system as shown in Figure A-1.

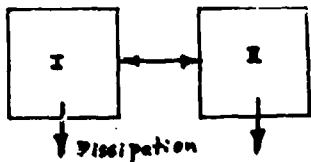


Figure A-1: Two energy-block SEA model

The power balance equation for the above system is:

$$\left\{ \begin{array}{l} \frac{\partial E_1}{\partial t} \\ \frac{\partial E_2}{\partial t} \end{array} \right\} + \left\{ \begin{array}{cc} (\eta_1 + \eta_{12})\omega_0 & -\omega_0 \eta_{21} \\ -\omega_0 \eta_{12} & (\eta_2 + \eta_{12})\omega_0 \end{array} \right\} \left\{ \begin{array}{l} E_1 \\ E_2 \end{array} \right\} = \left\{ \begin{array}{l} \Pi_{1,in} \\ \Pi_{2,in} \end{array} \right\} \quad \dots \quad (1)$$

Where

E_i = The total energy stored in the energy block i .

η_i = Material loss factor of block i (two times the critical damping ratio).

η_{ij} = Coupling loss factor from i to j .

Π_{in} = Power input into energy block i .

ω_0 = radian frequency.

t = time.

Let the system be excited to levels E_1 and E_2 . The excitations are then cut off. The above equation (1) becomes:

$$\frac{dE_1}{dt} + A_1 E_1 + A_2 E_2 = 0 \quad \dots \quad (2)$$

$$\frac{dE_2}{dt} + B_1 E_1 + B_2 E_2 = 0$$

Where $A_1 = \omega_0(\eta_1 + \eta_{12})$

$$A_2 = \omega_0 \eta_{12}$$

$$B_1 = \omega_0 \eta_{12}$$

$$B_2 = \omega_0(\eta_2 + \eta_{12})$$

$$E_1 = E_{10}$$

$$E_2 = E_{20} \quad \text{at} \quad t = 0$$

The homogenous solution of (2) is:

$$E_1 = C_1 e^{\alpha_1 t} + C_2 e^{\alpha_2 t}$$

$$E_2 = C_3 e^{\alpha_1 t} + C_4 e^{\alpha_2 t} \quad \dots \quad (3)$$

Where

$$\alpha_1, \alpha_2 = \frac{-(A_1 + B_2) \pm \sqrt{(A_1 + B_2)^2 - 4A_1 B_2 + 4A_2 B_1}}{2} \quad \dots \quad (4)$$

The solution is then

$$E_1 = C_1 e^{\alpha_1 t} + C_2 e^{\alpha_2 t}$$

$$E_2 = \frac{A_1 + \alpha_2}{A_2} C_1 e^{\alpha_1 t} + \frac{A_1 + \alpha_1}{A_2} C_2 e^{\alpha_2 t} \quad \dots \quad (5)$$

$$C_1 = E_{10} \frac{A_1 + \alpha_2}{\alpha_2 - \alpha_1} - E_{20} \frac{A_1 + \alpha_1}{\alpha_2 - \alpha_1}$$

$$C_2 = E_{20} \frac{A_1 + \alpha_1}{\alpha_2 - \alpha_1} - E_{10} \frac{A_1 + \alpha_2}{\alpha_2 - \alpha_1} \quad \dots \quad (6)$$

Depending on the initial condition E_{10} and E_{20} imposed upon the energy blocks, and the values of the coupling loss factors, η_{12} and η_{21} , equation (6) will predict different behaviors. Several special cases of interest have been studied and are presented in Table A-1.

It is seen from Table A-1 that the decay slope depends not only on the damping values, but also on the coupling loss factors between the energy blocks. For case 2, Figure A-2 shows the variation of slope 1, α_1 , and slope 2, α_2 , with respect to the coupling strength (normalized by the damping values, i.e. η_{12}/η_1).

Two distinct results can be derived from case No. 2 in Table A-1. When η_{12} is very small compared with η_1 , from Figure A-2, $\alpha_1 \approx -\omega_0 \sqrt{A_1 + \eta_1 \omega_0 \eta_{12}}$, $\alpha_2 \approx -(\omega_0 + \eta_2 \omega_0 \eta_{12}) \sqrt{A_2}$. The second block is almost completely decoupled from the first energy block, and there is little energy flow between them. The decay of the first block is due principally to the effect of its own damping. On the other hand, when coupling is very strong,

Initial Conditions E_{10}, E_{20}	Damping Factors $\eta_1, \eta_2, \eta_{12}, \eta_{21}$	Coupling Loss Factors E_1, E_2	Decay Curves	Comments
1 $E_0, 0$	$\eta_1 \neq \eta_2$ $\eta_{12} \neq \eta_{21}$	$E_1 = \frac{\eta_1}{2} \left[\frac{1 - \eta_{12}^2 - \eta_{21}^2}{1 + \eta_{12}^2 + \eta_{21}^2} \right] e^{\eta_1 t} + \frac{\eta_2}{2} \left[\frac{1 + \eta_{12}^2 + \eta_{21}^2}{1 + \eta_{12}^2 + \eta_{21}^2} \right] e^{\eta_2 t}$ $E_2 = \frac{\eta_2}{2} \left[\frac{1 - \eta_{12}^2 - \eta_{21}^2}{1 + \eta_{12}^2 + \eta_{21}^2} \right] e^{\eta_1 t} + \frac{\eta_1}{2} \left[\frac{1 + \eta_{12}^2 + \eta_{21}^2}{1 + \eta_{12}^2 + \eta_{21}^2} \right] e^{\eta_2 t}$		<ul style="list-style-type: none"> α_1, α_2 refer to Fig. 4. This is the most general case. The response at block No. 2 depends on η_{12}.
2 $E_0, 0$	$\eta_1, 0$	$\eta_{12} = \eta_{21}$ $E_1 = \frac{\eta_1}{2} \left[1 - \frac{\eta_{12}^2}{\eta_1^2 + \eta_{12}^2} \right] e^{\eta_1 t} + \frac{\eta_2}{2} \left[\frac{\eta_{12}^2}{\eta_1^2 + \eta_{12}^2} \right] e^{\eta_2 t}$ $E_2 = E_0 \frac{\eta_{12}}{\sqrt{\eta_1^2 + \eta_{12}^2}} \left[e^{\eta_1 t} - e^{\eta_2 t} \right]$		<ul style="list-style-type: none"> α_1, α_2 vs. η_{12}/η_1 Curve is shown in Figure 4.
3 $E_0, 0$	$\eta_1, \eta_{12}, 0$	$\eta_{12} = \eta_{21}$, 0 $E_1 = E_0 e^{-\omega_0 \eta_1 t}$ $E_2 = E_0 \frac{\eta_{12}}{\eta_1 - \eta_{12}} \left[e^{-\omega_0 \eta_1 t} - e^{-\omega_0 \eta_{12} t} \right]$		<ul style="list-style-type: none"> This case is identical to the example in Ref. 4.
4 $E_0, 0$	0, 0	$\eta_{12} = \eta_{21}$ $E_1 = \frac{\eta_1}{2} + \frac{\eta_2}{2} e^{-2\omega_0 \eta_{12} t}$ $E_2 = \frac{\eta_2}{2} \left[1 - e^{-2\omega_0 \eta_{12} t} \right]$		<ul style="list-style-type: none"> The only decay mechanism of block No. 1 is due to coupling of block No. 1 to block No. 2.
5 E_0, E_0	$\eta_1 = \eta_2$	$\eta_{12} = \eta_{21}$ $E_1 = E_0 e^{-\omega_0 \eta_1 t}$ $E_2 = E_0 e^{-\omega_0 \eta_2 t}$		<ul style="list-style-type: none"> This is the only case when there is no energy exchange between the energy block.
6 $E_0, 0$	0, η_2	$\eta_{12} \neq \eta_{21}$ $E_1 = \frac{1.96}{2} E_0 e^{\eta_1 t} + \frac{0.04}{2} E_0 e^{\eta_2 t}$ $E_2 = 0.1 \frac{\eta_2}{2} \left[e^{\eta_1 t} - e^{\eta_2 t} \right]$		<ul style="list-style-type: none"> This is the case when impulse is applied at the undamped side. numerical value is used to show the relative magnitude of response of different slopes.

Table A-1: Energy Decay Rate by SEA Concept

$\alpha_2 \leq \frac{1}{2} \gamma_2 w_0$ and $\alpha_1 \rightarrow \infty$.
Equations in Table 1 show that the energy
of block 1 is transmitted to block 2 almost
instantaneously. The responses of both
blocks then decay at the rate of the average
damping of the system, $1/2 \gamma_1$.

If damping is estimated from the initial
fast decay on the excited side, erroneously
high estimates will be obtained, as much of
the apparent energy loss in system I is due
merely to energy transfer to system II.
Generally, decay type damping estimates made
from measurements too near the excitation
suffer from this effect.

RESPONSE OF A SEQUENTIAL DAMPER TO SHOCK INPUTS

S. Rakheja

Research Assistant Professor

Department of Mechanical Engineering

Concordia University

Montreal, Canada

S. Sankar

Professor

Shock Isolation Performance of a shock mount consisting of a linear spring in parallel with a sequential damper is investigated. Sequential damper based on semi-active control offers a compromise between active and passive shock isolation systems. The sequential damper requires only minimal power to generate the command signal for modulating the orifice for fluid flow. Control schemes required to generate the command signal to achieve sequential modulation of the orifice are discussed. The shock isolation performance of the sequential damper is evaluated in terms of its acceleration, velocity and relative displacement response due to shock excitations. The performance characteristics of the sequential damper are compared to the response characteristics of a shock isolator with passive damping to demonstrate the superior performance of the sequentially damped shock isolator.

INTRODUCTION

Development of effective shock isolators to protect the equipment or human payloads from severe shock inputs involve the selection of suitable springs damping mechanisms. Shock motions either arise from the motion of the base or from the forces generated from the equipment. However these shock motions are mathematically analogous and cause detrimental effects on the payload. Shock isolators invariably, consist of linear or nonlinear springs, damper and the payload to be isolated from the shock loads. The spring and damping elements of a shock isolator are selected such that the acceleration transmitted to the payload is minimized, when a shock excitation is encountered.

Passive shock isolators employing linear and nonlinear springs, and viscous damper have been extensively investigated by Snowdon [1]. Shock isolators with some form of nonlinear damping have been proposed and analyzed by Snowdon [2], Mercer et al. [3], Hundal [4] and Caton et al. [5]. The performance of these isolators is often evaluated through the peak acceleration transmitted to the isolated mass and through the relative displacement across the isolator.

Passive shock isolation systems are undoubtedly the most reliable and inexpensive means to achieve shock isolation from shock loads. However, due to the inherent limitations of the passive shock isolation systems, specifically with the constant damping, various dual phase damper concepts have been proposed and analyzed. Snowdon

[2] proposed a dual phase viscous damper where the damping coefficient varies as a function of the relative velocity across the damper. The damper assumed high value of damping corresponding to low relative velocity, whereas the damping value is reduced considerably at high relative velocity. For intermediate velocities, there is a linear transition between the high and low values of damping. Guntur and Sankar[6] analyzed the shock isolation performance of six different kinds of dual phase damping shock mounts. Venkatesan et al [7] investigated the isolation performance of dual phase damping in landing gears and showed that dual phase damping provides superior isolation performance to constant or nonlinear orifice damping.

In this paper, the concept of semi-active sequential damping, similar to that of dual phase damping except for the linear transition between the high and low values of damping values, is presented. The isolator consists of a linear spring in parallel with a semi-active sequential orifice damper. The vibration isolation performance of such semi-active dampers have been investigated by a number of researchers [8,9,10]. These studies have established that semi-active damping mechanisms can achieve vibration isolation performance close to that of a fully active system. The concept of such semi-active controls is implemented to a shock isolation system experiencing rounded step and rounded pulse excitations. Two control schemes to achieve sequential damping are proposed and analyzed. The shock isolation characteristics of sequential damper are compared to that of a passive damper.

SEQUENTIAL DAMPING

Consider a shock mount comprising of conventional spring, damper and mass as shown in Figure 1. The mass acceleration due to base excitation can be expressed by the forces generated by the spring and damper, respectively:

$$\cdot \ddot{x} = -\frac{1}{m} (F_k + F_d) \quad (1)$$

where F_k and F_d are the spring and damping forces respectively and m is the isolator mass. In case of linear isolator components, the mass acceleration can be expressed as:

$$\ddot{x} = -\omega_0^2(x - y) - 2\zeta\omega(\dot{x} - \dot{y}) \quad (2)$$

where $\omega_0 = K/m$, $\zeta = C/(2m\omega_0)$ and y is the motion of the isolator base. K and C represent the spring constant and viscous damping coefficient, respectively. Solution of equation (2) for harmonic excitations has shown that passive damping tends to increase the magnitude of the mass acceleration during a part of the oscillation cycle, thus deteriorating the vibration isolation performance of the passive damper [10]. Poor isolation performance of passive damper is demonstrated by the steady state spring, damper and inertia forces trace as shown in Figure 2. The damper force opposes the spring force during a part of the vibration cycle, thus attenuating the magnitude of mass acceleration during the period $t_0 < t < t_0 + \pi/4$ and $t_0 + 3\pi/4 < t < t_0 + 3\pi/4$. Where π is the period of oscillation. The passive damper force tends to increase the amplitude of mass acceleration during the remaining part of vibration cycle. Deteriorated isolation performance due to fixed damping becomes more apparent at high excitation frequencies, when the magnitude of damping force is dominant.

An analogous phenomenon also exists in the shock isolation systems. Figure 3 shows the inertia, spring and damper force traces of a passively damped shock mount, subject to transient (Rounded Pulse Displacement) excitation at the base. It can be seen that the magnitude of mass acceleration approaches its peak value when damper force and spring force possess the same sign. The magnitude of mass acceleration decreases significantly when the damper force opposes the spring force.

Thus a sequential damping mechanism may be realised, which operates as a conventional damper with high value of damping coefficient during the periods when it acts to reduce the mass acceleration as demonstrated in Figures 2 and 3. The sequential damper assumes low value of damping coefficient during the period when a passive damper would normally increase the amplitude of mass acceleration. Such a sequential mechanism may be accomplished by modulation of the orifice size in a conventional hydraulic damper. The appropriate modulation of the orifice can be achieved by a two position valve operated by the appropriate command signal generated by the semi-active control scheme discussed in following

sections. The two-position valve offers certain orifice restriction to hydraulic flows during the high damping operation of the sequential damper. The orifice size is modulated to larger opening when damping force acts to increase the magnitude of mass acceleration. The damping force produced by such hydraulic damper is thus of velocity squared nature due to orifice flows, while neglecting leakage flows and seal friction. However, passive damping either viscous or velocity squared exhibits similar performance as presented in Figures 2 and 3.

CONTROL SCHEMES

Two control schemes for appropriate modulation of the orifice type sequential damper are presented in the following sections.

Sequential Damper Scheme I

The sequential damper scheme is established from the damping characteristics revealed by Figures 2 and 3. Figures 2 and 3 reveal that the damper force causes an increase in mass acceleration whenever the forces due to spring and damper bear the same sign. The mass acceleration decreases

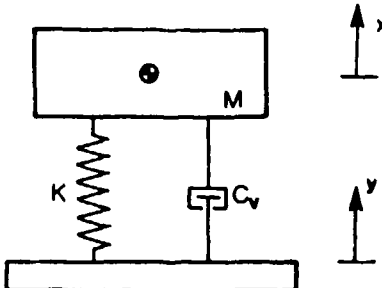


Figure 1 : Single Degree of freedom spring-mass-damper system.

considerably when the damper force opposes the spring force. Since the damper force generated

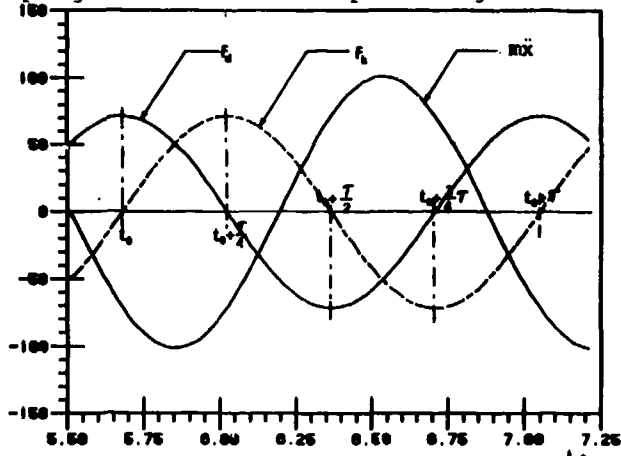


Figure 2: Spring, damper and inertia forces trace of SDOF passive isolator.

by the orifice restrictions is in phase with the relative velocity:

$$F_d = C_v (\dot{x} - \dot{y})^2 \operatorname{sgn}(\dot{x} - \dot{y}) \quad (3)$$

and the spring force is proportional to the relative displacement:

$$F_k = K (x - y) \quad (4)$$

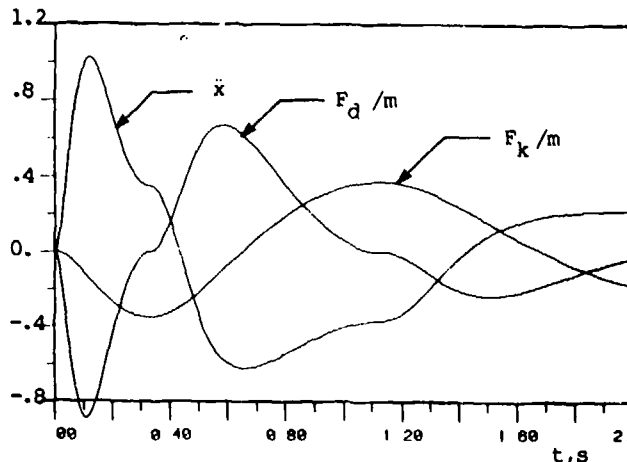


Figure 3: Spring, damper and inertia force trace of SDOF system subject to rounded pulse displacement at the base.

the sequential damper switching scheme can be established in the following manner:

$$F_d = C_v |\dot{x} - \dot{y}| (\dot{x} - \dot{y}), \\ \text{if } (\dot{x} - \dot{y})(x - y) < 0 \quad (5)$$

and

$$F_d = C_v^* |\dot{x} - \dot{y}| (\dot{x} - \dot{y}), \\ \text{if } (\dot{x} - \dot{y})(x - y) > 0 \quad (6)$$

where C_v is the coefficient of velocity squared damping associated with orifice flows and C_v^* is the damping coefficient when the damper is switched to low damping sequence. $\operatorname{sgn}(\cdot)$ function in equation 3 ensures that damper force is in phase with the relative velocity. The sgn function assumes a positive value when the relative velocity is positive and the value of sgn function changes to negative value for negative relative velocity:

$$\operatorname{sgn}(\cdot) = \begin{cases} 1. & \text{for } (\dot{x} - \dot{y}) > 0, \\ -1. & \text{for } (\dot{x} - \dot{y}) < 0. \end{cases} \quad (7)$$

The sequential damper operating with this control scheme will act as a conventional orifice damper with high damping, when the sign of relative velocity opposes the sign of relative displacement across the damper. The damper operates

with significantly lower value of damping coefficient, when relative velocity across the damper carries the same sign as the relative displacement.

Figure 4 presents the time traces of acceleration, spring force and damper force for the shock isolator employing such sequential damper and subject to rounded pulse displacement at the base. It can be observed that damper assumes extremely low damping, whenever the spring and damper forces bear the same sign. The damping force generated by the sequential damper rises sharply as the spring force opposes the damping force.

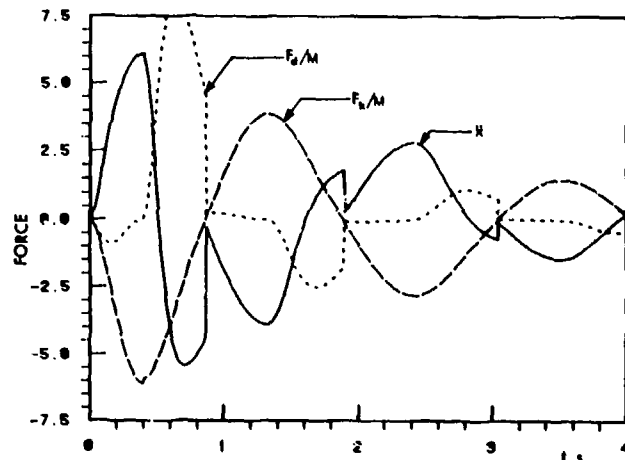


Figure 4: Acceleration, spring force and damper force traces of the SDOF shock isolator employing sequential damper I.

Sequential Damper Scheme II

Alternatively, a second sequential damping scheme, devised from the force generator concept of Karnopp[8] and Margolis[11]. It was established that mass deceleration can be accomplished when the sign of absolute velocity of the mass is same as that of the relative velocity across the damper. Thus the sequential damping scheme is formulated to yield the damping force in the following manner:

$$F_d = C_v |\dot{x} - \dot{y}| (\dot{x} - \dot{y}), \\ \text{if } \dot{x}(\dot{x} - \dot{y}) > 0. \quad (8)$$

and

$$F_d = C_v^* |\dot{x} - \dot{y}| (\dot{x} - \dot{y}), \\ \text{if } \dot{x}(\dot{x} - \dot{y}) < 0. \quad (9)$$

The sequential damper operating with this control scheme will operate as a orifice damper with high damping coefficient (C_v) when the absolute velocity of mass is in phase with the relative velocity across the damper. The damper offers low value of damping coefficient (C_v^*) when absolute velocity opposes the relative velocity across the damper. The damping behaviour

of sequential damper II alongwith the spring and inertia forces are shown in Figure 5.

INPUT DISPLACEMENTS

Two types of shock displacements are considered at the isolator base: rounded step displacement and rounded pulse displacement. These inputs have been used to evaluate the shock mounts in a number of investigations [1,2,6]. The

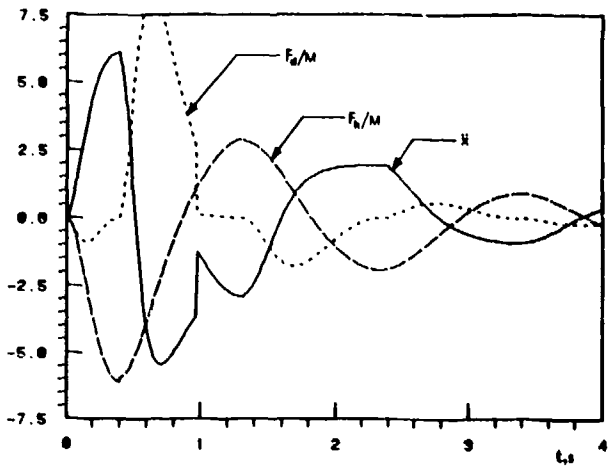


Figure 5: Acceleration, spring and damping force traces of the SDOF shock isolator employing sequential damper II.

base displacement corresponding to each type of input are expressed in the following manner:
Rounded Pulse Displacement:

$$y(t) = Y_{\max} \frac{e^2}{4} (\nu \omega_b t)^2 e^{-\nu \omega_b t}, t > 0. \quad (10)$$

Rounded Step Displacement:

$$y(t) = Y_{\max} [1 - e^{-\nu \omega_b t} (1 + \nu \omega_b t)], t > 0. \quad (11)$$

where $e = 2.71828$, Y_{\max} is the maximum input displacement and ν is the shock severity parameter, defined by

$$\nu = \frac{\pi}{\omega_0 r_i} \quad (12)$$

Where r_i is the duration of pulse and is equal to the duration of an equivalent rectangular pulse of the same area with maximum displacement 17.6% larger than Y_{\max} , in case of rounded pulse. In case of rounded step r_i is the time required for the displacement to reach its maximum value. Figures 6 and 7 present the displacements at the base with respect to time for various ν values.

PERFORMANCE EVALUATION OF SEQUENTIAL DAMPER

The equation of motion of the spring mass system shown in Figure 1 with sequential damper

is

$$\ddot{x} + \frac{a}{Y_{\max}} |\dot{x} - \dot{y}| (\dot{x} - \dot{y}) + \omega_0^2 (x - y) = 0. \quad (13)$$

where a is the damping parameter, given by the following expressions:

Passive Damper:

$$a = \frac{C_v}{m} Y_{\max} \quad (14)$$

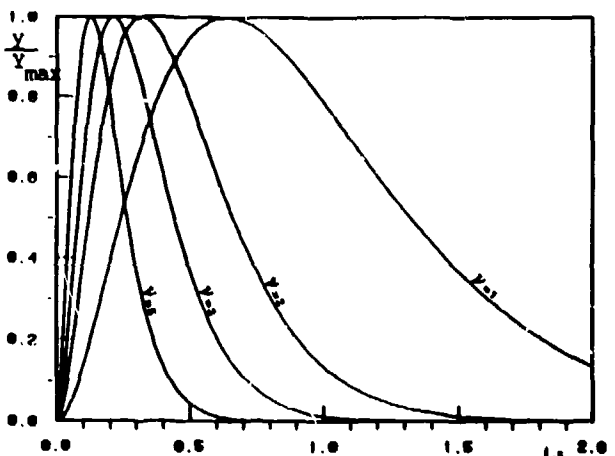


Figure 6: Rounded pulse displacement input for various severity parameters.

Sequential Damper I:

$$a = \begin{cases} \frac{C_v}{m} Y_{\max}, & \text{if } (\dot{x} - \dot{y})(x - y) < 0. \\ \frac{C_v^*}{m} Y_{\max}, & \text{if } (\dot{x} - \dot{y})(x - y) > 0. \end{cases} \quad (15)$$

Sequential Damper II:

$$a = \begin{cases} \frac{C_v}{m} Y_{\max}, & \text{if } \dot{x}(\dot{x} - \dot{y}) > 0. \\ \frac{C_v^*}{m} Y_{\max}, & \text{if } \dot{x}(\dot{x} - \dot{y}) < 0. \end{cases} \quad (16)$$

In the case of linear dampers, both passive and active, it is possible to arrive at closed form solutions for the response due to various base excitations. However, the equation of motion (13) of the sequentially damped shock isolator has step discontinuities and nonlinearity due to orifice flows, and hence closed form solutions are not attempted. In this study, the differential equation of motion is solved to determine the shock isolation performance, using direct integration techniques based on the fourth-order Runge-Kutta method.

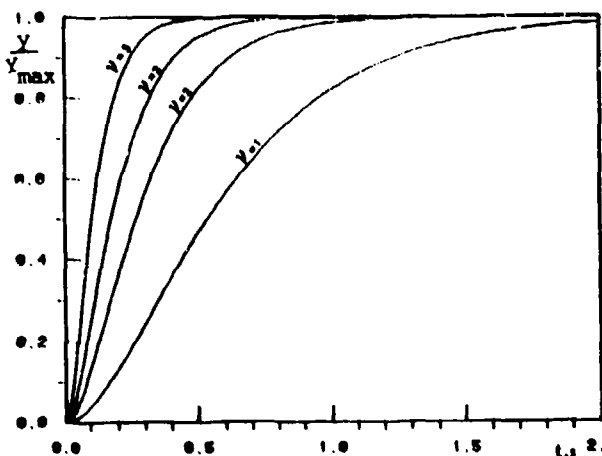


Figure 7: Rounded Step displacement input for various severity parameters.

In order to evaluate the performance of a sequentially damped shock isolator, suitable performance criteria are to be selected such that the performance characteristics of the sequential damper can be compared to that of a passive shock isolator. Since the isolator's basic requirement is to minimize the acceleration transmitted to the mass, the peak mass acceleration is perhaps, the most important criterion to evaluate the shock isolator performance. However, the physical considerations, such as the size and operating range of the isolator impose a restriction on the maximum relative displacement which can occur. Thus an effective isolator should provide a low acceleration transmitted and a low relative displacement, but in practice trade offs are to be made between these two quantities.

The performance of the shock isolator is evaluated in terms of the following response parameters:

Shock acceleration ratio, $SAR = |\ddot{x}(t)|_{\max} / |\dot{y}(t)|_{\max}$

Shock velocity ratio, $SVR = |\dot{x}(t)|_{\max} / |\dot{y}(t)|_{\max}$

Shock displacement ratio, $SDR = |x(t)|_{\max} / y_{\max}$

Relative displacement ratio, $RDR = |x(t) - y(t)|_{\max} / y_{\max}$ (17)

RESULTS AND DISCUSSIONS

Shock isolation performance of the passive and sequential dampers are presented in terms of SAR, SVR, and RDR characteristics for shock severity parameter ranging from 0.1 to 20. The shock isolation characteristics of the sequential damper is compared to that of the passive damper subject to rounded pulse and step displacements at the base. Figures 8 and 9 present the SAR response of the passive damper subject to rounded pulse and step displacement respectively, for various damping parameters, α . It can be seen that light damping provides better isolation at higher shock severities, while high damping yields better performance corresponding to lower

values of severity parameter. However, light damping implies mass oscillations for longer durations.

The response behaviour of sequential damper employing two schemes are evaluated for $x_{\max} = 0.1$ m, $\omega_0 = \pi$, α (high damping) = 12, while the ratio of damping coefficients ($\eta = C_v / C_v^*$) is varied in the range 0.1 to 0.5. The two sequential dampers exhibit identical isolation performance except for the settling time. Figures 10 and 11 present a comparison of SAR characteristics of passive and sequential dampers, subject to rounded pulse and step displacement inputs respectively, for various η values. The sequential damper provides extremely superior SAR response at high shock severities. The SAR response of the sequential damper is slightly larger than that of the passive damper at low values of shock severity. Also the response characteristics of the sequential damper approach that of the passive damper, as the η value is increased. The SVR characteristics of the sequential damper exhibit similar behaviour as shown in Figures 12 and 13 corresponding to rounded pulse and rounded displacement excitations, respectively. The response characteristics of sequential damper reveal that low η value provides extremely superior SAR and SVR performances.

The relative displacement ratio (RDR) response characteristics of sequential damper, subject to rounded pulse and step displacements respectively, are presented in Figures 14 and 15. The

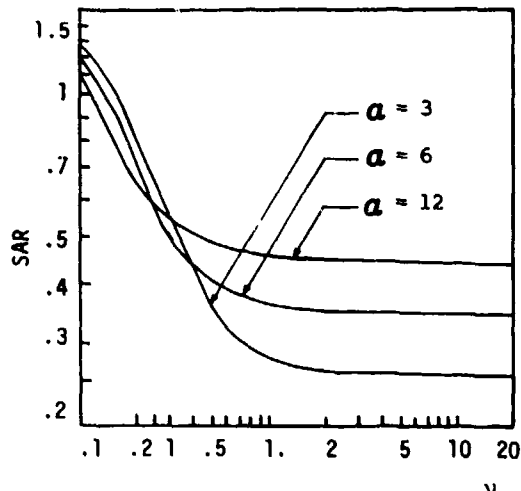


Figure 8: SAR response of passive shock isolator subject to rounded pulse displacement.

RDR characteristics of the sequential damper are deteriorated considerably corresponding to low η values and higher shock severities. However, the RDR response of the sequential damper approaches that of passive damper as the η value is increased. In case of rounded step displacement, the RDR response of sequential damper with $\eta = .25$ approaches the RDR response of passive damper at shock severity value of 50. The sequential damper with $\eta = .25$, provides SAR of 0.25 as compared to 0.45 provided by the passive damper, when subject to rounded pulse displacement. The corresponding

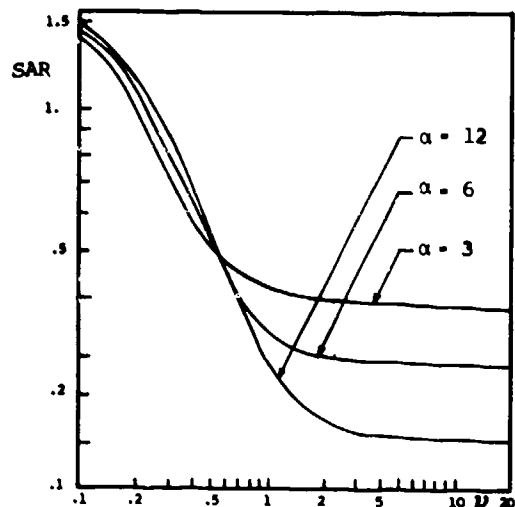


Figure 9: SAR response of passive damper.

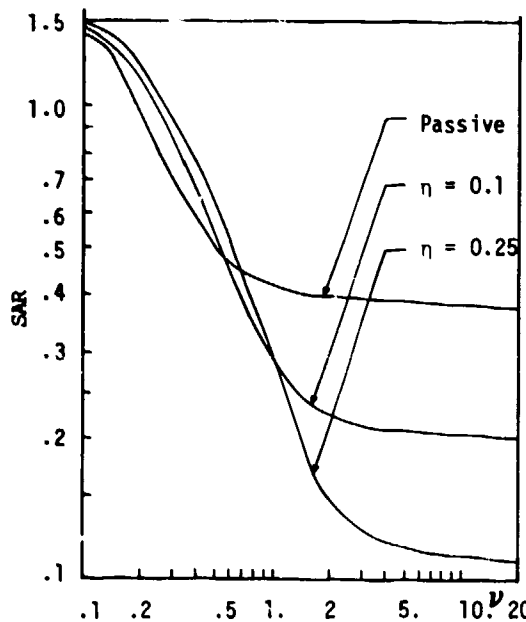


Figure 11: SAR response of sequential damper to rounded step displacement.

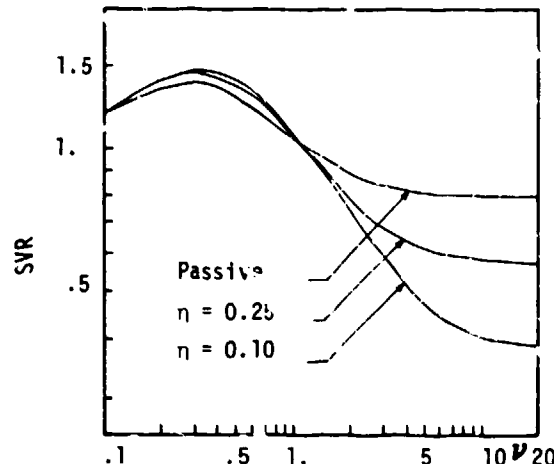


Figure 13: SVR response of sequential damper.

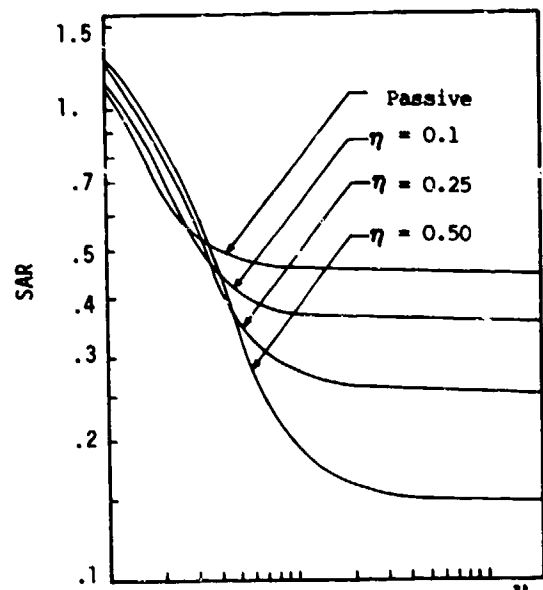


Figure 10: SAR response of sequential damper to rounded pulse displacement.

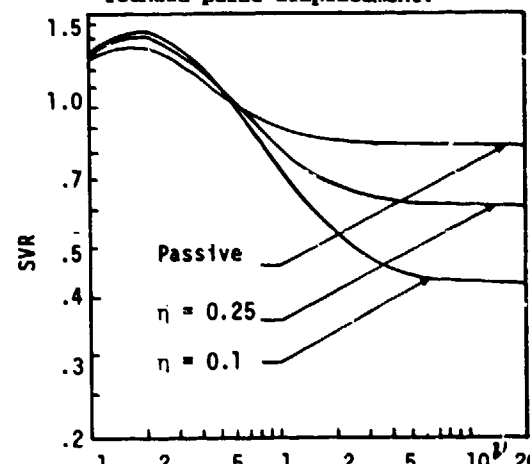


Figure 12: SVR response of sequential damper.

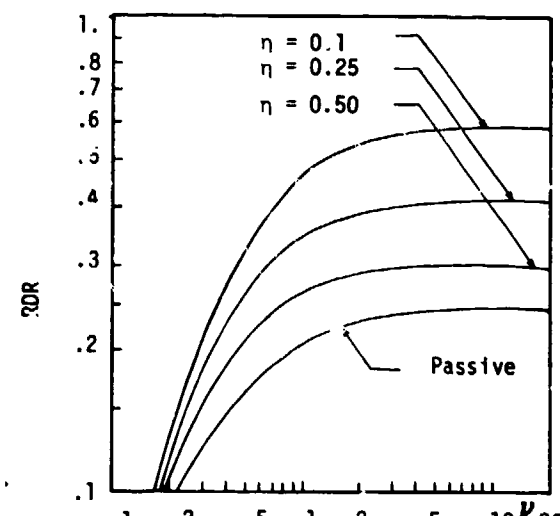


Figure 14: RDR response of sequential damper.

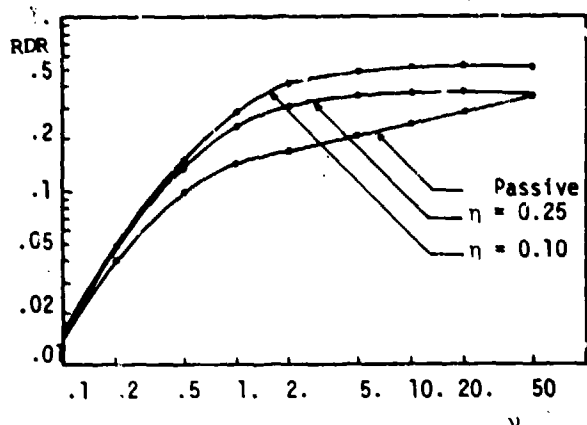


Figure 15: RDR response of passive and sequential dampers subject to rounded step displacement input.

RDR response of the sequential damper is 0.40 compared to 0.25 for the passive damper.

CONCLUSION

Isolation of equipment or human payloads, from the shock inputs, is effectively achieved through various damping mechanisms. However, the constant damping in passive shock isolation systems tends to increase the mass acceleration during a part of the oscillation cycle. Lower damping during this part of the oscillation cycle can significantly improve the isolation performance of the passive isolators. However, larger damping is required in the remaining part of the cycle to attenuate the mass acceleration. Hence, a sequential damper is devised, which provides high damping when damper acts to attenuate the mass acceleration. The damping value of the sequential damper is lowered considerably, when passive damping acts to accelerate the mass. A sequential damper may be realized by introducing a two-position valve in a conventional shock absorber, to modulate the orifice size to yield two sequences of orifice restrictions. Two control criteria are proposed and analyzed for their shock acceleration ratio (SAR), shock velocity ratio (SVR) and relative displacement ratio (RDR) characteristics. The response behaviour of the two proposed sequential dampers is identical except for their respective settling times. The response characteristics of the sequential damper reveal extremely superior SAR and SVR characteristics when compared to the similar characteristics of the passive damper, corresponding to higher shock severities. The RDR response of sequential damper is considerably greater than that obtained from a passive damper. However, the RDR response of the sequential damper approaches that of the passive damper as the value of n is increased.

REFERENCES

1. Snowdon, J.C., "Vibration and Shock in Damped

Mechanical Systems", John Wiley and Sons, New York, 1978.

2. Snowdon, J.C., "Isolation from Mechanical Shock with a Mounting System Having Nonlinear Dual Phase Damping", Shock and Vibration Bulletin 41, 21-45, 1970.
3. Mercer, J.A. and P.L. Rees, "An Optimum Shock Isolator", J. of Sound and Vibration, 18(4), 511-520, 1971.
4. Hundal, M.S., "Response of Shock Isolators with Linear and Quadratic Damping", J. of Sound and Vibration, 76(2), 723-728, 1981.
5. Caton, A.T. and R. Holmes, "Design and Performance of a Coulomb Shock Isolator", 15(4), 285-294, 1973.
6. Guntur, R.R. and S. Sankar, "Performance of Different Kinds of Dual Phase Damping Shock Mounts", J. of Sound and Vibration, 84(2), 253-267, 1982.
7. Venkatesan, C. and R. Krishnan, "Dual Phase Damping in a Landing Gear at Touch Down", J. of Aircraft, 12(10), 847-849, 1975.
8. Karnopp, D.C., M.J. Crosby and R.A. Harwood, "Vibration Control Using Semi-Active Force Generators", Trans. ASME, J. of Eng. for Ind. 96(B), 619-626, 1974.
9. Margolis, D.L., "The response of Active and Semi-Active Suspensions to Realistic Feedback Signals", Veh. System Dynamics, 11, 267-282, 1982.
10. Rakheja, S., "Computer-Aided Dynamic Analysis and Optimal Design of Suspension Systems for Off-Road Tractors", PhD Thesis, Concordia University, Montreal, Nov. 1983.
11. Margolis, D.L., "Semi-Active Suspensions for Military Ground Vehicles under Off-Road Conditions", Shock and Vibration Symp., 52, Oct. 27-29, 1981.

Acknowledgement

The authors acknowledge the financial assistance provided by Natural Sciences and Engineering Research Council of Canada.

LIQUID SPRING DESIGN METHODOLOGY FOR SHOCK ISOLATION SYSTEM APPLICATIONS

Marek L. Wintarz, P.E.

The BDM Corporation

Albuquerque, New Mexico

Liquid springs are one of the less well known types of spring/damper systems available to the shock isolation system designer. This paper describes current liquid spring applications, characteristics, and provides a simplified order-of-magnitude method for estimating size and weight of a liquid spring in any proposed application. This work was performed under contract funded by U.S. Army Corps of Engineers Omaha District.

INTRODUCTION

Among the various hardening strategies, shock isolation is the most important. Shock isolation systems are used in a wide spectrum of applications, from isolating personnel and equipment from road shock in surface vehicles, to mitigating nuclear weapons induced environment in missile silos. No other hardening scheme offers as much for the money as an effective shock isolation system.

All shock isolation systems use some type of force transmission limiting device, most commonly a spring/damper system, though other types of force limiting devices such as crushable or deformable media can be used in some specific, one-time applications.

Of the spring damper combinations, the most common are steel springs with external dampers, elastomer springs, pneumatic springs, and liquid springs. Steel springs include a variety of configurations such as leaf, helical (coil), torsion, constant force (clock type), and others with liquid dampers (automotive shock absorbers) or friction dampers. Elastomer springs include "rubber band" types, sometimes wound so that the adjacent layers expand at different rates thus providing damping by friction between layers. Foams are also examples of elastomeric spring media where air provides damping as well as some spring force when it is squeezed out of the foam cells. Foams have large hysteresis. Pneumatic or gas springs are pistons in cylinders compressing gaseous fluids. Internal orifices are used for damping.

Liquid springs resemble pneumatic springs except the spring force is achieved by compressing a liquid fluid. Damping is achieved by forcing the liquid through internal orifices.

For the sake of completeness it should be mentioned that hybrid systems, such as hydropneumatic springs, may be used to achieve specific tuning characteristics.

The liquid spring designs and applications have existed for years, and have gained wide acceptance in some areas. For the community at large, however, the liquid spring remains a largely esoteric device. The purpose of this paper is to acquaint the community with the characteristics of liquid springs, and to present a simplified "cookbook" methodology to allow a designer to evaluate whether a liquid spring is an appropriate device for his application.

DESCRIPTION OF LIQUID SPRINGS

The simplest type of compression type liquid spring is shown in Figure 1. It consists of four main components: cylinder, piston, compressible liquid, and seal. As the force is applied to the spring, the piston is inserted into the liquid. The corresponding decrease in volume of the liquid raises the internal pressure which acts on the opposite end of the piston resisting the applied force. The working pressure in the liquid reaches 276,000 kPa (40,000 psi) at the end of the stroke. At neutral (unloaded) position the springs are typically precharged to 10% of the maximum working pressure.

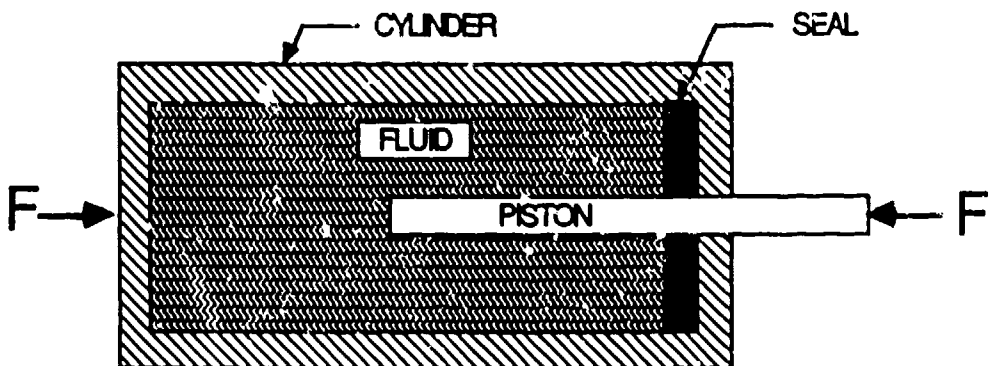


Figure 1. Simple Liquid Spring Schematic

The structural steel components, i.e., the cylinder and the piston, are fabricated from high strength 1,100,000 kPa (160 ksi) steel, typically ASTM 4340 heat treated. Since the springs operate at pressures as high as 276,000 kPa (40,000 psi), the pressure vessels (cylinders) are machined from a solid billet, shot peened, and stress relieved to achieve a long operating life. The pistons are finished to an exacting 0.2 micrometers (8 microinches) or less to achieve proper sealing.

The working fluid is typically a silicone oil of approximately 15% compressibility (roughly the same as water) at 250,000 kPa. The oil viscosities can be formulated over a wide range but 50-100 cS (centistokes) is a common range (Kinematic viscosity of water is 1 cS at 20 deg. C). It must be noted that viscosity varies widely with temperature, pressure, and rate of deformation. The numbers given are at STP, and may differ in actual applications.

The spring rate is dependent on the bulk modulus of the fluid which increases approximately linearly from 690,000 kPa at atmospheric pressure to 3,000,000 kPa at 250,000 kPa applied pressure (Figure 2).

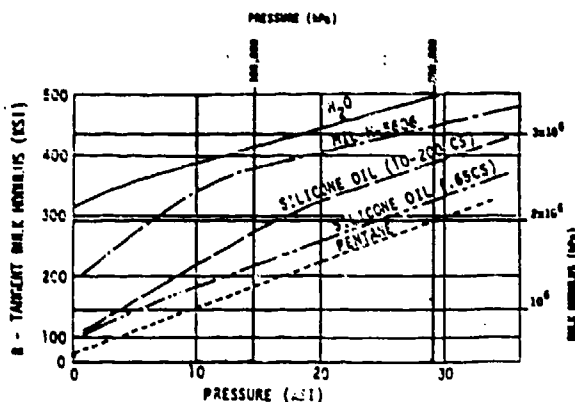
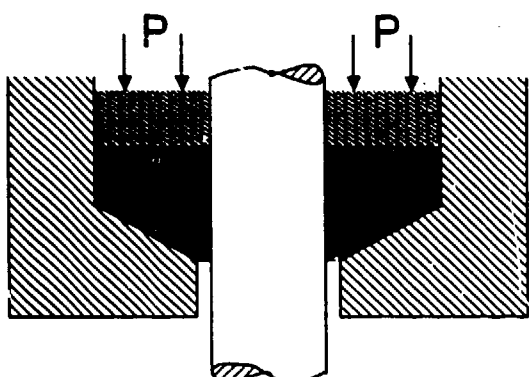
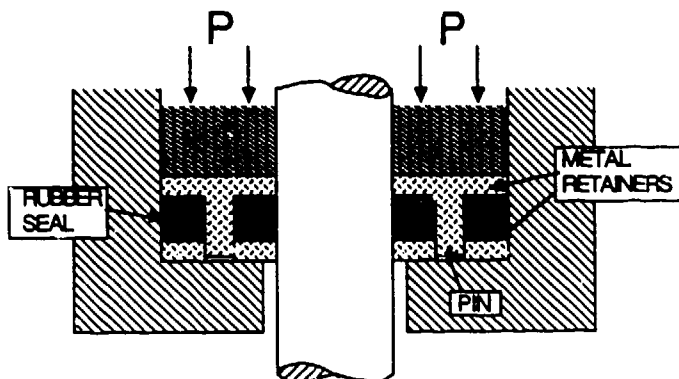


Figure 2. Bulk Modulus for Various Fluids



a. Differential Area Seal



b. Poisson Effect Seal

Figure 3. Liquid Spring Seal Types

Two common types of seals are used: differential area and Poisson effect. The differential area seal, shown in Figure 3a, works on the principle of pressing tighter against the piston and the cylinder as the pressure increases by virtue of its geometry. The Poisson effect seal is a sandwich of rubber between two metal plates. As the pressure increases, the rubber is squeezed longitudinally and grows radially, thus pressing against the piston and cylinder. Sometimes pins are used to decrease the effective rubber area thus increasing the pressure in the rubber beyond the pressure in the fluid. Both types of seals have been proven effective in liquid spring applications. In fact, burst tests show that cylinder structures fail before seals do. In other very high pressure applications, differential area seals are effective in excess of 3,500,000 kPa (500 ksi).

Damping is accomplished by use of damping or "drag" plates (Figure 4). The drag plates limit the area through which liquid flows around the piston, thus providing resistive force as a function of piston velocity. In actual applications the damping provides 50% or more of the resistive force. A solid drag plate is the simplest damping mechanism. Alternatively a drag plate may have a seal around it and orifices through it to allow liquid flow. Some structural rigidity may be gained by this approach (Figure 5a). The orifices may have check valves to tune damping as a function of direction, position, or velocity (Figure 5b). Finally, a sleeve may be used to vary the damping as a function of position. By covering the orifices at the end of the stroke, this design provides a "soft stop", preventing crashing the piston into the cylinder structure (Figure 5c). A combination of these mechanisms may be used to tune the damping to the designer's specifications. Additionally, the seals provide some frictional damping force, however the overall contribution is small.

In addition to the compression type, two more liquid spring configurations exist: extension or tension type and a combination compression-extension. The extension liquid spring, shown in Figure 6, works by insertion of a larger diameter rod into the liquid, thus compressing the fluid. The expansion spring has two seals, one at each end. A disadvantage of the extension spring is that this configuration is longer as the structure must have adequate space to contain the thick portion of the rod.

The compression-extension spring is a "folded" design, compressing the fluid regardless of whether the spring is extended or compressed. This design is shown in Figure 7 in the neutral, extended, and compressed configurations. The added flexibility comes at a price of increased weight and complexity.

LIQUID SPRING CHARACTERISTICS

Liquid springs have many virtues that are applicable in a wide range of applications. Since the working fluid is relatively incompressible and has a high bulk modulus, a very high spring rate can be achieved in a compact package. The spring rate can be easily tuned by varying the piston area and/or the volume of the liquid.

The liquid remains stable at high pressures and returns to the original volume and pressure after compression. The limiting factor for liquids is the phase change which occurs at high pressures (water becomes solid at 700,000 kPa (100 ksi)). However, the practical spring rate limiting factor is the structural capacity of the pressure cylinder. The spring becomes impractical when the size and weight of the structure become too great and negate the space saving advantages.

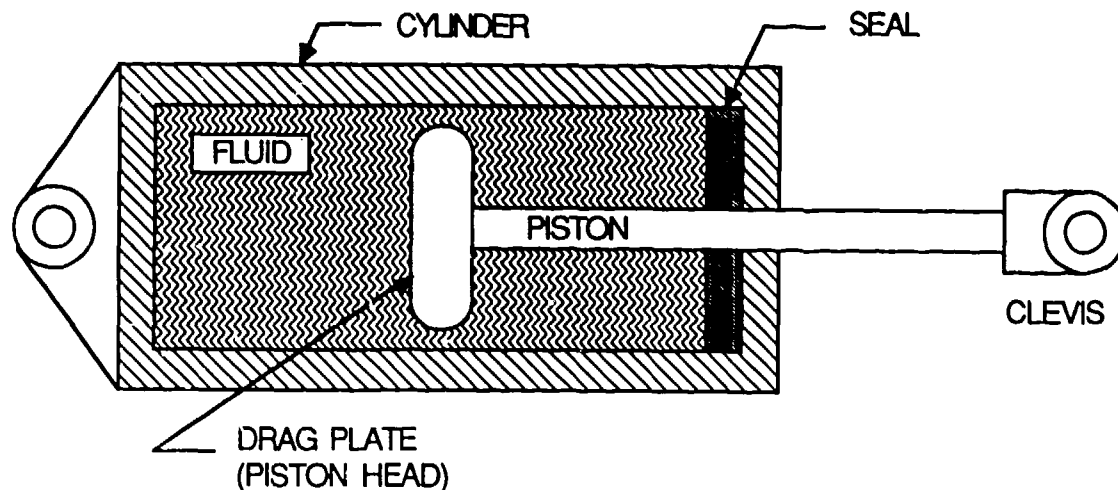
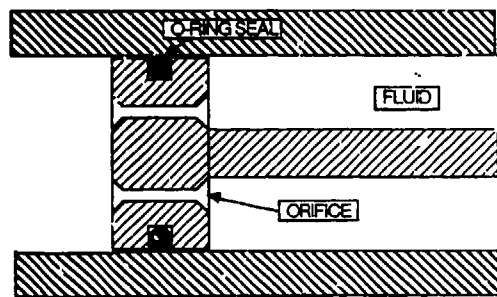
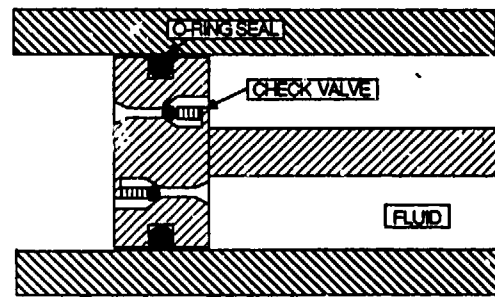


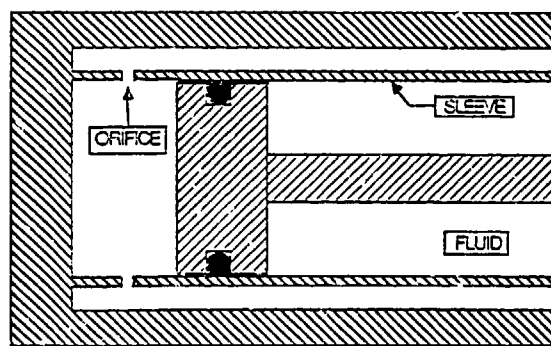
Figure 4. Compression Type Liquid Spring



a. Drag Plate with Orifice



b. Drag Plate with Check Valve Orifices



c. Sleeve Damping Mechanism

Figure 5. Typical Damping Mechanisms

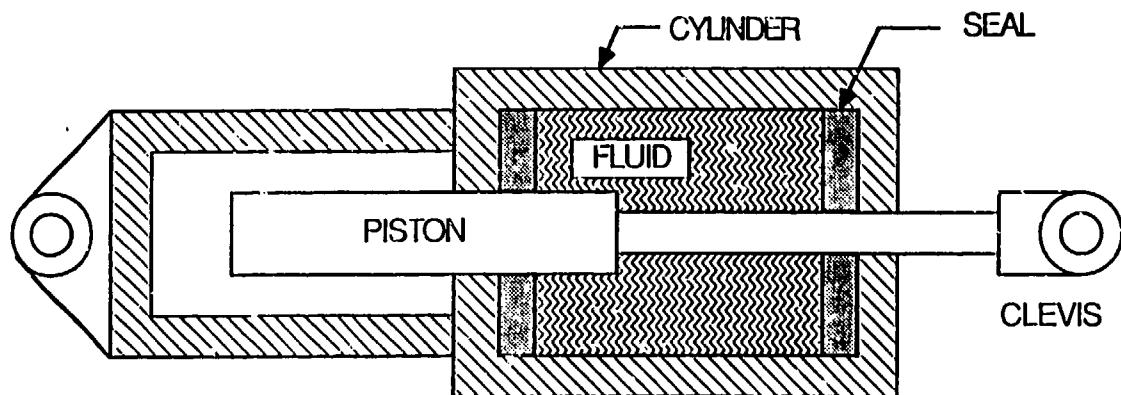


Figure 6. Extension Type Liquid Spring

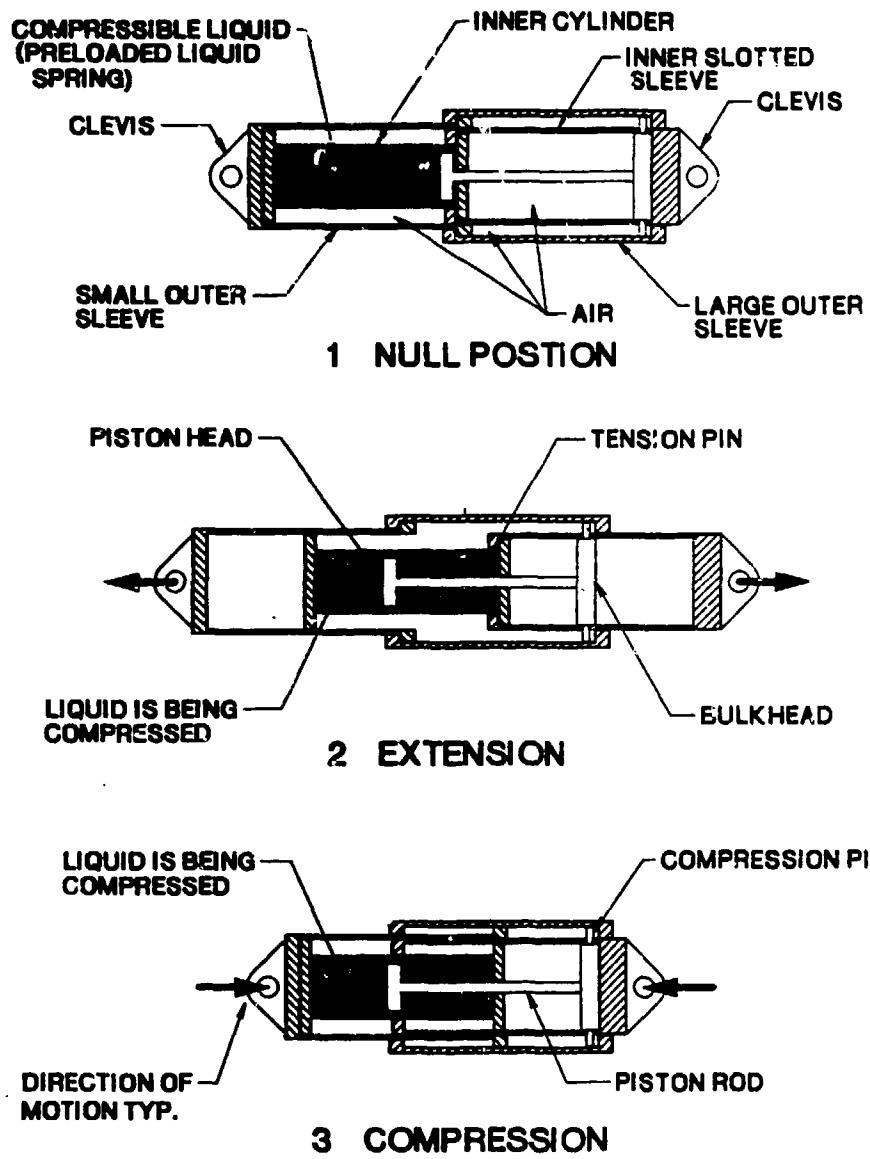


Figure 7. Compression/Tension Liquid Spring

The liquid spring medium exhibits no fatigue. This makes the spring ideal in applications where repeated loadings occur. Liquid spring response characteristics remain constant throughout its life, assuming no loss of liquid and no loss of rigidity in the spring structure. The spring structure does experience fatigue, however the strain magnitude of the structure is small compared to the strain of the liquid.

The liquid spring medium exhibits no creep. Therefore it is ideal in static applications where a constant preload must be maintained. Additionally, liquid spring can support various loads with no deflection (or a desired deflection) by varying the preload pressure in the liquid.

Liquid springs are reliable. Barring initial quality problems, several off-the-shelf designs exist with a known track record in various applications.

APPLICATIONS

The most numerous application of liquid springs has been in the aircraft landing gear applications. Virtually every commercial and military aircraft uses liquid springs as its landing shock mitigation system. Passenger aircraft such as Boeing 707, 727, 737, 767; McDonnell Douglas DC-10, and Lockheed L-1011 are a few examples. Fighter aircraft such as General Dynamics F-16 and Fairchild Republic A-10 use them. Liquid spring landing gear is also used on the Space Shuttle orbiters, Rockwell International B-1 Bombers (Figure 8), and numerous helicopters. These applications make use of the liquid springs' ability to mitigate repeated shock loadings, their compact size, and their light weight.

The liquid springs' static support ability with no creep has been an advantage in Minuteman missile silos and launch control facilities. Liquid springs have a very good maintenance-free record in this application.

In addition, liquid springs are used in facilities such as conventional and nuclear power plants to protect the equipment against seismic loads, in ships to isolate decks against underwater explosions, in submarines to protect missiles and launch tubes, and in large caliber guns to absorb recoil loads.

DESIGN METHODOLOGY INTRODUCTION

The following section presents a simplified step-by-step design methodology to allow the shock isolation system designer to estimate the approximate dimensions and weight of a liquid spring for his application. It must be stressed that the method presented here serves only to determine the approximate spring configuration. The actual spring behavior is quite complex as the specific fluid characteristics such as bulk modulus, viscosity, and compressibility are functions of temperature, pressure, and force application rate. Also a 10% variability may be expected in all parameters. In addition effects such as "breathing" (cylinder expansion due to increased internal pressure) further complicate the behavior.



Figure 8. Liquid Springs in Landing Gear Application

For these reasons no exact analytical procedure exists. Detailed design performed by liquid spring manufacturers is performed by mostly empirical methods supported by extensive testing to obtain the desired spring and damping characteristics.

The method presented here is for a compression type liquid spring. A second generation, enhanced version of this methodology, the theory, and additional methods for extension and compression-extension liquid springs may be found in Reference 1. Some of the background information comes from the Air Force Design Manual (Reference 2). No dynamic analysis was attempted - the stroke was assumed to be equal to the rattlespace requirement.

During the development of this methodology, the author wrote a BASIC computer program for the Apple II microcomputer which follows the steps presented below. This program, as well as ones for the extension and the compression - extension liquid spring types may be shared with interested individuals.

DESIGN PROCEDURE

Refer to Figure 9 for dimensional variables in the procedure. The procedure was developed using English units: inches, pounds, seconds.

1. Determine the compressive stroke (X) requirement. For weapons induced environments the stroke is assumed to be equal to the rattlespace requirement.
2. Determine the weight (W) of the mass to be shock isolated.
3. Determine the maximum allowed acceleration (A_{max}) of the object to be shock isolated.
4. Define the maximum spring operating pressure (P_{max}). A typical value is 276,000 kPa (40,000 psi).

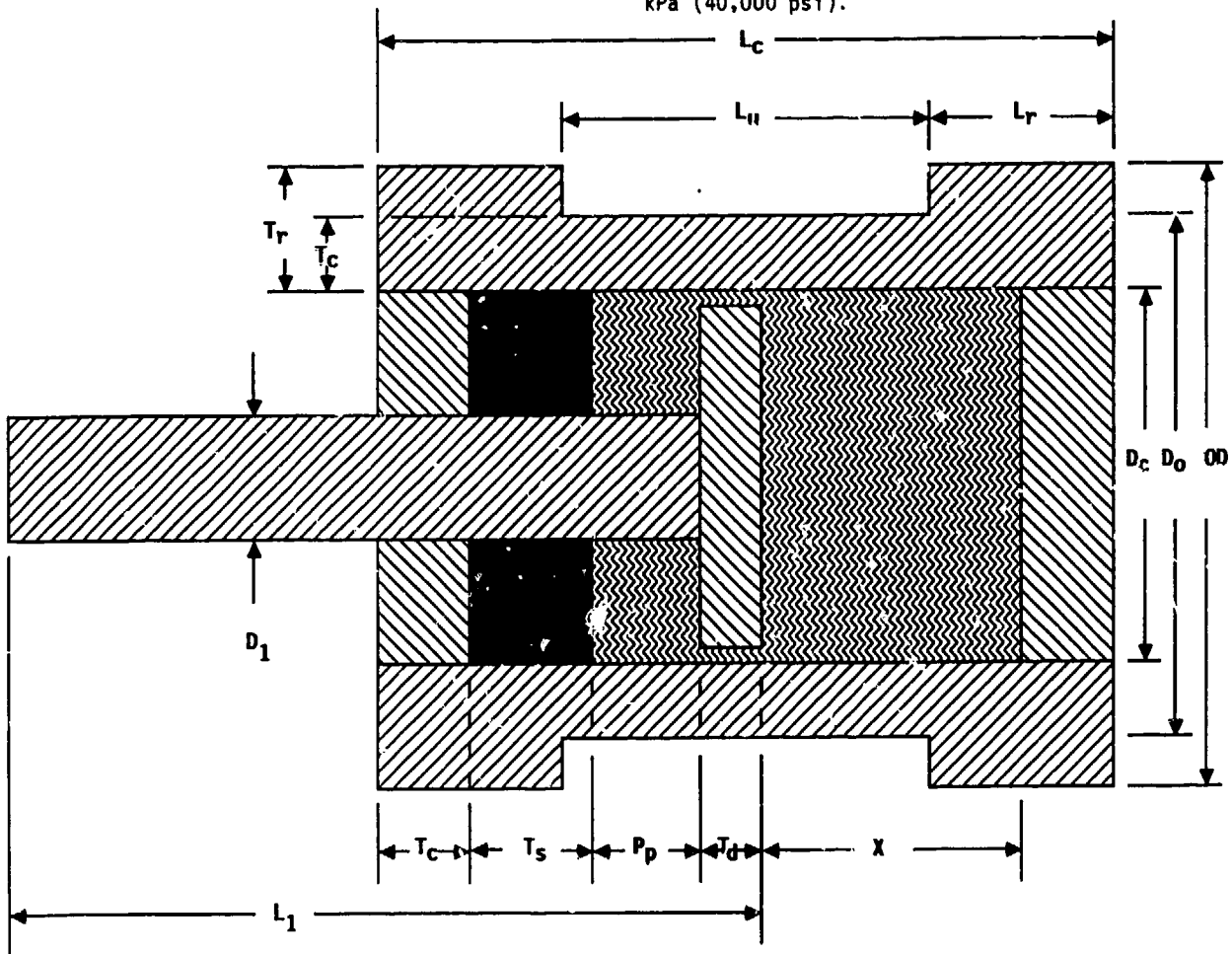


Figure 9. Compression Liquid Spring Geometry

5. Define the yield and ultimate stresses of the steel structure. A typical material is ASTM 4340 heat treated steel.

$$\text{Yield stress } \sigma_y = 980,000 \text{ kPa} \\ (142,000 \text{ psi})$$

$$\text{Ultimate stress } \sigma_u = 1,100,000 \text{ kPa} \\ (160,000 \text{ psi})$$

6. Determine the safety factors. These vary with application, however minimum safety factors for dynamic loads as recommended by liquid spring manufacturers are:

$$\text{Yield safety factor } N_y = 1.25 \\ \text{Ultimate safety factor } N_u = 2.0$$

7. Define material densities. These will be used to estimate the weight of the spring. In this procedure the density of the seals is assumed to be equal to the density of steel. Typical values are:

$$\text{Density of steel } \rho_s = 7.84 \text{ g/cm}^3 \\ (0.283 \text{ lb/in}^3)$$

$$\text{Density of fluid } \rho_l = 0.97 \text{ g/cm}^3 \\ (0.35 \text{ lb/in}^3)$$

(Dow Corning 200 cS Silicone Oil)

8. Determine externally applied preload force (F_p). This is the force necessary to carry a static load. This load will determine the preload pressure in the liquid. If no static load is to be carried, or if the load is lighter than the normal preload pressure will support, then the preload pressure will be 10% of the maximum working pressure (27,600 kPa).

9. Determine the preload position (P_p). Preload position is the position of the piston displaced from the fully extended position (it can be zero). Total stroke (S) is:

$$(1) S = X + P_p$$

10. Calculate total maximum force (F_m).

This maximum force contains both the spring force and the damping force components.

$$(2) F_m = A_m \times W / C_g$$

where A_m is allowable acceleration
 W is the weight of the object
 C_g is the gravitational constant
 (386.4 in/sec^2)

11. Calculate the maximum spring component of the force (F_k). Assume that the spring force provides one-half of the maximum force contribution.

$$(3) F_k = 0.5 \times F_m$$

12. Calculate the preload force (F_f) which the spring will support with no deflection. This is normally 10% of the maximum spring force.

$$(4) F_f = 0.1 \times F_k$$

13. If the externally applied static load (F_p from step 8) exceeds the normal preload force in step 12, then the external preload force is used.

$$(5) \text{If } F_f < F_p \text{ then } F_f = F_p$$

14. Calculate the spring rate (k). Assume a linear spring.

$$(6) k = (F_k - F_f) / X$$

15. Calculate the effective piston area (A_e).

$$(7) A_e = k \times X / P_{max}$$

16. Calculate the piston diameter (D_1)

$$(8) D_1 = (4 \times A_e / \pi)^{1/2}$$

17. Check for buckling resistance. The buckling analysis was done using the methods in Reference 3. Complete derivation is shown in Reference 1. Calculate the minimum or critical rod diameter (D_{min}).

$$(9) D_{min} = (64 \times F_m \times (S + 2)^2 / (\pi^3 \times E))^{1/4}$$

where E is Young's Modulus = 29,000,000 for steel

and $S + 2$ is the length of the rod.

The 2 (inches) is an arbitrary addition to the length of the rod and may be changed depending on specific circumstances.

18. If the minimum buckling diameter (D_{min}) is greater than D_1 then this is the diameter that must be used. Effective piston area will be changed as well.

$$(10) \text{ If } D_{min} > D_1 \text{ then } D_1 = D_{min}$$

$$\text{and } A_e = \pi \times D_1^2 / 4$$

In addition maximum spring operating pressure must be changed to satisfy equation 7.

$$(11) P_{max} = k \times X / A_e$$

19. Calculate compressibility (C) from maximum spring operating pressure (Figure 10). Compressibility may also be scaled approximately from the curve.

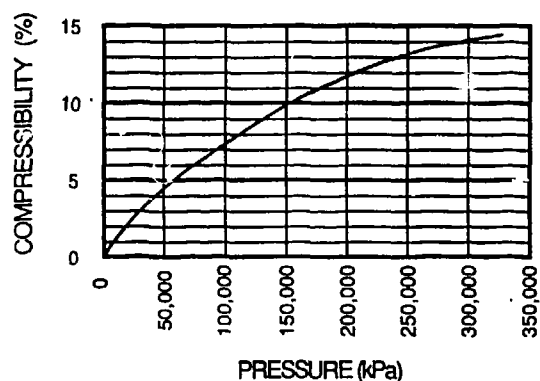


Figure 10. Silicone Fluid Compressibility

A curve fit equation was developed which allows calculation of compressibility. Procedure is as follows:

19a. Convert maximum operating pressure from pounds per square inch (psi) to thousands of pounds per square inch (ksi)

$$(12) P = P_{max} / 1000$$

19b. Solve curve fit equation

$$(13) C' = 8.0 + 0.373827 \times (P - 16.172) \\ - 0.00645 \times (P - 16.172)^2 \\ + 0.0001667 \times (P - 16.172)^3 \\ - 0.0000059 \times (P - 16.172)^4 \\ + 0.00000003 \times (P - 16.172)^5$$

19c. Convert from percent to decimal

$$(14) C = C' \times 0.01$$

20. Calculate the liquid volume (V_0)

$$(15) V_0 = A_e \times X / C$$

21. Determine the working stress (σ_w) from steel properties and safety factors (steps 5 and 6)

$$(16) \sigma_1 = \sigma_y / N_y$$

$$(17) \sigma_2 = \sigma_u / N_u$$

Use the lesser of the two:

$$(18) \text{ If } \sigma_1 < \sigma_2 \text{ then } \sigma_w = \sigma_1$$

$$(19) \text{ If } \sigma_2 < \sigma_1 \text{ then } \sigma_w = \sigma_2$$

22. Calculate the inside diameter of the cylinder (D_c)

$$(20) D_c = ((4 \times V_0 / \pi + D_1^2 \times P_p) / (X + P_p))^{1/2}$$

23. Calculate the drag plate thickness (T_d). This is a scaling procedure based roughly on the dimensions of currently existing liquid springs.

$$(21) \quad T_d = 0.2 \times D_c$$

24. Calculate the seal thickness (T_s). This is also a scaling procedure as in Step 23 above.

$$(22) \quad T_s = 0.3 \times D_c$$

25. Calculate the outside diameter (D_o) of the pressure cylinder. Complete derivation is presented in Reference 1 based on methods in Reference 4.

$$(23) \quad D_o = D_c \times (\sigma_w / (\sigma_w - P_{max}))^{1/2}$$

or

$$(24) \quad D_o = D_c \times \exp(P_{max} / \sigma_w)$$

Use the greater value of D_o from equations 23 and 24.

26. Calculate the cylinder wall thickness (T_c) from the outside and inside diameters of the cylinder.

$$(25) \quad T_c = (D_o - D_c) / 2$$

27. Near the ends of the cylinder additional stresses exist due to bending near the end plates. The cylinder wall thickness is greater in these regions by approximately 50%. Calling it the reinforced section of the cylinder, the reinforced wall thickness (T_r) is scaled from the unreinforced wall thickness.

$$(26) \quad T_r = 1.5 \times T_c$$

28. Calculate the outside diameter of the reinforced section of the cylinder (OD)

$$(27) \quad OD = D_c + (2.0 \times T_r)$$

29. Calculate the end plate thickness (T_e). The end plate thickness is scaled from existing spring designs and it equals approximately twice the reinforced cylinder wall section.

$$(28) \quad T_e = 2.0 \times T_r$$

30. Calculate the reinforced section length. This is a scaled dimension from existing designs and it equals approximately 2.5 times the thickness of the end plates.

$$(29) \quad L_r = 2.5 \times T_e$$

31. Calculate the total cylinder length (L_c).

$$(30) \quad L_c = S + T_s + T_d + (2.0 \times T_e)$$

32. Calculate the unreinforced cylinder section length (L_u).

$$(31) \quad L_u = L_c - (2.0 \times L_r)$$

33. Calculate the rod length (L_1).

$$(32) \quad L_1 = S + T_s + T_e + T_d + 2.0$$

where 2.0 (inches) is added arbitrarily and may be changed depending upon application. It means that 2 inches of the rod remain outside the cylinder at full compression.

34. Calculate fully extended spring length (L_x).

$$(33) \quad L_x = L_c + L_1 - T_e - T_s - T_d$$

35. Calculate fully compressed (minimum) length (L_{min}).

$$(34) \quad L_{min} = L_c + 2.0$$

36. Calculate volume of steel in the unreinforced section of the cylinder (V_u).

$$(35) \quad V_u = \pi / 4 \times (D_o^2 - D_c^2) \times L_u$$

37. Calculate volume of steel in the reinforced sections of the cylinder (V_r).

$$(36) \quad V_r = \pi / 4 \times (OD^2 - D_1^2) \times 2.0 \times L_r$$

38. Calculate volume of the end plate on the rod side of the cylinder (V_{e1}).

$$(37) \quad V_{e1} = \pi / 4 \times (D_c^2 - D_1^2) \times T_e$$

39. Calculate volume of the end plate on opposite side (V_{e2}).

$$(38) \quad V_{e2} = \pi / 4 \times D_c^2 \times T_e$$

40. Calculate volume of the seal (V_s)

$$(39) \quad V_s = \pi / 4 \times (D_c^2 - D_1^2) \times T_s$$

∴ Calculate volume of drag plate (V_d).

$$(40) \quad V_d = \pi / 4 \times (D_c^2 - D_1^2) \times T_d$$

42. Calculate volume of the piston rod (V_1).

$$(41) \quad V_1 = A_e \times L_1$$

43. Calculate total volume of steel (V_t). For the purpose of this calculation it is assumed that the seal is made of steel.

$$(42) \quad V_t = V_u + V_r + V_{e1} + V_{e2} + V_s + V_d + V_1$$

44. Calculate the weight of steel in the liquid spring (W_s).

$$(43) \quad W_s = V_t \times \rho_s$$

45. Calculate the weight of liquid in the spring (W_1).

$$(44) \quad W_1 = V_1 \times \rho_e$$

46. Calculate total weight of the liquid spring (W_t).

$$(45) \quad W_t = W_s + W_1$$

The above procedure calculates the necessary parameters to determine the order-of-magnitude spring geometry and weight.

EXAMPLE

The example in Figure 11 shows the calculated parameters for sample shock isolation criteria.

* LIQUID SPRING.COM *
* MAREK L. WINIARZ *
* REV 2, SEPT 28, 1986 *

INPUT PARAMETERS

MAX FREE FIELD DISPLACEMENT IS 24 INCHES
MAX ACCELERATION ALLOWABLE IS 1.1 G'S
WEIGHT OF ISOLATED MASS IS 40000 LB
MAX SPRING OPERATING PRESSURE IS 17326.4368 PSI
MATERIAL YIELD STRESS IS 142000 PSI
MATERIAL ULTIMATE STRESS IS 160000 PSI
YIELD SAFETY FACTOR IS 1.25
ULTIMATE SAFETY FACTOR IS 2
PRELOAD POSITION IS 0 IN
SPRING PRELOAD FORCE IS 2200 POUNDS

OUTPUT PARAMETERS

SPRING DIMENSIONS
SPRING OUTSIDE DIAMETER IS 3.7453966 IN
CYLINDER LENGTH IS 27.3877103 IN
CYLINDER INSIDE DIAMETER IS 2.73538863 IN
ROD DIAMETER IS 1.20623856 IN
FULLY EXTENDED LENGTH IS 53.3877103 IN
FULLY COMPRESSED LENGTH IS 29.3877103 IN
TOTAL STROKE IS 24 IN

LIQUID VOLUME IS 141.038874 IN^3

WEIGHT OF SPRING IS 46.8663728 LB

Figure 11. Liquid Spring Design Example

ACKNOWLEDGEMENTS

The author wishes to express gratitude to the U. S. Army Corps of Engineers Omaha District who funded this work under Contract No. DACA45-86-D-0027. Special thanks go to Mr. Bill Gaube, Chief Structural Engineer.

Additional thanks go to the BDM team members: Mr. E. J. Dorchak, Program Manager, Mr. M. F. Hessheimer, for methodology review, as well as Mr. M. E. Patton and Dr. H. B. Ebrahimi for technical assistance.

Boeing Aerospace Co. and Menasco Inc. deserve special recognition for their assistance in describing liquid spring characteristics, applications, and design details.

REFERENCES

1. The BDM Corp., Deliverable No. 3: Shock Isolation Studies, Isolator Hardware, Final Report, July 22, 1986. Delivered to U.S. Army Corps of Engineers Omaha District under Contract No. DACA45-86-D-0027.
2. R. E. Crawford, C. J. Wiggins, and E. H. Bultmann, "The Air Force Manual for Design of Hardened Structures", Air Force Weapons Laboratory, AFWL-TR-74-102.
3. J. E. Shigley, "Mechanical Engineering Design", McGraw-Hill, 1977.
4. R. J. Roark and Warren C. Young, "Formulas for Stress and Strain", McGraw-Hill, 1982.

DESIGN AND TEST OF A SPACECRAFT INSTRUMENT SHOCK ISOLATOR

D. Schiff, N. Jones and S. Fox
Assurance Technology Corporation
Carlisle, Massachusetts

A shock isolator is required to protect the accelerometer in a satellite attitude control system against pyrotechnic shock. This shock isolator must also yield an acceptable response to the random vibration environment, maintain angular alignment within 0.25 degrees of arc, and meet restrictive weight and volume requirements. The time available for design, fabrication and test precluded the custom fabrication of elastomeric parts. After consideration of several design concepts, an approach was selected which utilizes commercially available O-Rings as the springs for the shock isolator. The final design provided acceptable accelerations at the attitude control system when tested to the specified shock and vibration environments, and maintained angular alignment well within required limits.

1.0 INTRODUCTION

Some spacecraft are equipped with an Attitude Control System (ACS) which contains Accelerometer Sensor Assemblies (ASA). These ASAs are used on spinning orbital space vehicles as part of an active nutation control system. They must perform to specification after being subjected to pyrotechnic shock and random vibration environments, and they must also maintain their angular alignment with respect to the mounting plane. A shock isolator is required to protect the ASA from the shock environment.

This paper describes the design and test of an ASA shock isolator for a specific application, but the methods and analysis may be used for the design of other instrument shock isolators. In the present case, in addition to shock reduction, the isolator must yield an acceptable response to the random vibration environment, maintain the angular alignment within 0.25 degrees, fit within a 2.4 inch diameter x 1.8 inch high envelope and weigh less than 0.6 pounds. Commercially available shock isolators are too large and too soft and will not maintain angular alignment after exposure to the acceleration environments. The time that was available for design, fabrication and test of the shock isolator precluded the custom fabrication of an elastomeric part. After consideration of several design concepts, an

approach was selected which utilizes commercially available silicone O-Rings as the shock isolator spring elements, integrated with readily machined aluminum and stainless steel parts.

2.0 ACCELERATION ENVIRONMENTS AND ACCELEROMETER CHARACTERISTICS

The pyrotechnic shock acceleration response spectrum and the random vibration power density spectrum specified for the shock isolator are shown in Tables 1 and 2, respectively. These specifications were estimates of the shock and vibration environment to which the shock isolator would be exposed, and they were used as design guidelines. It was subsequently discovered, in pyrotechnic shock testing of the flight configuration, that the actual pyrotechnic shock environment was more severe than specified at some frequencies. See Section 7.0.

The accelerometer is tested by the manufacturer to meet all performance specifications after being subjected to a 250g peak, 11 millisecond, half sine shock in three mutually perpendicular axes and a 25g (peak) sine sweep from 20Hz to 2,000Hz in all axes. The accelerometer body is 1.00 inch diameter x 1.00 inch high, with a 1.16 inch square mounting flange, and a total weight of 0.143 lbs. Two views of the accelerometer are shown in Figure 1.

TABLE 1
PYROTECHNIC SHOCK RESPONSE SPECTRUM

FREQUENCY (Hz)	SHOCK RESPONSE ACCELERATION (g)
100	48
100-3,400	+7.0dB/Octave
3,400-6,000	2828
6,000-10,000	-3.4dB/Octave
10,000	2121

NOTES.

1. Shock testing is done when the accelerometer is non-operational.
2. The test tolerance is ± 3 dB of the specified acceleration from 100Hz to 3,000Hz. Above 3,000Hz, the acceleration is maintained as close as possible to specified values within the limits of the test facility.
3. The shock is imposed in both directions in each of three mutually perpendicular axes for a total of six shocks.

TABLE 2
RANDOM VIBRATION POWER DENSITY SPECTRUM

FREQUENCY (Hz)	POWER SPECTRAL DENSITY (g ² /Hz)
20	0.02
20-60	+10 dB/Octave
60-200	0.80
200-400	-4 dB/Octave
400	0.32
400-2,000	-9dB/Octave
2,000	0.0026

NOTES.

1. Grms = 16.7g, with a $\pm 10\%$ tolerance.
2. Random vibration testing is done when the accelerometer is non-operational.
3. The tolerance is ± 1.5 dB of the specified power spectral density from 20Hz to 500Hz, and ± 3.0 dB from 500Hz to 2,000Hz.
4. The random vibration is imposed for 120 seconds in each of three mutually perpendicular axes for a total of 360 seconds.

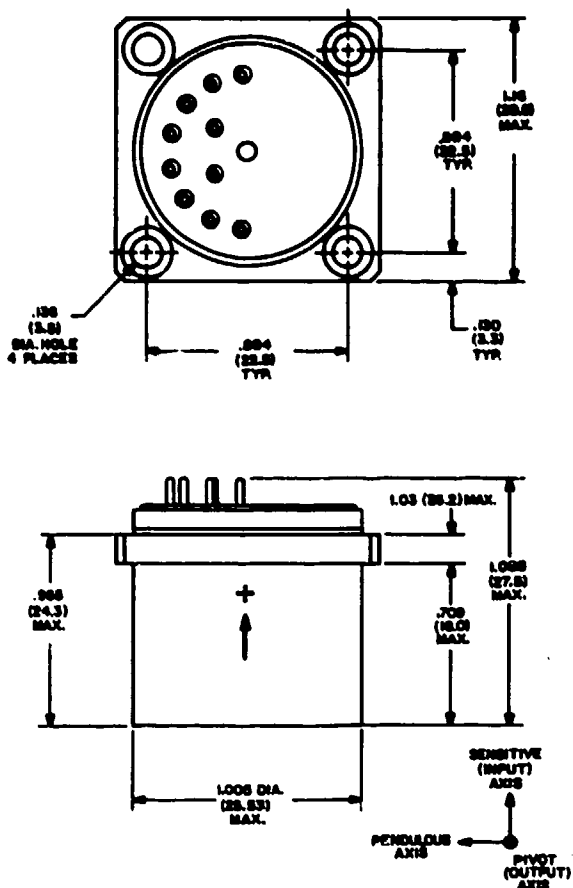


FIGURE 1: ACCELEROMETER OUTLINE

3.0 SELECTION OF SHOCK ISOLATOR FUNDAMENTAL NATURAL FREQUENCY

Applying the normalized, four coordinate shock spectrum⁽¹⁾ with 5% damping to the 250g peak, 11 millisecond half sine shock pulse (used by the manufacturer for quality assurance test purposes) characterizes the shock response acceleration as shown in Figure 2. The manufacturer also provided the information that the accelerometer component which failed, at acceleration levels much greater than 250g, has a fundamental natural frequency in the range of 2,000Hz to 2,500Hz. Based on this data, a design parameter was imposed on the shock isolator that its fundamental natural frequency, F_0 , correspond to a response acceleration of less than 250g as determined from the specified pyrotechnic shock response spectrum of Table 1. This results in an upper limit of $F_0 = 415\text{Hz}$.

The maximum value of the 3-sigma peak acceleration (G_{pk}) due to the random vibration environment specified in Table 2 is $G_{pk} = 117\text{g}$ which occurs at $F_0 = 200\text{Hz}$. This value of G_{pk} was obtained using a value of transmissibility, $Q = 6$, in the equation

$$(1) G_{pk} = 3 (\pi/2 \cdot PSD \cdot Q \cdot F)^{1/2}, \text{ where PSD = power spectral density.}$$

The value $Q = 6$ was found to be approximately correct when the shock isolator

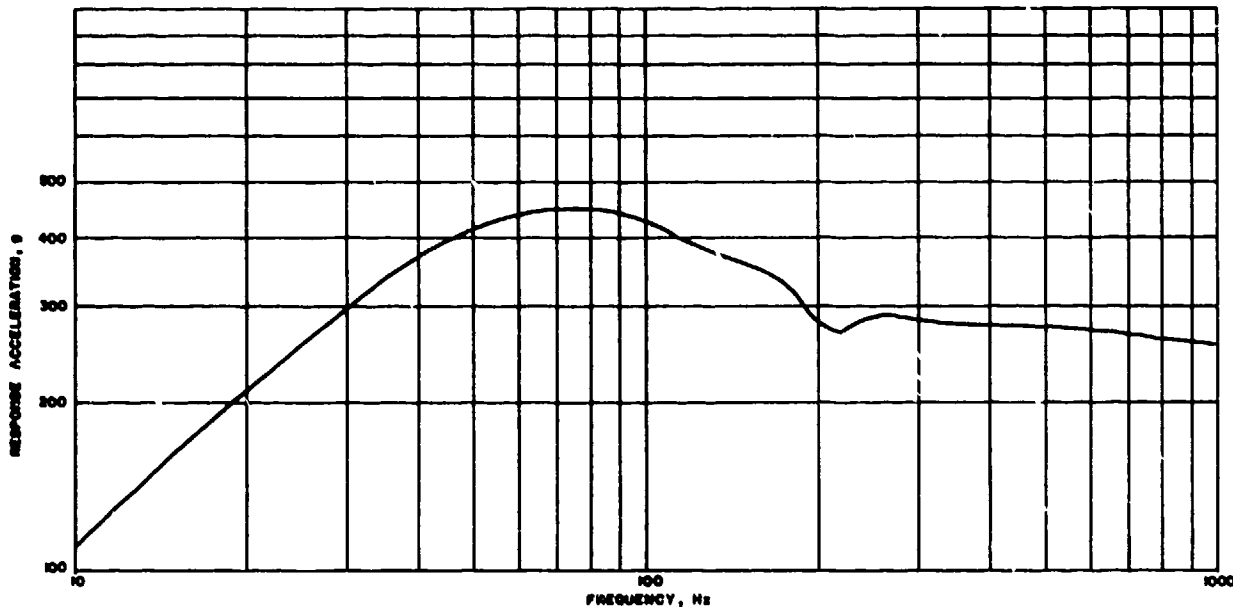


FIGURE 2: ACCELERATION RESPONSE SPECTRUM FOR 250g PEAK, 0.011 SECOND HALF-SINE SHOCK PULSE

was subjected to sine sweep tests and random vibration tests. The result is that the random vibration environment produces peak accelerations which are well below the 250g limit of the accelerometer.

The lower limit on F_0 is determined by the maximum allowable deflection in the shock isolator, given by

$$(2) D = 9.8G/F_0^2 \text{ inches},$$

with G in units of g = 386 inch/second², where it is assumed that all the deflection occurs in the shock isolator. The O-Ring shock isolator design allows a maximum deflection of 0.030 inch in all three axes before the O-Rings are compressed to where the metal parts come into contact. In the random vibration environment, a 3-sigma peak deflection of 0.030 inch occurs at $F_0 = 194$ Hz; in the pyrotechnic shock environment, a 0.030 inch deflection occurs at $F_0 = 171$ Hz.

The median value of F_0 between the upper limit of 415Hz imposed by acceleration and the lower limit of 194Hz imposed by displacement is 305Hz. A design goal of $F_0 = 300$ Hz was chosen, with a desired range of $F_0 = 250$ Hz to 350Hz to allow for uncertainties in spring constants due to material variability and analytical estimates. Table 3 shows the calculated accelerations and displacements due to the shock and random vibration environments. At $F_0 = 250$ Hz, the 0.022 inch displacement is 73% of the design clearance of 0.030 inch. At $F_0 = 350$ Hz, the acceleration of 206g is 82% of the design limit of 250g. In both cases it is the pyro-

technic shock which provides the more severe environment.

4.0 SHOCK ISOLATOR DESIGN

The O-Ring shock isolator design is shown in Figure 3. The base plate, outside support and center support are 6061-T6 aluminum; the mounting plate, top support and screws are 303 stainless steel. The O-Rings are commercially available and are silicone. The Z axis is parallel to the accelerometer sensing axis and normal to the base plate. The X axis is normal to the Z axis and also represents the third (Y) axis in analysis and test. The larger, upper and lower O-Rings are the springs for the Z axis motion; the smaller, center O-Ring is the spring for the X-axis motion. All three O-Rings have the same thickness of 0.103 inch. The shock isolator design allows a 0.030 inch clearance between metal parts separated by O-Rings, i.e., the O-Rings must be compressed 0.030 inch before the metal parts touch. The total weight of the shock isolator is 0.952 lbs., and the weight supported by the O-Rings is 0.577 lbs. The center of gravity (CG) of this 0.577 lbs. is at the center of the three O-Ring configuration.

The base plate fundamental natural frequency was measured to be 3,100Hz (sine sweep tests) and the outside support fundamental natural frequency was estimated to be in excess of 25,000Hz. These frequencies are much greater than the 300Hz shock isolator design goal and are effectively isolated from the accelerometer by the shock isolator.

TABLE 3
CALCULATED ACCELERATIONS AND DISPLACEMENTS

F_0 (Hz)	PYROTECHNIC SHOCK		RANDOM VIBRATION 3-SIGMA VALUES*	
	ACCELERATION (g)	DISPLACEMENT (INCH)	ACCELERATION (g)	DISPLACEMENT (INCH)
250	139	0.022	112	0.018
300	172	0.019	109	0.012
350	206	0.017	106	0.009

*Values based on an assumed transmissibility of Q=6

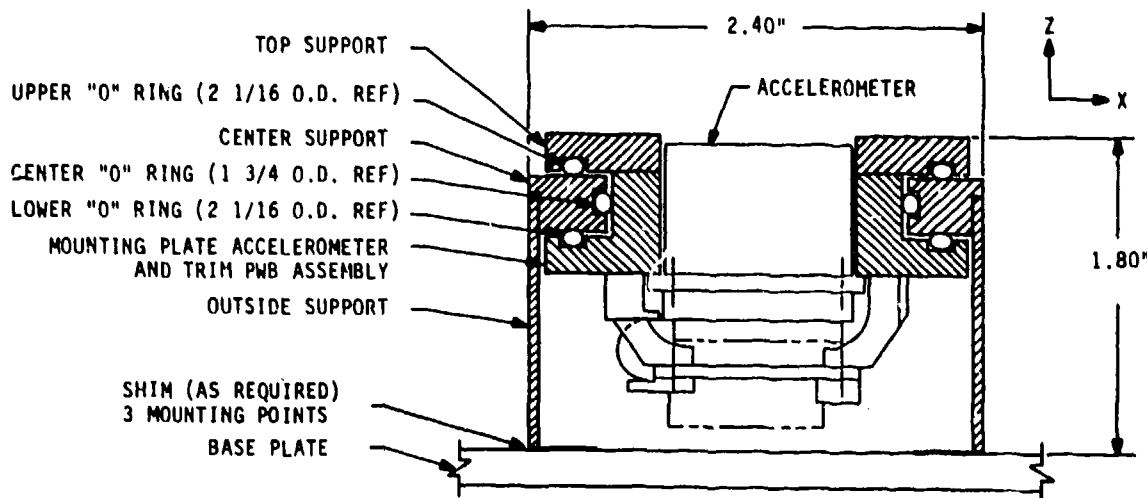


FIGURE 3: SHOCK ISOLATOR DESIGN

5.0 SHOCK ISOLATOR ANALYSIS

The O-Rings support a total mass of $m = 0.577$ lbs. With a design goal of $F_0 = 300\text{Hz}$ for the shock isolator fundamental natural frequency, the required spring stiffness, K , may be found from the expression

$$(3) \quad F_0 = (1/2\pi) \cdot (Kg/m)^{1/2}$$

Using the above values of F_0 and m in equation (3) yields

$$(4) \quad K = 5,310 \text{ lbs./inch,}$$

the spring constant required for motion in both the Z and X directions.

The silicone O-Ring material is typical of many rubber-like materials and has non-linear stress-strain characteristics, with the static modulus of elasticity increasing with strain and also dependent on the shape factor (geometric configuration) of the material being strained. This results in the static spring stiffness, K , increasing with strain. The O-Rings are preloaded by compressing them to a designed fraction of their unloaded thickness, in order to accommodate the displacements shown in Table 3. The spring stiffness calculated for this preloaded condition is used as the mean value of K and is designed to be equal to the value of 5,310 lbs/inch obtained in equation (4).

5.1 Z Direction Analysis

In the Z direction the two O-Rings act as parallel springs between the movable mass, m , and the fixed center support (see Figure 3). The static

spring constant for a single O-Ring along an axis normal to the plane of the O-Ring is given by (2)

$$(5) \quad K = 3.95 E D (\delta/d)^{1/2} \text{ lbs/inch}$$

where E = Young's modulus
 D = mean diameter of O-Ring
 d = thickness of O-Ring
 δ = preload compression of O-Ring

This formula provides results in close agreement with experiment up to values of $(\delta/d) = 0.15$, and yields lower K values than experiment for $(\delta/d) > 0.15$. The underestimate of K at $(\delta/d) = 0.24$ is apparent from the sine sweep and random vibration tests.

The O-Rings chosen for the Z direction springs have values of $D = 1.97$ inch and $d = 0.103$ inch, and the shock isolator is designed to preload and compress them by $\delta = 0.025$ inch. Since the two O-Rings are in parallel, each one must produce half the stiffness specified by equation (4), or 2655 lbs/inch. Substituting these values into equation (5) and solving for the Young's modulus yields a value of $E = 693$ psi. The O-Ring material is characterized by its hardness as measured on the Shore Durometer A Scale, which is related to Young's Modulus, E . (3,4) A value of $E = 693$ psi corresponds to a durometer of 62 ± 2 . As stated above, however, the actual K value will be greater than calculated for the $(\delta/d) = 0.24$ design value, and the 62 durometer value is an overestimate. Also, the correlation between hardness and Young's modulus is only reliable under static conditions. In rubber-like materials such as silicone the dynamic modulus of

elasticity is complex and is a function of frequency and displacement amplitude from the equilibrium position, as well as other factors.^(5,6) Fundamental natural frequencies calculated from static measurements of E may be in error by a factor of 2 or more, either too large or too small, compared to dynamic measured values of F_0 . Since the dynamic complex values of E versus frequency are not known for most materials used in commercially available O-Rings, the best that can be done is to use the static value of E as a starting point and modify the choice of durometer based on the experimental results.

From equation (5) it is seen that the spring constant is nonlinear and proportional to the square root of the compression, δ . However, when two O-Rings are used in parallel as shown in Figure 3, and the supported mass is dynamically displaced a distance γ from the equilibrium position where both O-Rings have the same value of δ due to the designed preload, then one O-Ring has a larger value of $\delta' = \delta + \gamma$ and the other O-Ring has a corresponding smaller value of $\delta' = \delta - \gamma$. The addition of the resulting spring constants in parallel yields

$$(6) \quad K = K(\delta + \gamma) + K(\delta - \gamma) \\ = (3.95ED/d^2) \cdot [((\delta + \gamma)^{1/2} + (\delta - \gamma)^{1/2})^2 \\ = 3.95ED(\delta/d)^{1/2} [1 - 1/8 (\gamma/\delta)^2]$$

where γ = dynamic displacement from equilibrium position.

From equations (5) and (6) it may be shown that a dynamic displacement by γ inches from a preload position results in much less non-linearity for the two O-Rings in parallel, compared to a single O-Ring:

$$(7) \quad (K' - K)/K = 1/2 (\gamma/\delta) - 1/8 (\gamma/\delta)^2 \\ \text{for one O-Ring,} \\ = -1/8 (\gamma/\delta)^2 \text{ for two O-Rings in parallel,}$$

where K' = spring constant when the supported mass is dynamically displaced a distance γ from the preload compression δ , K = spring constant at preload compression δ .

For $(\gamma/\delta) = 0.5$, a typical dynamic operating value, equation (7) will yield a value of $(K' - K)/K = +0.219$ for one O-Ring versus -0.031 for two O-Rings in parallel, or a 22% increase in K versus a 3% decrease in K . The two O-Ring design will introduce less non-linearity than would a single O-Ring.

5.2 X Direction Analysis

In the X direction one O-Ring acts

as a spring between the movable mass, m , and the fixed center support (see Figure 3). The static spring constant for an O-Ring along an axis lying in the plane of the O-Ring is given by (7)

$$(8) \quad K = 8 LG,$$

where

$$(9) \quad \beta = \frac{80\pi(A^2+B^2)}{[25(A^2+B^2)\ln(A/B) - 9(A^2-B^2)]}$$

where G = shear modulus

L = thickness of compressed O-Ring in the direction normal to the plane of the O-Ring,
 A = outside diameter of compressed O-Ring in the O-Ring plane,
 B = inside diameter of compressed O-Ring in the O-Ring plane.

The single O-Ring chosen for the X direction spring has a mean diameter of 1.652 inch and a thickness of 0.103 inch. It is placed in the center support groove and compressed by insertion of the mounting plate to conform to values of $A = 1.709$ inch and $B = 1.552$ inch. This compression results in a value of $L = 0.106$ inch, based on a constant volume O-Ring cross section. Using these values in (8) and (9) results in $\beta = 163$ and

$$(10) \quad K = 17.3G \text{ lbs/inch}$$

Using in equation (10) the value of $K = 5,310$ lbs/inch from equation (4), the shear modulus is found to be

$$(11) \quad G = (307 \text{ psi})$$

for the single O-Ring, corresponding to a durometer of 74 ± 2 .

As noted previously, values of F_0 calculated from static measurements of G may be in error by a factor of 2 or more in either direction, and the durometer value found above for the X-axis O-Ring should be used only as a starting point to be modified based on experimental results.

6.0 SINE SWEEP AND RANDOM VIBRATION TESTS

6.1 Test Description

Sine Sweep and random vibration tests were performed at National Technical Systems in Acton, MA. Both types of tests utilized a Ling Model A-300 shaker table with PCB Model 302A and 303A03 single axis accelerometer and a Hitachi Model U-134 oscilloscope to monitor wave forms. The accelerometers have an accuracy of $\pm 5\%$ over the frequency range of 20Hz to 2,000Hz. In the sine

sweep tests an Unholtz Dickie Model OSP-4 oscillator was used to control the input frequency, and a log converter was used with an MFE Model 715 x-y plotter to plot output acceleration versus frequency. For the random vibration tests a GenRad Model 2503 vibration analyzer was used in conjunction with a Honeywell Model 5600E tape deck. Each test was made with an accelerometer on the shock isolator base plate, used as a control to measure input acceleration, and an accelerometer on the top of the dummy accelerometer, to measure acceleration after the shock isolator. The two accelerometers were oriented to measure acceleration in the same direction, i.e., along the X axis or along the Z axis.

Several tests were made for each axis orientation for all sine sweep levels (1g, 5g, and 10g) and for random vibration tests. The random vibration tests were also run at AVCO Systems Division in Wilmington, MA over temperature ranges of -20°C to +25°C in the X axis and -30°C to +50°C in the Z axis. The difference in temperature ranges was due to available test time.

6.2 Test Results

Tables 4 through 6 present the results of the sine sweep and random vibration tests. In these three tables the durometer value is for the O-Ring(s) acting as a spring along the axis indicated in the table title. Test type SS is a sine sweep and test type RV is a random vibration test. The fundamental natural frequency, F , and transmissibility, Q , are found directly from the resonance peaks (see Figures 4 and 5), using the measured input acceleration, G , for the sine sweep tests and the measured input power spectral density at F for the random vibration tests. For the sine sweep tests, the dynamic displacement, γ , is calculated from the measured values of G , Q and F using the relation

$$(12) \quad \gamma = 9.8 G Q/F^2$$

For the random vibration tests, the 3-sigma peak output acceleration, G_{pk} , is calculated from the measured values of F , Q and power spectral density using equation (1). The dynamic displacement, γ , is then found by substituting G_{pk} for $G Q$ in equation (12), yielding a 3-sigma peak dynamic displacement.

TABLE 4
SINE SWEEP AND RANDOM VIBRATION TEST RESULTS
Z AXIS 40 DUROMETER

TEST TYPE	FUNDAMENTAL NATURAL FREQUENCY, F (Hz)	TRANSMISSIBILITY AT RESONANCE Q	INPUT ACCELERATION AT RESONANCE, G_{IN} (g)	OUTPUT ACCELERATION AT RESONANCE, G_{OUT} (g)	DYNAMIC DISPLACEMENT γ (INCH)	DYNAMIC STRAIN ϵ
SS	283	6.2	1	6.2	0.001	0.01
SS	260	5.3	5	26.5	0.004	0.05
SS	246	5.6	10	56.0	0.009	0.12
RV*	248±2	6.1±0.3	-	114±2	0.018±0	0.23±0

Static Calculation: $F = 165\text{Hz}$

*The random vibration input level is $Grms = 16.7\text{g}$, and the output acceleration, dynamic displacement and dynamic strain are three-sigma peak values. These three-sigma peak values are increased by 18±1 percent if the relationship $G_{pk}=3\text{ Grms}$ (out) is used in place of equation (1). These data are an average of three tests.

TABLE 5
SINE SWEEP AND RANDOM VIBRATION TEST RESULTS
X AXIS 60 DUROMETER

TEST TYPE	FUNDAMENTAL NATURAL FREQUENCY, F (Hz)	TRANSMISSIBILITY AT RESONANCE Q	INPUT ACCELERATION AT RESONANCE, G _{IN} (g)	OUTPUT ACCELERATION AT RESONANCE, G _{OUT} (g)	DYNAMIC DISPLACEMENT Y (INCH)	DYNAMIC STRAIN ε
SS	254	6.8	1	6.8	0.001	0.01
SS	230	6.8	5	34.0	0.006	0.08
SS	223	7.7	10	77.0	0.015	0.19
RV*	184±1	6.2±0.7	—	113±6	0.033± 0.001**	0.42 ±0.01

Static Calculation: F = 210Hz

*The random vibration input level is Grms = 16.7g, and the output acceleration, dynamic displacement and dynamic strain are three-sigma peak values. These three-sigma peak values are increased by 9±1 percent if the relationship G_{pk}=3 Grms (out) is used in place of equation (1). These data are an average of three tests.

**This deflection exceeds the design clearance of 0.030 inch.

TABLE 6
SINE SWEEP AND RANDOM VIBRATION TEST RESULTS
X AXIS 70 DUROMETER

TEST TYPE	FUNDAMENTAL NATURAL FREQUENCY, F (Hz)	TRANSMISSIBILITY AT RESONANCE Q	INPUT ACCELERATION AT RESONANCE, G _{IN} (g)	OUTPUT ACCELERATION AT RESONANCE, G _{OUT} (g)	DYNAMIC DISPLACEMENT Y (INCH)	DYNAMIC STRAIN ε
SS	387	5.7	1	5.7	0.0004	0.005
SS	343	5.3	5	26.5	0.002	0.03
SS	322	6.2	10	62.0	0.006	0.08
RV*	230±4	5.7±0.2	—	112±2	0.021 ±0.001	0.27 ±0.01

Static Calculation: F = 268Hz

*The random vibration input level is Grms = 16.7g, and the output acceleration, dynamic displacement and dynamic strain are three-sigma peak values. These three-sigma peak values are increased by 10±0 percent if the relationship G_{pk}=3 Grms (out) is used in place of equation (1). These data are an average of three tests.

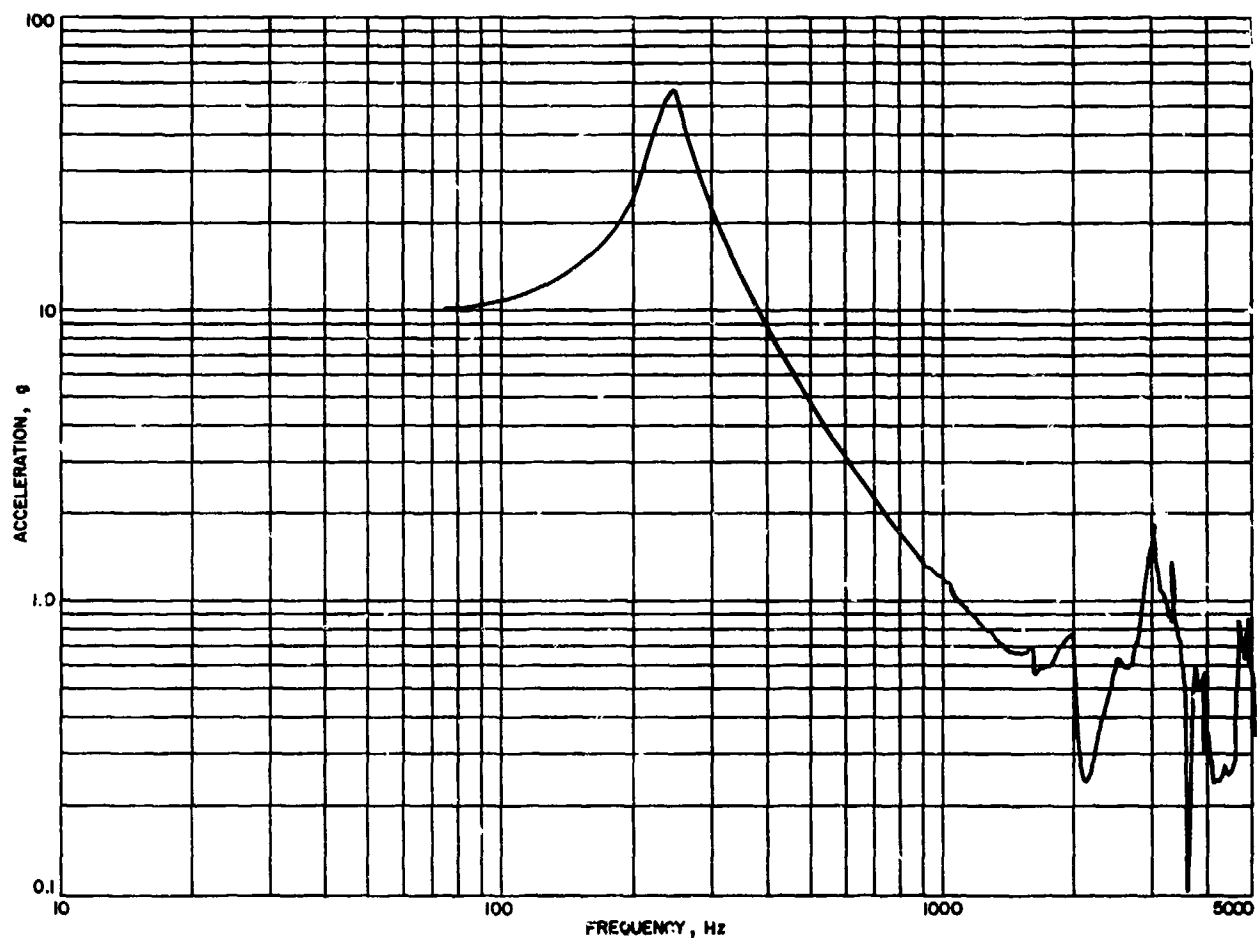


FIGURE 4: TYPICAL ISOLATOR ACCELERATION OUTPUT, SINE SWEEP TEST

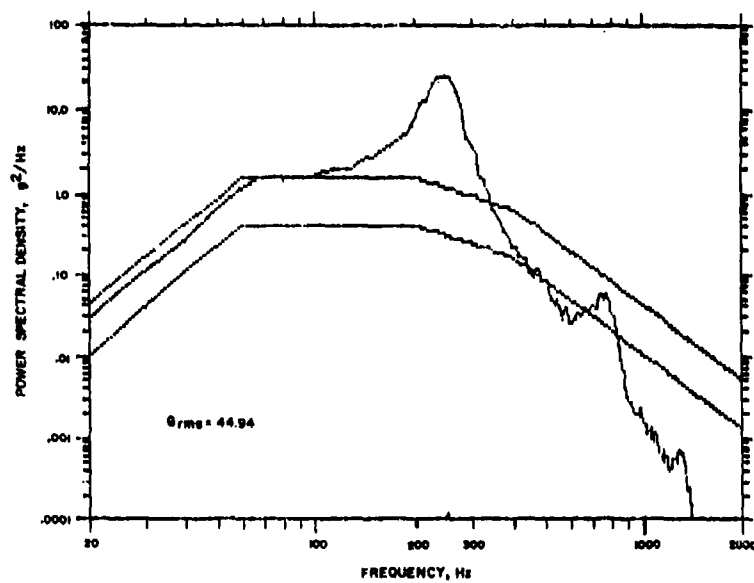


FIGURE 5: TYPICAL ISOLATOR ACCELERATION OUTPUT, RANDOM VIBRATION TEST

The dynamic strain is obtained from

$$(13) \quad \epsilon = Y/0.078$$

where the preloaded O-Ring thickness of 0.078 inch equals the undeformed O-Ring thickness of $d = 0.103$ inch minus the design preload compression of $\delta = 0.025$ inch. No change in F was measured over the temperature ranges of -20°C to $+25^{\circ}\text{C}$ in the X axis and -25°C to $+50^{\circ}\text{C}$ in the Z axis.

The static calculation of frequency at the bottom of each table was done using equations (3) and (4), with equation (5) for Table 4 and equation (10) for Tables 5 and 6. In equation (5), the value of $E = 213$ psi was used for the 40 durometer material, and in equation (10) the values of $G = 150$ psi and $G = 245$ psi were used for the 60 durometer and 70 durometer materials, respectively.(3)

6.3 Discussion of Test Results

The design resonance peaks are clearly seen in Figures 4 and 5, which are typical of the sine sweep and random vibration test data. The small secondary peak seen in Figure 5 at about 700Hz is present in all of the random vibration test data and is completely absent in all of the sine sweep test data. This 700Hz peak is most likely due to non-linear effects which occur in the random vibration tests and are absent in the sine sweep test.

The disparity between the static calculations of F and the measured dynamic values of F in Tables 4 through 6 is not surprising in view of the comments in Section 5.1. Also, the very low static value of F in the Z direction (Table 4) may be due in part to the inaccuracy of equation (5) and its tendency to underestimate stiffness at large values of δ/d .

The monotonic decrease of frequency with increasing dynamic strain in all three tables is attributed to the decrease in dynamic modulus with increasing dynamic strain observed in rubbers and other polymers.(8) See equations (3), (5) and (10). The increasing dynamic strain is due to the increasing acceleration, as seen from equations (12) and (13). The absence of any measurable change in F , over the temperature ranges of -20°C to $+25^{\circ}\text{C}$ in the X axis and -30°C to $+50^{\circ}\text{C}$ in the Z axis indicates the temperature range over which the shock isolator may be used without performance degradation.

From Table 4, it may be concluded that a slightly higher durometer, 45,

would bring the Z axis frequency closer to the 300Hz goal, but the dynamic displacements are well within the design allowable maximum of 0.030 inch. Comparing Tables 5 and 6, the 60 durometer material results in an excessive dynamic displacement in random vibration, whereas the 70 durometer material is acceptable. A choice of 65 durometer for the X axis O-ring would come closer to the 300Hz goal. The small standard errors of the data from the repeated random vibration tests in all three tables adds to the confidence in the test data.

During the second and third random vibration tests in the Z axis (Table 4) and the second and third random vibration tests in the X axis with the 70 durometer O-Rings (Table 6) an electrical circuit was used to detect any transient short circuits which might occur between the center support and either the top support or the accelerometer and trim PWB assembly. See Figure 3. No short circuits occurred, indicating that the O-Rings were not compressed sufficiently to allow metal-to-metal contact.

The ability of the shock isolator to maintain the accelerometer angular alignment with respect to the mounting plane was tested by measuring the distance from the bottom of the outside support to the top of the top support (see Figure 3) at three reference points 120° apart on the two inch diameter perimeter of the top support. These measurements were made before and after random vibration testing by removing the base plate, placing the outside support on a surface plate, and using a drop gauge with a dial indicator accurate to 0.0001 inch to measure the height from the surface plate to the three reference points. These measurements indicated a change in angular alignment with the surface plate of approximately 0.02° , an order of magnitude less than the allowable angular alignment change of 0.25° .

In summary, the sine sweep and random vibration tests demonstrate that the shock isolator will provide a resonance frequency in the design range of 250Hz to 350Hz with substantial acceleration attenuation at higher frequencies. When subjected to the specified random vibration environment the dynamic displacement of the movable parts are well within the acceptable design range, the change in the angular alignment is considerably less than allowed by specification, and the three-sigma peak output acceleration at the resonance frequency is much less than the accelerations to which the accelerometer is subjected by the manufacturer's test procedure. Comparing the three-sigma acceleration of 112 to 114g (Tables 4 through 6) to the

manufacturer's acceleration response test spectrum (Figure 2) at the resonance frequencies of 184 to 284Hz, it may be seen that the manufacturer's test spectrum is far above the three-sigma peak output acceleration from the specified random vibration environment.

7.0 PYROTECHNIC SHOCK TESTS

7.1 Test Description

The shock isolator with a dummy accelerometer, as described in Section 6.1, was instrumented with three, single axis accelerometers stacked on top of one another and attached to the top of the dummy accelerometer. See Figure 3. 40 durometer material was used for the Z axis O-Rings and 70 durometer material for the X axis O-Ring. The base plate was mounted to an ACS flight structure. The shock was produced by separation ordinance to simulate actual flight conditions. Figure 6 shows the accelerometer shock isolator and the beam to which it was bolted, with the X, Y and Z axis indicated. The only sensor instrumenting the beam was a single axis accelerometer mounted on the back of the beam and oriented to measure the X-axis response. All of the accelerometer signals were amplified, recorded, and processed through a shock spectrum analyzer. Both real time acceleration histories and shock response acceleration versus frequency data were obtained.

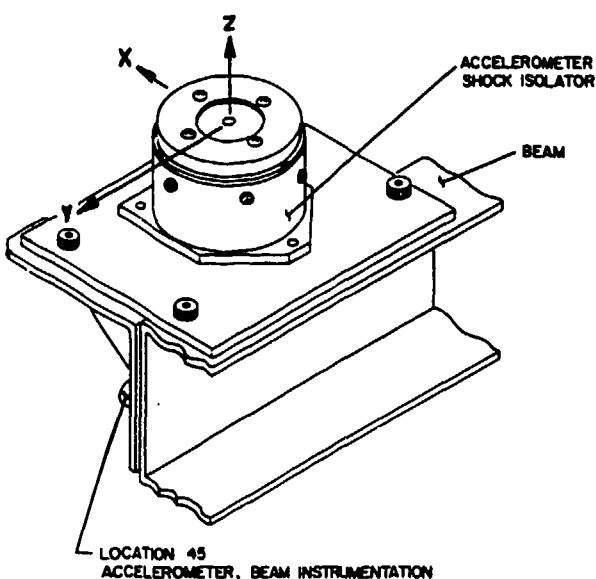


FIGURE 6: ACCELEROMETER SHOCK ISOLATOR/BEAM CONFIGURATION WITH COORDINATE AXES

Data were obtained for three separate shock tests of increasing severity. The third test, which resulted in the largest accelerations, was judged to closely simulate the flight situation and it is this data which is reported in the following sections.

7.2 Test Results

Figures 7, 8 and 9 show the shock response spectra measured at the dummy accelerometer along the three axes. These axes are oriented the same as in Section 6: the Z axis is normal to the base plate; the X and Y axes are parallel to the base plate. (see Figure 6). The X and Z axes are transverse to the beam, and the Y axis is in the beam longitudinal direction. Figure 10 shows the X axis shock response spectrum of the beam to which the accelerometer shock isolator base plate was bolted. This spectrum (Figure 10) is the input to the accelerometer shock isolator in the X axis. The double trace seen in the shock response spectra of Figures 7 through 10 is the positive and negative acceleration response due to the asymmetry of the time history data in the +G and -G directions. The shock responses of the beam in the Y and Z axes were not measured, and no data is available for the input to the accelerometer shock isolator in the Y and Z axes. Figures 11 and 12 show the type of time history data from which Figures 7 through 10 were generated.

Table 7 presents the pyrotechnic shock test results in terms of the peak frequencies and accelerations recorded in Figures 7 through 10. The peak frequencies and measured accelerations were taken directly from the figures, and were then used in equation (2) to estimate the deflection or compression of the O-Rings in the shock isolator, next to the last column of Table 7. Also shown in Table 7 for comparison purposes are the values of the originally specified accelerations from Table 1 and the manufacturer's screening test values of the accelerations from Figure 2 at the measured peak frequency. The last column in Table 7 presents the absolute values of the peak accelerations taken from the time history data. See Figures 11 and 12 for examples.

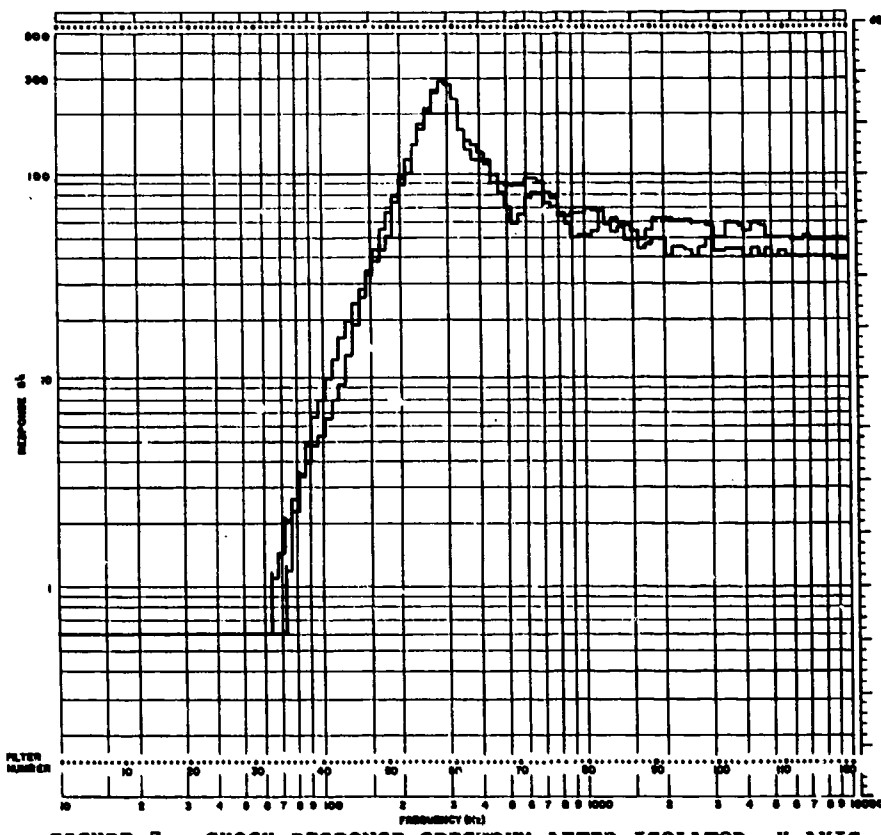


FIGURE 7: SHOCK RESPONSE SPECTRUM AFTER ISOLATOR, X AXIS

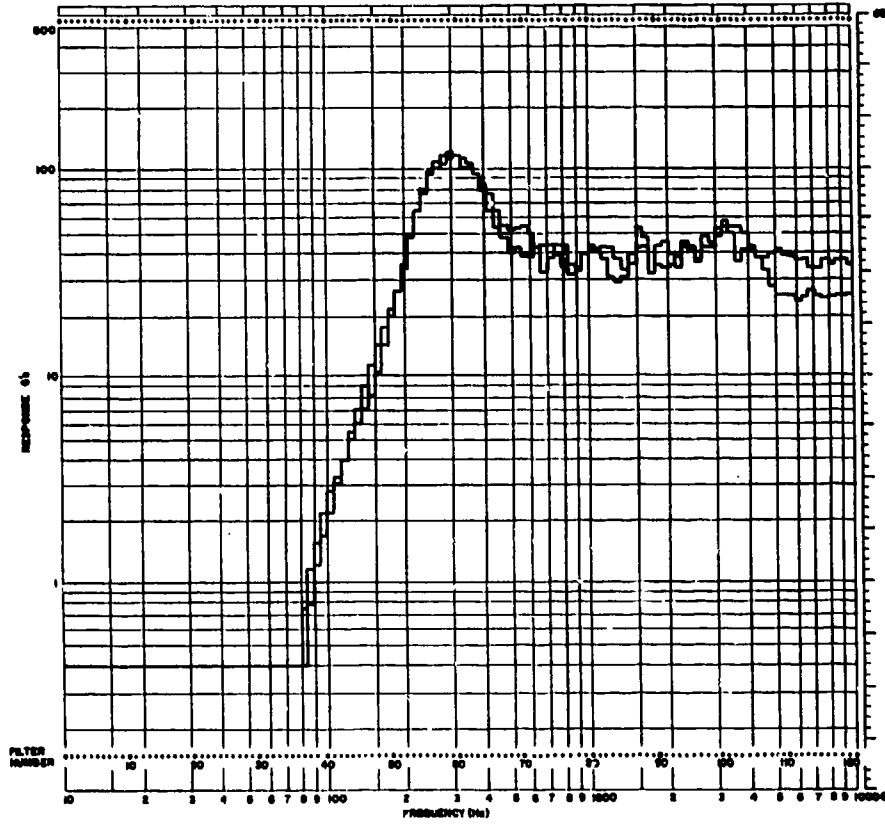
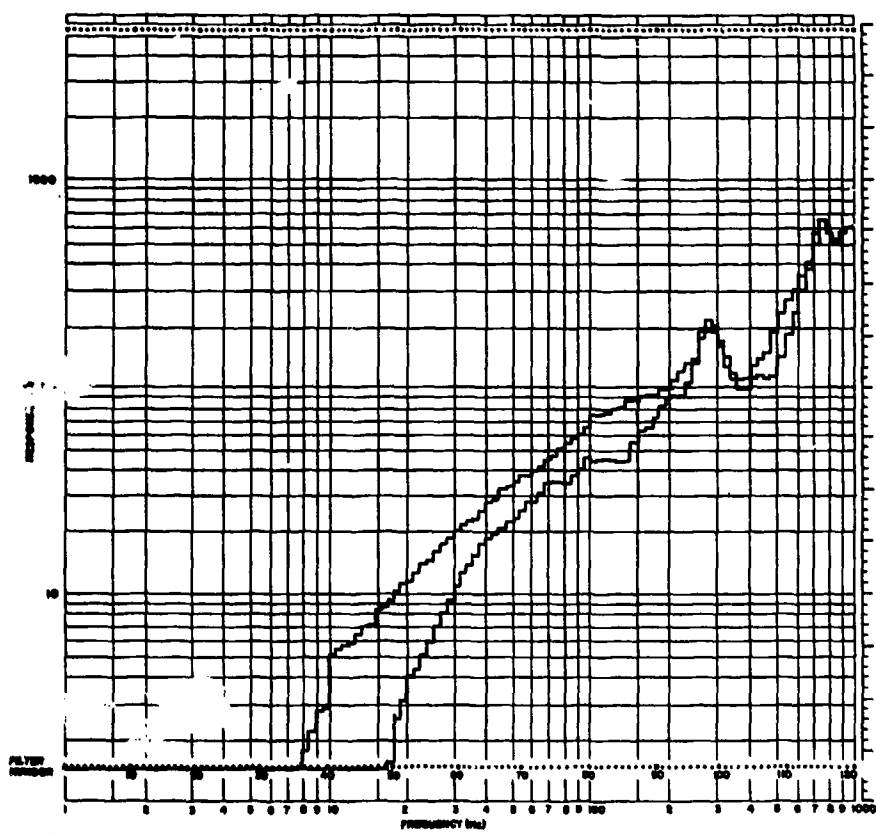
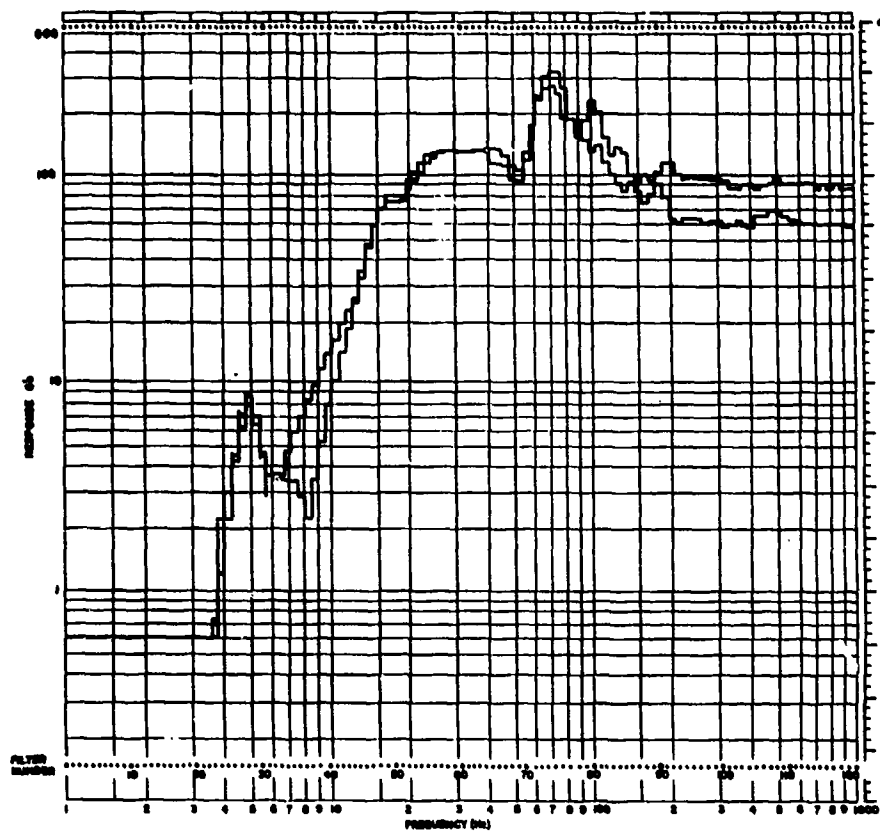


FIGURE 8: SHOCK RESPONSE SPECTRUM AFTER ISOLATOR, Y AXIS



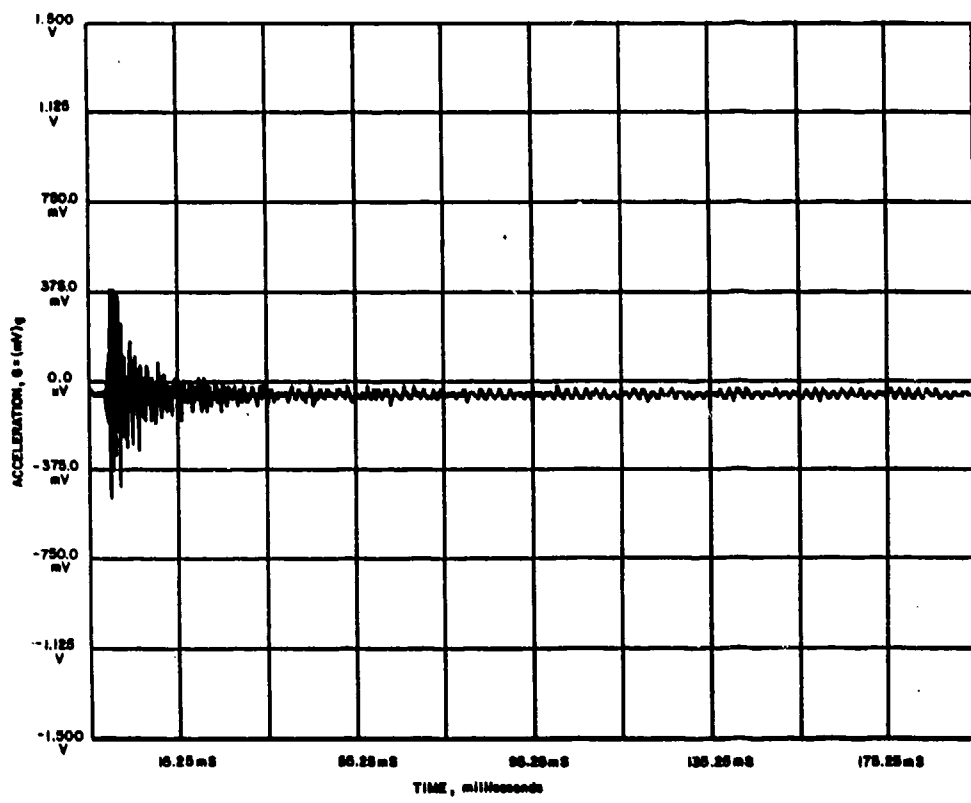


FIGURE 11: TIME HISTORY SHOCK RESPONSE, ASA SUPPORT BEAM, X AXIS

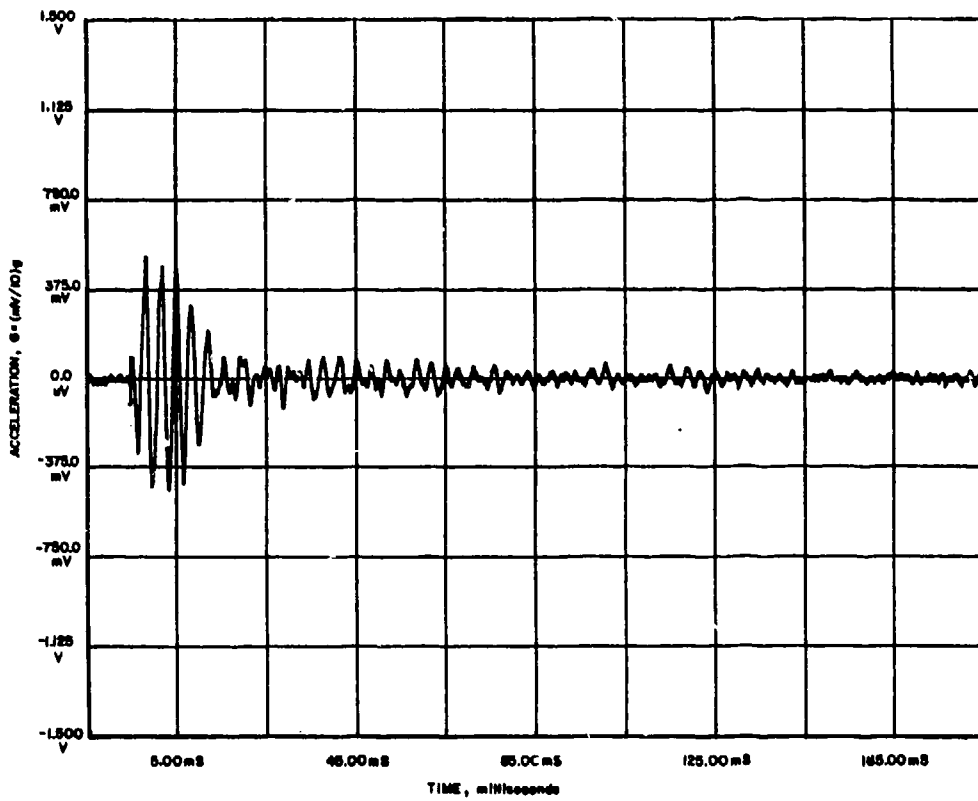


FIGURE 12: TIME HISTORY SHOCK RESPONSE, AFTER ISOLATOR, X AXIS

TABLE 7
PYROTECHNIC SHOCK TEST RESULTS

LOCATION	AXIS	PEAK FREQUENCY (Hz)	PEAK ACCELERATION VALUES, G (g) ⁽¹⁾			ESTIMATED DEFLECTION ⁽²⁾ D (INCH)	TIME HISTORY ⁽³⁾ PEAK G (g)
			MEASURED	SPECIFIED	SCREENED		
Beam	X	280	213	159	286	0.027	495
Beam	X	750	650	500	263	0.011	495
Dummy Accelerometer	X	284	287	162	286	0.035 ⁽⁴⁾	52
Dummy Accelerometer	Y	300	120	172	285	0.013	36
Dummy Accelerometer	Z	284	133	162	286	0.016	93
Dummy Accelerometer	Z	700	327	461	265	0.007	93

NOTES: 1. Measured values of G are taken directly from Figures 7-2 thru 7-5. Specified values are calculated from the originally specified pyrotechnic shock response spectrum of Table 2-1, for the peak frequency. Screened values are those used by the manufacturer for screening tests and are obtained from Figure 3-1 for the peak frequency.

2. The estimated deflection is calculated from equation (2) using the values of peak frequency and measured G.
3. This is the absolute value of the maximum positive or negative acceleration recorded on the time history plots.
4. This deflection exceeds the design clearance of 0.030 inch.

The maintenance of accelerometer angular alignment was tested by making measurements before and after pyrotechnic shock tests, as described in Section 6.3. The results indicated a change in angular alignment an order of magnitude less than the allowable value of 0.25°.

7.3 Discussion of Test Results

Examination of Table 7 shows a 327g acceleration peak at 700Hz measured at the dummy accelerometer along the Z axis. This peak exceeds the manufacturer's screening test acceleration of 265g at 700Hz. Although the input shock from the beam was not measured in the Z direction, there was a 650g peak at 750Hz measured in the beam in the X direction, compared to a specified level of 500g at 750Hz. This 750Hz peak may have been present in the beam in the Z direction also and may account for the 700Hz peak seen at the dummy accelerometer in the Z direction. All other acceleration response data at the dummy accelerometer fall on or below the manufacturer's screening test values.

At the frequency peaks seen in Figures 7 through 9 (284Hz-300Hz) the shock response acceleration, G_0 , at the dummy accelerometer should be the same as the shock response acceleration at the shock isolator base plate. The shock response acceleration in the beam, G_B , to which the shock isolator base plate is bolted should be greater than G_0 at these frequencies, since there will be some attenuation of the shock in transversing the bolted joint between the shock isolator base plate and beam. Examination of the G_0 values (measured peak acceleration values) in Table 7 shows that G_0 , and consequently G_B , are significantly larger than the specified acceleration in the X axis. In the Y and Z axes G_0 is less than the specified acceleration. Also, there is an anomaly in the X axis measured values of acceleration which shows the response at 284Hz in the dummy accelerometer, $G_0 = 287g$, to be greater than in the beam, $G_B = 213g$. This may be explained by the estimated deflection of 0.035 inch in the dummy accelerometer, a deflection which exceeds the design clearance of

0.030 inch. If metal-to-metal contact occurred, it could result in the higher acceleration seen in the dummy accelerometer. It should be noted, however, that the dummy accelerometer's measured X axis acceleration of 287g at 284Hz is essentially equal to the manufacturer's screening test acceleration at 284Hz.

In summary, the only occurrence of exceeding the manufacturer's screening accelerations was where the input acceleration was greater than the design specification. Based on manufacturer's information (Section 3.0) the measured acceleration of 327g at 700Hz should be acceptable.

8.0 FLIGHT UNIT TESTS

The first four flight units produced for spacecraft use were subjected to sine sweep (SS) and random vibration (RV) tests as part of a screening procedure prior to shipment. Each unit was subjected to a 1g SS and a RV test (Grms = 16.7g) in each of the X, Y and Z axes. Four parameters were chosen for comparing test results among flight units. These parameters are:

- The measured resonance frequency, F_0 ;
- The transmissibility at resonance, $Q(F_0)$;
- The frequency, $F(Q=1)$, at which the value of Q equals unity; and
- The transmissibility at $F = 1,000$ Hz, $Q(F=1,000)$.

These parameters were used for comparison purposes on both the SS data and the RV data. Table 8 presents the coefficient of variation (CV) of the test results from the four units for each of the four parameters for both the SS and RV tests. The data was generated by normalizing each of the four test values for a given axis to the average value for that axis, and then using the twelve normalized values from all three axes to obtain the CV. These units were all tested at AVCO Systems Division in Wilmington, Massachusetts, and show remarkably little variability in test results.

Table 9 shows the variability between the three axes based on the average values for all four units in each axis separately. There is little variation of F_0 or $F(Q=1)$ between axes; and only the SS tests show a modest variability between axes for the parameters $Q(F_0)$ and $Q(F=1,000)$. These are small variations considering the difference in

spring design between the Z axis and the X/Y axes.

Table 10 summarizes the average values of the four parameters for the four flight units. The F_0 and $F(Q=1)$ values for the SS tests may be expected to decrease as the input acceleration is increased beyond 1g, as is seen in Tables 4 through 6. The peak accelerations due to RV will be much less than 250g, and the SS data indicates adequate attenuation of the observed shock response spectrum for the higher frequencies.

TABLE 8
VARIABILITY BETWEEN FOUR FLIGHT UNITS

PARAMETER	SINE SWEEP TESTS	RANDOM VIBRATION TESTS
F_0	3.3%	4.4%
$F(Q=1)$	5.7%	4.5%
$Q(F_0)$	11.1%	3.3%
$Q(F=1,000)$	5.8%	8.6%

NOTES: 1. The numbers in the table are the coefficient of variation, $CV = 100 \times (\text{standard deviation})/(\text{mean})$.
2. See text for definition of parameters and explanations of the table.

TABLE 9
VARIABILITY BETWEEN THREE AXES

PARAMETER	SINE SWEEP TESTS	RANDOM VIBRATION TESTS
F_0	4.5%	3.9%
$F(Q=1)$	5.5%	6.3%
$Q(F_0)$	15.2%	4.9%
$Q(F=1,000)$	10.7%	3.3%

NOTE: See notes to Table 8

TABLE 10
AVERAGE PARAMETER VALUES FOR FOUR FLIGHT UNITS

PARAMETER	SINE SWEEP TESTS	RANDOM VIBRATION TESTS
F_0 , Hz	351	270
$F(Q=1)$, Hz	558	383
$Q(F_0)$	7.9	5.1
$Q(F=1,000)$	0.28	0.47

ACKNOWLEDGEMENTS

Dr. David Nokes of Charles Stark Draper Laboratory, Inc., Cambridge, Massachusetts, furnished the design concept for the shock isolator described in this paper and provided essential consultation during the development and test of the device. Mr. William Connolly of Electronic Design Associates, Dover, Massachusetts supplied important insights throughout the course of the project. The authors wish to thank both of these contributors for their help.

REFERENCES

1. Gertel, M. and Holland, R., "Development of a Technique for Determination of Component Shock Specifications", Report No. 607-4-1, December, 1964, prepared by Mitron Research and Development Corporation, 899 Main Street, Waltham, MA 02154, for NASA Marshall Space Flight Center on Contract No. NAS-8-11090. Final Report - Volume II, Figure II-53, page 66.
2. Lindley, P.B., "Engineering Design with Natural Rubber", Technical Bulletin No. 8 of The Natural Rubber Producers' Association, 19 Buckingham Street, London, W.C. 2. Printed in Great Britain by J.W. Arrowsmith Ltd., Bristol 3. 1964. Pages 33 and 34.
3. Lindley, ibid., pages 7 and 8.
4. Harris, C.M. and Crede, C.E., "Shock & Vibration Handbook", Second Edition, McGraw-Hill Book Company, 1976. Pages 35-2 and 35-3.
5. Lindley, ibid., page 12.
6. Harris, ibid., pages 35-8 through 35-10.
7. Lindley, ibid., pages 27 and 28.
8. Harris, ibid., page 35-12.

DYNAMIC ANALYSIS OF A STRUCTURE WITH SLIDING BASE

T.C. Liauw, BSc(Eng), DIC, PhD, DSc, FICE, FHKIE
Department of Civil & Structural Engineering
University of Hong Kong
Hong Kong

Q.L. Tian, BSc, MCSM, MCSA, FCSOE
Institute of Mechanics
Chinese Academy of Sciences
Peking
China

and

Y.K. Cheung, BSc, PhD, DSc, DE, FICE, FIStructE
FIE(Aust), FASCE, FHKIE
Department of Civil & Structural Engineering
University of Hong Kong
Hong Kong

In this paper, the vibration isolation technique of mounting a structure on a surface which permit sliding is studied.

The periodic response of the structure with many degrees of freedom on sliding base is calculated by the use of Fourier series to represent the frictional force. The occurrence of subharmonic resonance frequencies is explained, and the prevention of these subharmonic is discussed with the support of a model test together with an analytical calculation. Lastly, a stochastic analysis for such a system is presented.

INTRODUCTION

Sliding base is a very simple and economical device for vibration isolation which has aroused considerable interests in aseismatic engineering [1 - 4]. It has been shown that the response level at resonance frequency of a structure resting on a sliding base can be much lower compared with that on a non-sliding fixed base. However, a sliding system also has several subharmonic resonant frequencies and the peak response of such a system to harmonic excitation may not necessarily be less than that of a fixed base system [1]. This can be a problem to the engineering applications of the sliding base system.

In this paper, the periodic response of the sliding base system with single and many degrees of freedoms are analysed by developing the

Coulumb frictional force into a Fourier series. The series solution of the periodic response shows clearly that those subharmonic resonant peaks are induced by the superharmonic components of the frictional force. Hence, if the frictional force is controlled so that the sliding interface is locked rigidly when the exciting frequency is lower than the fundamental frequency of the system, and the interface slides at the resonant frequency, then all the subharmonics below the fundamental frequency will disappeared. Since the resonant response is much higher than those non-resonant responses, it is not difficult to realize such control in the frictional force. With this control, the fundamental frequency of a system with sliding base will not changed from that of the same system with fixed base. Therefore, it is applicable for the isolation of those structures having low fundamental

frequency to low frequency excitation, such as buildings or engineering structures to withstand earthquake, wind or wave loading.

FOURIER SERIES SOLUTION OF A SLIDING OSCILLATOR TO HARMONIC EXCITATION

Since the resonant response is much higher than those responses at non-resonance frequencies, only the slip-slip periodic motion of a system to harmonic excitation at its resonance frequency is considered. The analytical model of the system is shown in Fig. 1.

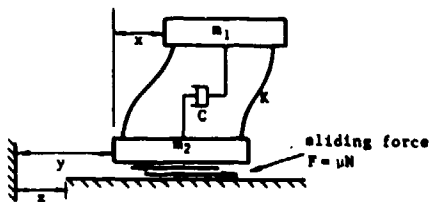


Fig. 1 - Coordinate systems for the sliding oscillator

The motion equations of the system for the state of slip-slip motion are given [1]:

$$\ddot{x} + 2\omega_n' \xi' \dot{x} + \omega_n'^2 x = \frac{-\mu g}{1-\gamma} \operatorname{sgn}(\dot{z} - \dot{y}) \quad (1)$$

$$\ddot{y}(t) = \mu g \cdot \operatorname{sgn}(\dot{z} - \dot{y}) - \gamma \ddot{x} \quad (2)$$

where $\omega_n = \sqrt{(k/m_1)}$, $\xi = \frac{c}{2\sqrt{km_1}}$,

$$\gamma = \frac{m_1}{m_1 + m_2}$$

$$\omega_n' = (1 - \gamma)^{-\frac{1}{2}} \omega_n, \text{ and}$$

$$\xi' = (1 - \gamma)^{-\frac{1}{2}} \xi$$

In Eqs. (1) and (2), $\mu g \cdot \operatorname{sgn}(\dot{z} - \dot{y})$ is the frictional force which can be expressed by a Fourier series as

$$-\mu g \operatorname{sgn}(\dot{z} - \dot{y}) = + \sum_{n=1,3,5...}^{\infty} \frac{4\mu g}{n\pi} \sin n\omega t \quad (3)$$

The advantages of using Fourier series to represent the Coulomb force are that (1) the occurrence of subharmonics can be explicitly explained, (2) simple solutions corresponding to each subharmonics can be derived, and (3) most importantly the series solution of a many-degrees-of-freedom system can be easily obtained.

$$\text{Let } x = \sum_{n=1,3,5...}^{\infty} x_n \quad (4)$$

$$y = \sum_{n=1,3,5...}^{\infty} y_n \quad (5)$$

then a system of infinite linear equations can be obtained:

$$\ddot{x}_n + 2\omega_n' \xi' \dot{x}_n + \omega_n'^2 x_n = \frac{4\mu g}{(1-\gamma)n\pi} \sin n\omega t \quad \dots \dots \dots \quad (6)$$

$$\ddot{y}_n(t) = \frac{+4\mu g}{n\pi} \sin n\omega t - \gamma \ddot{x}_n \quad (7)$$

in which $n = 1, 3, 5, \dots, \infty$ and x_n, y_n are the n th harmonic components corresponding to the n th harmonic excitation of the frictional force.

Equation (6) is the motion equation of a system with a single-degree-of-freedom. The solution is given as

$$x_n(t) = \frac{\frac{4\mu g}{(1-\gamma)n\pi}}{\sqrt{[\omega_n'^2 - (n\omega)^2]^2 + [2\omega_n' \xi' (n\omega)]^2}} \cdot \sin(n\omega t + \phi_n) \quad \dots \dots \dots \quad (8)$$

$$\phi_n = \tan^{-1} \frac{2\xi' \omega_n' (n\omega)}{\omega_n'^2 - (n\omega)^2} \quad (9)$$

The peak values and the corresponding frequencies are given respectively by:

$$\ddot{x}_n = - \sqrt{\frac{m_1 + m_2}{m_2}} \frac{2\mu g}{n\pi\xi} \quad (10)$$

$$\omega = (\sqrt{1 - 2\xi'^2} \omega_n')/n, \quad n = 1, 3, 5, \dots, \infty \quad (11)$$

These are the n subharmonic resonant peaks which are induced by the superharmonic components of the frictional force.

FOURIER SERIES SOLUTION OF A MANY-DEGREES-OF-FREEDOM SYSTEM WITH SLIDING BASE TO HARMONIC EXCITATION

The motion equations of a many-degrees-of-freedom system with a frictional sliding base are

$$\underline{M} \ddot{\underline{x}} + \underline{C} \dot{\underline{x}} + \underline{K} \underline{x} = -\underline{M} \underline{l} \ddot{\underline{y}} \quad (12)$$

$$m_0 \ddot{y} + Q(t) = -F_0 \operatorname{sgn}(\dot{z} - \dot{y}) \quad (13)$$

where F_0 is the magnitude of Coulumb force.

The simple model of this system is shown in Fig. 2. Equation (12) is the motion equation of the clamped upper-structure excited by a base acceleration movement \ddot{y} , where \underline{l} is a vector in which every element is 1. Equation (13) is the motion equation of the base, where m_0 is its mass and Q is the shearing force at the root section of the clamped upper-structure.

Following the treatment of the system with single-degree-of-freedom,

the Fourier series expansion for the frictional force for the system with many-degrees-of-freedom is

$$-F_0 \operatorname{sgn}(\dot{z} - \dot{y}) = + \sum_{n=1,3,5...}^{\infty} \frac{4F_0}{n\pi} \sin n\omega t \quad (14)$$

$$\text{Let } y = \sum_{n=1,3,5...}^{\infty} y_n \quad (15)$$

$$x = \sum_{n=1,3,5...}^{\infty} x_n \quad (16)$$

$$Q = \sum_{n=1,3,5...}^{\infty} Q_n \quad (17)$$

$$z = \sum_{n=1,3,5...}^{\infty} z_n \quad (18)$$

then a system of infinite linear equations can be obtained:

$$\underline{M} \ddot{\underline{x}}_n + \underline{C} \dot{\underline{x}}_n + \underline{K} \underline{x}_n = -\underline{M} \underline{l} \ddot{\underline{y}}_n \quad (19)$$

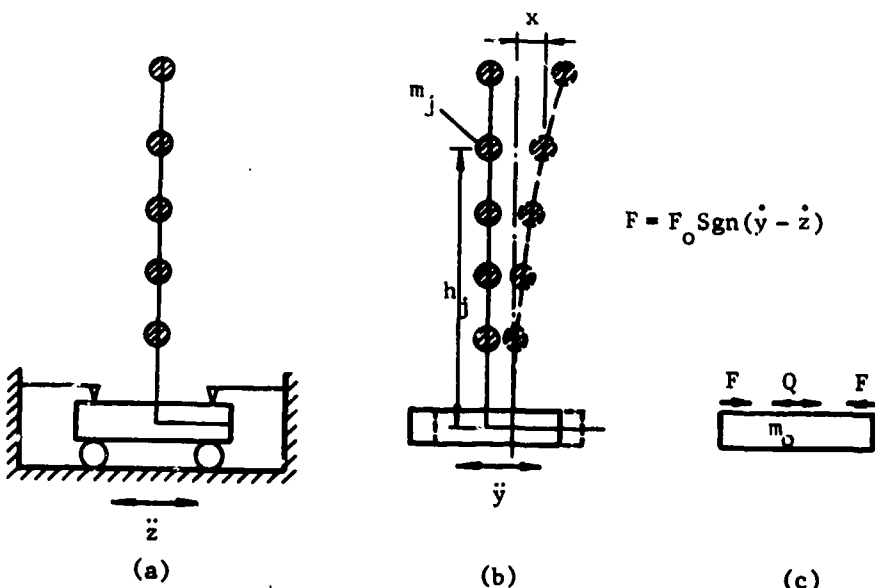


Fig. 2 - Simple model of a structure with sliding base
 (a) model of a structure with sliding base
 (b) motion of the system
 (c) forces on the base

$$Q_n(t) + m_0 \ddot{y}_n(t) = \frac{4F_0}{n\pi} \sin n\omega t$$

$$= \frac{4F_0}{n\pi} \text{Im}(e^{in\omega t}), \quad (20)$$

The solution of Eq. (19) gives the displacement response

$$x_n = -[-\omega_n^2 M + i\omega_n C + K]^{-1} M \ddot{y}_n \quad (21)$$

The inverse matrix in Eq. (21) is the transfer function matrix of the clamped super-structure. It can be calculated by a general finite element program:

$$H_n = [-\omega_n^2 M + i\omega_n C + K]^{-1}$$

$$= \phi^T \left[\frac{1}{\omega_n^2 - \omega^2 + 2i\xi \omega_n \omega} \right] \phi \quad (22)$$

where the matrix ϕ is composed of the eigenvectors, the matrix $\left[\frac{1}{\omega_n^2 - \omega^2 + 2i\xi \omega_n \omega} \right]$ is a diagonal spectrum matrix, index "T" means transpose and $\omega_n = n\omega$.

In Eq. (20), $Q_n(t)$ is the nth harmonic of base shearing force which can be determined by the summation of inertia or internal forces:

$$Q_n(t) = -\sum_{j=1}^m m_j \omega_n^2 x_j = -\mathbf{1}^T [i\omega_n C + K] \mathbf{x}_n$$

$$= \mathbf{1}^T [i\omega_n C + K] H_n M \mathbf{1} \ddot{y}_n$$

$$= \bar{Q}_n \ddot{y}_n \quad (23)$$

Using Eqs. (22), (23), Eqs. (19) and (20) become:

$$\ddot{y}_r(t) = \frac{4F_0}{n\pi} \cdot \frac{1}{\bar{Q}_n + m_0} \text{Im}(e^{in\omega t}), \quad (24)$$

$$x_n = -H_n M \mathbf{1} \ddot{y}_n(t) \quad (25)$$

For a system with m degrees-of-freedom, there are m natural frequencies, and the frictional force contains up to n th harmonic components. Hence, there will be $(m \times n)$ subharmonics in the system. The response of a 5 D.O.F. system with sliding base has been calculated. For clarity, however, only the peak responses corresponding to the first and the second modes are plotted in Fig. 3.

PREVENTION OF SUBHARMONICS

The occurrence of subharmonics can be explained by the Fourier series solution of the slip-slip periodic equations (1), (2) and (12), (13). If the excitation is so small that the base shear cannot overcome the frictional force, then the system will be locked rigidly at its own base. Hence there is no sliding movement and $y = z$. The oscillator system in Fig. 1 will be reduced to a simple damping mass spring system. Its frequency response is

$$\ddot{x}(t) = \frac{\ddot{z}_0 \sin(\omega t + \phi)}{\sqrt{[1 - (\frac{\omega_n}{\omega})^2]^2 + (2\frac{\omega_n}{\omega}\xi)^2}} \quad (26)$$

$\ddot{z} = \ddot{z}_0 \sin \omega t$ is the movement acceleration of ground surface with the peak value

$$|\ddot{x}(t)|_{\text{max}} = \frac{\ddot{z}_0}{2\xi} \quad (27)$$

which occurs at the frequency $\omega = \omega_n$.

It must be pointed out that if the base of the system is so designed that it locks when exciting frequency is lower than the fundamental natural ω_n , and yet it slides at this frequency, then the frequency response of the oscillator system will be determined by equation (26), and all the subharmonics which are less than ω_n will disappear.

During resonance $\omega = \omega_n$, the peak responses of the system are continuously growing linearly in time. Once the response of base shearing force overcomes the frictional force, then the sliding occurs. After some transient cycles, a stable periodic states will be achieved: the envelope of the peak responses will be at a constant level and there is no more growth in the peak response.

Since sliding occurs at $\omega = \omega_n$, the peak value of the response of the oscillator is not determined by Eq. (27), but determined by Eq. (8) at $\omega = \omega_n$:

$$|\ddot{x}_n(t)| = \frac{4\mu g}{n\pi} \sqrt{\frac{1}{[(1 - \gamma) - \frac{1}{n^2}]^2 + (\frac{2\xi}{n})^2}} \quad \dots \dots \quad (28)$$

Since the response of fundamental mode is dominant, so the peak response can be approximated as

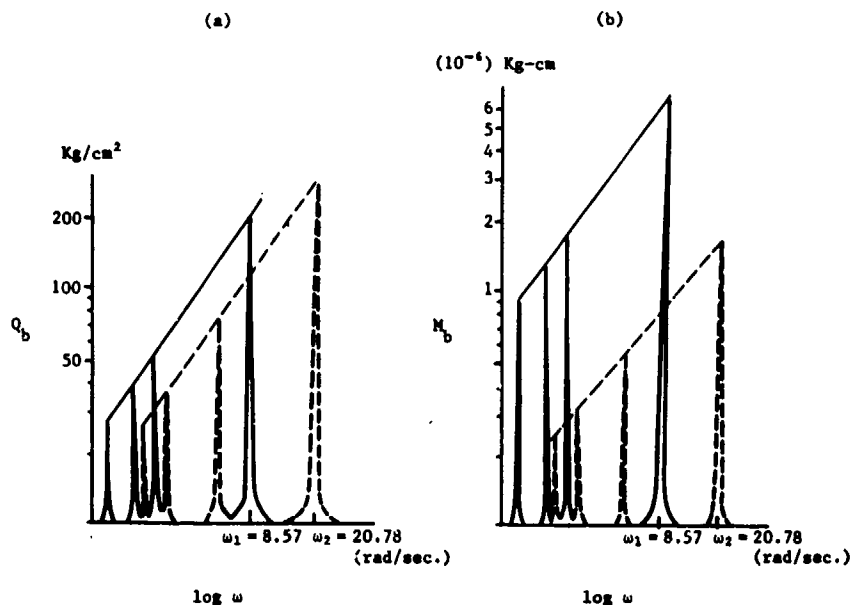


Fig. 3 - Response at the first 2 slip modes of a 5 D.O.F. sliding system
 Solid line = Subharmonics corresponding to ω_1
 Dash line = Subharmonics corresponding to ω_2
 (a) base shear response (b) overtuning moment response

$$\begin{aligned}\ddot{x}(t)|_{\omega_n} &= \sum \ddot{x}_n(t)|_{\omega_n} \doteq x_1(t)|_{\omega_n} \\ &= \frac{4\mu g}{\pi} \frac{1}{\sqrt{\gamma^2 + (2\xi)^2}} \\ &\dots \dots \dots \quad (20)\end{aligned}$$

It is obvious that this peak response is independent of the excitation of ground surface, and can be controlled by the frictional coefficient μ . Similary, this result is also valid for a many-degrees-of-freedom system with sliding base as shown in Fig. 2. In order to verify this point, the development of the resonant response of the base shear at the root section of a simple model with sliding base to harmonic excitation is calculated using the program ADINA [5], and the results are shown in Fig. 4. Obviously the transient process differs from the normal resonance process in that the peak responses are not continuously growing linearly in time, but once the peak response of the base shear has

overcome the frictional force, then the sliding occurs and the envelope of the peak responses holds at a constant level, which is dependent on the mass, the damping factor of the system and the magnitude of the frictional forces. In order to study this problem further, a bare steel frame model was tested with the base fixed and then free to slide on a simple sliding table in response to steady state horizontal harmonic base motion between 1 to 10 Hz. The experimental arrangement is shown in Fig. 5.

The base shearing frequency response curves of this model is shown in Fig. 6, from which the following points are noted: (1) When the base is free to slide at the resonance frequency, the base shear is reduced considerably as compared to that when the base is fixed. (2) The fundamental frequencies of these two states differ only slightly. (3) The frequency response curves show that the base sliding introduces a significant damping during resonance. (4) It

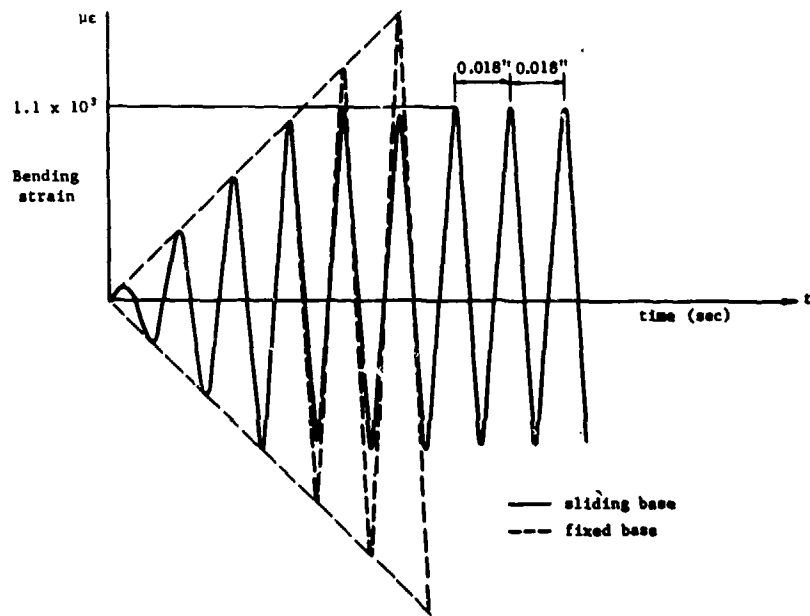


Fig. 4 - Transient response of a simple model during resonance

shows no subharmonics resonant frequencies, when exciting frequency is less than the fundamental frequency ω_n of the fixed base model. Through the study of the periodic response of a sliding system, it has been shown that the sliding supports can be quite effective in controlling the level of response of structures. However, isolation of the upper structure is achieved at the expense of slip displacement between the upper structure and its foundation. The estimation of these displacements becomes an important aspect in the application of such systems. Since the earthquake excitation is random in character, the random analysis is also important. Such work has been done to analyse a rigid mass supported on a sliding frictional surface subject to random excitation [8-12].

In this paper, the stochastic linearized method is used to study the stationary response spectrum of a simple structure with the sliding frictional base shown in Fig. 2 and the motion equations expressed by Eqs. 12 and 13. Let the acceleration of ground

motion z be represented by a discrete spectrum:

$$\ddot{z} = \sum_{j=1}^n \sqrt{2S_g(\omega_j)} \omega_j \cos(j\omega t + \psi_j) \quad (30)$$

where $S_g(\omega_j)$ is the spectrum of ground motion, and ψ_j is a random phase angle uniformly distributed between 0 to 2π . To obtain an approximate solution, equation (13) is replaced by the "equivalent" linear form using the stochastic linearized method [6,7]

$$m_0 \ddot{y} + Q(t) = -\beta \dot{x}_s \quad (31)$$

$$\text{where } \beta = -F_0 \frac{2 \int_0^{\infty} \dot{x}_s \dot{f}_s(x_s) dx_s}{\sigma_{x_s}^2}$$

$$= \left(\frac{2}{\pi}\right)^{\frac{1}{2}} \frac{F_0}{\sigma_{x_s}^2} \quad (32)$$

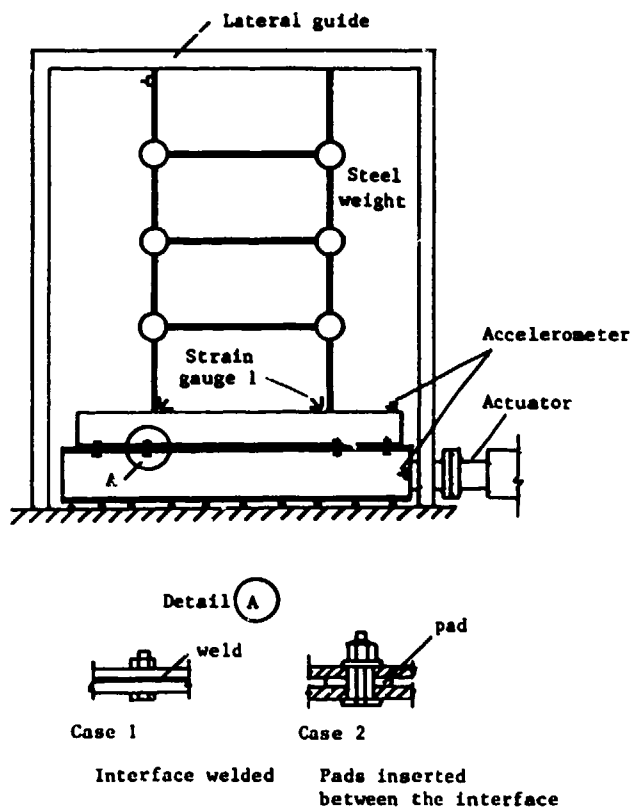


Fig. 5 - Experimental arrangement for frame on sliding base

$$f_{\dot{x}_s}(\dot{x}) = \frac{1}{(2\pi)^{\frac{1}{2}}\sigma_{\dot{x}_s}} \exp\left(-\frac{\dot{x}^2}{2\sigma_{\dot{x}_s}^2}\right) \quad (33)$$

$$\dot{x}_s = \dot{y} - \dot{z} \quad (34)$$

Integrating Eq. (30) and substituting it with Eqs. (15) - (18) into Eq. (13), changing the index n to j , the absolute and relative velocities can be obtained respectively:

$$\dot{y}(t) = \sum_{j=1}^n \frac{\sqrt{2S_g(\omega_j)\omega}}{j\omega} \sin\gamma_j \cos(j\omega t + \psi_j - \gamma_j) \quad \dots \quad (35)$$

$$\dot{x}_s(t) = \sum_{j=1}^n \frac{\sqrt{2S_g(\omega_j)\omega}}{j\omega} \cos\gamma_j \sin(j\omega t + \psi_j - \gamma_j) \quad \dots \quad (36)$$

$$\text{where } \gamma_j = \tan^{-1} - \frac{\beta}{(m_0 + Q)\omega_j} \quad (37)$$

By using Parseval equation, the variance of \dot{x}_s can be obtained:

$$\sigma_{\dot{x}_s}^2 = \sum_{j=1}^n \frac{2S_g(\omega_j)}{j^2\omega} \cos^2\gamma_j \quad (38)$$

Since $\sigma_{\dot{x}_s}^2$ and β are dependent on each other, they must be determined by iterations or by a graphical method.

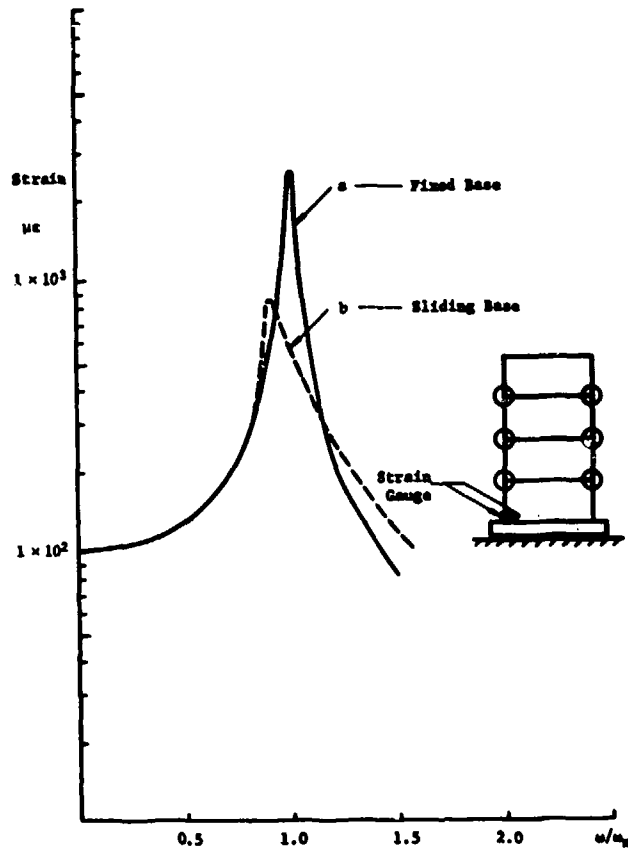


Fig. 6 - Frequency response curve of bending strain at root section of frame

CONCLUDING REMARKS

1. The resonant response of a structure to harmonic excitation can be reduced considerably by mounting the structure on a sliding base.
2. During sliding, there are $m \times n$ subharmonics which can be induced by the superharmonic components of the nonlinear frictional force, where m is the number of degrees-of-freedom of the structure, n is the number of superharmonics of the frictional force. Hence, the response of a sliding base system can be higher than those of a fixed base system for the frequencies less than the fixed base natural frequency ω_n .
3. If the frictional force is con-
4. Trolled so that the sliding interface is locked rigidly when the exciting frequency is lower than the fundamental frequency of a system but the interface slides at the resonant frequency, then all the subharmonics below the fundamental frequency will disappear. With such control the resonant response will be reduced considerably and the fundamental frequency of a system will not change. Therefore, it is applicable for the isolation of those structures having low fundamental frequency to low frequency excitation.
4. Though earthquake loading is non-periodic, the periodic response of a structure to harmonic excitation can explicitly show the fundamental

dynamic behaviour of a system.

5. Stochastic equivalent linearized approach has been used to study the steady random response of the structure-sliding base system. Since the earthquake excitation is a non-stationary random process, further research on non-stationary random analysis is needed.

ACKNOWLEDGEMENT

The work described in this Paper was undertaken in the Department of Civil & Structural Engineering, University of Hong Kong. The financial support of the Croucher Foundation to Mr. Tian is gratefully acknowledged.

APPENDIX

NOTATIONS

β	= equivalent linearized damping coefficient
F_o	= magnitude of Coulumb force
$f_{\dot{x}_s}$	= probability density function of \dot{x}_s
H_n	= nth transfer function matrix of the clamped super-structure
k	= spring constant of a sliding oscillator
m_1	= top mass of a sliding oscillator
m_2	= base mass of a sliding oscillator
m_o	= base mass of a simple model of a structure
Q	= base shearing force
Q_n	= nth harmonic of base shearing force
\bar{Q}_n	= nth harmonic of base shearing force induced by a unit base movement
x	= elastic displacement of upper structure
x_p	= nth harmonic component of structure displacement
$x_s - y - z$	= relative displacement between base and foundation

y	= movement of base
y_n	= nth harmonic component of base movement
z	= movement of ground surface
$Sgn(z-y)$	= $(\dot{z}-\dot{y})/ \dot{z}-\dot{y} $
γ	= $m_1/(m_1 + m_2)$
μ	= friction coefficient
ξ	= mode damping coefficient
ξ_r	= rth mode damping coefficient
$\sigma_{\dot{x}_s}$	= root mean square value of sliding displacement
ϕ_n	= hysterestic phase
ψ_j	= random phase angle
ω	= exciting frequency
γ_j	= hysterestic phase angle between sliding base and ground surface
ω_n	= $n \times \omega$
ω_j	= $j \times \omega$

MATRIX NOTATIONS

C	= damping matrix of the frame
K	= stiffness matrix of the frame
M	= mass matrix of the frame
Φ	= eigenvector matrix

REFERENCE

1. B. Westermo and F. Udwadia, "Periodic Response of a Sliding Oscillator System to Harmonic Excitation", Earthquake Engineering and Structural Dynamic, Vol. II, pp. 135-146, 1983.
2. N. Mostaghali, M. Hejazi and J. Tanbakuchi, "Response of Sliding Structures to Harmonic Support Motion", Ibid., Vol. II, pp. 355-366, 1983.
3. M. Qamaruddin, B. Chandra and A.S. Arya, "Dynamic Testing of Brick Building Models", Proc. Inst. Civ. Engrs., Pt. 2, Vol. 77, pp. 353-365. Sept. 1984.

4. T.C. Liauw, Q.L. Tian and Y.K. Cheung, "Dynamic Response of Infilled Frame with Sliding Base Device", Proc. I.C.E., Pt. 2, Vol. 81, pp. 55-69, 1986.
5. Kleus-Jurgen Bathe, "ADINA - A Finite Element Program for Automatic Dynamic Incremental Non-linear Analysis", M.I.T., U.S.A.
6. T.K. Caughey, "Random Excitation of a System with Bilinear Hysteresis", J. Appl. Mech., pp. 649, Dec. 1960.
7. Y.K. Lin, "Probabilistic Theory of Structural Dynamics", McGraw Hill, New York, 1967.
8. T.K. Caughey and J.K. Dienes, "Analysis of Nonlinear First-order System with a White Noise Input", J. Appl. Phys. 32(11), pp. 2476-2479, 1961.
9. S.H. Crandall, S.S. Lee and J.H. Willams, "Accumulated Slip of a Friction-controlled Mass Excited by Earthquake Motions", J. Appl. Mech., ASME 41: pp. 1094-1098, 1974.
10. S.H. Crandall and S.S. Lee, "Biaxal Slip of a Mass on a Foundation Subject to Earthquake Motion", Ing-Arch. 45, pp. 361-370, 1976.
11. G. Ahmadi, "Stochastic Earthquake Response of Structures on Sliding Foundation", Int. J. Eng. Sci. 21(2), pp. 93-102, 1983.
12. Constantinou and Jadjbakrsh, "Response of a Sliding Structure", J. Struct. Mech., 12(3), 1984.

A MODAL CONTROL BASED LIMITING PERFORMANCE FORMULATION FOR SHOCK EXCITED SYSTEMS

Y. Narkis
State of Israel Ministry of Defense
Armament Development Authority
Haifa, Israel

and

W. D. Pilkey
Department of Mechanical and Aerospace Engineering
University of Virginia
Charlottesville, Virginia 22901

The limiting performance of shock isolation of multi-degree-of-freedom systems is studied by a combined modal analysis, modal control approach. The isolating elements are replaced by a control forces, which are then approximated by a time series based on the natural frequencies of the system. Assuming that the equations of motion, the performance index, and the constraints are all linear, the optimization problem is formulated as one of linear programming. A two-degree-of-freedom example is solved to demonstrate the feasibility of the proposed method and its advantages over other methods. The modal analysis - modal control approach is then applied to the solution of the limiting performance problem of shock isolation of a cantilever beam.

INTRODUCTION

Knowing the limiting performance of a system (its absolute optimal response), is of considerable value to the designer. It may provide either a basis for indirect synthesis of the appropriate system or a reference for evaluating an existing design. To calculate the limiting performance, those portions of the system being designed are replaced by control forces which do not refer to any particular design. These controls are then determined so that a relevant performance index is optimized, while satisfying a given set of constraints imposed on response variables. Carrying out this procedure for several constraint levels results in a limiting performance trade-off curve of the optimal performance index (e.g., minimal acceleration) vs. prescribed constraints (e.g., rattlespace).

The formulation of a limiting performance calculation by linear programming is given in detail in a monograph by Sevir and Pilkey [1], which deals mainly with shock isolation. The response of mechanical systems subjected to steady-state loading is considered in [2]. A modal approach to the investigation of optimal shock damping of systems was recently suggested by [3].

When the problem studied here is of a transient nature; control forces are usually time-discretized as piecewise-constant functions. While easing the task of developing a linear programming formulation, this

discretization method has some drawbacks: (1) by decreasing the size of the time step to improve accuracy, one increases the number of variables and thereby the time needed for numerical solution. (2) the optimal piecewise constant solution is frequently a bang-bang control, which is difficult to synthesize by conventional damping elements. (3) In many cases, the optimal control starts at high force values, requiring a "prediction" mechanism, which is unavailable in passive elements. In order to overcome these shortcomings, the limiting performance problem was reformulated [4] using smooth control forces, represented by a Fourier series. The fundamental period of the Fourier expansion is determined arbitrarily, e.g., by the time interval of interest. The method was applied with satisfactory results to two- and three-degree of freedom systems.

While any control function can be described accurately by a Fourier series using a sufficient number of terms, this may not always be the most efficient way. When the system under consideration has some natural frequencies of its own (unlike the examples of Ref. 4), these frequencies can be used in the time-series expansion, instead of developing the series in an arbitrary basic frequency. The present paper deals with limiting performance evaluation for shock isolation of multi-d.o.f. systems. A modal approach is used both for the structural dynamics analysis and for the controls, resulting in a simplified dynamic analysis and an efficient linear programming computation.

FORMULATION OF THE OPTIMIZATION PROBLEM

To find the limiting performance of a dynamic system, those portions of the system to be designed, e.g., dampers, are replaced by control forces. The equation of motion of a linear N-degree-of-freedom system, subjected to a known excitation $f(t)$ and control forces $u(t)$ is

$$M \ddot{x} + C \dot{x} + K x + Vu = Ff \quad (1)$$

where x is the displacement vector of the system, M , C , K are the $N \times N$ mass, damping, and stiffness matrices, respectively, V is an $N \times J$ matrix whose elements are 0, 1 or -1, which assigns each of the J control forces to its appropriate d.o.f., and F is an $N \times N$ coefficient matrix, relating the N external excitation forces to the system.

The initial conditions associated with the dynamic equation, $x(\text{zero})$ and $\dot{x}(\text{zero})$, are known. In practice, one usually assumes static initial conditions, i.e., $x(0) = \dot{x}(0) = 0$.

The optimization problem is to find $u(t)$ which will minimize a given performance index, while complying with a certain set of constraints imposed upon the response. The control $u(t)$ may, in general, assume any value, but in some cases may be bounded or included in the performance index.

The performance index is the maximum value (in space and time) of a given linear combination of the response parameters and the external forces

$$\psi = \max_i \max_t (P_1 \ddot{x} + P_2 \dot{x} + P_3 x + P_4 u + P_5 f) \quad (2)$$

where the P_k are prescribed coefficient matrices.

The constraints can be specified by a similar linear combination

$$|Y_1 \ddot{x} + Y_2 \dot{x} + Y_3 x + Y_4 u + Y_5 f| \leq Y_{ci} \quad (3)$$

where Y_k are the prescribed coefficient matrices and Y_{ci} is the bound on absolute value of the i -th constraint.

The optimization problem may then be stated as finding $u(t)$ which will minimize ψ , subject to equation (1) and constraints (3).

METHOD OF SOLUTION

Modal Solution of Undamped Systems

While damping exists in most isolation devices, the structural damping of the excited system itself is usually much lower, and can be neglected when treating short-time transients.

In what follows, an undamped system ($C=0$) will be discussed.

To obtain the natural characteristics of the given system, solve the homogeneous equation

$$M \ddot{x} + K x = \text{zero} \quad (4)$$

and find the natural frequencies ω_ℓ and modeshapes ϕ_ℓ , $\ell=1, \dots, NF$, $NF \leq N$

The equation of motion may be uncoupled by substituting

$$x = \Phi q \quad (5)$$

into (1)

$$M \ddot{\Phi} q + K \ddot{\Phi} q + Vq = Ff \quad (6)$$

and premultiplying by Φ^T :

$$\Phi^T M \ddot{\Phi} q + \Phi^T K \ddot{\Phi} q + \Phi^T Vq = \Phi^T Ff \quad (7)$$

Designating the modal mass and stiffness matrices (both diagonal) by

$$\Phi^T M \Phi \equiv M_\Phi \quad (8a)$$

$$\Phi^T K \Phi \equiv K_\Phi \quad (8b)$$

the governing equation becomes

$$M_\Phi \ddot{\Phi} q + K_\Phi \ddot{\Phi} q + \Phi^T Vq = \Phi^T Ff \quad (9)$$

with the given initial conditions $q(0)$, $\dot{q}(0)$.

The matrix equation (9) constitutes a set of uncoupled linear differential equations. The external forces f, u will generally excite (or control) all of the modes.

To simplify the solution, the coordinate vector q can be resolved into two parts,

$$q = q^F + q^U \quad (10)$$

where q^F satisfies the equation of motion governed by the external excitation and the initial conditions

$$M_\Phi \ddot{\Phi} q^F + K_\Phi \ddot{\Phi} q^F = \Phi^T Ff(t) \quad (11)$$

$$q^F(0) = q(0)$$

$$\dot{q}^F(0) = \dot{q}(0)$$

q^F can be calculated independently of q^U by

integrating (11) to obtain $q^F(t)$ at any needed time.

The other part of q , i.e., q^u , will have to satisfy the controlled form of the equation of motion, subject to static initial conditions.

$$M_{\phi} \ddot{q}^u + K_{\phi} q^u + \frac{1}{2} t V u = 0 \quad (12)$$

$$q^u(0) = \dot{q}^u(0) = 0$$

From this set, one can find the controlled part of the motion $q^u(y, t)$. The explicit form of the expression depends on the method chosen for discretizing the control $u(t)$.

Discretization of the Controls

As already noted above, both piecewise-constant and Fourier series methods have their drawbacks when dealing with the transient motion of multi-d.o.f. systems. In the present work, a solution will be derived by expanding the control forces in trigonometric time-series, similar to Fourier series, but instead of using an arbitrary time interval as the fundamental period of the series, use will be made of the natural frequencies of the system.

Assume each of the control forces may be expressed as

$$u = u_0 + \sum_{\ell} (A_{\ell} \cos \omega_{\ell} t + B_{\ell} \sin \omega_{\ell} t) \quad (13)$$

where ω_{ℓ} are the natural frequencies of the system, determined previously by solving (4). When dealing with a continuous system, or a discrete system with a large number of d.o.f., a truncated series should be used, the number of the terms retained being in accordance with the needed accuracy.

In this connection, a difference between piecewise constant and time series discretization should be noted. In the first method, improving the accuracy is done by decreasing the time step. In the second method, better accuracy may be achieved by either using smaller time intervals or taking more terms in the series. However, these two possibilities are not totally independent. As will be shown in the appendix, there is a limit to the number of terms which may be used for a given number of time intervals, whereas there is no upper limit to the number of time intervals.

One of the advantages of using smooth control forces is the ability to simulate better real-world damping elements. Assuming a stationary system before the application of the shock.

$$x(0) = \dot{x}(0) = 0 \quad (14a)$$

Any shock can be treated as starting from zero, and having a finite rise time, so the excited

system starts also at zero acceleration

$$x(0) = 0 \quad (14b)$$

For a controller which is located between any two points of the system and made of passive elements (springs and viscous dampers), the force will be a function of the differential displacement and velocity between those points. Thus,

$$u = f(\delta x, \dot{\delta}x) \quad (15a)$$

which will be zero for zero differential displacement and velocity. The time derivative of this control force is

$$u = \frac{\partial f}{\partial(\delta x)} \delta x + \frac{\partial f}{\partial(\dot{\delta}x)} \dot{\delta}x \quad (15b)$$

Introducing (14a,b) into (15a,b), one obtains the initial conditions for the control force

$$u(0) = \dot{u}(0) = 0 \quad (16)$$

Although these conditions interfere somewhat with the pure notion of limiting performance as an absolute optimum, they enhance the practicability of the results.

Substituting $t=0$ in (13) and its derivative, and making use of (16), the final expansion of the control force is obtained as

$$u = \sum_{\ell} A_{\ell} (1 - \cos \omega_{\ell} t) + \sum_{\ell} B_{\ell} \sin \omega_{\ell} t \quad (17)$$

$$\text{and} \quad \sum_{\ell} B_{\ell} \omega_{\ell} = 0$$

Thus, besides producing a more realistic limiting performance solution, use of the conditions (16) may decrease the number of unknowns by two.

Now that the control force is expressed in a series form, Eq. (12) can be solved for q^u . Rewrite (12) as

$$\ddot{q}^u + M_{\phi}^{-1} K_{\phi} q^u = -M_{\phi}^{-1} \frac{1}{2} t V u \quad (18)$$

Designating $-M_{\phi}^{-1} \frac{1}{2} t V = C$ and employing the fact that (18) is a set of uncoupled equations, one can write the equation governing the i -th mode

$$\ddot{q}_i^u + \omega_i^2 q_i^u = \sum_j C_{ij} u_j \quad (19)$$

Substituting the series expansion (17) for u_j in the above equation

$$\ddot{q}_i^u + \omega_i^2 q_i^u = \sum_{j=1}^J \sum_{\ell=1}^{NF} C_{ij} [A_{j\ell}(1 - \cos \omega_\ell t) + B_{j\ell} \sin \omega_\ell t] \quad (20)$$

The summation on the right hand side is done over NF relevant modes ($NF \leq N$) and over all J controls.

The solution of (20) is

$$\begin{aligned} q_i^u = q_{i0} + \sum_{\ell} (D_{i\ell} \cos \omega_\ell t + E_{i\ell} \sin \omega_\ell t) \\ + q_{ic} t \cos \omega_i t + q_{is} t \sin \omega_i t \end{aligned} \quad (21)$$

The constants in this expression can be found by differentiating it twice, putting it into (20), and equating the coefficients of functions of identical frequencies. This results in

$$q_{i0} = \frac{1}{\omega_i^2} \sum_j \sum_{\ell} C_{ij} A_{j\ell} \quad (22a)$$

$$D_{i\ell} = -\frac{1}{\omega_i^2 - \omega_\ell^2} \sum_j C_{ij} A_{j\ell} \quad \ell \neq i \quad (22b)$$

$$E_{i\ell} = \frac{1}{\omega_i^2 - \omega_\ell^2} \sum_j C_{ij} B_{j\ell} \quad \ell \neq i \quad (22c)$$

$$q_{ic} = -\frac{1}{2\omega_i} \sum_j C_{ij} B_{ji} \quad (22d)$$

$$q_{is} = -\frac{1}{2\omega_i} \sum_j C_{ij} A_{ji} \quad (22e)$$

The constants D_{ii} , E_{ii} cancelled during the calculation but can be evaluated directly from (21) by imposing the initial conditions $q^u(0) = \ddot{q}^u(0) = 0$

$$D_{ii} = - (q_{i0} + \sum_{\ell \neq i} D_{i\ell}) \quad (22f)$$

$$E_{ii} = -\frac{1}{\omega_i} (q_{ic} + \sum_{\ell \neq i} E_{i\ell} \omega_\ell) \quad (22g)$$

This completes the solution of the dynamic equations, resulting in an expression for the time variation of the displacements, in modal form, in terms of the control coefficients

$$q = q^F + q^u = q(t, A_{j\ell}, B_{j\ell}) \quad (23)$$

Computational Procedure

After having developed the needed relations for the dynamic solution, the complete

computational procedure of the limiting performance can be outlined.

1. Solve the free system (4), obtain the natural frequencies and modeshapes.
2. Calculate the elements C_{ij}
3. Express the coefficients of q^u in terms of $A_{j\ell}$, $B_{j\ell}$ according to the set (22).
4. Find q^F and q^u at the appropriate time intervals (t_1, t_2, \dots, t_f) from (11) and (21) respectively.
5. Express the displacement vector x and its derivatives at (t_1, t_2, \dots, t_f) in terms of $A_{j\ell}$, $B_{j\ell}$ using (5).
6. Solve the linear programming problem of minimizing the performance index (2), subject to the constraints (3).

EXAMPLE - TWO DOF SYSTEM

To demonstrate the feasibility and advantages of using the natural frequencies in studying the limiting performance of a transient system, the two d.o.f. system of Figure 1 was investigated. It consists of two equal masses $m_1 = m_2 = m$, connected by unequal springs to two separate bases. One of the bases is stationary whereas the other one is excited by a known shock. The element between the two masses is to be designed so that the acceleration of m_1 will be minimal, subject to a displacement constraint on m_2 . The shock is assumed to be a half-sine displacement. Replacing the unknown isolation device by a general control force, the dynamic equations of the system are uncoupled:

$$\begin{aligned} \ddot{x}_1 + \omega_1^2 x_1 + u/m &= a \sin \omega t & 0 < t \leq t_f \\ &= 0 & t > t_f \end{aligned} \quad (24a)$$

$$\ddot{x}_2 + \omega_2^2 x_2 - u/m = 0 \quad (24b)$$

Approximate the control by a two-frequency series, having three unknown constants

$$\begin{aligned} u &= A_1 (1 - \cos \omega_1 t) + A_2 (1 - \cos \omega_2 t) \\ &+ B_1 \sin \omega_1 t - B_1 \frac{\omega_1}{\omega_2} \sin \omega_2 t \end{aligned} \quad (25)$$

The optimization problem can be stated as:

Find the constants A_1, A_2, B_1 such that

$$\max |x_1| \rightarrow \min \quad |x_2| \leq d$$

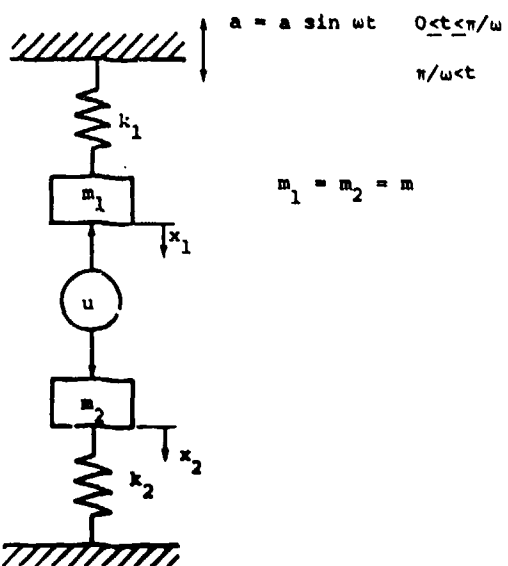


Fig. 1 Two-degree-of-freedom transient system

The limiting performance of this system was studied using the procedure presented above. Figure 2 shows the time-variation of u , x_1 and x_2 for the following set of parameters:

$$m = 1 \text{ kgm}, \omega_1 = 100 \text{ r/sec}, \omega_2 = 70 \text{ r/sec},$$

$$d = 1 \text{ mm}, a = 10 \text{ m/sec}^2.$$

The shock duration in this case is $t_f = 0.06$ sec, and therefore $\omega = \pi/t_f = 52.36 \text{ r/sec}$. The time step for the calculation was chosen as $1/8$ of t_f , and the total time $1.25 t_f$.

The results as given in Figure 2 show that limiting performance calculation using a natural frequencies series is feasible, yielding a smooth control force, which satisfies the initial physical conditions. The maximal acceleration of mass m_1 is found here to be 3.71 m/sec^2 (compared with 13.96 m/sec^2 for an uncontrolled mass).

In order to assess the efficiency of the present approach versus the Fourier-series approximation of the control, the same limiting performance problem was solved using a comparable two-frequency Fourier series. The $\min(\max x_1)$ found by both methods is presented in Figure 3 for a range of shock durations. As can be seen, the natural frequency method gives better results than the Fourier series for most of the range, except for shock duration of 0.06 to 0.09 seconds. For these values the shock frequency, and hence the basic Fourier frequency are close to the natural frequencies, of the dynamic system, and the two methods should produce similar solutions. For longer shock

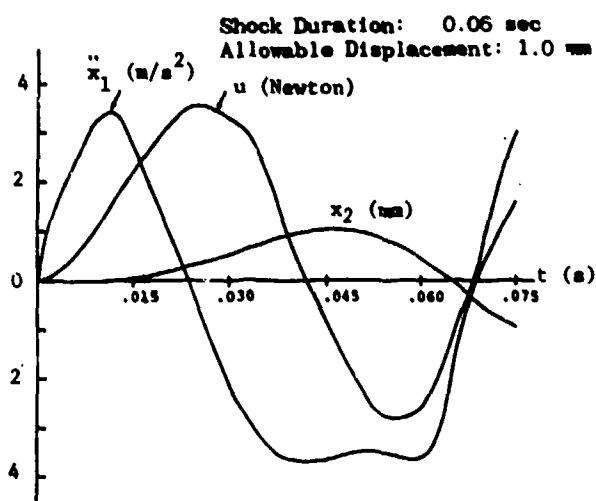


Fig. 2 Time variation of control u , acceleration x_1 , and displacement x_2 by use of natural frequencies

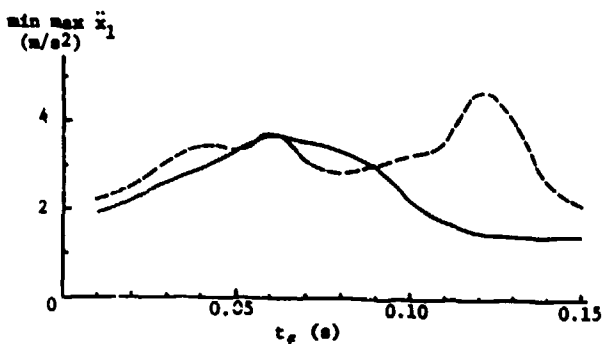


Fig. 3 Limiting performance by natural frequencies (solid line) and Fourier series (dashed line) for varying shock duration

durations, the expansion in natural frequencies proves to be much superior to the Fourier series.

SHOCK DAMPING OF BEAMS

The modal analysis - modal control approach which was described above is especially suitable for finding the limiting performance of continuous systems. Consider the undamped, uniform cantilever beam sketched in Figure 4. Masses are attached to the beam at its midpoint and free tip, and the connecting mechanical elements have been replaced by generic control forces. The beam is excited by a given shock at its built-in end. In the present example, this shock is assumed to be a decaying oscillation described by

$$y = Y_0 (1 - \cos \omega_s t) e^{-t/t_D} \quad (26)$$

As the dynamic system is linear, its response is directly proportional to Y_0 . In the following analysis, a unit shock ($Y_0 = 1$) is considered.

Treatment of the passive dynamic version of this system usually concentrates on finding optimum values of absorber tuning and damping for steady state excitation (e.g., [5], [6]). The transient case of the same configuration, with a different loading, was treated in [3].

The objective function to be minimized is the maximal acceleration of the free end, while the constraints are imposed on the rattlespaces between the beam and the two masses.

The dynamic problem will be treated by the finite element method, using conventional beam elements. However, since the system under consideration is a uniform cantilever beam, available relationships for its mode shapes and natural frequencies can be used.

The beam is divided into N elements, each with four degrees of freedom. There are two degrees of freedom at the built-in end for which the angular displacement is identically zero and the transverse displacement is the given external shock. The dynamic system is therefore of order $2N$. Let x be the generalized displacement vector having $2N$ elements, and let y be the known fixed end translation. Following the procedure presented above, one considers first the uncontrolled system. The dynamic equation of motion in this case will be

$$C_m \begin{bmatrix} 0 \\ 0 \\ \vdots \\ 54 \\ 13AL \\ \hline 0 0 \dots 54 13AL \end{bmatrix} x + C_k \begin{bmatrix} 0 \\ 0 \\ \vdots \\ -12 \\ -6AL \\ \hline 0 0 \dots -12 -6AL \end{bmatrix} y = f \quad (27)$$

where M and K are the $2N \times 2N$ mass and stiffness matrices of the cantilever beam, AL is the length of a single element and

$$C_m = \frac{\rho AL}{420} \quad C_k = \frac{EI}{AL^3}$$

The last equation of this set determines the

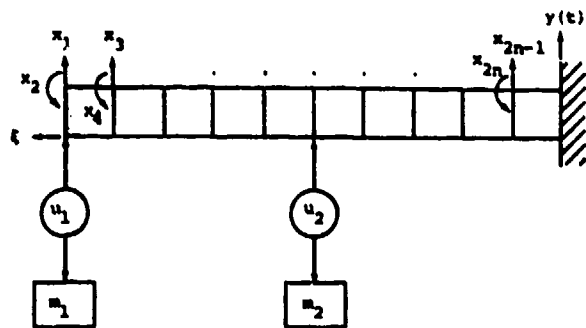


Fig. 4 Cantilever beam with two damping masses

force at the built-in end. Considering only the $2N$ active degrees of freedom, Eq. (27) can be rewritten as

$$M \ddot{x} + K \ddot{x} = C_m \begin{bmatrix} 0 \\ 0 \\ \vdots \\ 54 \\ 13AL \end{bmatrix} y - C_k \begin{bmatrix} 0 \\ 0 \\ \vdots \\ -12 \\ -6AL \end{bmatrix} y \quad (28)$$

Proceed as outlined above; substitute $x = \phi q$ and multiply by ϕ^T

$$M \ddot{\phi} q^F + K \ddot{\phi} q^F = \phi^T \begin{bmatrix} 0 \\ 0 \\ \vdots \\ y_1 \\ y_2 \end{bmatrix} \quad (29)$$

where

$$\begin{aligned} y_1 &= -54 C_m \ddot{y} + 12 C_k \ddot{y} \\ y_2 &= -13AL C_m \ddot{y} + 6AL C_k \ddot{y} \end{aligned}$$

For the i -th mode of the uncoupled set (29), division by $M \ddot{\phi}_i$ results in the governing equation

$$q_i^F + \omega_i^2 q_i^F = \frac{\phi_{2N-1,i}}{M \ddot{\phi}_i} y_1 + \frac{\phi_{2N,i}}{M \ddot{\phi}_i} y_2 \quad (30)$$

The mode shapes and natural frequencies will be taken from the exact beam solution (e.g., [7])

$$\begin{aligned} \ddot{\phi}(F) &= \sum_i A_i \left[(\sin \beta_i F - \sinh \beta_i F) \right. \\ &\quad \left. (\sin \beta_i F - \sinh \beta_i F) \right] \\ &= (\cos \beta_i F + \cosh \beta_i F)(\cos \beta_i F - \cosh \beta_i F) \end{aligned} \quad (31)$$

$$\omega_i = (\beta_i F)^2 \frac{EI}{mL^4} \quad (32)$$

where $\beta_1 L = 1.8751$, $\beta_2 L = 4.6941$, etc.

Replace the longitudinal coordinate f by the distance of the n th node from the fixed end

$$f = (N-n+1)\Delta L \quad (33)$$

so that normal modes for use in (30) are obtained. For displacements

$$\begin{aligned} \phi_{2n-1,1} = & (\sin \beta_1 L - \sinh \beta_1 L) [\sin(N-n+1)\beta_1 \Delta L - \\ & \sinh(N-n+1)\beta_1 \Delta L] + (\cos \beta_1 L + \\ & \cosh \beta_1 L) [\cos(N-n+1)\beta_1 \Delta L - \\ & \cosh(N-n+1)\beta_1 \Delta L] \end{aligned} \quad (34)$$

and for slopes

$$\begin{aligned} \phi_{2n,1} = & -\beta_1 \{ (\sin \beta_1 L - \sinh \beta_1 L) \} \\ & [\cos(N-n+1)\beta_1 \Delta L - \cosh(N-n+1)\beta_1 \Delta L] \} \\ & - (\cos \beta_1 L + \cosh \beta_1 L) [\sin(N-n+1)\beta_1 \Delta L \\ & + \sinh(N-n+1)\beta_1 \Delta L] \} \end{aligned} \quad (35)$$

The solution of (30) is

$$q_i^F = A_i \sin \omega_i t + B_i \cos \omega_i t + f_i(t) \quad (36)$$

where $f_i(t)$ is the particular solution which depends on the eternal excitation. For the decaying shock (26) it can be shown that

$$f_i(t) = (F_0 + F_1 \cos \omega_s t + F_2 \sin \omega_s t) e^{-t/t_D} \quad (37)$$

The values of F_0 , F_1 and F_2 are given in Appendix 2. The coefficients A_i and B_i can be determined using the initial conditions of the system. Assuming that the beam is started from rest,

$$A_i = \frac{F_0/t_D + F_1/t_D - \omega_s F_2}{\omega_i} \quad (38a)$$

$$B_i = -F_0 - F_1 \quad (38b)$$

For the next step of the solution, consider the response of the beam to the control forces. The $(2N \times 2)$ coefficient matrix V of Equation (1) has only two non-zero elements, namely $V(1,1)=1$ and $V(N+1,2)=1$. Using the notation of Equation (19), the values of the constants in the uncoupled equation will be

$$C_{11} = -\phi_{1,1} / M_{\phi 1} \quad (39a)$$

$$C_{12} = -\phi_{N+1,1} / M_{\phi 1} \quad (39b)$$

Introduction of Eqs. (39a,b) into Eqs. (22)

results in the response of the beam being expressed in terms of the unknown control coefficients A_{j1} , B_{j1} of Eq. (17). The complete response is obtained by superposition of the forced and controlled motions, and transformation of the solution from modal variables to the real displacement vector x . Inserting this into the expressions for the objective function (2) and the constraint set (3), and employing a linear programming code, the optimal values of A_{j1} and B_{j1} may be found.

The problem was solved for the beam of [3], having $EI = 62.58 \times 10^8$ lb.in 2 , $L = 150$ inch, and $\rho = 2.6$ lb.sec 2 /in 2 , divided into $N = 10$ elements. The appended masses were each 10% of the total beam mass, and the shock parameters were $t_s = 2\pi/\omega_s = 0.1$ sec, $t_D = 0.05$ sec.

Objective Function
(in/sec 2)

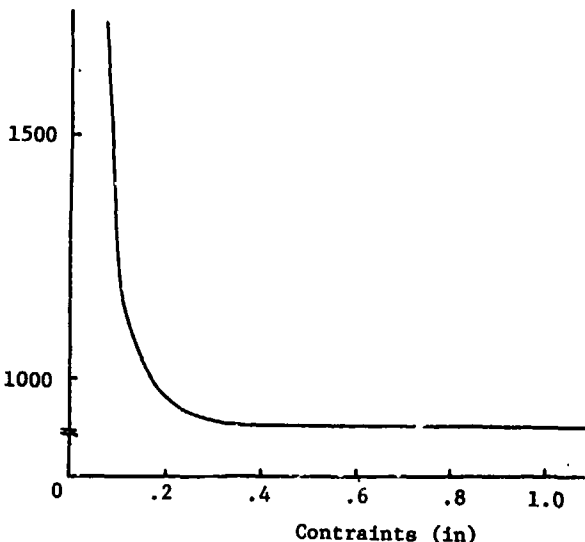


Fig. 5 Trade-off curve for beam isolation

The trade-off curve for equal constraints on the two rattlespaces is given in Figure 5. The calculations were made for 25 time intervals of 0.004 sec. each, taking into account three modes. These results should be compared with the maximal free end acceleration of the

uncontrolled response, which is 2200 in/sec 2 . This means that using three modes, up to 60% of the acceleration might be damped out, and the residual is at higher frequencies. As the constraints are tightened, the possible damping is reduced. To estimate the convergence of the procedure, the calculations were repeated for both rattlespace constraints equal to 1, with different numbers of modes. The results are given in the table below and display quite a satisfactory convergence for the limited number of modes considered. Further increase in the number of modes employed does not change the results significantly.

No of Modes	Objective Function
1	1980
2	1096
3	901

Application of Digital Signal Processing,
Prentice-Hall, Inc., 1975.

CONCLUSIONS

In this study, the limiting performance problem for the shock isolation of linear multidegree-of-freedom systems was treated, using modal analysis for the structural dynamics and for smooth control forces. A general formulation was presented in which the control forces were approximated by a time series based on the natural frequencies of the system. This modal control approach can be applied to any multi-d.o.f. discrete system and to continuous systems. The limiting performance of a two-d.o.f. system was investigated by the proposed method and by expanding the control in a conventional truncated Fourier series. The results confirm the feasibility of using natural frequencies in analyzing transient processes. For most of the range of shock durations investigated, the modal control method was found to be superior to a Fourier series of the same number of terms. To demonstrate the application of the method to continuous systems, the limiting performance for the shock isolation of a cantilever beam was explored. Satisfactory results were obtained by using three modes.

REFERENCES

1. Sevin, E. and Pilkey, W.D., Optimum Shock and Vibration Isolation, SVIC, Washington, D.C., 1971.
2. Wang, B. P. and Pilkey, W.D., "Limiting Performance Characteristics of Steady State Systems," ASME J. of Applied Mechanics, Vol. 41, Sep. 1975, pp. 721-726.
3. Pilkey, W.D. and Kitis, L., "Limiting Performance of Shock Isolation Systems by a Modal Approach," Earthquake Engineering and Structural Dynamics, 1965.
4. Chen, Y.H., Kalinowski, A.J. and Pilkey, W.D., "Indirect Synthesis of Multidegree-of-Freedom Transient Systems," J. of Optimization Theory and Application, Vol. 20, Nov. 1976, pp. 331-346.
5. Snowdon, J.C., Vibration and Shock in Damped Mechanical Systems, Wiley, N.Y., 1968.
6. Satter, M.A., "Vibration of Beams Carrying Discrete Dampers and Masses," ASME J. of Mechanical Design, Vol. 101, Apr. 1979, pp. 317-321.
7. Meirovitch, L., Analytical Methods in Vibrations, Macmillan, N.Y., 1967.
8. Rabiner, L.R. and Gold, B., Theory and

NOTATION

a	- constant
A_{ij}	- coefficients
B_{ij}	- coefficients
C	- damping matrix
C_k	- beam element stiffness coefficient
C_m	- beam element mass coefficient
C_{ij}	- coefficients
d	- displacement constraint
D_{ij}	- coefficients
E	- beam Young's modulus
E_{ij}	- coefficients
f	- force
F	- coefficient matrix
F_i	- constants
I	- beam moment of inertia
J	- number of controls
K	- stiffness matrix
K_ϕ	- modal stiffness matrix
L	- length of beam
AL	- length of beam element
m	- mass
M	- mass matrix
M_ϕ	- modal mass matrix
N	- degree of system; number of beam elements
NC	- number of constraints
NF	- number of modes
NL	- number of external excitations
NT	- number of time discretizations
P_1, P_2, P_3	- coefficient matrices
q	- modal coordinates
t	- time
t_D	- time constant
t_S	- shock period
u	- control force vector
V	- coefficient matrix
x	- displacement vector
y	- external shock (displacement)
y_c	- constraint vector
Y_1, Y_2, Y_3	- coefficient matrices
β_i	- beam eigenvalues
ϵ	- mass density per unit length
ϕ	- mode shape
ψ	- performance index
ω	- frequency
ξ	- longitudinal beam coordinate

superscripts:

F	- external force
U	- control force
t	- transpose

APPENDIX 1

ESTIMATION OF THE MAXIMUM ALLOWABLE NUMBER OF TERMS IN THE SERIES EXPANSION

In the formulation of the linear programming problem, the objective function and the given constraints are expressed as inequalities which have to be satisfied at every time instance. The number of inequalities is therefore proportional to the number of time intervals NT . When the control force is expanded in any time series, the number of unknown coefficients will be equal to the number of terms one chooses to take into consideration. In the case of a sine-cosine series, truncating the series after NF frequencies results in having $2NF$ unknowns (assuming that the free term is determined by demanding zero initial force). The optimization problem is to minimize the performance index ψ , subject to a given NC constraint. In LP formulation this is expressed as $1+NC$ inequalities which have to be met at all NT time instances, resulting in $(1+NC) \times NT$ inequalities.

Consider now two extreme cases. When the constraints are very narrow, approaching zero in the limit, the inequalities turn into equations. One may search an optimal solution for which $\psi=0$. In this case there are $(1+NC) NT$ equations in $2NF$ unknowns, and if

$$2NF \geq (1+NC) NT \quad (A1.1)$$

they can practically be solved to obtain an optimal solution, for which the performance index reaches an absolute minimum value, i.e., $\psi=0$, at all NT time instances. This solution has no physical significance, since the performance index will differ from zero all the time, except for a finite number of time instances. Equation (A1.1) sets an upper bound to the number of terms which may be taken in the truncated series in order to avoid the trivial solution

$$NF < \frac{1+NC}{2} NT \quad (A1.2)$$

When the constraints are wider, the same solution of $\psi=0$ can be obtained with fewer terms. The other extreme case will be when the constraints are wide enough, so that they may be disregarded. In this case $NC=0$, and the condition for nonexistence of the trivial solution $\psi=0$ is

$$NF < 1/2 NT \quad (A1.3)$$

The acceptable ratio of the number of frequencies and time steps should be determined for each specific problem by parametric convergence tests.

If one wishes to improve the accuracy of the solution to the LP problem by using a smaller time step, this can always be done. However, if there are more terms in the series,

one should be aware of a possible need to change the time step size accordingly.

The above mentioned phenomenon is analogous to the aliasing in spectral analysis of discretely sampled information [8]. In that case the well known sampling theorem states that the continuous information has to be sampled at a rate which is at least two times higher than its maximal frequency.

APPENDIX 2

EVALUATION OF CONSTANTS FOR A DECAYING SHOCK REPRESENTATION

If the shock of Eq. (26) is placed into the governing equation (30), it appears as

$$q_i^F + \omega_i^2 q_i^F = (a_0 + a_1 \cos \omega_s t + a_2 \sin \omega_s t) e^{-t/t_D} \quad (A2.1)$$

where

$$a_0 = (12\phi_{2n-1,i} + 6\phi_{2n,i} \Delta L) \frac{C_k}{N\phi_1} - (54\phi_{2n-1,i} + 13\phi_{2n,i} \Delta L) \frac{C_m}{N\phi_1} / t_D^2 \quad (A2.2)$$

$$a_1 = -(12\phi_{2n-1,i} + 6\phi_{2n,i} \Delta L) \frac{C_k}{N\phi_1} - (\omega_s^2 - 1/t_D^2) \frac{C_m}{N\phi_1} \quad (A2.3)$$

$$a_2 = 2\omega_s (54\phi_{2n-1,i} + 13\phi_{2n,i} \Delta L) \frac{C_m}{N\phi_1} / t_D \quad (A2.4)$$

Substitution of the particular solution (37) into Eq. (A2.1) yields

$$F_0 = \frac{a_0}{\omega_i^2 + 1/t_D^2} \quad (A2.5)$$

$$F_1 = \frac{(1/t_D^2 - \omega_s^2 + \omega_i^2) a_1 - 2\omega_s a_2 / t_D}{(1/t_D^2 - \omega_s^2 + \omega_i^2) + 4\omega_s^2 / t_0^2} \quad (A2.6)$$

$$F_2 = \frac{(1/t_D^2 - \omega_s^2 + \omega_i^2) a_2 - 2\omega_2 a_1 / t_D}{(1/t_D^2 - \omega_s^2 + \omega_i^2) + 4\omega_s^2 / t_D^2} \quad (A2.7)$$

ANALYTICAL STUDY OF THE EFFECT OF EARLY WARNING ON OPTIMAL SHOCK ISOLATION

Y. Narkis
State of Israel Ministry of Defense
Armament Development Authority
Haifa, Israel

and

W. D. Pilkey
Department of Mechanical and Aerospace Engineering
University of Virginia
Charlottesville, Virginia 22901

The optimal shock isolation of a single-degree-of-freedom system with early warning is accomplished by an active or -bang control. It is shown that this problem can be solved analytically using a kinematic approach. For a typical shock input, the optimal control is found to consist of a main positive pulse, and possibly additional initial and terminal negative pulses. The existence of a maximum usable early warning time, beyond which there can be no further improvement in isolation, is identified.

INTRODUCTION

Shock isolation systems can be generally classified as either passive or active. A passive system responds to the shock input without any external control, and is composed of passive elements, which are usually spring and dashpot combinations. An active system has some sensing and computation devices, which control force-producing elements. The limiting performance of a shock isolation system is the optimal response of an active system, for a given index of performance and a given set of state constraints.

The problem of optimal shock isolation synthesis is defined and reviewed by Sev'n and Pilkey [1]. Several methods for calculation of the limiting performance are given in the same reference. A particularly interesting study was performed by Klein [2], who proved that the optimal response of a single mass, three-degree-of-freedom (DOF) system would be translation only, a fact which enhances the importance of analyzing single DOF systems.

When the system to be isolated is expensive or important enough, an effort might be made to alleviate its response by making use of an early warning system (EW). If the typical shocks exciting the system are large ground motions, for instance, this EW may be implemented by installing several accelerometers at known distances and directions from the system.

The problem of finding the limiting performance in the presence of EW is treated briefly in both references. They calculated it by numerical optimization codes, and found that using an EW has significant advantages in shock isolation. In this work it will be shown that an analytical solution exists for most cases of an EW. Besides simplifying the calculation procedure, this solution will highlight some important characteristics of the optimal isolation using an EW.

ANALYSIS

The present work considers the optimum shock isolation of a single DOF system, shown in Figure 1. For a limiting performance study the elements connecting the mass m to its base are replaced by a generic control force u . As the acceleration in this case is directly

proportional to the force, $u=mx$, the control will be expressed throughout this work in terms of acceleration, and the analysis is independent of the mass m .

The base is subjected to a given shock $y(t)$. When dealing with large ground motion, the shock is frequently assumed to be

$$y = 0.5 a_0 t^2 e^{-t/t_0} \quad (1a)$$

where a_0 is the maximum acceleration and t_0 is a

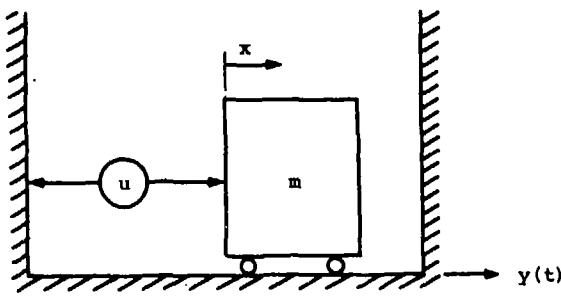


Fig. 1 Schematic of single DOF system

decay time constant. The maximal base displacement for this shock will be

$$y_m = 2 a_0 t_0^2 e^{-2} \quad (1b)$$

The velocity and acceleration associated with this shock are obtained by differentiation

$$y = 0.5 a_0 (2t - t^2/t_0) e^{-t/t_0} \quad (1c)$$

$$y' = a_0 [1 - (2t/t_0) + 0.5t^2/t_0^2] e^{-t/t_0} \quad (1d)$$

The problem at hand is to find the control force $u(t)$ which will minimize the rattlespace

$$\max |x-y| \quad (2)$$

while satisfying a given acceleration constraint, determined by the ability of the system to sustain loads

$$|x'| \leq a_m \quad (a_m < a_0) \quad (3)$$

Generally [1], this problem is solved by using a numerical optimization technique, e.g., linear programming. The optimal control for the present case is known to be of a bang-bang type, and the problem is to find the timing (and number) of switchings. It will be shown that this can be done analytically using a kinematic approach.

Consider first the case of no early warning. The control can start (ideally) simultaneously with the shock, and its magnitude is bounded by the maximal allowable acceleration. As has been recognized [1], the minimal rattlespace is achieved by starting the control at $t=0$, maintaining its maximal value until $t=t_1$, when the velocity of the mass reaches that of the base. As the relative velocity is zero, the relative displacement will be maximal at that moment and decrease afterward. The optimal control for $t > t_1$ is not unique since the maximal rattlespace has already occurred, and the control should just prevent the system from exceeding that value.

The time of equal velocities is calculated from the kinematic relationship

$$v = a_m t_1 = y(t_1) = 0.5 a_0 (2t_1 - t_1^2/t_0) e^{-t_1/t_0} \quad (4)$$

The rattlespace is then

$$D = |x-y|_{t=t_1} = 0.5 a_0 t_1^2 e^{-t_1/t_0} - 0.5 a_m t_1^2 \quad (5a)$$

or, in a non-dimensional form

$$\frac{D}{y_m} = \frac{e^{-2}}{8} \left[\frac{t_1}{t_0} \right]^3 e^{-t_1/t_0} \quad (5b)$$

Solve for t_1/t_0 from (4) in terms of a_m/a_0 and substitute it in (5b). This portrays a limiting performance trade-off curve, which is shown in Figure 2.

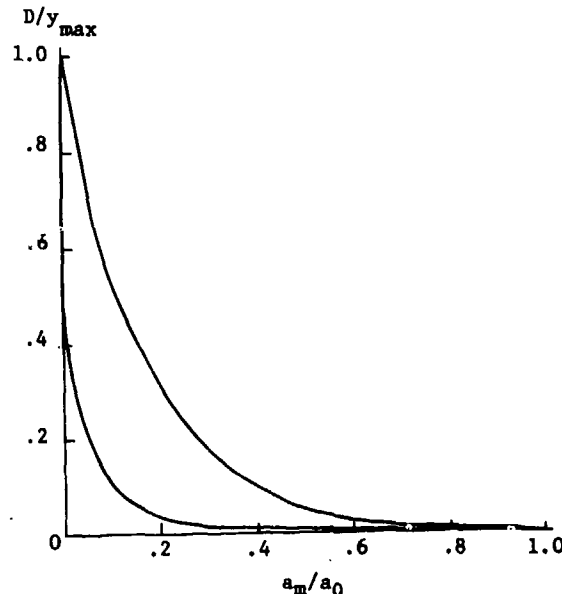


Fig. 2 Limiting performance trade-off curves

Consider now the case where early warning is present (Figure 3). For a short EW, the optimal control strategy will still be to accelerate the mass immediately at the maximum allowable value, until its velocity matches that of the base. As before, from this moment on the optimal control is not unique. The velocities of the mass and the base will assume the same value twice in the acceleration process: the first time during the rapid base acceleration, and the second time when its acceleration is smaller than a_m . When the EW time is short, the first occurrence will correspond to a small relative displacement, and the maximum will be attained at the second passage (see Figure 3, curve 1). When the EW time is increased, the relative displacement will increase for the first passage, and decrease for the second one. At some critical value of the EW time, t_c , the

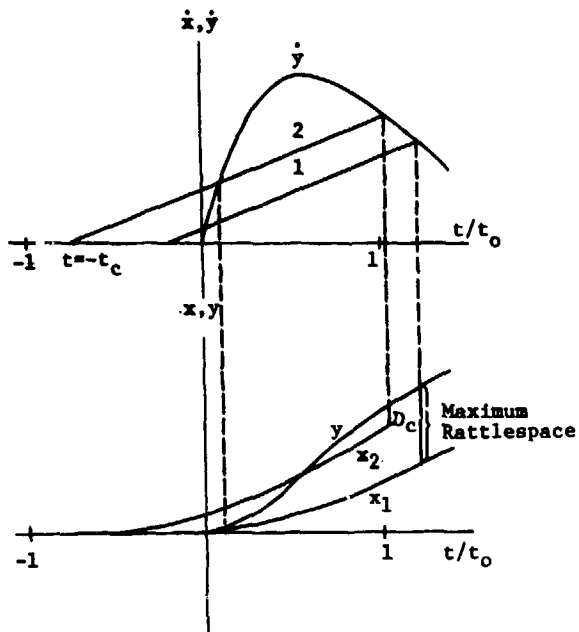


Fig. 3 Shock and response state variables

two rattlespaces will be equal (curve 2 of Figure 3).

For $t_{EW} \leq t_c$, the min-max relative displacement will still be found by its value at the second velocity passage, t_2 . The kinematic relations are similar to those with $t_{EW} = 0$.

$$v_i = a_m(t_{EW} + t_i) \\ = 0.5 a_o (2t_i - t_i^2/t_0) e^{-t_i/t_0} \quad (6a)$$

$$D_i = 0.5 a_o t_i^2 e^{-t_i/t_0} - 0.5 a_m (t_{EW} + t_i)^2 \quad (7a)$$

The subscript $i=1,2$ refers to the first or second velocity passage, respectively. These equations can be written in a non-dimensional form as

$$\frac{a_m}{a_o} = \frac{1 - \frac{1}{2} \frac{t_i}{t_0}}{1 + (t_{EW}/t_0)/(t_i/t_0)} e^{-t_i/t_0} \quad (6b)$$

$$\frac{D_i}{y_m} = \frac{e^2}{4} \left[\left(\frac{t_i}{t_0} \right)^2 e^{-t_i/t_0} - \frac{a_m}{a_o} \left(\frac{t_i}{t_0} + \frac{t_{EW}}{t_0} \right)^2 \right] i \\ = 1.2 \quad (7b)$$

For given a_m/a_o and t_{EW}/t_0 one can find

t_2/t_0 from (6b) and then D_2/y_m from (7b). This will be the solution to the min-max problem as long as $t_{EW} \leq t_c$. For a certain value of t_{EW}/t_0 one finds $|D_1/y_m| = |D_2/y_m|$, and that time ratio corresponds to the critical value t_c/t_0 . The rattlespace for that EW time will be designated D_c . The solution of these algebraic equations is shown in Figure 4 as curves of D/y_m versus t_{EW}/t_0 , for several values of a_m/a_o (marked M).

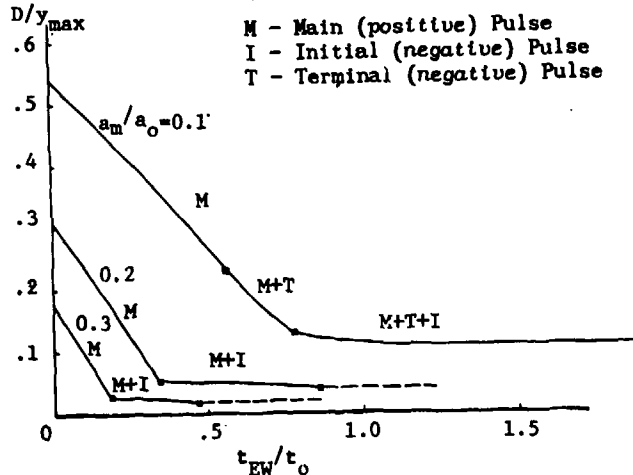


Fig. 4 Min-max rattlespace versus EW time and allowable acceleration

For $t_{EW} > t_c$ the control will no longer be a constant maximum force. Suppose that the control is started slightly before the critical early warning time, $t = -t_c$. The relative displacements in this case will satisfy $|D_2| < D_c$, but $|D_1| > D_c$. Yet, if some extra EW time is available, the system could be brought to more favorable initial conditions, at some $t = -t_e$ (see Figure 5), which would result in a net reduction of the rattlespace. Notice that changing the initial location $x(-t_e)$ is equivalent to translating vertically the whole displacement curve. Reducing D_1 may be achieved by starting at a negative $x(-t_e)$. This means that the main control pulse should be preceded by a negative pulse. This initial pulse should comply with the imposed acceleration constraint, and its length should be such as to make $|D_1| = |D_2|$. When the available EW time is increased, the rattlespace $|D_1| = |D_2|$ may be reduced further, but this would require a larger initial displacement $x(-t_e)$. The optimum will be reached, for an unlimited EW time, as all three external rattlespaces, i.e., at $-t_e$, t_1 , and t_2 , are equal

$$|x_e| = |x_e + x_1 - y_1| = |x_e + x_2 - y_2| \quad (8a)$$

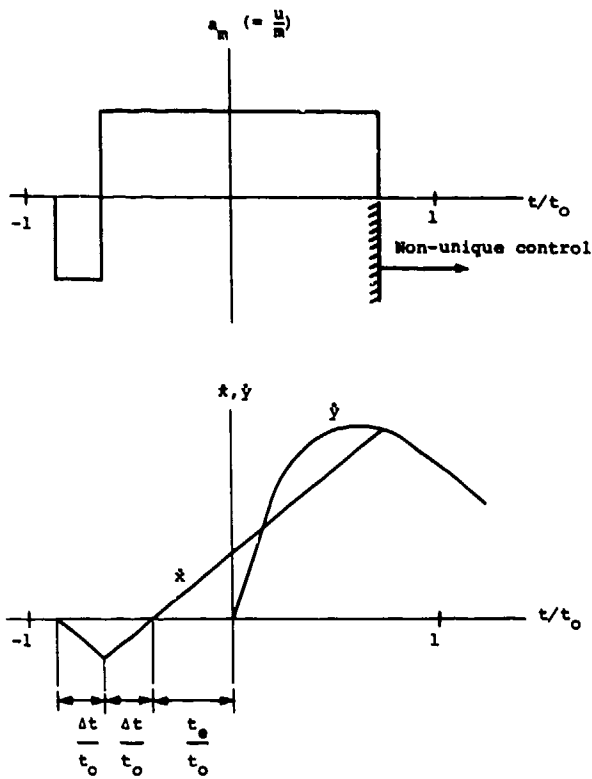


Fig. 5 Optimal two-impulse (main + initial) control, $a_m/a_{m0} = 0.2$

Since x_e is an extremum, it is obvious that the velocity associated with it is zero.

$$\dot{x}(-t_e) = 0.$$

Two relations may be deduced from (8a):

$$y_2 - x_2 = 0 \quad (8b)$$

$$x_e = -0.5(x_1 - y_1) \quad (8c)$$

Using (8b) and the condition of equal velocities at t_2 :

$$0.5 a_{m0} t_2^2 e^{-t_2/t_0} - 0.5 a_m (t_e + t_2)^2 = 0 \quad (9a)$$

$$v_2 = a_m (t_e + t_2) = 0.5 a_{m0} (2t_2 - t_2^2/t_0) e^{-t_2/t_0} \quad (9b)$$

After some manipulations one obtains

$$\frac{a_m}{a_{m0}} = \left[1 - 0.5 \frac{t_2^2}{t_0} \right]^2 e^{-t_2/t_0} \quad (10)$$

$$\frac{t_e}{t_0} = \frac{0.5 \left[\frac{t_2}{t_0} \right]^2}{1 - 0.5 \frac{t_2}{t_0}} \quad (11)$$

from which t_2 and t_e can be calculated. Using (8c) and the condition of equal velocities at t_1 , one obtains

$$\frac{a_m}{a_{m0}} \left[\frac{t_e}{t_0} + \frac{t_1}{t_0} \right] = \left[\frac{t_1}{t_0} - 0.5 \frac{t_1^2}{t_0} \right] e^{-t_1/t_0} \quad (12)$$

from which t_1 is calculated, and finally

$$\frac{D_{opt}}{y_m} = \frac{e^2}{8} \left[\left[\frac{t_1}{t_0} \right]^2 e^{-t_1/t_0} - \frac{a_m}{a_{m0}} \left[\frac{t_e}{t_0} + \frac{t_1}{t_0} \right]^2 \right] \quad (13)$$

This might be termed the absolutely minimal rattlespace, since under the given acceleration bound, a_m , there is no way of getting a smaller min-max relative displacement.

The control for $t_{EW} \rightarrow \infty$ is not unique.

However, it is of much practical importance to find the control which will result in the absolutely minimal rattlespace, while minimizing the required EW time. Again, using the maximum allowable acceleration a_m , this control will be a bang-bang type, made of two equal but opposite impulses, which will bring the system to $x = x_e$. $\dot{x} = 0$ at $t = -t_e$. If each acceleration impulse is of magnitude a_m and length Δt , the velocity at the end of the second impulse will be zero, and the displacement will be $a_m \Delta t^2$. Equating this to x_e , one gets the relation

$$\frac{\Delta t}{t_0} = \frac{1}{e} \left[2 \frac{D_{opt}}{y_m} / \frac{a_m}{a_{m0}} \right]^{1/2} \quad (14)$$

The control force which corresponds to this criterion is therefore found to be a 2-pulse force for the whole shock isolation process, as sketched in Figure 5. The minimum rattlespace corresponding to this control is marked M+I (main plus initial) on Figure 4.

In most of the practical cases, where the allowable acceleration is not too low, the min-max relative displacement is governed, as stated above, by the isolation process until time t_2 . For $t > t_2$, the optimal control is not unique, and that part of the decaying shock has no effect whatsoever on the solution. For small

a_m/a_o , care should be taken of this "tail" of the shock too. In order to prevent the build-up of large negative relative displacements, one will have to decelerate the system until the velocities of the mass and its base match for the third time. The optimal control here is made of two pulses: a main positive pulse and a terminal negative one. When the allowable acceleration is small enough and the EW time is long, even using the maximum reversed control for all of the time until the velocities become equal again results in a displacement D_3 which is larger than D_2 . Increasing t_{EW} beyond the value for which $|D_3|=|D_2|$ makes the optimal control reverse its direction before catching up with the base velocity at t_2 , as sketched in Figure 6. The additional unknown, the reversal time t_r , is determined by equating $|D_2|=|D_3|$.

Klein [2] solved a problem of the early warning type, where $a_o=2$ in/sec², $t_o=1$ sec, $t_{EW}=0.75$ sec. He imposed a rattlespace constraint $|x-y|<0.1$ inch and using an LP numerical optimization program found the minimum acceleration to be 0.183 in/sec². Using the same parameters in the present kinematic approach, it is found that $t_r=0.966$ sec and min-max $|x|=0.1805$ in/sec². Besides being a somewhat better solution than Klein's, this is the exact solution in the sense that it is obtained directly from a set of 4 algebraic equations.

As before, the situation changes for even larger EW times. At a certain value of t_{EW} one finds that the two final rattlespaces $|D_2|=|D_3|$ become equal to the initial rattlespace D_1 . Increasing t_{EW} beyond this value makes D_1 greater, and an initial negative control force should be applied, as before. In this case the optimum control is made of 3 pulses: a positive main pulse plus initial and terminal negative pulses. This situation is represented in Figure 4 by that part of the curve (for $a_m/a_o=0.1$) marked M+I+T. Again, t_{EW} may be increased until the maximum usable EW time is encountered, for which $|x(-t_e)|=|D_1|=|D_2|=|D_3|$.

The trade-off curve for unlimited t_{EW} is shown in Figure 2. It is interesting to note that whereas trade-off curves usually assume the value $D/y_m=1$ at $a_m/a_o>0$, in this case the ratio is $D/y_m=0.5$. When the available EW time is infinite, even an infinitesimally small acceleration a_m may be used to drive the mass to the middle point $x=0.5 y_m$ at $t=0$, thereby assuring that the relative displacement will never exceed $|D|<0.5 y_m$.

The maximum usable EW time is shown in Figure 7 as a function of the acceleration

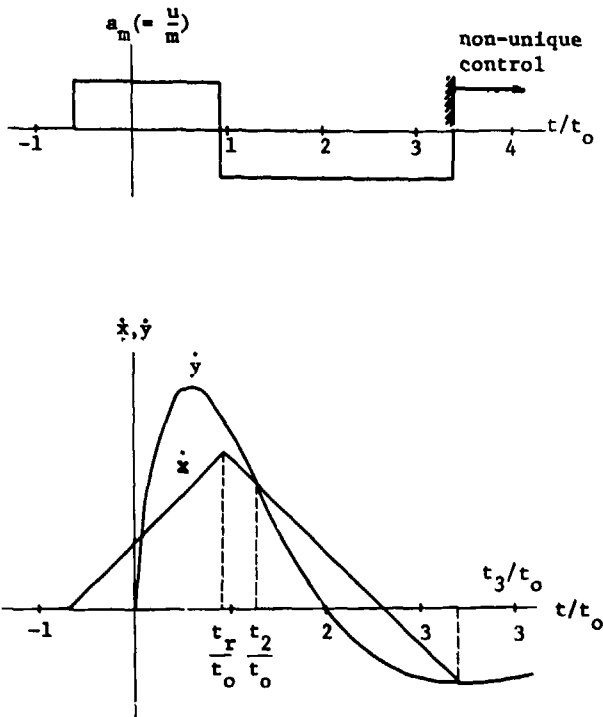


Fig. 6 Optimal two-pulse (main + terminal) control. $a_m/a_o = 0.1$ $t_{EW}/t_o = 0.7$

constraint. The whole domain is divided into four subdomains, according to the type of optimum control: main pulse only (M), main + initial (M+I), main + terminal (M+T) or 3-pulse (M+I+T).

CONCLUSION

The present work investigated the optimal isolation of a single-DOF system excited by a typical large motion shock, when early warning may be available for use in improving the performance of the isolation system. The main conclusions of this investigation are:

- 1) The optimal control is a bang-bang type, the timing and number of switchings can be found analytically using a kinematic approach.
- 2) The optimal control consists of a main positive pulse, and possibly additional initial and terminal negative pulses.
- 3) For any given acceleration constraint there is a corresponding absolutely minimal rattlespace, which is obtained when the EW time is long enough.
- 4) There is a maximum usable EW time, at which the absolutely minimal rattlespace may be attained by means of a 2 or 3-pulse control. Longer EW time cannot produce a smaller rattlespace. All the above

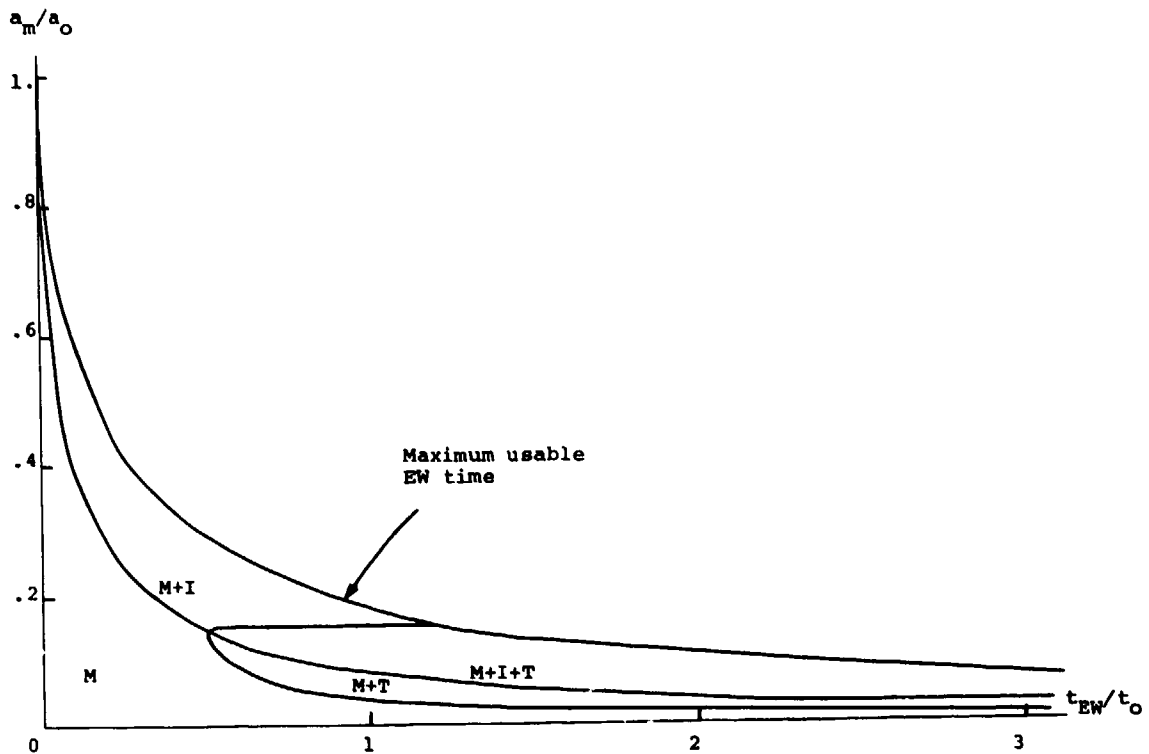


Fig. 7 Maximum usable EW time versus acceleration constraint. Subdomain division according to required control pulses

conclusions are qualitatively valid for shocks of any shape, and the kinematic approach presented here can be applied to their quantitative analysis.

REFERENCES

1. Sevin, E., and Pilkey, W. D., Optimum Shock and Vibration Isolation, SVIC, Washington, D.C., 1971.
2. Klein, G. H., "Optimization of Linear, Nonlinear and Active Multi-Degree-of-Freedom Shock Isolation Systems," Ph.D. Dissertation, UCLA, 1971.

VIBRATION TEST CRITERIA

TECOM'S RESEARCH EFFORTS IN THE DYNAMIC ENVIRONMENTS

John A. Robinson
U.S. Army Combat Systems Test Activity (USACSTA)
Aberdeen Proving Ground, Maryland

The U.S. Army Test and Evaluation Command's Shock and Vibration Technical Committee is actively involved in research efforts in the dynamic environments associated with the transport of materiel in a wide variety of vehicles. The results of these efforts provide the technical community with vital and timely information for use in test tailoring. The results of the completed research are described as are the objectives of the current and near-future research efforts.

INTRODUCTION

The U.S. Army Test and Evaluation Command (TECOM) formally organized its Shock and Vibration Technical Committee in 1972. The objective of this committee has remained the same since its inception--to research the dynamic environments of vibration and shock, particularly for ground vehicles and equipment handling operations but also for missiles, and for Army fixed and rotary wing aircraft and to provide the technical community with realistic laboratory test procedures and techniques.

During the first few years, the various TECOM installations and activities submitted numerous research proposals addressing a wide variety of shock and vibration aspects. Duplications often occurred; funded efforts were sometimes too small in magnitude to thoroughly address the subject; and others were too large in scope --so large that the investigators grew weary before results were achieved. At the March 1978 meeting of the TECOM Shock and Vibration Technical Committee, the entire shock and vibration methodology program (as it is referred to) was revised to establish an integrated set of investigations.

This original plan of action provided the mechanism to give the needed positive direction to this shock and vibration methodology program which, in turn, permitted the committee to proceed in an aggressive fashion towards the end result of updating laboratory shock and vibration test schedules. With the emphasis today on test tailoring, the results that have already been

gained, plus the results yet to be gained through pending research, can provide the technical community with invaluable and cost-effective technical information to aid in prescribing the most realistic simulation environments.

This paper will encapsulate the results already obtained, describe the current efforts and will detail the future that is planned for TECOM's research efforts in the dynamic environments.

RESULTS OBTAINED

Investigation Number 1 addressed the loading configuration for military ground vehicles. Its objective was to determine the procedures and techniques used by the U.S. Army to load and secure/restrain ammunition and items of general equipment in these vehicles. This investigation was completed and reported in 1979 and found that ammunition and general equipment are transported in the same general manner--that being either palletized or containerized from the manufacturer to the forward supply point and then either palletized or as separate items from the forward supply point to the using unit. The report documented that the cargo load, as a percentage of rated capacity, tends to be at or near the capacity (either weight or size) of the particular vehicle. The investigation also revealed that there is a wide variation in cargo restraint. There are instances where cargo is secured both vertically and horizontally on the transport vehicle; and there are instances where no securing mechanism is used at all. It was determined that for the

majority of the time, cargo is restrained in the two horizontal planes but not in the vertical plane, and the horizontal restraints vary from rigid to loose. The investigation also indicated that steel banding was a representative means of securing the test load to the vibration exciter.

The second investigation addressed the distances that ammunition and items of general equipment may be transported in air, ground and rail vehicles, both commercial and military. The investigation was completed and reported in 1981. It determined that the maximum distance that Army materiel will be moved by road and/or rail transport systems within the continental United States is 7241 km (4000 mi). Movement of materiel to overseas areas is expected to cover a distance of 6463 to 16,000 km (4000 to 10,000 mi) by either ocean-going vessels or aircraft. Since the vibration environment associated with these two modes of transportation is considerably less severe than that of ground vehicles, the distances associated with these transport environments need not be included in laboratory testing. The cargo transport distance for ground vehicles in overseas theaters was established to be 804 km (500 mi) from the overseas port of debarkation to the using unit. The method of cargo restraint for 563 km (350 mi) of that 804 km could vary as found in investigation No 1. This second investigation concluded that the final 241 km (150 mi) would be from the Corps storage area to the using unit and that the cargo would be loosely stowed.

The third investigation in this plan studied the effects that variations in load weight and configuration had on the dynamic response (or input to the cargo) of the vehicle bed. This involved studying the effective mass of a trailer and developing a technique for deriving derating factors--all under laboratory conditions. This investigation was completed and reported in December 1981 and concluded that it was possible to obtain derating factors from frequency response functions. The investigation had found that, generally, increasing load reduced the response of the vehicle bed which would mean a decrease in the vibration input to the cargo load.

The fourth investigation of this plan addressed the subject of loose cargo and certification of the current loose cargo (bounce) test. This investigation, which was conducted by the U.S. Army White Sands Missile Range, was completed and reported in July 1983. The significant achievement from this effort was the design, construction and verification of a measurement device referred to as a model hardware specimen (MHS). This was a mechanical structure having a series of 16 cantilevered beams, attached to an aluminum beam, which were

tuned at frequencies from 5 to 160 Hz and separated in frequency by one-third of an octave. Each beam was instrumented with a fatigue life gauge and a strain gauge. This assembly was mounted on a base plate. An accelerometer was mounted on the assembly to measure the input acceleration to the MHS in the axis of excitation of the beams. Some preliminary work was done with the MHS in measuring the field environment and the laboratory environment of the package tester in order to verify the validity and reliability of the MHS as a mechanism to measure this rather harsh and intermittent environment which is a combination of shock and vibration. The goal of using the MHS was to correlate the cumulative fatigue data, generated by the fatigue gauges, between the field and laboratory environments.

Another completed investigation had as its objective the measurement of the actual field vibration environments for secured cargo transported in various military ground vehicles and the translation of these data into laboratory vibration simulation test schedules. The results obtained from the first three investigations of this overall plan were used in support of this effort. Inasmuch as many items of cargo (e.g., ammunition, general types of equipment) can be transported as secured cargo (secured in all three planes), this investigation addressed the secured cargo method of transport and the resulting vibration environment. As steel banding had been found to be representative of the securing medium used in the field, it was used to secure the load vertically; and blocking was utilized as needed for the horizontal planes. Consideration was also given to the results of the effective mass and loading configuration investigations. The loading configuration results indicated that cargo vehicles tended to be loaded at or near their capacity, and the effective mass study found that decreasing the load increases the vibration levels on the cargo bed. In order to add some conservatism to this schedule development effort to account for variations in loading, a cargo load of 75% of the vehicle's weight capacity was used as the load for each vehicle. Because of the established loading techniques for ammunition and general types of cargo, no effort was made to develop any type of derating factor.

Vibration data were measured at nine symmetrical locations on the cargo beds (on structural members under the actual cargo bed floor) of 1-1/4-ton, 2-1/2-ton, and 5-ton cargo trucks, a 12-ton semi-trailer, the 1/4- and 1-1/2-ton two-wheeled trailers and the 6-ton M548 tracked cargo carrying vehicle. The wheeled vehicles were operated over four different fixed profile courses in the Combat Systems Test Activity's Munson Test Area, and the tracked vehicle was operated on a flat paved road. The courses used for the wheeled

vehicles are considered to be indicative of the terrain described in available cargo scenario information as secondary road, trails and off-road and have been found to produce the most severe vibration effects on wheeled vehicles; likewise, the paved road produces the most severe vibration environment of tracked vehicles.

Similarity of the data between the cargo trucks and 12-ton semi-trailer permitted the data from all of these vehicles to be overlayed and combined into one laboratory schedule for each axis, identified as composite wheeled vehicle; similarly the data from both two-wheeled trailers were combined into one laboratory schedule for each axis, identified as composite two-wheeled trailer. These composite schedules are broadband random vibration. The M548 vehicle had a series of schedules developed for each axis due to the limitations that existed with digital control systems at that time. Those schedules are referred to as swept narrowband random-on-broadband random since the various phases reflect the background vibration arising from sources such as the engine and transmission plus the narrow band of random energy created at each vehicle speed by the interaction of the track with the drive sprocket and the track with the road surface. These narrowbands are very much speed dependent, and each fundamental and its harmonics appear simultaneously for the particular road speed; but no other fundamentals and harmonics are present. The sweeping of the narrowbands of random vibration energy is used to simulate the various road speeds at which the vehicle is operated.

The test times for these various schedules and resultant amplitude levels were determined from both the results of the mileage data documented in the second investigation and from the Operational Mode Summary for an Ammunition Production Validation Test. The resulting scenario is shown in Figure 1 and represents cargo transport in overseas theaters of operation.

Based on the transport distance, average vehicle speed and percentage of the total distance depicted by the four Munson test courses, the resulting real time test for the composite wheeled vehicle was 20 hours per axis, which was considered too long for a laboratory test. An exaggeration factor (not to exceed 25% of the peak field data measured) was calculated to reduce the test time to 2 hours; this factor became 1.85. The two-wheeled trailer real time calculated to be 96 minutes per axis, which was considered to be a reasonable laboratory test time; thus no exaggeration factor was necessary. The M548 tracked cargo carrier presented the opposite problem. The total time the cargo would be subjected to the most severe vibration environment was 4.8 minutes,

which was too short of a time to be accommodated by the digital control software that was available. The philosophy thus used was that if fatigue is the damage mechanism, which is the assumption used when applying exaggeration factors, then the real world test levels could be "de-exaggerated" (or apply an exaggerated factor of less than unity) to extend the test time. The exaggeration factor thus used was 0.51. A few concerns have been expressed over the "de-exaggerated" philosophy, specifically that applying a factor of less than unity could place the test levels at or below the endurance limit of the material and thus no fatigue damage would ever be incurred by the item. The basis for applying a less-than-one exaggeration factor is that when acceleration levels are measured in the field, one has no real idea where on the slope of the S-N curve for the material these levels fall. Therefore, if one assumes applying a factor of exaggeration above one will keep the test levels somewhere on the slope of the curve, the converse can also be true. If one suspects that the field levels are actually close to the endurance level and that applying a less-than-one factor would put the levels at or below this endurance level, there is probably no reason to run the test even at the actual field levels since no significant fatigue damage would probably be incurred anyway. The M548 test schedules run for 60 minutes per axis, which is divided equally among the number of phases per axis.

The resulting test schedules from this investigation represent a one-time transport by the particular vehicles through the identified scenario of Figure 1.

The shock environment for secured cargo in various military ground vehicles was addressed in another completed investigation. The objective of that study was to measure the actual field shock environment for secured cargo transported in various military ground vehicles and to translate those environments into laboratory shock simulation test schedules.

The vehicles used for this study were the same types that were used for the secured cargo vibration study with the one exception that the 1-1/4-ton vehicle was not surveyed. The locations of the accelerometers were the same as for the secured cargo vibration study except only five locations were utilized due to the symmetry of locations and the similarity of vibration data between all locations. The wheeled vehicles were operated over the Munson Belgian Block, Two-inch Washboard, Three-inch Spaced Bump and the Radial Washboard courses with cargo loads of 100% and 50% of the individual vehicle's load weight capacity. The loads were secured in all three planes. Additionally, all the wheeled vehicles were run over a 30.5-cm (12-in.) wide semicircular pipe anchored to a

gravel road and protruding 12.7 cm (5 in.) above the ground. The M548 tracked cargo carrier was operated on the Combat Systems Test Activity's Cross-Country No. 3 and Secondary A courses of the Perryman Test Area.

A previous investigation completed by the Materiel Testing Directorate of Aberdeen Proving Ground (now the U.S. Army Combat Systems Test Activity) in February 1977 established the criterion for separating shock data from vibration data. This criterion is that any acceleration level in the field data which equals or exceeds a value of six times the rms level of the overall data run is considered to be shock. That criterion was used in the secured cargo shock investigation, and all data were analyzed to determine those conditions (vehicle, load and course) which resulted in shock being present at any measurement location.

On the wheeled vehicles, some of the test courses produced no shock pulses while others did produce some. In some instances of shock, the overall data run had very low rms levels (less than 0.5 grms). To facilitate the analysis, rms levels of 1.0 g and above were considered as significant and the number of shocks exceeding six times these levels were tabulated. A comparison of these various g rms levels were made to the overall g rms level of the various laboratory random vibration test schedules developed during the previously discussed investigation. As it is reasonable to assume the distribution of random amplitudes in the field and laboratory environments are nearly the same, the rms levels which served as the basis for determining the shock occurrences were encompassed within the rms levels of the laboratory schedule; thus any shock levels would be contained in the random vibration test schedules.

The data from the single bump produced rms levels generally less than those from the various test courses, hence no further consideration was given to those data. No shocks were found on the cargo deck of the M548 tracked cargo carrier. The conclusions of that investigation were that there was no justification for developing laboratory shock test schedules for secured cargo transport.

Another of the many investigations identified in the overall TECOM Plan of Action addressed the number of miles that various Army materiel, including ammunition in ready racks within combat vehicles, are transported as installed equipment. This investigation was completed and the report written in December 1983. Installed equipment is defined as items such as communications equipment, optical devices and reference systems which are actually individual items but are mounted on or in

military vehicles and are required for those vehicles to meet their mission responsibilities. Ammunition loaded in racks in combat vehicles (such as main battle tanks) is considered to be installed equipment even though it is expended.

This study was conducted through literature searches and numerous contacts with military testing centers in an effort to identify realistic mileages that installed equipment is expected to withstand and still remain functional. For wheeled vehicles this was identified as 40,233 km (25,000 mi), which is the approximate halfway point to the major rebuild of most wheeled vehicles. The major rebuild point for tanks was identified as the amount of transport that installed equipment (excluding ammunition) is to withstand; this distance was established to be 9656 km (6000 mi).

Ammunition is treated a little differently. Its vibration simulation was based on the number of years that the same ammunition was found to have been in main battle tanks and the annual mileage statistics for the various types of combat vehicles. A study conducted by the U.S. Army Materiel System Analysis Activity (AMSA) identified the number of months that ammunition was uploaded in the ready racks of tanks. A survey of the annual mileage of literally hundreds of individual tanks and self-propelled howitzers was used to statistically establish annual mileage figures. From all of this research, it was established that ammunition and ammunition components in combat tanks should be vibrated as installed equipment to the equivalent of 8047 km (5000 mi) of field transport in each of the three axes. Similarly the separate-loaded 155-mm projectiles transported in the M109 series of self-propelled howitzers should be vibrated to the equivalent of 6840 km (4250 mi) of field transport (again in each of the three axes). It was established that the separate-loaded 175-mm and 8-inch projectiles transported on their respective self-propelled howitzers need not be subjected to the installed equipment vibration environment since there are only two rounds carried on a howitzer, these rounds undoubtedly would be the first ones fired, and thus they would see little in the way of transport mileage.

The final investigation which has been completed and approved by TECOM was concerned with determining and quantifying the vibration characteristics of military vehicles during operations in a cold regions environment. This investigation was completed and documented by the U.S. Army Cold Regions Test Center in Fort Greeley, Alaska in December 1982. The concern which led to this investigation was that the suspension characteristics--and thus the

vibration signature of military vehicles--possibly would be significantly different as a result of being stiffer due to the extreme cold. The same vehicles were run at the Arctic Test Center under both summer and extremely cold winter conditions, and vibration data on the vehicles were recorded. The findings were that those vibration characteristics were no more severe in the cold regions' winter environment than those in its summer (temperate) conditions. The reason for this was that after a relatively short distance of travel in the winter, the suspension had "warmed up" and functioned normally.

INVESTIGATIONS RECENTLY COMPLETED

This portion of the paper discusses the investigations which have been completed and are undergoing TECOM staffing for review and accommodation of comments prior to final approval by TECOM.

One of these investigations was the development of vibration schedules for M109/M110 self-propelled artillery. For this investigation, the installed equipment vibration environment for the M109A3, 155-mm self-propelled howitzer was measured at various locations throughout the vehicle during paved road operations; and laboratory vibration test schedules were developed. The resulting schedules were for the ammunition bustle rack, the ammunition deck racks, ammunition locations on the vehicle sponson, propelling charges, turret and hull. Similarly, the vibration signature of the M110A2, 8-inch self-propelled howitzer was measured; and laboratory simulation schedules were developed. The specific areas for this vehicle were the gun trunnion, the top deck, the gun mount and the hull driver's compartment. No schedules were developed for the ammunition due to the findings of the investigation on installed equipment mileages that were discussed in the preceding portion of this paper.

As these were both tracked vehicles, and the vibration environment of all tracked vehicles is characterized by a series of high energy, speed-dependent fundamental frequencies along with their individual harmonics on a relatively low-level broadband random spectra, these environments are simulated by the swept narrowband random-on-broadband random laboratory test spectra. As with the previously discussed tracked vehicle test schedules, each axis had to be divided into phases in order to conduct the test using the available digital control software.

Based on the installed equipment mileages documented in the previously discussed investigation, exaggeration factors had to be calculated and applied to the real world spectra in order to accommodate the vibration

simulation in a reasonable amount of time in the laboratory.

A second investigation recently completed was on the subject of loose cargo test schedules. This was the follow-on investigation to the one conducted by the U.S. Army White Sands Missile Range (WSMR) in developing the MHS. This paper will give a brief overview of this second investigation as one of the following papers in this session entitled "A Proposed Technique for Ground Vehicle Loose Cargo Vibration Simulation" by Mr. Connon, will provide the details of this particular investigation.

Due to the recognized fragility of the tuned beams of the MHS, a mathematical model of the MHS was developed and the accelerometer data were inputted to that model to compute cumulative fatigue. The acceleration input to the MHS was measured during transport over various test courses in a 5-ton truck, a 3/4-ton two-wheeled trailer and the 6-ton, M548 tracked cargo carrier. Data were also collected under a variety of test conditions on a laboratory package tester.

A series of computer programs were used to reduce the vibration data into power spectral densities (PSDs) which were then computer-transformed into vibration schedules. The field and laboratory schedules were then compared to develop a test equivalence.

The findings of this investigation were that the loosely stowed cargo test conducted on a package tester is an inexact, uncontrolled test which should be conducted to determine external damage to the test item and should not be used as a substitute for a well-controlled laboratory secured-cargo test; and operation on a package tester with a plywood-covered bed at 300 rpm for 45 minutes provides a reasonable simulation of the loose cargo transportation environment (all three axes simultaneously) of ammunition boxes in a wheeled vehicle or two-wheeled trailer. The investigation also found that the package tester does not simulate tracked vehicle cargo transport environments.

Rail impact test procedures have been addressed in a third investigation recently completed, and the draft report is currently being revised to address all the staffing comments. A paper entitled "Updating Rail Impact Test Methods" was presented by Mr. Robert McKinnon at the 1985 Shock and Vibration Symposium in Monterey, CA. Since that presentation, additional data have been received from various sources on the actual impact speeds. With speed data from a total of over 125,000 impacts, the number of impacts exceeding 12.9 km/hr (8 mph) was found to be only two percent, whereas the data previously available covered only a

little over 16,000 impacts and indicated that 7.9 percent were over 12.9 km/hr. The latest data further substantiates the recommendations of the report that the maximum speed be 12.9 km/hr.

The rail impact procedure developed in that investigation is considered realistic for creating the environment of cars rolling into other cars during train makeup in classification yards and for simulating the number of classification yards a particular car and item may go through during a cross-country trip. The procedure utilizes two stationary buffer cars, each with standard draft gear and each being rigidly upweighted to a total gross weight of 55,700 kg (125,000 lb). A standard draft gear car with the test item properly positioned and secured to it, is set in motion and the buffer cars at a speed of 9.7 km/hr (6 mph). This three-car configuration is then impacted (at the test item car) by a 174,800-kg (365,999-lb) rigidly weighted, standard draft gear hammer car. The two-impact procedure is then repeated at 11.3 km/hr (7 mph) and 12.9 km/hr. At the completion of the sixth impact, the test car is turned around and the six-impact sequence is repeated.

Data which are required for this test are the impact speed and coupler force in order to identify the initial input conditions for both comparative purposes with other tests and to provide meaningful information to the designer of the item for failure analyses. Cable tensions must also be measured initially so that identical conditions can be established for comparison tests. (The tie-downs are not adjusted once the test starts.)

CURRENT EFFORTS

Presently, there are four investigations being conducted as part of the TECOM Plan of Action. These are addressing the development of vibration schedules for installed equipment in military ground vehicles; the development of vibration schedules for helicopter equipment and cargo; the development of a shock and vibration data base for vehicles and equipment; and defining the maximum exaggeration factor to be used in developing laboratory simulated vibration test schedules. An overview of each of these investigations follows.

REALISTIC VIBRATION SCHEDULES FOR INSTALLED EQUIPMENT IN MILITARY VEHICLES

Investigations since the early 1980's have documented the real world environment to be either random (wheeled vehicles) or complex random (swept narrowband random-on-broadband random) (tracked vehicles) vibration spectra. New laboratory vibration test schedules for installed

equipment have been developed only for ammunition in the M60A3, M1 and M1A1 Main Battle Tanks (although not as a part of this TECOM Plan) and for ammunition and installed equipment in the M109 and M110 families of howitzers as discussed previously in this paper.

The current investigation deals with measuring the vibration inputs to installed equipment (with the exception of that ammunition and installed equipment already completed as described above) in all military ground vehicles currently in the Army inventory and translating these data into laboratory vibration test schedules. Some vehicles have been completed and a few others remain to be done.

VIBRATION SCHEDULES FOR HELICOPTER EXTERNAL STORES

The current test schedules for the laboratory simulation of the vibration environment for equipment installed in Army helicopters is a spectra of broadband random with superimposed sinusoidal vibration peaks. These schedules are general in nature and were developed several years ago and were perhaps restricted in realism at that time by the analysis equipment. Insufficient data currently exist to adequately define this environment in order to develop realistic laboratory vibration simulation schedules. Two other techniques that could possibly better simulate the actual helicopter vibration environment are the narrowband random-on-random that is used for tracked vehicles or a shaped random. The goal of this particular investigation is to develop laboratory vibration test schedules for external stores, installed equipment and cargo on helicopters. The overall responsibility for this study lies with the U.S. Army Yuma Proving Ground (USAYPG); USAYPG has tasked WSMR, USACSTA and the U.S. Army Aviation Development and Testing Activity (USAADVNTA) to provide assistance in this rather ambitious effort.

A limited number of flights have been made with the AH-1S (Cobra) and UH-60A (Blackhawk) helicopters from which data were obtained. Efforts are presently continuing in the reduction and analysis of the Cobra flight data and the development of laboratory test schedules. This effort on the Blackhawk at USACSTA was recently completed, the report written, staffed and approved by TECOM. As a limited number of flights actually occurred, there were insufficient data available to adequately define the cargo area and certain installed equipment areas of this cargo helicopter. The only schedules thus developed were for a forward electronics package. These schedules, however, are designated as preliminary ones since the helicopter was flown with the external fuel tanks in place

(which are used for extended range flights only), and any difference in vibration levels with the tanks removed is unknown at this time.

In spite of the problems of insufficient data, significant advancements were made in the analysis of helicopter data and in establishing an event-weighting technique during the development of the test schedules.

An analysis of the distribution of the amplitude of the PSD function at the fundamental forcing frequency and at the second and third harmonics was made to determine whether these frequencies were sinusoidal. The data showed significant scatter in the amplitude regardless of the flight condition. It was concluded that although the frequency of the fundamental and its harmonics does not vary the amplitude value at those particular frequencies does vary. Since the amplitude is not constant, the data cannot be considered to be sinusoidal. This conclusion led to the recommendation that the helicopter vibration environment be simulated by a shaped random test.

Limited flight scenario information has been obtained by USAYPG from USAAVNDTA. This information was discussed and reviewed by the TECOM Shock and Vibration Technical Committee's Helicopter Working Group which ultimately categorized the various events into groups and identified the corresponding percentages of flight time for the groups. This is shown in Table 1 for both the UH-60A and AH-1S helicopters.

The development of the test schedules from the scenario information was accomplished on a weighted bases, i.e., the contribution of each flight event to the final schedule was based on the percentage of time that event occurred during the 1.5-hour scenario, as indicated in Table 2. Normalizing the time/event values to the smallest whole number results in a ratio of one for group 1 events; eight for the group 2 events; and two for the group 3 events. The final PSD plot (from which the schedule data were derived) was, therefore, a composite of the PSD data from one each of the two events comprising group 1; eight of the group 2 events; and two each of the three events comprising group 3 (total of 16 data files).

The final schedules (which have been designated as preliminary) are a shaped random as shown in Figure 2.

It is evident that the laboratory schedule contains only a fundamental frequency plus a harmonic. A comparison of this schedule to the PSD data is shown in Figure 3. Although other high level, narrowband frequencies do exist in the data,

they are not harmonically related to the fundamental. Due to the preliminary nature of these schedules, these frequencies were arbitrarily eliminated since their authenticity could not be determined--the data were received for processing so long after the flights that there was no way to trace through the instrumentation system to validate the data source.

The expected result of this helicopter study is a program to instrument and fly these helicopters again and to ensure that sufficient and unquestionable data are acquired. However, it is again felt that significant advancements in analysis techniques have been made on development of helicopter vibration test schedules.

SHOCK AND VIBRATION DATA BASE

Numerous laboratory vibration test schedules have been developed through methodology investigations in recent years for both the cargo vehicles and combat vehicles in the Army's inventory. Additionally, many road shock and vibration, rail impact, drop and firing shock tests have been conducted on a wide variety of vehicles and equipment as part of the TECOM's development and product-improvement testing missions. As a result of these many efforts, a large amount of meaningful data have been gathered, processed and reported to meet the specific requirements of the various investigations and tests. With such a great quantity of data known to exist, numerous contacts are being made by Government activities, program manager offices and private contractors (involved with developmental design for a Government contract) to acquire specific data. Currently, these data exist in many data files which must be researched to obtain data for a specific request. The goal of this ongoing study is to formulate a shock and vibration environment data base for the various military vehicles and for equipment mounted on/in these vehicles. This data base will be upgraded and expanded on a continuous basis to provide the most current information available on this dynamic environment.

EXAGGERATION FACTORS

The development of laboratory simulation schedules for vibration tests often necessitates the compressing of time by means of increasing laboratory input stress values (accelerated testing) beyond those actually measured under field use conditions. This procedure assumes fatigue to be the cause of structural damage and has been well defined by Miner's Theory. This accelerated testing procedure has been used for numerous years by the USACSTA, other AMC installations and private contractors. There have been occasions when the field stress multiplier

value (derived from Miner's Theory) (exaggeration factor) has been questioned--should it be 1.25, 2 or some other value. There has been no apparent effort to thoroughly research the establishment of such a number. This investigation is providing the necessary research and will establish the maximum exaggeration factor that should be used in developing laboratory vibration test schedules from field data.

Future Plans.

Although several investigations have been finalized, several others have recently been completed and are undergoing final review, and still others are ongoing, many more investigations remain as a part of the TECOM Plan of Action. This section of the paper will identify these future efforts.

NEW VEHICLE VIBRATION TEST SCHEDULES

The cargo bed and installed equipment vibration environments of the military ground vehicles (cargo and combat) currently in the Army's inventory either have been or are being measured and translated into laboratory vibration test schedules. New vehicles, however, continue to be developed; and in order to keep the laboratory test schedules current, the vibration characteristics of the new vehicles need to be measured and translated into revised/new laboratory vibration test schedules for secured cargo and installed equipment. Without maintaining current and accurate laboratory vibration schedules, the vibration testing community cannot continue to accomplish the most realistic testing. This investigation will measure the secured cargo and/or installed equipment vibration environment under field conditions for new military cargo transport trucks, trailers, semitrailers or combat vehicles, and update the current laboratory vibration test schedules used for simulation testing.

RAIL IMPACT SIMULATION

There are instances where the shock environment associated with rail impact testing could be simulated under controlled laboratory conditions, thus eliminating the need for actual railcars, locomotive and locomotive crew; such could be a cost-effective means of testing but is dependent upon the size of the item and the capacity of the laboratory simulation system (e.g., hydraulic vibration system). With more hydraulic systems now available, it has become desirable to develop laboratory simulation schedules for rail impact testing. In order to do so, data are required from actual rail impact tests. This investigation will acquire the necessary data to develop laboratory shock test schedules for simulating rail impact on electrodynamic

vibration excitors or shock machines and will provide these data to USAWSMR for their use in the following study.

RAIL IMPACT SIMULATION ON HYDRAULIC EXCITERS

The USAWSMR study will utilize the rail impact data provided from the previously mentioned study to develop laboratory simulation of the rail impact environment on their large hydraulic exciter system.

COMBAT VEHICLE SCENARIOS

The new laboratory vibration test schedules for ammunition and installed equipment in combat vehicles are the complex, or swept narrowband random-on-random, spectra reflecting the amplitudes and frequencies that have been determined to be dependent on the vehicle ground speed. The new schedules are based on minimal scenario information that has been obtained relating to combat vehicle operations. Since refinements are being made in digital vibration controller software, improvements need to be made in the test schedules by weighting these schedules based on more realistic vehicle speed/duration relationships. The objective of this study is to define the movement scenarios (speeds, durations and terrain) of combat vehicles in order to upgrade existing laboratory vibration test schedules plus utilize this information in development of future schedules.

SHOCK SCHEDULES FOR INSTALLED EQUIPMENT

Although test specifications define shock pulses to be used in laboratory shock testing of equipment installed in military ground vehicles, there is a lack of any known correlation between the specified shock pulses and the shock environment which exists under field operating conditions. In order to adequately simulate this field shock environment, the environment must be measured and analyzed and then proper laboratory pulses and test procedures must be developed to simulate this field environment. This investigation will measure the shock environment for installed equipment (including ammunition in the vehicles) in all military ground vehicles and translate these environments into realistic laboratory test schedules.

VIBRATION CONTENT OF TRACKED VEHICLE/HELICOPTER DATA

The complex random vibration test schedules which have recently been developed for tank and self-propelled artillery ammunition and installed equipment have been characterized as a sweeping narrowband random-on-broadband random spectrum. Concerns have been expressed that the narrowband random environment is not random but might perhaps be sinusoidal in nature.

Similarly, existing helicopter vibration test schedules consist of four sinusoidal frequencies superimposed on a broadband random vibration environment. Based on the preliminary helicopter schedules discussed earlier in this paper, concern has again been expressed by some that the sinusoidal portion of the spectrum is not sinusoidal but might perhaps be random in nature. This investigation will be conducted to further examine and define the nature of these two environments.

ARMAMENT FIRING SHOCK SCHEDULES

A significant shock environment for combat vehicles occurs during the firing of the main armament. For the vehicle to remain completely operational, equipment mounted in and on the vehicle must be capable of withstanding this shock environment. To verify this by actual firing the armament numerous times becomes cost prohibitive, thus the need for laboratory simulation. There is presently no known laboratory simulation schedules for this shock environment. This study will measure the shock levels at equipment locations in and on combat vehicles that result from main armament firing and develop realistic laboratory shock simulation schedules from these data.

Shock Test Schedules Simulating Ballistic Impact.

Another shock environment which exists in combat vehicles is the resultant shock from ballistic impacts. For the vehicle to remain completely operational, the equipment mounted in the vehicle must be capable of withstanding this shock environment. To verify this by actually firing projectiles into a vehicle is time-consuming and not cost effective; laboratory simulation can often be used. There are currently no laboratory simulation schedules for this shock environment. The goal of this study is to measure the shock levels at equipment locations in and on combat vehicles that result from ballistic impacts and to develop realistic laboratory shock simulation schedules from these data.

VALIDATION OF HELICOPTER VIBRATION SCHEDULES

This study will be conducted following the development of the helicopter vibration test schedules that is currently ongoing. As there will be new schedules, efforts will need to be made to validate them. The objective of this study is to utilize typical items mounted on/in helicopters for validation of the new test schedules by measuring both the real world and the laboratory testing responses and comparing the same.

DETERMINATION OF REALISTIC DROP TEST PROCEDURES

Drop testing has been utilized for many years by testing agencies as a cost effective means of verifying that various accidental drops of packaged and unpackaged materiel will not render that materiel unserviceable or unsafe for further handling. The present test procedures and schedules have been existent for over 15 years, and the rationale for them has been obscured with time. Additionally, new size vehicles have become a part of the Army's inventory and new handling procedures are being used. For all of these reasons, the scenario needs to be redefined in order to provide the most realistic drop tests and procedures. This study will define the various parameters associated with these accidental drops (i.e., height, surface, orientation) measure the shock levels associated with these various drops as required, and translate these environments into realistic laboratory drop schedules and procedures.

Relationship of Test Courses to Real World Terrain.

Laboratory vibration test schedules are developed from data obtained during operation of vehicles on prepared test courses such as those in USACSTA's Munson and Perryman Test Areas. These particular courses (as well as several others) have been in existence for well over 30 years, and the rationale behind their characteristics has become obscured with time. In order to continue to develop/upgrade laboratory vibration test schedules to meet the thrust of test realism, the relationship of prepared test courses to real world terrain needs to be determined. This determination will address factors such as profile and length comparisons, will provide the relationship of prepared test courses to the real world terrain, and will utilize this information for upgrading laboratory simulated vibration test schedules based on scenario information.

EXPANSION OF DIGITAL VIBRATION CONTROL SYSTEM CAPABILITIES

The continuing investigation efforts since 1980 to develop more realistic laboratory vibration test schedules has lead to the replacement of swept sine vibration testing with complex random schedules (shaped and swept narrowband random-on-broadband random). As efforts continue along these lines, both for ground vehicles and helicopters, the need to fully develop the capabilities of the digital control systems used in test laboratories has been identified. This development is essential to tracked vehicle vibration simulation where the frequency/amplitude relationship is both harmonically related and ground-speed

dependent. In order to reproduce these relationships in the best possible manner in test laboratories, the control systems must be expanded to the limits of their capabilities. This study is designed to ensure vibration controller software and hardware are expanded to the maximum capability of the system in order to upgrade current test schedules for improved realism in testing.

SUMMARY

The Plan of Action adopted by the TECOM Shock and Vibration Technical Committee in 1978 contained 13 separate investigations (one dealing with the dynamic response of human simulators was ultimately dropped from the plan). As the wheels of progress in conducting these investigations started to turn, the committee continued for several years to identify additional areas that needed investigation. The original 13-investigation plan became 12 (when the one was dropped) and from there has grown to 27 investigations. Eight investigations have been finalized; three have recently been completed and the reports are being staffed; and another four are currently ongoing. This leaves another 12 yet to be started.

The advancements that have been made have resulted in new laboratory vibration test schedules being developed for wheeled and tracked vehicles, both cargo and combat, that are considered to be more realistic representations of the real world environment. Some of these schedules have found their way into MIL-STD-810D; many more are found in the TECOM International Test Operation Procedure 1-2-601; and these schedules are gaining international acceptance in the ongoing test standardization efforts. As more of these investigations are completed, the results will find their way into updated Military Standards and TECOM Test Operation Procedures. This overall massive effort has started, and will continue, to update laboratory simulation test schedules for the dynamic environments of vibration, bounce and drop. The plan is a dynamic one and has grown and changed over the years; and it will continue to change and grow as new horizons come into view.

September 1986

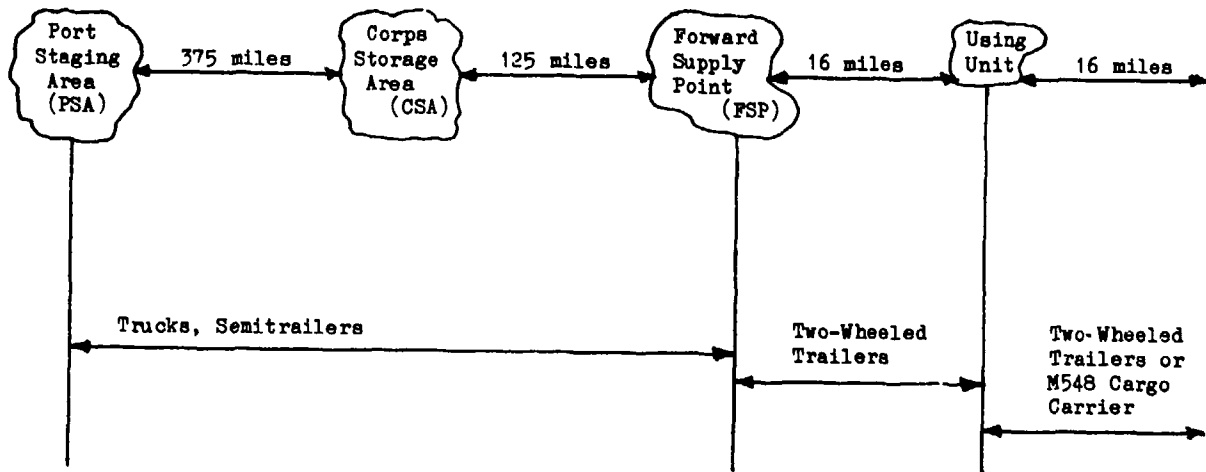


Figure 1. Cargo Transportation Scenario

LAB VIBRATION SCHEDULE. UH-60 AVIONICS. VERTICAL (PRELIM)

RMS = .50

BREAKPOINTS

FREQ	PBD VALUE
5	.0007
15	.0007
17	.0703
19	.0007
22	.0007
34	.0008
38	.0007
800	.0007

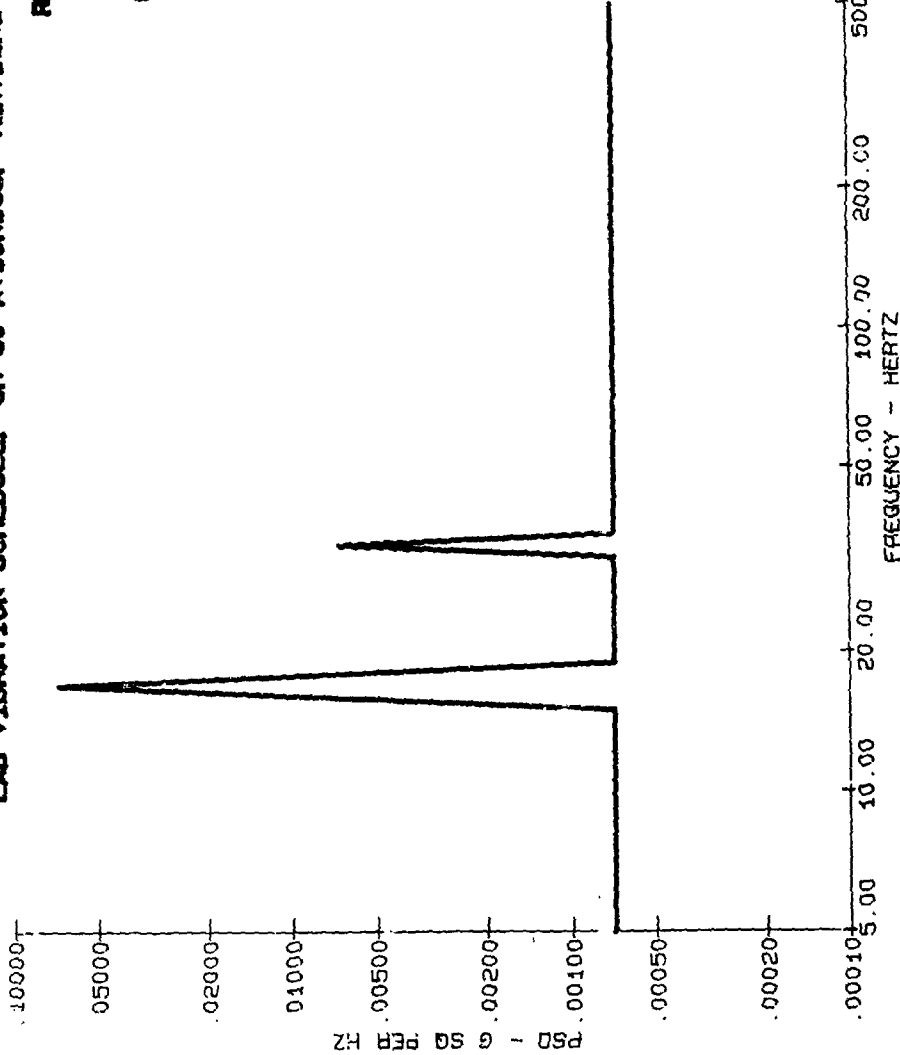


Figure 2. Shaped-Random Laboratory Vibration Schedule

UH-60 HEAVY AVIONICS VERTICAL (PRELIM)

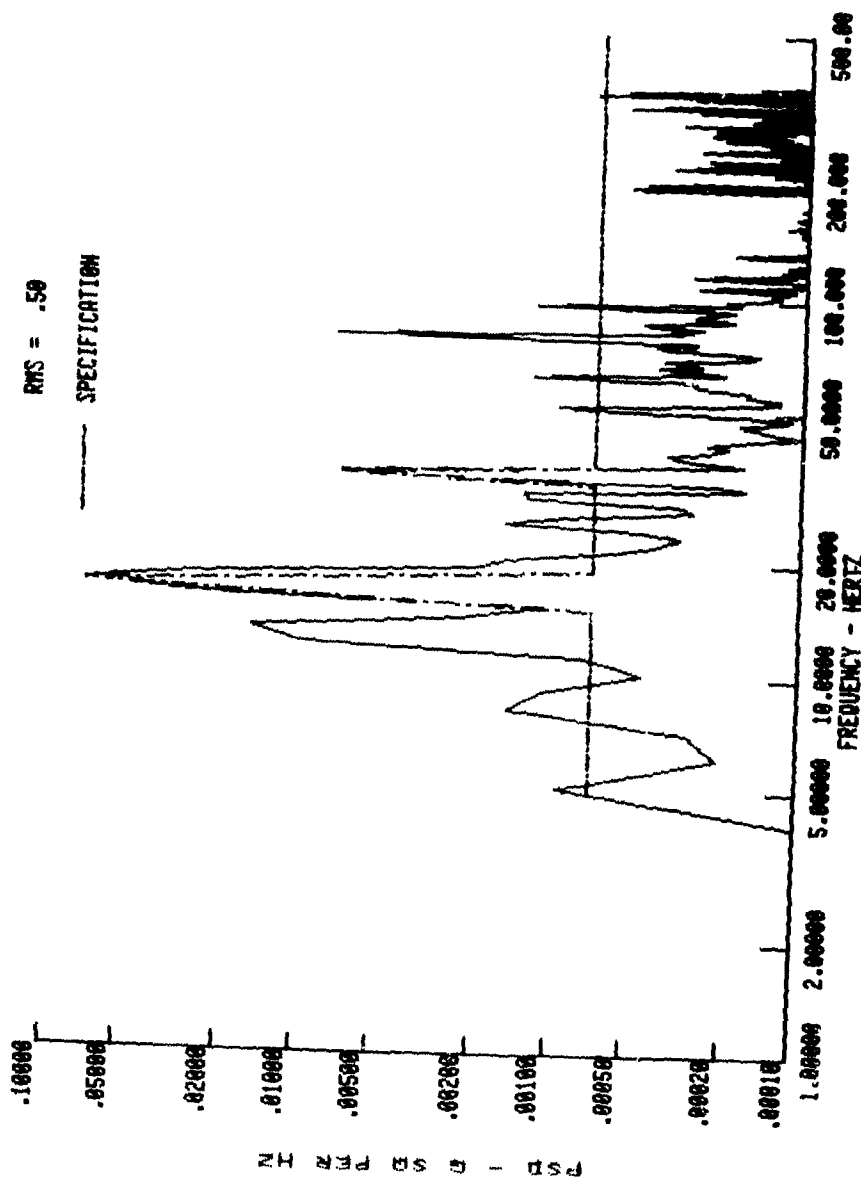


Figure 3. Shaped-Random Laboratory Vibration Schedule Comparison to the PSD Data

September 1986

TABLE 1. FLIGHT SCENARIO

<u>Group</u>	<u>Events</u>	<u>Percentage of Flight Time %</u>
1	Takeoff, hover, landing	13
2	Level flight, maximum speed	57
3	Maneuvers (turns, ascend, descend, Nap-of-the-Earth Flight (NOE))	30

The UH-60A events that met the group requirements were as follows:

Group 1 Combat landing (2 events) - no other data available.

Group 2 Level flight at maximum speed (1 event) - 130-knot airspeed.

Group 3 Maneuvers (3 events) - right turn, left turn (both at 130 knots), NOE.

September 1986

TABLE 2. DETERMINATION OF WEIGHTING FACTORS (90-MINUTE SCENARIO)

<u>Event Group</u>	<u>% of Time</u>	<u>No. of Events</u>	<u>Scenario Time/Group, min</u>	<u>Scenario Time/Event, min</u>	<u>Normalized Time/Event</u>
1	13	2	12	6	1
2	57	1	51	51	8
3	30	3	27	9	2

THE DEVELOPMENT OF LABORATORY VIBRATION TEST SCHEDULES--PHILOSOPHIES AND TECHNIQUES

Richard D. Baily
U.S. Army Combat Systems Test Activity (USACSTA)
Aberdeen Proving Ground, Maryland

This paper describes the philosophies and techniques developed and used within the U.S. Army Combat Systems Test Activity (USACSTA) at the Aberdeen Proving Ground, MD, to derive laboratory vibration test schedules that simulate the field transportation vibration environment associated with tactical vehicles. The logical progression from acquiring data on a tactical vehicle over fixed-profile test courses through the analysis and manipulation of the data to the final laboratory schedule of amplitudes, frequencies, and test times is covered.

INTRODUCTION

Material used by the Army must be designed to withstand the vibration environment normally encountered during ground vehicle and helicopter transport as secured cargo and/or installed equipment without losing the ability to perform its intended mission. As a means to ensure this, laboratory vibration tests are used extensively in lieu of the more time-consuming and less cost-effective technique of loading or installing equipment in a broad array of vehicles and operating those vehicles for appropriate distances over test courses. Such laboratory vibration tests consist of amplitudes at given frequencies for stated periods of time (hereafter referred to as test schedules) and in the past have had little correlation with field operations.

This paper, which is taken for the most part from the recently published International Test Operation Procedure ITOP 1-1-250 (ref 1), describes the facilities, scenario information, and techniques used within the U.S. Army Combat Systems Test Activity (USACSTA) at the Aberdeen Proving Ground, MD, to develop laboratory schedules that simulate the field transportation vibration environments associated with tactical vehicles.

SCHEDULE DEVELOPMENT FACTORS

Factors that must be considered during the development of a vibration test schedule include facilities, scenario information, vehicle speeds, and fatigue considerations.

Facilities

One of the primary facility requirements is tactical vehicles. The term "tactical" defines wheeled and tracked vehicles designed for travel on paved and secondary roads, trails, and cross-country terrain as either cargo or combat vehicles; also helicopters used as cargo carriers and attack vehicles are included in this definition. The vehicles used at USACSTA were randomly chosen either from the USACSTA fleet of test vehicles or from those currently undergoing other testing at APG. The only helicopter tested was a CH-47D used as a cargo carrier. There was no attempt to upgrade any of the vehicles for our particular application; to keep things as typical as possible, they were vehicles that had been subjected to normal maintenance performed at forward-area motor pools. The tire pressures and track tensions used were those prescribed for the particular vehicle on the particular type of terrain.

Another facility of primary importance is the test courses. At USACSTA the Munson and Perryman automotive test courses are now, and have been for many years, standards. The Munson courses are fixed profiles simulating terrain features that create the most severe vibration environment that a tactical vehicle might encounter in meeting its transport requirements. The courses used were the Two-inch Washboard, Belgian Block, Radial Washboard, and Spaced Bump from the Munson area and the Three-mile, high-speed, paved straightaway at the Perryman area. The Munson courses depict terrains found on

unimproved secondary roads, trails, and cross-country and were designed to provide profiles that are not altered by changing climatic conditions. This is important because it ensures repeatability among vehicle tests for comparison purposes. The Perryman course, as its name implies, is three miles of straight, smooth-surface, bituminous concrete used in the schedule development process for tracked vehicle operations. Both areas are described in detail in reference 2.

The final important facility requirement is a data acquisition and analysis system. Having run the gamut from umbilical hook-ups between the test vehicle and data van through on-board recorders and FM telemetry, USACSTA has developed an Automated Data Acquisition and Processing Technology (ADAPT) system using Pulse Code Modulation (PCM) telemetry for acquiring the data. This system has proven to be the most effective way of acquiring and processing large quantities of interference-free data. A description of the system and the data processing procedures are contained in reference 1.

Scenario Information

a. Distance. For cargo items, the ground distance is determined on the basis of transport mileage between each of the designated supply points occurring between the port staging area (PSA - the point where ground transportation begins) and the user of the item. Figure 1 is a typical cargo scenario taken from ITOP 1-2-601 and MIL-STD-810D.

For installed equipment items, the ground distance is determined on the basis of the maintenance schedule for the vehicle on which the equipment is mounted or on the basis of a designer/user agreed upon repair/replacement schedule for the particular installed equipment item. Ammunition in racks is considered installed equipment, and the ground distance is based on user requirements.

The scenario for cargo and installed equipment transported by helicopter is generally measured in time rather than distance. The time begins with the ground run-up phase of helicopter flight and progresses through ascent, level flight, maneuvers, and ends with descent and landing. It is imperative that the scenario information for a given helicopter type provides sufficient flight conditions and corresponding times for the individual conditions to adequately describe the most severe vibration environment. For example, level flight should include a range of speeds between minimum and maximum and the expected flight time at each speed for a normal mission in order to determine the most severe level flight condition.

b. Ground vehicle type. The choice of cargo vehicle is determined by the type of terrain encountered between the supply points and by the physical size of the cargo items. As ground transport progresses from the PSA to the user, the terrain changes from multi-lane paved roads to trails and cross-country, and vehicles are designed accordingly. As the types of vehicles change, consideration must be given to whether the cargo will physically fit in a particular type. If not, that vehicle should not be used to develop a schedule for that particular cargo item.

c. Terrain conditions. As stated above, the terrain and severity of the vibration environment changes from relatively smooth paved roads through unimproved secondary roads to trails and virgin cross-country profiles. Unimproved secondary roads, trails, and cross-country terrains provide the most severe vibration environment for wheeled vehicles, while hard-surfaced roads provide the most severe environment for tracked vehicles.

d. Flight conditions. For helicopters, vibration severity is related to flight conditions. The vibration environment at a given location in or on a helicopter is affected by the power output of the engine, the aerodynamic buffeting of the rotor(s), and atmospheric conditions. Table 1 lists the typical flight conditions for a cargo helicopter as determined after direct discussion with a complete flight crew including the cargo master.

Vehicle Speeds. The application of vehicle speeds is critical to the severity of the vibration environment, the field transport time, and ultimately to the laboratory vibration test time. It is reasonable to assume that a vehicle operator under tactical conditions will travel at a maximum speed consistent with the terrain, and the ability to control the vehicle and retain load-restraint integrity. For wheeled cargo vehicles, this speed usually produces the most severe vibration environment on the cargo bed, but this should be determined/verified for each schedule development effort.

Vehicle speeds and required scenario distances are used to determine the field transport time from which the laboratory test time is derived. For tracked vehicles, the designated convoy speed is used since it is the speed at which this type of vehicle is usually operated on paved roads, which, as stated above, constitutes the most severe vibration environment. For wheeled vehicles, the critical speeds vary with the types of terrain. If more than one terrain (test course) is used to simulate the scenario requirements, the average of all critical

speeds is used to determine the field transport time.

Fatigue and Wear Considerations.

a. Cumulative damage equivalence. A major cause of items failing to perform their intended function is material fatigue accumulated over a time period as a result of vibration-induced stress. This cumulative damage and the theory involved provide the basis for choosing vehicle-terrain combinations and for determining laboratory test times as a function of scenario distance in the development of a vibration schedule.

b. The particular aspect of the damage equivalence theory used is Miners' Method, which describes data curves of stress versus number of cycles (S-N) for various materials. An excellent review of the cumulative damage theory is given in reference 3.

c. Terrain severity. Since theory states that damage will occur at the highest stress levels, it follows that the developed schedule must reflect the most severe vibration environment. For wheeled vehicles, this has been determined to occur during operations on unimproved secondary roads, trails, and cross-country. Transport over paved roads with a wheeled vehicle produces vibration levels that are insignificant in comparison; therefore, that portion of a scenario can be ignored for schedule development purposes.

On the other hand, paved roads provide the most severe vibration levels in a tracked vehicle because of the relatively constant impact of the track blocks on the hard surface. Hard-packed gravel or dirt secondary roads will produce levels nearly equivalent to paved roads; but in temperate climates, secondary roads do not retain their hard packed surfaces for any appreciable length of time, and therefore, the scenario times on those types of courses are discounted. However, for tracked vehicles designed primarily for operational scenarios in desert or arctic climates where the unpaved road surface is consistently hard packed, such terrains should be used. At this time, however, no scenario information is available for these types of operations. Consequently, only the paved road portion of a tracked vehicle scenario is relevant to schedule development for that type of transport.

d. Exaggeration factor. The cumulative damage theory affects the laboratory test time through the use of an exaggeration factor. As previously mentioned, it is normally not practical to test equipment by transporting it in or on vehicles on a real-time basis. To compress the many hours

of field environment into an equivalent laboratory test requires a relationship between time and vibration level. Since stress is proportional to vibration level, it is possible to apply the cumulative fatigue damage hypothesis and relate number of cycles (or time) at one amplitude level to an exaggerated level for a fewer number of cycles. For random vibration environments, this relationship is defined as:

$$\left(\frac{W_1}{W_2}\right)^{b/n} = \frac{T_2}{T_1}$$

in which:

W_1 = real time amplitude (G/Hz)

W_2 = laboratory test amplitude (G/Hz)

T_1 = real time

T_2 = laboratory test time

$b = 9$ (generally used endurance curve constant)

$n = 2.4$ (generally used stress damping constant)

The ratio of W_1 to W_2 becomes the exaggeration factor. For factors greater than 1, the laboratory test time is reduced; and, conversely, for factors less than 1, the laboratory time is increased.

Caution must be exercised in using this exaggeration factor. It appears foolish to attempt to compress test time to the point that the increased amplitude will exceed the yield or ultimate strength of the material. Reference 3 suggests limiting the exaggeration of test levels so as not to exceed the ratio of ultimate strength to endurance strength of the material being tested. In an attempt to determine a maximum exaggeration value, a search was conducted of the mechanical properties of 25 metals that have been used most often in a large variety of test items (ref 4). The ratios of ultimate stress (U) to the elastic limit (Y) and ultimate stress (U) to the endurance limit (EN) were calculated for each of the metals and averaged, producing values of $U/Y = 1.37$ and $U/EN = 2.73$. These ratios were then averaged, producing a value of 2.08 (see table 2). Based on this information, the value of 2 is suggested as the maximum limit for exaggeration factors.

This approach is based upon a combination of experience and some valid assumptions. Experience has shown that equipment is designed so that its structural integrity lies above the endurance limit of the

material because fatigue failures do occur in the field. It is known that items are not designed at the ultimate limit of the material, however, because these failures do not occur on the first vibration cycle. Assuming that equipment is designed so that its structural characteristics lie somewhere in the midpoint region between the endurance and elastic limits (see figure 2), splitting the approximate difference would produce a value of 2 which thus lends credence to the use of 2 as the maximum exaggeration factor.

Exaggeration factors for materials whose fatigue characteristics are unknown or for failure mechanisms other than fatigue (such as loosening of threaded connections) cannot be calculated. Real time test levels and durations should be used in these instances unless there is sufficient information about the particular application to allow the use of a reasonable exaggeration factor.

VEHICLE PREPARATION FOR DATA ACQUISITION--CARGO

Specific Load. If the load and tie-down method are specified, no further instructions are necessary; the specifications will be followed.

General Cargo Simulated Load. For general applications when loads and tie-down methods are not specified, typical cargo packages should be chosen. These should be boxes, drums, or cartons designed to provide a simulated load that covers as much of the cargo bed as possible consistent with the tie-down method and that weights the vehicle with approximately 75% of its rated payload. This weight limitation is a somewhat arbitrary figure that is based on a study that discovered that in the field, load weights varied but tended to be at, or near, full load. Another study revealed that the severity of the cargo bed vibration environment was minimal at full load and increased dramatically as load decreased. Based on these two studies, the value of 75% of rated payload was chosen to provide a degree of conservatism.

Large rigid items such as steel plates, beams, or concrete blocks should not be used as simulated loads because their monolithic nature inhibits the flexibility of the cargo bed.

Tie-down. The simulated load must be securely attached to the vehicle cargo bed using steel banding, web strapping, and/or dunnage. It must be secure enough to prevent impacting between load and bed and must prevent relative movement in the horizontal planes.

Accelerometers. Accelerometers must be mounted on the structural members of the

cargo bed at locations that will measure the input acceleration forces imparted to the load. The number of locations must be sufficient to describe the overall cargo bed environment. Care should be taken to avoid placing accelerometers on the relatively thin steel plate that comprises most cargo bed surfaces. This surface, particularly between structural members, exhibits high acceleration levels but has very small effective mass, thus producing little force on the cargo. The acceleration measurements must be taken in the three primary axes of the bed--vertical, transverse, and longitudinal.

VEHICLE PREPARATION FOR DATA ACQUISITION--INSTALLED EQUIPMENT

Accelerometers must be mounted on the vehicle walls, deck, and roof, as well as on brackets and shelves that are integral parts of the vehicle, as close as possible to the point(s) of attachment of the existing/planned installed equipment. The purpose is to measure the vibration environment of the vehicle at the input location(s) of the installed equipment which has the same configuration as the equipment which will subsequently be used as a test item during laboratory testing. For instance, if a piece of equipment is mounted on a bracket in the vehicle and that bracket will not appear as part of the equipment during subsequent laboratory testing, the environment should be measured on the bracket as the input to the equipment.

If a mounting platform exists on a vehicle and the test item to be installed thereon is not available, a model of the item with the same mass and center of gravity should be used. This ensures that the reaction of the installed test item will be included in the data recorded at the input to the mounting platform. In all cases, the measurements must be taken in the three primary axes.

The difference between the mechanical impedances of mountings for field-installed and laboratory-installed equipment should be considered, particularly for relatively massive items. A comparison of the field and laboratory frequency response functions is one method of evaluating this difference; and the use of average, extreme, or response laboratory vibration control techniques are considered valid approaches to minimizing any impedance mismatch.

DATA ACQUISITION PROCEDURES

Cargo Schedules.

a. Attach triaxial accelerometers to the structural members of the cargo bed in order to measure the vibration environment along the three mutually perpendicular axes usually noted as vertical (V), transverse (T), and

longitudinal (L). Normally, these axes are relative to the axes of the vehicle, i.e., vertical is up/down, transverse is side/side, and longitudinal is front/rear. This notation is not mandatory but tends to be least confusing to the overall vibration testing community.

- b. Check the tie-down system to ensure security of the load.
- c. Run a systems check of instrumentation, and perform the necessary calibrations.
- d. Operate the vehicle at the prescribed speed(s) over the designated fixed profile courses, and record the data.

Installed Equipment Schedules.

- a. Attach triaxial accelerometers at the actual or proposed vehicle-installed equipment interface points to measure the input to the equipment as it will subsequently be tested in the laboratory. Orient the accelerometers to measure data in the V, T, and L axes as described above.
- b. Run a systems check of instrumentation, and perform the necessary calibrations.
- c. Operate the vehicle at the prescribed speed(s) over the designated fixed profile courses, and record the data.

DATA REQUIRED

Care must be taken when recording data to ensure that it can be correlated with any data taken during previous tests of the same type of vehicle. Parameters such as sampling rate and filtering will affect the ability to compare/combine environments during analysis. The analysis filter bandwidth is particularly important; comparing/combining different data sets must be done using the same analysis filter bandwidth. The following data must be obtained:

- a. An accurate log of accelerometer locations and orientations.
- b. An accurate log of test courses and speeds.
- c. Recorded data in terms of acceleration amplitudes versus time for time intervals sufficient to ensure accurate analysis.
- d. Graphic representation (photographs, sketches, etc.) of the cargo load/installed equipment mounting configuration.

DATA PRESENTATION

Data Characteristics. Past tests and studies concerned with analysing vehicle vibration data have resulted in the following conclusions:

a. Wheeled vehicle vibration data can be best simulated by using wideband random techniques.

b. Tracked vehicle vibration exhibits a wideband random threshold with superimposed high level random amplitudes at frequencies that are integer multiples. The frequencies of these higher level data are created by the interaction between the tracks and the hard road surface, and they are proportional to vehicle speed. This proportion can be described as follows:

$$f = \frac{0.28v}{p}$$

in which:

$$\begin{aligned} f &= \text{frequency (Hz)} \\ p &= \text{track pitch (m)} \\ v &= \text{velocity (km/h)} \end{aligned}$$

c. Cargo helicopter data are wideband random with superimposed high level random amplitudes occurring at the harmonically related frequencies that are associated with the rotating helicopter components.

Combined Data.

a. Cargo. It is impractical to use an actual vehicle cargo bed as a mounting platform in the laboratory. Therefore, a smaller fixture must be designed to perform this function. This simulated cargo bed precludes placing control accelerometers at the same locations used on the vehicles during the acquisition of field data. It remains then to combine the data from each field test location into a single set of data that represents the entire cargo bed environment along each of the mutually perpendicular axes (V, T, L).

Further data combining is required when more than one fixed profile course is used to describe the scenario terrain for wheeled vehicles. In this case, the data describing the entire cargo bed from each course are combined to provide a single set of data for each axis that represents the required terrain environment for a given vehicle.

The final combining of data occurs if it is required to combine the individual data sets from each of a series of similar vehicles in order to develop a schedule for an entire vehicle classification. Reference 4 describes the procedures for this combining of locations, courses, and vehicles.

For cargo helicopters, this additional combining is required to encompass the different flight conditions involved in a typical scenario. Reference 1 describes a technique that combines flight conditions on a weighted basis, i.e., the contribution of each flight event to the final composite schedule was based on the percentage of time those events occurred during the scenario flight.

b. Installed Equipment. Developing a schedule for equipment already installed in a particular vehicle normally will not require the combining of data channels/locations. Most equipment is small enough to require a minimal number of locations which can be duplicated on a laboratory test fixture. However developing more general schedules for vehicle internal and external surfaces that will subsequently become mounting platforms for installed equipment (hull and turret walls, decks, roofs, etc.) requires many data acquisition locations, even more than on cargo beds. It would be extremely impractical to develop a schedule for each location. The data from each location must therefore be examined and statistically compared in order to determine the feasibility of combining them.

The statistical parameters used to compare the data include the overall root mean square (RMS) acceleration values for each channel, the mean and standard deviation of these values, and the confidence level pertinent to the choice of using the mean overall RMS value as the comparison factor. This comparison will control the number of schedules required to adequately describe the vibration environment in and/or on a given vehicle, and obviously this number should be a minimum.

Data Processing. The first step in the data handling process is to ensure the integrity of recorded time/amplitude data from the test courses, i.e., the data must be free of noise, signal loss, etc.

Once good data are assured, the second step is to make the conversion from the time domain to the frequency domain in the form of power spectral density (PSD) measured in G^2/Hz versus frequency. A PSD curve for each data channel should be computed, plotted, and checked as a final test of data integrity.

The third step involves combining data channels and locations, if required. The best method for accomplishing this is by using electronic data-processing techniques, as described in reference 2.

At this stage in data presentation, plots of G^2/Hz versus frequency have been made for

each individual data channel or for composite data resulting from combined channels.

The final step in data presentation requires converting these PSD curves to a series of break points suitable for programming laboratory vibration control instrumentation. A break point is defined as a given G^2/Hz amplitude at a given frequency. A series of break points connected by straight lines becomes the acceleration amplitude frequency portion of a laboratory schedule. Figures 3 and 4 are typical plots of wheeled and tracked vehicle break points.

SCHEDULE

The break point data and test time derived from the vehicle speed, scenario distance, and exaggeration factor (if required) comprise a laboratory vibration test schedule.

Reference 2 contains the procedures and instrumentation used by USACSTA for developing some of the secured cargo and installed equipment laboratory vibration schedules. It is taken from a USACSTA report and is included in the reference as a typical example for application of the information contained in this paper. In the interest of brevity, examples of data plots for the cargo schedules were limited to the vertical axis only; and those for the installed equipment are not included.

SUMMARY

The process of translating field vibration data into realistic laboratory vibration test schedules requires a lot of up-front planning to ensure all of the proper data in sufficient quantity are collected during field operations. The operational scenario for the materiel must be established in order to produce the desired realism in the laboratory test. As can be seen, it is not a process of merely taking a few measurements and reducing the data. It is a process which requires a lot of knowledge about the item and its intended use if realistic laboratory testing is to be conducted. This paper has briefly addressed each area which is involved or addressed by the U.S. Army Combat Systems Test Activity in developing laboratory vibration test schedules.

REFERENCES

1. International Test Operations Procedure (ITOP) 1-1-050, Development of Laboratory Vibration Test Schedules, U.S. Army Test and Evaluation Command, Aberdeen Proving Ground, MD, 16 May 1986.
2. Test Operations Procedure (TOP) 1-1-011, Vehicle Test Facilities at Aberdeen Proving Ground, US Army Test and Evaluation Command, Aberdeen Proving Ground, MD, 6 July 1981.
3. Curtis, Allen J.; Tinling, Nicklaus G.; and Abstein, Henry T. Jr; Selection and Performance of Vibration Test, Shock and Vibration Information Center, SVM-8, 1971.
4. Structural Alloy Handbook, Mechanical Properties Data Center, Balfour-Stulen, Inc., Traverse City, MI, 1977 edition.

FOREIGN THEATER CARGO SCENARIO

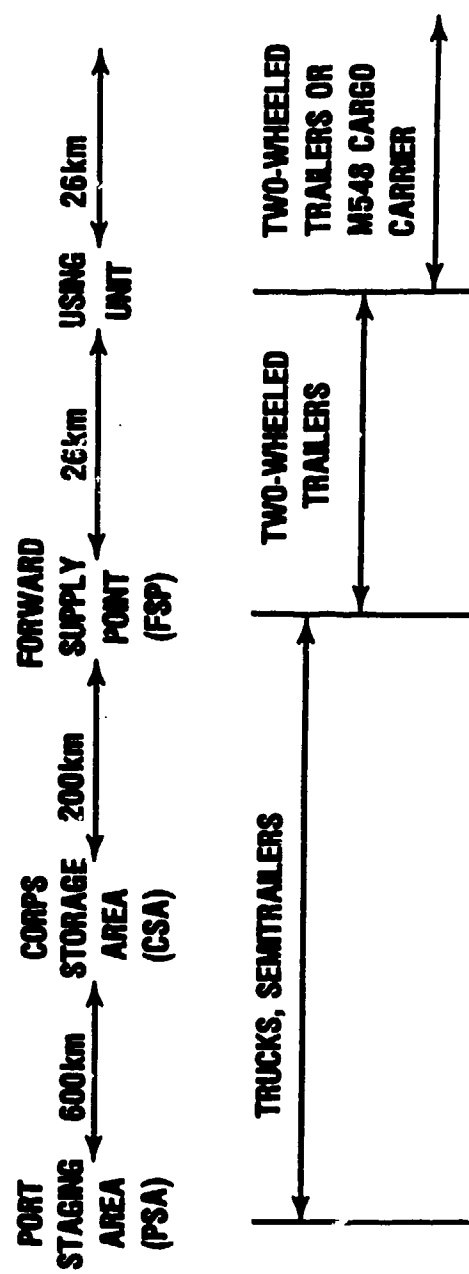


Figure 1

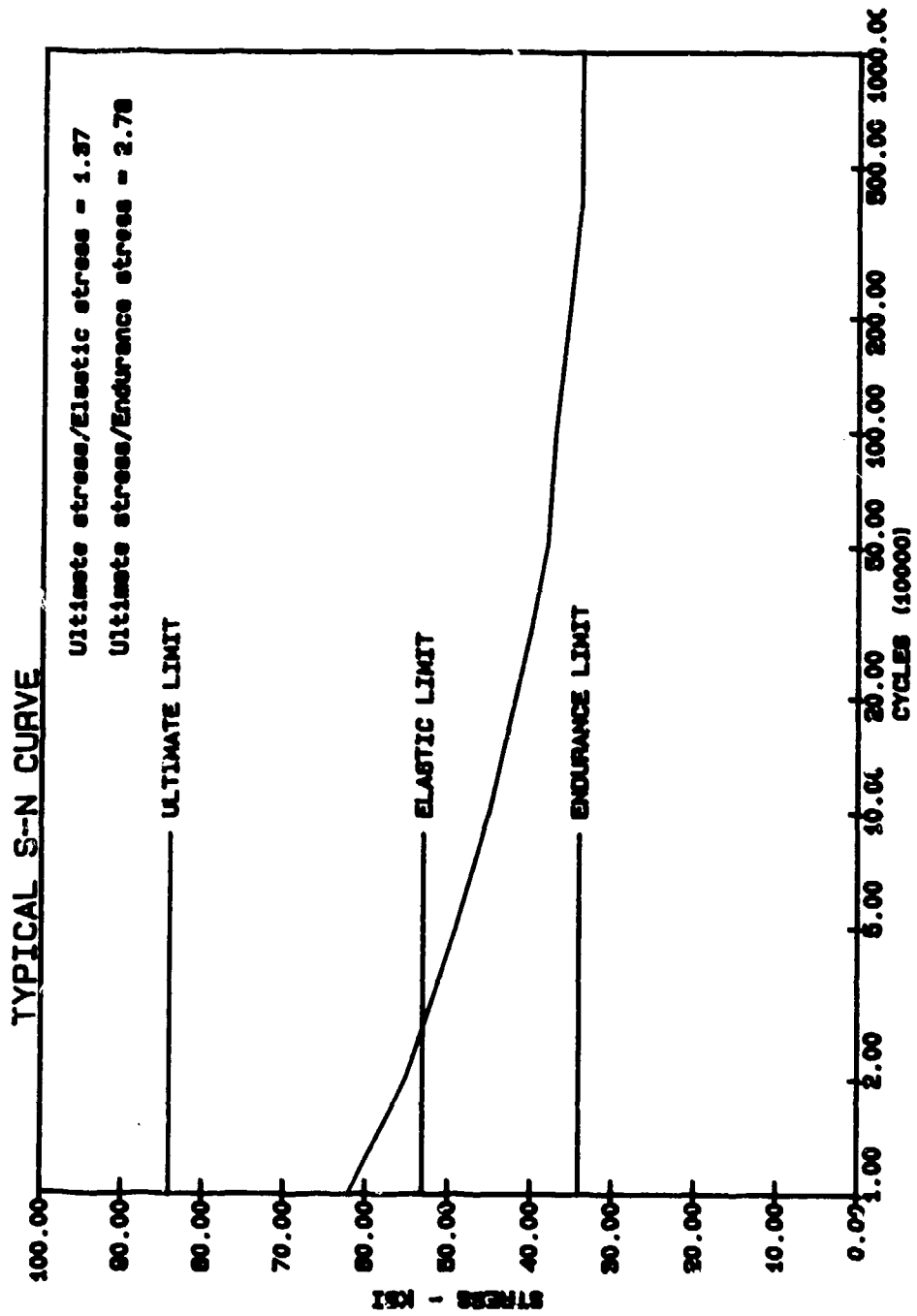


Figure 2

LAS VIBRATION SCHEDULE, XM783 & M422 ROUNDS, M106A2 C80 BED, VERT

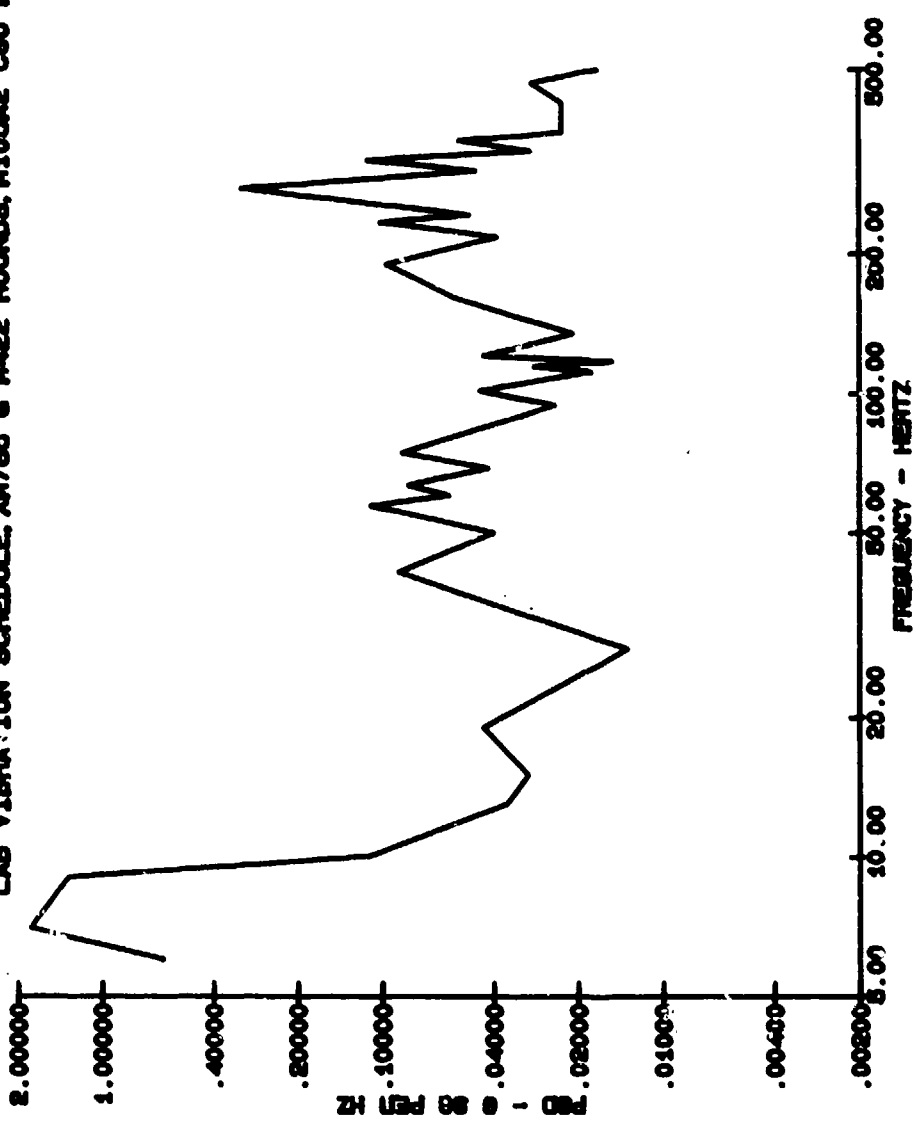


Figure 3

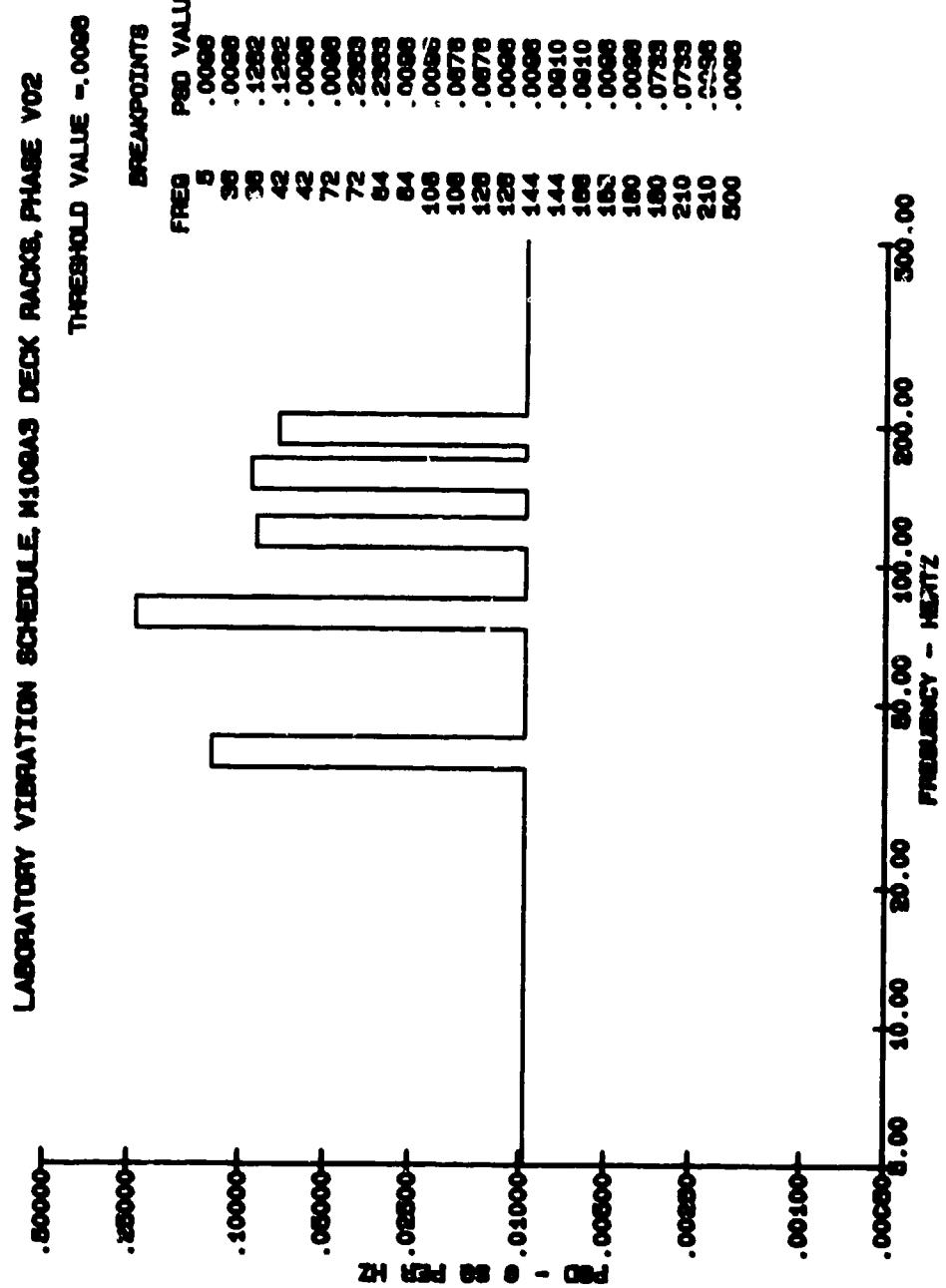


Figure 4

September 1986

TABLE 1. HELICOPTER FLIGHT CONDITIONS

Event No.	Event Description
1	Ground run-up
2	In-ground effect (IGE) hover
3	Out-of-ground effect (OGE) hover
4	Climb - 80 knots indicated air speed (KIAS), 500 fpm
5	Level flight - 80 KIAS - 1000 feet mean sea level (MSL)
6	Standard rate turn - 80 KIAS - 1000 feet MSL
7	Level flight - 130 KIAS - 1000 feet MSL
8	Standard rate turn - 130 KIAS - 1000 feet MSL
9	Level flight - 0.95 V_H^* - 1000 feet MSL
10	Standard rate turn - 0.95 V_H^* - 1000 feet MSL
11	Level flight - 80 KIAS - 5000 feet MSL
12	Standard rate turn - 80 KIAS - 5000 feet MSL
13	Level flight - 130 KIAS - 5000 feet MSL
14	Standard rate turn - 130 KIAS - 5000 feet MSL
15	Level flight - 0.95 V_H^* - 5000 feet MSL
16	Standard rate turn - 0.95 V_H^* - 5000 feet MSL
17	Descent - 80 KIAS - 500 fpm

* V_H is the maximum horizontal velocity obtainable without losing altitude.

TABLE 2. METALS AND MECHANICAL PROPERTIES

	ELASTIC LIMIT (Y)	ENDURANCE LIMIT (EN)	ULTIMATE (U)	RATIO (U/Y)	RATIO (U/EN)
1. Steel, 0.4% C, H. Rolled	53	38	84	1.59	2.21
2. Steel, Stainless (18-8) Annealed	36	40	85	2.36	2.13
3. Steel, Stainless (18-8) Cold rolled	165	90	190	1.15	2.11
4. Alum, Cast, 195T-6	24	7	36	1.53	5.14
5. Alum, Wrought, 2014-T4	41	18	62	1.51	3.44
6. Alum, Wrought, 2024-T4	48	18	68	1.42	3.78
7. Alum, Wrought, 6061-T6	40	13.5	45	1.13	3.33
8. Magnesium, Extrusion, AL60X	35	19	49	1.40	2.58
9. Magnesium, Sand Cast, AZ63-HT	14	14	40	1.00	2.86
10. Monel, Wrought, Hot Rolled	50	40	90	1.80	2.25
11. Steel, 1040	60	43	90	1.50	2.09
12. Steel, 1340	63	59	102	1.62	1.73
13. Steel, 4130	63	47	97	1.54	2.06
14. Steel, 4140	143	66	165	1.15	2.50
15. Steel, 4340	200	58	222	1.11	3.27
16. Steel, 5140	169	82	190	1.12	2.32
17. Steel, HY140	142	70	149	1.05	2.13
18. Steel, Marage 200	215	100	225	1.05	2.25
19. Steel, Marage 350	345	110	352	1.02	3.20
20. Alum, Cast, 113	15	9	24	1.60	2.67
21. Alum, Cast 335, T61	35	10	39	1.11	3.90
22. Alum, Cast, 224, T7	48	12	61	1.27	1.27
23. Alum, Cast, A249, T7	50	11	60	1.20	5.46
24. Cast Iron, Malleable	33	28	58	1.76	2.07
25. Cast Iron, Ductile	55	30.5	80	1.46	2.62

AVERAGE U/Y = 1.37

AVERAGE U/EN = 2.78

AVERAGE U/Y - U/EN = 2.08

2

LABORATORY VIBRATION TEST SCHEDULES
DEVELOPED BEYOND MIL-STD-810D

Richard D. Baily
U.S. ARMY COMBAT SYSTEMS TEST ACTIVITY (USACSTA)
ABERDEEN PROVING GROUND, MARYLAND

This paper lists the documentation and describes the work that has been accomplished in deriving laboratory vibration test schedules for tactical vehicles since the introduction of such schedules in MIL-STD-810D. Approximately 20 schedules have been developed from field data acquired on 15 different vehicles.

INTRODUCTION

The development of laboratory vibration test schedules from real-time field transportation data began at Aberdeen Proving Ground (APG) in the early 1960s. Prior to that time most of the laboratory tests were conducted according to schedules found in Air Force documents such as Military Specification MIL-E-5272C which called for swept-sine tests from 5 to 2000 Hz at anywhere from 2 to 20 g's, with resonance dwells of up to 30 minutes in duration. Such a resonance dwell on an item of general equipment was often more hazardous than testing live ammunition. Popped rivets and sheared bolt heads ricocheted around the test cell like angry hornets. Finally, one of the test sponsors, having had many of his test items returned looking like unassembled Christmas toys, requested that APG measure the field environment of a particular vehicle/test-item configuration to determine if the vibration levels even came close to those being used in the laboratory (if remembered correctly, it was a shelter and air conditioner mounted on an M113 chassis). Acquiring the data on analog tapes was easy. Trying to compare the resulting random data (or complex random as it was labeled) to sinusoids was a different story. It was evident that sinusoidal vibration and resonance response at maximum amplification did not occur in the field. Efforts were then channeled, over several years, toward improving the capability to analyse data to determine the real nature of the environment. These efforts progressed slowly through the era of analog recording and analysis equipment to the breakthrough of digital data acquisition systems and computer/Fast Fourier Transform analysis instrumentation. At the USACSTA, this evolution resulted in the

design, installation and implementation of the Automated Data Acquisition and Processing Technology (ADAPT) system. With the advent of the ADAPT system, its library of more than 100 data processing and presentation software programs, and the increased emphasis on the importance of methodology studies, the development of laboratory vibration schedules simulating the field transportation environment of tactical vehicles moved forward rapidly.

The initial efforts along these lines were the development of the combined wheeled vehicle, two-wheeled trailer and M548 tracked cargo carrier laboratory vibration test schedules for secured cargo that became a part of MIL-STD-810D. At that time, persons involved with the writing of that military standard were aware that those particular schedules were limited to a very few vehicles that had been surveyed at USACSTA. Inasmuch as they were a far more realistic representation of the real-world environment, the decision was made to place those schedules into MIL-STD-810D with the intention of updating them through the use of changes to that standard.

Numerous vibration test schedules have been developed since the publishing of MIL-STD-810D. Most of these have been, and are being, accomplished under the U.S. Army Test and Evaluation Command (TECOM) Methodology program with the remainder being done through specialized program needs. This paper will define the specific test schedules that have been developed and the fact that they have been documented.

MIL-STD-810D. The vehicle data used to develop the secured cargo transport schedules in the original version of Method 514.3 in

MIL-STD-810D were taken from the 1-1/2-ton M1052 two-wheeled trailer, the 5-ton M813 truck, the 12-ton M27 semitrailer and the 6-ton M548 tracked cargo carrier as part of a test program conducted in 1982. Since then, data have been acquired on 15 different vehicles; and approximately 20 test schedules have been developed. Three of these schedules have been submitted to the MIL-STD-810D Tri-Service Committee for the revision of the two-wheeled trailer, composite tactical wheeled vehicle, and tracked vehicle cargo schedules.

Schedule Documentation. As previously mentioned, the schedules that have been developed thus far were done as part of the ongoing TECOM methodology program or through projects designed for specific vehicle/test-item combinations. Those resulting from methodology efforts are (or will be) included in Test and Evaluation Command International Test Operations Procedure (ITOP) 1-2-601 (ref). This document is rapidly becoming a standard for laboratory vibration testing concerned with military tactical vehicles. As stated in its scope definition, it is a dynamic document and is constantly being changed to include new and updated cargo and installed equipment schedules. The highly specialized laboratory schedules are documented in the individual project reports.

Wheeled Vehicle Schedules. In 1983, a methodology study was completed which provided laboratory schedules for general purpose cargo. The following vehicles were used to obtain the data:

Semitrailer, 12-ton, M127
Truck, 5-ton, M813
Truck, 5-ton, M814 (stretch body)
Truck, 2-1/2-ton, M36 (stretch body)
Truck, 1-1/4-ton, M1009 Commercial Utility Cargo Vehicle (CUCV)
Trailer, 1/4-ton, 2-wheeled, M416
Trailer, 1-1/2-ton, 2-wheeled, M105A2

Each vehicle was loaded to 75% of its rated payload with wooden ammunition boxes containing the fiber containers used to house the rounds of ammunition; these were filled with sand to simulate the actual box weight. The boxes were secured to the cargo bed with steel banding and blocking, and they covered the entire usable surface of the bed. Triaxial accelerometers were attached at nine locations on the underlying structural frame of the cargo area. The locations were designated as curbside, center, and roadside at the forward, center and aft portions of the bed. The data from the nine triaxial locations were electronically composited--which resulted in a single set of data in each of the three axes that represented the cargo bed environment of each vehicle. These data sets for each vehicle

were then plotted in an overlay pattern and compared. It was obvious from the overlay that the M105A2 trailer vibration environment completely overshadowed that of the other vehicles. Since these trailers have a limited cargo capacity and a limited sphere of operations in the field, it was decided to separate the data and develop a schedule for 2-wheeled trailers and another for the composite of the five cargo trucks. The work is documented in a methodology report concerning cargo transported in wheeled vehicles. The resulting schedules appear in ITOP 1-2-601 and are the ones that have been submitted for inclusion in the revised version of MIL-STD-810D.

The 1986 methodology effort has produced, among other things, general cargo schedules for two additional wheeled vehicles, i.e., the Truck, 1-1/4-ton M998 High Mobility Multi-Purpose Wheeled Vehicle (HMMWV) and the 10-ton M985 Heavy Expanded Mobility Tactical Truck (HEMTT). The data from these vehicles were acquired in the same manner as described above and will soon be integrated into the existing composite wheeled vehicle schedule.

Further schedule development for wheeled vehicles concerned installed equipment (a separate piece of equipment which is installed in/on a vehicle and becomes a part of that vehicle to enable it to perform the intended mission (e.g., radio)). Schedules were obtained for various components of the NAVSTAR/Global Positioning System (GPS) mounted on the cargo bed and in the driver's compartment of a Commercial Utility Cargo Vehicle (CUCV) and in the cargo bed and on the fender of a High Mobility Multipurpose Wheeled Vehicle (HMMWV). The laboratory vibration test schedules derived for this project have been documented in a laboratory report; and the data indicate that, from a vibration standpoint, the fender of a HMMWV is not an appropriate place to mount anything (except maybe a cocktail shaker).

Tracked Vehicle Schedules. A general cargo schedule for the M548 tracked vehicle, which is the only tracked vehicle designated as a cargo carrier, was also developed during the 1983 methodology study. It is included in ITOP 1-2-601 and was submitted for the MIL-STD-810D revision.

Schedules for equipment installed in tracked vehicles fall into two categories: first, ammunition carried in racks specifically designed for that ammunition and mounting locations; and second, general items that are or will be mounted elsewhere in the vehicle.

The initial schedules developed for this installed-equipment effort were for 120-mm ammunition transported in the hull and turret racks of the XM1 Tank. This was accomplished as part of the rack development phase for

this vehicle; and schedules were derived for both the "A" and "B" versions but were not included in any general documentation. When the rack design was finalized, a methodology program was formalized to study not only the 120-mm ammunition in the M1A1 tank but also the rack-mounted 105-mm ammunition in the M1 and M60A3 tanks. The hull and turret areas of all three tanks were instrumented triaxially at each rack interface with walls, decks, and roofs. The results of the study were a schedule for 120-mm ammunition installed in the M1A1 tank's hull rack (which experienced the most severe vibration input of all the racks in that vehicle) and a schedule for 105-mm rounds installed in the M1 tank's hull rack. A comparison of the overall acceleration values at the input to each rack located in the M1 and M60A3 tanks revealed that the vibration environment in the M1 hull area was the most severe of all racks in both vehicles. These schedules are documented in a formal report and are included in ITOP 1-2-601.

The second methodology investigation that was concerned with ammunition racks dealt with the M109A3 (155-mm) self-propelled howitzer. Data were taken at the inputs to the projectile bustle and deck racks, and at the propellant charge and ammunition round stowage areas on the sponsons. Schedules were developed for each of the four locations. Although the deck rack was found to have a more severe vibration environment than the bustle rack, schedules for both racks were developed because certain 155-mm projectiles do not fit in the deck racks and are transported solely in the bustle.

As part of this same investigation and in the interest of installed equipment other than ammunition, data were acquired at seven locations in the turret and two locations in the hull of the M109A3 and five locations on the M110A2 (8-inch) self-propelled howitzer. The instrumented areas were chosen for items currently mounted in the vehicle as well as to provide a data base for future installations. The data from each location were analyzed and compared--with the result that individual schedules were developed for the turret and for the hull of the M109A3 and for the trunnion, the gun mount, the deck, and the driver's compartment wall of the M110A2. The relatively low variance of the overall acceleration values for each of the seven locations in the M109A3 turret was the basis for combining the data and arriving at a single schedule that describes the overall turret environment. Nevertheless, the data at each location is still available in the data bank for any test tailoring applications. The study made on these two vehicles is described in a methodology report and all the schedules are included in ITOP 1-2-601.

As part of the aforementioned 1986 methodology program, installed equipment data have been recorded at 20 places on the M113 Armored Personnel Carrier. The locations were chosen to provide information on the overall vibration environment of the roof, deck, and bulkheads of that tracked vehicle. As in the case of the M109A3 howitzer, the data at each location will be processed and compared and, if feasible, combined to provide a single vibration schedule that describes the entire M113 environment. If insufficiency of commonality precludes a single schedule, the next approach will be to compare and combine the data to develop individual schedules for the roof, deck, and bulkheads. The work will then be documented in a forthcoming methodology report and will be included in ITOP 1-2-601. In addition to the methodology studies which are concerned basically with general types of installed equipment, test schedules have been developed on four test projects dealing with specialised items, i.e., a driver's viewer mounted through the driver's hatch cover of the M1 tank; a mine dispensing system (VOLCANO) attached to the bed of the M817 5-ton dump truck; the applique armor components on the turret and hull of an M60A3 tank; and the external lights mounted fore and aft on the M113 Armored Personnel Carrier (APC) and the M60A3 tank (report in progress). Although these schedules will not be included in any general documentation such as ITOPs or Military Standards, they and the data used to develop them have been or will be reported and will be retained in the U.S. Army Combat Systems Test Activity (USACSTA) data bank.

Future Projects.

In the near future, as vehicles become available, ammunition and/or installed general equipment schedules will be developed for the Field Artillery Supply Vehicle (FASV), the M1A1 Abrams Tank, and the M2 Infantry Fighting Vehicle (Bradley).

In addition, plans are being formulated to compare and combine (where feasible) all installed equipment data for both wheeled vehicles and tracked vehicles in an effort to minimize the number of schedules.

SUMMARY

Much progress has been made in the area of developing laboratory vibration test schedules that simulate the field environment of tactical vehicles since their introduction into MIL-STD-810D a short three years ago. Much work remains. As new sources of transportation vibration are developed, it is imperative that they be adequately investigated and properly documented. This overall process will ensure that the much-needed vibration data for test tailoring

is readily available to both the design and the testing communities.

REFERENCE

International Test Operations Procedure (ITOP) 1-2-601, Laboratory Vibration Schedules, AD No. A155856, U.S. Army Test and Evaluation Command, Aberdeen Proving Ground, 11 June 1966.

A PROPOSED TECHNIQUE FOR GROUND PACKAGED VEHICLE LOOSE CARGO VIBRATION SIMULATION

WILLIAM H. CONNOR, III
U.S. ARMY COMBAT SYSTEMS TEST ACTIVITY
ABERDEEN PROVING GROUND, MARYLAND

This paper describes a laboratory test method used to simulate packaged items (wooden crates) being transported as loosely stored cargo in military ground vehicles. A literature search was conducted to attempt to determine the failure modes of materiel transported as loose cargo and to determine the loose cargo transportation scenario. It was determined that items transported as loosely stored cargo are done so for a maximum distance of 150 miles in open top bed trucks, 32 miles in two-wheeled trailers or 16 miles in tracklaying cargo carriers. Data were collected by mounting triaxial accelerometers at the base of a model hardware specimen which was then securely mounted in a standard 105-mm ammunition box upweighted to its standard weight. Field data were collected by loading each test vehicles used (an M813 5-ton truck, and M101 3/4-ton two-wheeled trailer and an M548 tracklaying vehicle) with similar ammunition boxes one layer deep and operating each vehicle over a variety of cross-country and special surface courses. Laboratory data were collected using a commercially available package tester as the excitation source. Acceleration data on the instrumented test package were recorded during 20 different modes of operation on the package tester. Test equivalence was determined by selecting one of the laboratory test methods which supplied some acceleration amplification over the field data to reduce test time, had similar time domain acceleration amplitude distribution and had similar spectral energy distribution. The laboratory test condition of a plywood-covered bed operated in a synchronous mode at 300 rpm was determined to best meet the comparison criteria. The acceleration amplification for this condition resulted in a fatigue equivalent test time of 45-minutes.

1. BACKGROUND

Laboratory simulation of the transport environment for all types of military equipment has been conducted by the U.S. Army Test and Evaluation Command (TECOM) for a number of years as an expeditious means of determining if a given piece of equipment will survive the real world environment. The laboratory test schedules, both vibration and loosely-stowed cargo, given in MIL-STD-810C and various TECOM test documents were developed in the early 1960's based on shock and vibration data measured on vehicles tested under controlled conditions of loading and fixed-course configurations. Recent investigations have revealed that existing laboratory simulation tests are not descriptive of the real world cargo transport environment and thus have posed a serious question as to the validity of the entire laboratory-simulated testing approach, including the amount of time materiel is

subjected to both vibration and loose cargo testing as well as the type and amount of restraint imposed on cargo during laboratory testing.

This paper describes a technique for measuring the actual field environment for loose cargo transported in various military ground vehicles and developing a procedure for realistic laboratory simulation of this environment.

2. LITERATURE SEARCH

A formal literature search was conducted to attempt to determine the failure modes of materiel transported as loose cargo and to determine the loose cargo transportation scenario.

Definite information concerning failure mechanisms of test items transported as loose cargo was nonexistent. The reports surveyed

contained statements such as "damage includes fatigue and chafing" or "failures of cargo items were observed to occur in the form of fatigue fracture more than wear" without any substantiating data.

In contrast, the transportation scenario was well documented. It was determined that most items transported as loosely stowed cargo are done so in a forward area between a corps staging area (CSA) and a front line user (U), a maximum distance of 150 miles. The vehicles utilized were identified as dump body and open top bed trucks, the M548 track laying vehicle and two-wheeled trailers. Another source further refined the scenario as a cargo storage area (CSA), forward supply point (FSP) and user (U) with two-wheeled trailers being utilized from the FSP to, and at, the U for a distance of 32 miles and the M548 being utilized at the user point for a distance 16 miles.

Since no definitive data could be located to determine the predominate failure mode of loosely stowed cargo, it was decided that laboratory and field test equivalence would be based on equivalent fatigue in a cargo specimen rather than abrasion or chafing of the outer surface of the specimen. Chafing was disregarded because the present loose cargo tests were based on an abrasion study which was well documented and had little chance for improvement (i.e., the technology of the time would be repeated today). In addition, cargo damage due to chafing, except for critical items such as unprotected rounds of ammunition, may affect the appearance of an item without affecting the mission performance, whereas fatigue failures in an item generally have a much greater consequence.

A model hardware specimen (MHS) used in a previous investigation was used as the typical cargo specimen (the MHS is described in more detail in para 3.1). The approach chosen was to equate laboratory and field fatigue of the MHS by measuring the fatigue in each of the strain-gaged MHS beams and by measuring the triaxial acceleration of the base of the MHS and developing test equivalency by existing laboratory schedule development techniques (references 3 and 4).

3. DATA ACQUISITION

3.1 MOLEL HARDWARE SPECIMEN (MHS)

The MHS consisted of 14 cantilever steel beams tuned to frequencies from 6.25 to 160 Hz and separated by one-third of an octave (the 40-Hz beam was missing). Each beam was instrumented with a model EA-06-250BF-350 strain-gage. The beams were mounted onto a 2- by 3- by 12-in. aluminum beam which in turn was bolted to a 12 by 12 by 1/2 in. aluminum baseplate. The four vertical sides of the MHS were covered with wood to provide some protection for the instrumentation while

the top was left open to provide access. Strain-gage type accelerometers were mounted in three axes at the top center of the aluminum beam to which the beams were mounted and in the left rear corner of the baseplats. In order to simulate a typical military cargo item, the MHS was securely mounted in the middle of a 105-mm ammunition box (M467) which was then upweighted to approximately 110 pounds to duplicate the weight of standard ammunition boxes.

3.2 INSTRUMENTATION

In addition to the strain-gages and accelerometers already described, three strain-gage accelerometers were mounted triaxially on the test vehicle frame near the location of the MHS or on the package tester frame.

An on-board pulse code modulation (PCM) telemetry system was used as the data acquisition system. This system transmitted data which was digitized at a rate of approximately 2000 samples per second per channel to a remote data handling station where the data were ultimately stored on digital tape for later analysis.

3.3 TEST CONDITIONS

The MHS was tested on an electrodynamic shaker to determine the transfer function of each of the beams, on three different vehicles over a variety of test courses to provide field data and on LAB Models 3000 and 8000 package testers to provide laboratory data. These phases are discussed in the following paragraphs.

3.3.1 Electrodynamic shaker.

Because the beams were somewhat fragile, it was decided to develop a procedure to compute the strain in any of the beams based on the acceleration input to the MHS. The basic MHS (without the ammunition box) was rigidly banded to the table (head expander or slip table) of a model UD 4000 electrodynamic shaker. The output of the shaker was controlled by a digital vibration control system in order to provide broadband random (5 to 500 Hz) motion at amplitudes of 0.25 g rms, 0.5 g rms, 0.75 g rms (vertical only) and 1.0 g rms. Data were recorded for each run for approximately 1 minute. These tests were conducted in both the vertical and longitudinal (along the beam axis) directions.

3.3.2 Field data.

Data runs were made with the MHS in its ammunition box loosely stowed in the most rearward portion of the cargo area of an M813 5-ton truck, an M101 3/4-ton two-wheeled trailer (pulled by the 5-ton truck) and an M548 6-ton track laying cargo vehicle. Each vehicle was loaded with enough weighted (to

110 lb) ammunition boxes to provide a load one layer deep with approximately a 2-in. gap between adjacent boxes. The number of boxes used (including the MHS) were 20, 7, and 16 for the truck, trailer and track laying vehicle, respectively, for loads of 2200, 770, and 1760 pounds which represented loads of 22%, 51%, and 15%, respectively, of rated capacity. The vehicles were operated on the test courses at the speeds listed in Table 1.

The cross-country and special surface courses were considered to be representative of the terrain described in available cargo scenario information as secondary road, trails, and off-road; the paved road course typified primary road conditions.

Data were recorded for approximately 1 minute during operation at each speed on each of the courses.

3.3.3 Package tester.

LAB Models 3000 and 8000 commercial package testers were used for this portion of the test. The package tester was capable of synchronous motion with the driver shafts in phase, which produced circular motion in a vertical plane, synchronous motion with the shafts 30° out of phase, which produced elliptical motion and asynchronous motion which produced circular motion with table tipping. Various test modes were selected to represent tests in current use. A list of runs conducted and the applicable test specifications are presented in Table 2.

The distances from the center of the package tester to the center of the MHS are listed in Table 3. Data were recorded for approximately 1 minute for each test condition.

4. TEST RESULTS

4.1 GENERAL

Prior to further processing of any of the acquired data, all data were screened for validity by performing a check for stationarity using the same data reduction parameters (data segments, block sizes) as would be used for future data processing. This technique was also used to locate and cull bad data from the overall data bank.

4.2 ELECTRODYNAMIC SHAKER

Transfer functions were initially computed between the shaker table and the base of the MHS and between the shaker table and the top of the strain gage mount platform. The transfer function and coherence function between the shaker table and the base of the MHS were essentially 1 from 5 to 500 Hz, while the transfer function between the shaker table and the strain gage mount platform exhibited some amplification in the 350 Hz region. For this reason, the

base of the MHS was considered to be the input to the MHS (rather than the strain gage mount beam) for all transfer functions between the MHS and the individual beams and in later work in development of the test schedule.

When vibrated in the vertical mode, each of the beams exhibited a large amplification (different for each beam), at its natural frequency with no other modes apparent. The transfer function data were stored in files for later use.

When vibrated in the longitudinal mode (along the axis of the beams), the amplification of the response compared to the input was small, indicating that the beams were relatively insensitive to purely longitudinal motion or the longitudinal vector of three-dimensional motion.

Although the levels used for this portion of the experiment were benign compared to a field environment, several problems were encountered with the strain gages on the lower frequency (maximum displacement) beams which required replacement of the strain gages.

4.3 FIELD DATA

After a few failures within 100 meters of operation in the M813 truck over moderate terrain (local roads), it was apparent that the strain gages would not have a reasonable life during the conduct of the test. The initial concept was to compute the response of each beam from the input to the base of the MHS using the transfer functions previously developed rather than repair each beam as required. This computed information was then to be analyzed by a fatigue life estimation technique based on counting magnitude and frequency of occurrence of stress reversals as described in Reference 11. This would have proven to be a complex, time consuming process, but could have been accomplished with the data acquired. After some reflection, this technique was abandoned in favor of using fatigue equivalence methods based on measures of acceleration as described in References 3 and 4. Acceleration measurements made in three axes at the base of the MHS were used for all further analyses and comparisons, although all the original accelerometer channels and all remaining active strain gage channels were recorded throughout the remainder of the test. The decision to abandon the strain calculation technique was based on two primary concepts. First, the transfer functions previously calculated had shown the MHS to be a one-dimensional device, thus modeling fatigue in the beams would not account for the other axes. Second, the beams had proven to be unrealistically fragile (i.e., no useful structure to be subjected to a military environment would be designed in this fashion), and to model this

structure for comparison purposes might distort results from those which would be obtained using more rugged structures.

4.3.1 M813 5-ton truck.

The accelerometer data from the base of the MHS were reduced in the form of PSDs for each data run. The critical speed for each test course, i.e., the speed at which the vertical rms acceleration was greatest, was then identified. These speeds are listed in Table 4.

The data from cross-country course 3 were not used in the analysis because the values were significantly lower than for the other courses. Data from the other three courses were overlaid into a vibration schedule procedure for each axis using the techniques described in Reference 5. For this analysis, the PSDs from each of the courses were weighted by the exposure times likely to be encountered in actual field use. In computing the course exposure time, it was assumed that the real-world terrain corresponding to the various test courses exists in the ratio of the lengths of the test courses. While there is no evidence to either support or refute this assumption, the assumption does not seem unreasonable when considering real-world experience with the types of terrain involved. (Expected travel distance over terrain types corresponding to these test courses should be determined in a future study.) The course lengths, speeds, and exposure times are presented in Table 5.

Thus, the spaced bump data were assigned a unity weighting factor while the 2-inch washboard and Belgian block data were assigned weighting factors of 3 and 4, respectively. In the analysis procedure, this was accomplished by combining the spaced bump PSD with three PSDs (the same one) from the 2-inch washboard and four PSDs from the Belgian block. The effect of the weighting process is to assign a value of 0.5 to the Belgian block data, 0.375 to the 2-inch washboard data, and 0.125 to the spaced bump data rather than 0.333 for each of the courses. The effect on the M813 data was minimal because the Belgian block and spaced bump data were similar in value and because the weighting factor for the 2-inch washboard data, which was considerably higher than the other data, was only slightly different than the evenly weighted value. The resultant PSD (vertical only) from the M813 is presented in Figure 1. The overall weighted average course speed was 18.6 mph. It was determined that 65% of the 150 mile test scenario, or 98 miles, was over terrain similar to that used to acquire data -- which equates to a real-world exposure time of 5.27 hours.

4.3.2 M101 trailer.

Critical speeds for the test courses were chosen using the same technique as the

M813 truck -- with the same results. However, unlike the data from the M813 truck, data from the trailer on cross-country 3 at 20 mph proved to be the most severe and were used in the analysis. This unexpected result might be attributed to the amplified movement of the loose cargo -- induced by the rolling nature of the course terrain which causes vehicle pitching -- which is not present in secured cargo or in the basic vehicle structure. These data were overlayed, as previously described, using the weighting factors, previously described, with an additional weighting factor of 6 for cross-country 3 data (course length utilized 1 mile). The resultant PSD (vertical only) is presented in Figure 2.

Data recorded on test items secured to a two-wheeled trailer are generally more severe than data recorded on items secured in other wheeled vehicles. In this case, primarily because of data from the 2-inch washboard course, the vertical data from the loose cargo on the M813 truck were higher than that on the trailer. This, coupled with the longer exposure time based on the real world scenario (para 2), led to the elimination of M101 trailer data from further analysis.

4.3.3 M548 track laying vehicle.

Data from the paved road operation were used to characterize the loose cargo environment for the M548. Because of the presence of speed-related periodics, the data were segregated by speed rather than overlayed. A typical vertical PSD is displayed in Figure 3. After examining PSDs generated from the package tester, it was obvious that the package tester does not simulate track laying vehicle transportation, and any further attempts at comparisons were abandoned. Many cargo schedules from track laying vehicles already exist to provide fatigue data, and chafing type damage can be accomplished using the M813 truck procedure.

4.4 PACKAGE TESTER

The PSD for each axis for each of the different configurations tested became the test schedule for that condition (i.e., no overlays were performed). Based on visual observations and the need for readjustment of the signal conditioning packages to prevent clipping, it was determined that operation in the asynchronous mode was much more severe than in any of the synchronous modes. It was also determined that operation on a steel-covered bed was less severe than operation on a plywood-covered bed (also previously reported in a previous study).

5. TEST EQUIVALENCE DETERMINATION

When the schedules for the M813 were first developed using the procedures discussed in reference 5, it was determined that the schedule for the truck was higher

than that for operation on the package tester--which seemed unreasonable based on visual observations and examination of rms acceleration levels. The comparison which had yielded that determination had been made by computing a pseudo transfer function (app A) between the truck data and the package tester data.

The transfer function data between the M313 truck and the laboratory package tester were then recomputed using average spectra rather than average plus one standard deviation spectra as is the normal process in laboratory vibration schedule development. The effect was to produce reasonable correlation between laboratory and field data. The normal technique is done to build conservatism into a closely controlled test. This investigation was faced with the unique problem of equating two uncontrolled situations (laboratory and field) rather than tailoring a closed-loop system to duplicate a set of previously measured events. This situation arises due to the very nature of the transportation mode being examined. Since the motion of the items are largely unconstrained (except for the establishment of outer boundaries of travel), it is impossible to form a closed-loop control system such as exists with an item rigidly mounted to an electrodynamic shaker which is continuously controlled by some form (analog or digital) of a feedback system. It was decided to make the laboratory and field comparisons on averaged spectral data to reduce the effects of data scatter which were more predominant in the field environment than the laboratory environment (figure 4). In addition to the field data run shown, data from runs on two other courses were blended with the run shown, further increasing the scatter of data.

As an aid to choosing a reasonable laboratory test, the pseudo transfer functions between the field data (input) and the laboratory data (response) were averaged over equivalent frequency bands (Table 6). The average and standard deviation of the equivalent average values were then computed to determine the average magnitude and the scatter of the transfer function.

The data from the various laboratory test conditions were then analyzed to select a condition which provided some acceleration amplification over the field data (to provide test item compression) without amplifying the data by more than a factor of 2 (a general rule of test level exaggeration) and which exhibited minimum scatter in the transfer function as a function of frequency. Another criterion was that the spectral distribution of energy be similar for the laboratory and field data. The appropriate spectral densities (PSDs) were cumulatively integrated in 50-Hz increments from 0 to 500 Hz, and the percent of the total rms level of the signal (based on 100% at 500 Hz) was calculated. The test condition of a plywood-covered bed operated in the synchronous mode at 300 rpm was chosen as the condition which best fit the above criteria (vertical only shown in figure 5-6). The values of the computed transfer functions in each of the three axes (from the same test, i.e., simultaneously) are listed in Table 7.

The two primary axes of vibration, vertical and longitudinal, have essentially identical average transfer function values which means that, on the average (for all frequencies from 2 to 500 Hz), the package tester amplifies the field data the same amount in these two axes simultaneously. The transverse axis has a transfer function reasonably close to the other two axes. By using the average value of the transfer function for use in test time compression, the result is a slightly longer test than is necessary in the vertical and longitudinal axes and a slightly shorter test than is necessary in the transverse axis.

Based on information acquired from the literature search, the test scenario to be simulated is 150 miles of transportation -- of which 65%, or 98 miles is over terrain represented by the Munson test courses utilized. At an average speed of 18.6 mph, the "real world" exposure time is 5.27 hours. Using an average transfer function value of 1.3,² the average ratio of PSD levels is (1.3)² or 1.69 (see app A).

Using the accepted equation for test time compression,

$$\left(\frac{W_2}{W_1}\right)^{\frac{B}{N}} = \frac{T_1}{T_2}$$

Where

$$\begin{aligned} W_1 &= \text{PSD Amplitude} \\ W_2 &= \text{Laboratory PSD Amplitude} \\ T_1 &= \text{Field Time} = 5.27 \text{ hours} \\ T_2 &= \text{Laboratory Time} = \text{Unknown} \\ B &= 9 \\ N &= 2.4 \end{aligned}$$

the value of $T_2 = 0.737$ hours = 45 minutes of laboratory test time. A test condition of a plywood-covered bed (as described in reference 6) operated in a synchronous mode at 300 rpm for 45 minutes should give a reasonable approximation of items being transported in a 5-ton truck for 150 miles.

To verify that the selected test did not overly stress the test item (i.e., have peak data greatly in excess of that experienced in the field even though the average data did not do so), time domain amplitude data were plotted using a "box plot" technique to show the amplitude distributions of the data. The results, shown (vertical only) in figure 7, indicate that the data distributions for field and laboratory data for each of the axes are reasonably similar.

Vertical acceleration amplitude distributions for the package tester methods at 300 rpm were plotted along with the wheeled vehicle distribution (figure 8) using the box plot technique to compare the amplitude distribution of the various methods. As can be seen from this figure, the plywood bed, sync mode best approximates the wheeled vehicle data, while operation on a steel bed would impose a slight undertest and asynchronous operation would impose a severe overtest on the item.

Since the motion of the test item is unconstrained (except to establish outer boundaries), the loose cargo test should be considered an inexact, uncontrolled test designed to uncover exterior problems (chafing, denting, etc.) in items transported in this manner and should not be used to determine transportation fatigue life on items. Well-controlled tests which are generally more severe (reference 1 and 6) have been established to accomplish this. It should be stressed that the equivalence developed was for a certain size and mass of loosely stored cargo. Other forms of cargo, such as loose rounds of ammunition may behave differently, but, because of the intended use of this test, it is considered adequate to cover all cargo configurations.

The proposed test technique is compared to existing test procedures in Table 8. Note that the proposed procedure does not represent a radical departure from existing procedures and, in terms of severity, is bounded by the existing procedures.

6. LOOSE CARGO VIBRATION SCHEDULES

Because the purpose of this investigation was to produce laboratory vibration schedules, these were developed for each of the three axes for the 5-ton truck and the two-wheeled trailer using the standard procedures (overlays of the average plus one standard deviation spectra) detailed in reference 5. The test times were scaled with an exaggeration factor derived from the previous equation to produce a reasonable test time. The values used are tabulated in Table 9.

The resultant schedules are presented graphically (vertical only shown) in Figures 9 and 10. Note that the schedules are based on motion of the cargo specimen, not the vehicle frame or bed.

It would be difficult, if not impossible, to control an electrodynamic shaker using a control source not directly connected to the shaker. It would be possible to run the test by rigidly mounting the test specimen to the shaker table and running the schedule like any other test schedule. There are two major problems with this approach which disqualify its use. First, the amplitude distribution of the laboratory test data would most likely not duplicate the field distribution of the data and would definitely not duplicate the distribution if a 3-sigma clipping control scheme were invoked. Secondly, while test item fatigue would theoretically be duplicated, the other affects of loose cargo transportation (chafing, impact damage) would not be duplicated.

Even though the loose cargo environment and the associated test schedules are severe, there are existing laboratory schedules that are equally or more severe. Comparisons of the loose cargo schedules for each vehicle and each axis with an appropriate existing test schedule (reference 6) are shown graphically (vertical only) in Figures 11 and 12. Note that in some cases the loose cargo test schedule has been altered from the previously presented schedule by use of a different exaggeration factor to match the standard schedule test time (reference 11). The comparisons are also summarized in Table 10.

Although the loose cargo schedules exceeded the existing schedules in severity at some frequencies, particularly in the range of 10 to 75 Hz, the overall severity (as measured by the rms value) of each of the

selected existing schedules was more severe than that of the corresponding loose cargo schedule. This indicates that rigidly securing a specimen to a shaker and then running the loose cargo schedule would serve no purpose. This point is further strengthened when it is considered that the conservatism built into the loose cargo schedule by addition of the spectral standard deviation of the data is higher than that for secured cargo because of the presence of shocks in the data which increase the deviation.

Because of the increased computational effort involved in developing a schedule for track laying vehicles, a test schedule was not developed for the M548. The rms acceleration values of average plus one standard deviation spectra were combined over the speed ranges used in compilation of the existing M548 schedules (reference 11) and were exaggerated to simulate the existing test time. The results are tabulated in Table 11.

Although the package tester does not duplicate the track laying vehicle environment, the fatigue characteristics are exceeded by existing schedules, and the abrasion and impact damage can be addressed by running the test derived in paragraph 5.

7. CONCLUSIONS

It is concluded that:

a. Operation on a package tester with a plywood-covered bed (as described in reference 6) at 300 rpm for 45 minutes provides a reasonable simulation of the loose cargo transportation environment (all three axes simultaneously) of ammunition boxes in a wheeled vehicle or two-wheeled trailer.

b. The loosely stowed cargo test conducted on a package tester is an inexact, uncontrolled test which should be conducted to determine external damage to the test item and should not be used as a substitute for a well-controlled laboratory secured-cargo test such as defined in references 1 and 6.

c. Operation on a package tester with a steel-covered bed in a synchronous mode is an undertest, and operation with a plywood-covered bed in an asynchronous mode is an overtest.

d. The package tester does not simulate the track laying environment.

8. FUTURE EFFORTS

Future work of a limited nature will be conducted to determine the effect of location and orientation of the test item on the package tester and the effects of various types of retainer fences. Loose cargo

transport of unpackaged items such as loose rounds of ammunition will also be studied.

REFERENCES

1. MIL-STD-810D, Environmental Test Methods and Engineering Guidelines, 19 July 1983.
2. Bendat, Julius S., and Piersol, Allan G. Random Data: Analysis and Measurement Procedures, Wiley-Interscience, 1971.
3. Curtis, Allen J., Tinling, Nicholas G., and Abstein, Henry T. Jr., Selection and Performance of Vibration Tests. Shock and Vibration Information Center, SVN-8, 1971.
4. Harris, Cyril M. and Crede, Charles E., Shock and Vibration Handbook, Second Edition: McGraw-Hill, 1976.
5. Connon, William H. III, Automated Vibration Schedule Development for Wheeled and Tracked Vehicles at Aberdeen Proving Ground, Institute of Environmental Sciences, 1983 Proceedings.
6. TECOM ITOP 1-2-601, Laboratory Vibration Schedules, 11 March 1985.
7. Defense Standard 07-55, Environmental Testing of Service Materiel, Ministry of Defense, London, 10 February 1975.
8. L.A.B. Corporation, Institute Manual for L.A.B. Vibration Transportation Simulators, July 1968.
9. Strayer, R. M. Vibrations in Road Vehicles.
10. MIL-STD-810C, Environmental Test Methods, 10 March 1975.
11. Soci, Darrell F., Fatigue Life Estimation Techniques, Technical Report 145, Electro General Corp., Minnetonka, MN, 1981.
12. TECOM TOP 4-2-602, Rough Handling Tests, 1 April 1979.

APPENDIX A
COMPUTATION OF A PSEUDO TRANSFER FUNCTION

It is obvious that a true transfer function can only be calculated from events which are recorded simultaneously. However, for this investigation, it was necessary to compare separate events (non-simultaneous) as a function of frequency. A description of the technique follows.

Let G_{xx} = input power spectrum

G_{yy} = response power spectrum

G_{xy} = cross power spectrum

TF_a = transfer function computed by "CSTA Method"

TF_c = transfer function computed by classical method

CSTA Method

Classical Method

$$TF_a = \frac{G_{xy}}{G_{xx}}$$

$$TF_c = \frac{G_{xy}}{G_{xx}}$$

Coherence function

$$\gamma_{xy}^2 = \frac{G_{xy}^2}{G_{xx} G_{yy}}$$

for a "perfect" transfer function $\gamma_{xy}^2 = 1$ thus $G_{xy} = G_{xx} G_{yy}$

Compute the squares of the above function

$$TF_c^2 = \frac{G_{xy}^2}{G_{xx}^2} = \frac{G_{xx} G_{yy}}{G_{xx}^2} = \frac{G_{yy}}{G_{xx}}$$

Thus $TF_a = TF_c^2$ thus computing the square of the transfer function

Therefore compute new $TF_a = (TF_a)^{1/2}$

$$TF_a = \left[\frac{G_{xy}}{G_{xx}} \right]^{1/2} = TF_c$$

assume that coherence function is some value less than 1 = η

$$\gamma_{xy}^2 = \eta = \frac{G_{xy}^2}{G_{xx} G_{yy}} \quad , \quad G_{xy} = \eta (G_{xx} G_{yy})$$

$$T_c = \frac{G_{YY}}{G_{XX}} = \frac{(G_{XX} G_{YY})}{G_{XX}}^{1/2}, \quad T_c^2 = \frac{G_{YY}}{G_{XX}} = \frac{G_{YY}}{G_{XX}^2}$$

$$T_a = \frac{G_{YY}}{G_{XX}}^{1/2}, \quad T_a^2 = \frac{G_{YY}}{G_{XX}}$$

$$\frac{T_a^2}{T_c^2} = \left[\frac{T_a}{T_c} \right]^2 = \frac{\frac{G_{YY}}{G_{XX}}}{\frac{G_{YY}}{G_{XX}^2}} = \frac{1}{2}$$

$$\text{ratio } \frac{T_a}{T_c} = \sqrt{\frac{1}{2}}$$

Value of Coherence Function	Ratio of CSTA function to classical function
1	1
0.9	1.05
0.8	1.12
0.7	1.20
0.6	1.29
0.5	1.41
0.4	1.58
0.3	1.83
0.2	2.24
0.1	3.15

TABLE 1. TEST COURSES AND SPEEDS

<u>Vehicle</u>	<u>Course</u>	<u>Speed, mph</u>
M813 3-ton truck and M101 trailer	Belgian block	20, 25
	Spaced bump	15, 20
	2-inch washboard	8, 10
	Cross-country 3	10, 15, 20
M548	Cross-country 3	10, 15, 20
	Paved road	8 to 30 in 2 mph increments

TABLE 2. PACKAGE TESTER MODES

<u>Mode</u>	<u>Speed, FPM</u>	<u>Phase, deg</u>	<u>Bed</u>	<u>No. Package</u>	<u>Package Direction^a</u>	<u>Applicable Document</u>
Synchronous	284	0	Plywood	1	Longitudinal	MIL-STD-810C
Synchronous	284	0	Plywood	1	Transverse	MIL-STD-810C
Synchronous	300	0	Plywood	1	Longitudinal	MIL-STD-810D
Synchronous	300	0	Plywood	1	Transverse	MIL-STD-810D
Synchronous	284	30	Plywood	1	Longitudinal	None
Synchronous	284	30	Plywood	1	Transverse	None
Synchronous	300	30	Plywood	1	Longitudinal	None
Synchronous	300	30	Plywood	1	Transverse	None
Asynchronous	284	Random	Plywood	1	Longitudinal	DEF-STAN07-55
Asynchronous	284	Random	Plywood	1	Transverse	DEF-STAN07-55
Asynchronous	300	Random	Plywood	1	Longitudinal	None
Asynchronous	300	Random	Plywood	1	Transverse	None
Synchronous	284	0	Steel	1	Longitudinal	None
Synchronous	284	0	Steel	1	Transverse	None
Synchronous	300	0	Steel	1	Longitudinal	TOP-4-2-602
Synchronous	300	0	Steel	1	Transverse	TOP-4-2-602
Synchronous	284	0	Steel	2	Longitudinal	None
Synchronous	284	0	Steel	2	Transverse	None
Synchronous	300	0	Steel	2	Longitudinal	TOP-4-2-602, MIL-STD-810D
Synchronous	300	0	Steel	2	Transverse	TOP-4-2-602, MIL-STD-810D

^aThe direction refers to the direction of the instrumented beams which were perpendicular to the long axis of the ammunition box.

TABLE 3. OFF-CENTER DISTANCES

<u>Ind.</u>	<u>Package Direction</u>	<u>Distance, in.</u>
Wood	Longitudinal	33 1/2
Wood	Transverse	16 1/2
Steel	Longitudinal	14 1/2
Steel	Transverse	31 1/2

TABLE 4. CRITICAL SPEEDS FOR M813

<u>Course</u>	<u>Speed, mph</u>
Belgian block	25
Spaced bump	20
2-inch washboard	8

TABLE 5. COURSE DATA

<u>Course</u>	<u>Length, ft.</u>	<u>Speed, mph</u>	<u>Time, min</u>	<u>Weighting Factor</u>
Belgian block	3946	25	1.791	4
2-inch washboard	820	8	1.167	3
Spaced bump	764	20	0.434	1
<u>Average weighted</u>			<u>18.6</u>	

TABLE 6. TRANSFER FUNCTION INTEGRATION BANDS

Band No.	Frequency Range, Hz	Center Frequency, Hz
1	2 to 10	6
2	2 to 50	26
3	50 to 100	75
4	100 to 150	125
5	150 to 200	175
6	200 to 250	225
7	250 to 300	275
8	300 to 350	325
9	350 to 400	375
10	400 to 450	425
11	450 to 500	475

TABLE 7. AVERAGE VALUE OF TRANSFER FUNCTIONS, WOOD
TABLE SYNC MODE 300 RPM SPECTRA/WHEELED
VEHICLE SPECTRA

Axis	Value	Deviation From Average, %
Vert	1.40	+ 7.7
Trans	1.09	-16.1
Long	1.41	+ 8.3
Average	1.30	

TABLE 8. COMPARISON OF TEST PROCEDURES

Document	Mode	Bed	RPM	No. of Items	Time, hr.
TOP 4-2-602	Sync	Steel	300	Any number	0.5
MIL-STD-810C	Sync	Plywood	284	1	3
MIL-STD-810D	Sync	Steel	300	Several	0.5
MIL-STD-810D	Sync	Plywood	300	1	3
DEF STAN 07-55	Sync	Plywood	285	1 or more	1, 0.25, .083
Proposed	Sync	Plywood	300	1	0.75

TABLE 9. EXAGGERATION FACTORS

<u>Vehicle</u>	<u>Real World Exposure Time, hr</u>	<u>Test Time, hr</u>	<u>Exaggeration Factor</u>
M813 truck	5.27	2	1.295
M101 trailer	1.31	1.31	1.000

TABLE 10. TEST SCHEDULE COMPARISON

<u>Vehicle</u>	<u>Axis</u>	<u>Standard Schedule (ref 13)</u>	<u>Loose Cargo Real Time, hr</u>	<u>Test Time Standard hr</u>	<u>Exaggeration Factor (loose Cargo)</u>
M813 truck	Vert	Two-wheeled trailer, vertical	5.27	1.6	1.374
	Trans	Comp wheeled vehicle, transverse	5.27	2	1.295
	Long.	Two-wheeled trailer, longitudinal	5.27	1.6	1.374
M101 trailer	Vert	Two-wheeled trailer, vertical	1.31	1.6	*1.0
	Trans	Comp wheeled vehicle, transverse	1.31	2	*1.0
	Long.	Two-wheeled trailer, longitudinal	1.31	1.6	*1.0

^aNote that the existing test time (standard) is longer than the loose cargo real time. An exaggeration factor of 0.948 could have been used but was unnecessary since the existing schedules were more than the loose cargo schedules.

TABLE II. HS48 TEST SCHEDULE COMPARISON

<u>Axis</u>	<u>Test Phase</u>	<u>Real Time, min</u>	<u>Test Time, min</u>	<u>Exaggeration Factor^a</u>	<u>Loose Cargo rms</u>	<u>Test rms</u>
Vertical	V01	0.96	12	0.387	0.43	1.30
	V02	0.96	12	0.387	0.50	1.27
	V03	0.96	12	0.387	0.54	2.36
	V04	0.96	12	0.387	0.71	2.52
	V05	0.96	12	0.387	0.67	3.03
Transverse	T01	0.96	12	0.387	0.26	1.04
	T02	0.96	12	0.387	0.37	1.01
	T03	0.96	12	0.387	0.55	1.76
	T04	0.96	12	0.387	0.58	2.20
	T05	0.96	12	0.387	0.63	2.50
Longitudinal	L01	0.96	12	0.387	0.25	1.19
	L02	0.96	12	0.387	0.37	0.78
	L03	0.96	12	0.387	0.45	1.77
	L04	0.96	12	0.387	0.59	1.99
	L05	0.96	12	0.387	0.57	2.45

^aThe exaggeration factor shown is the square root of the calculated value to account for operating on the rms value than the PSD value.

LOOSE CARGO ON M813 VERTICAL

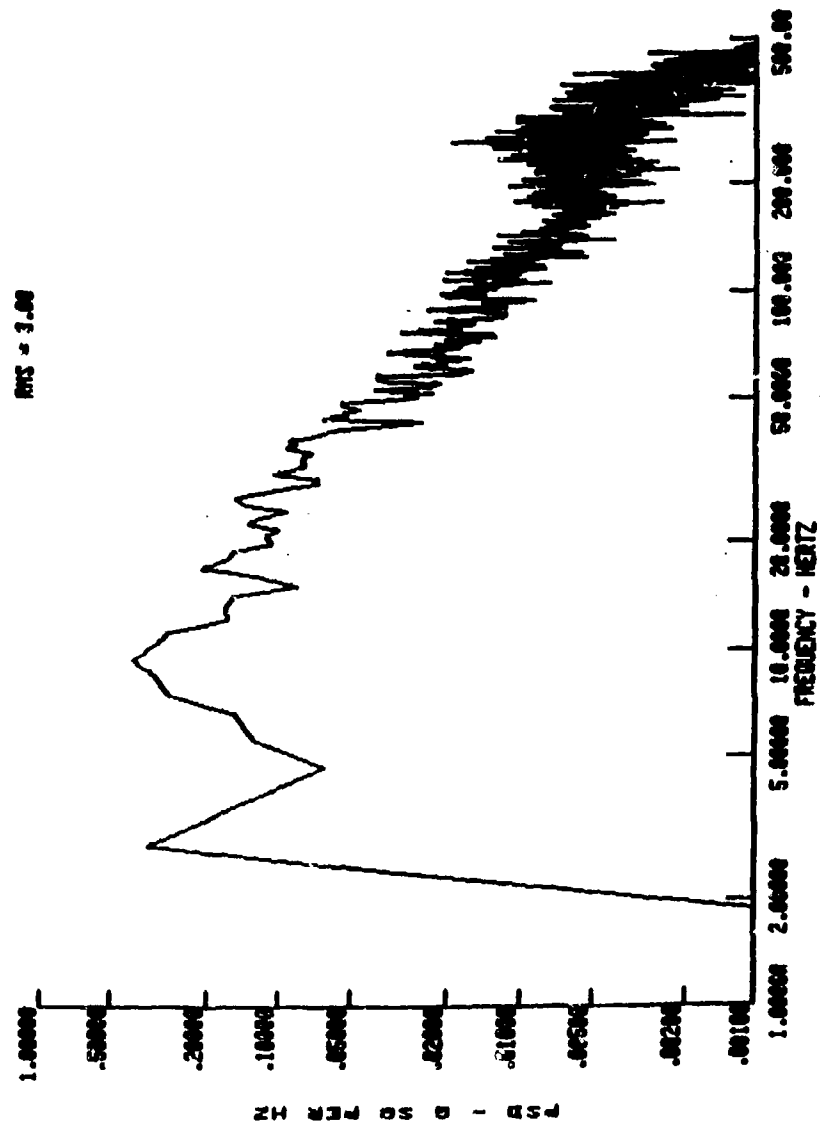


Figure 1

LOOSE CARGO ON M101 VERT

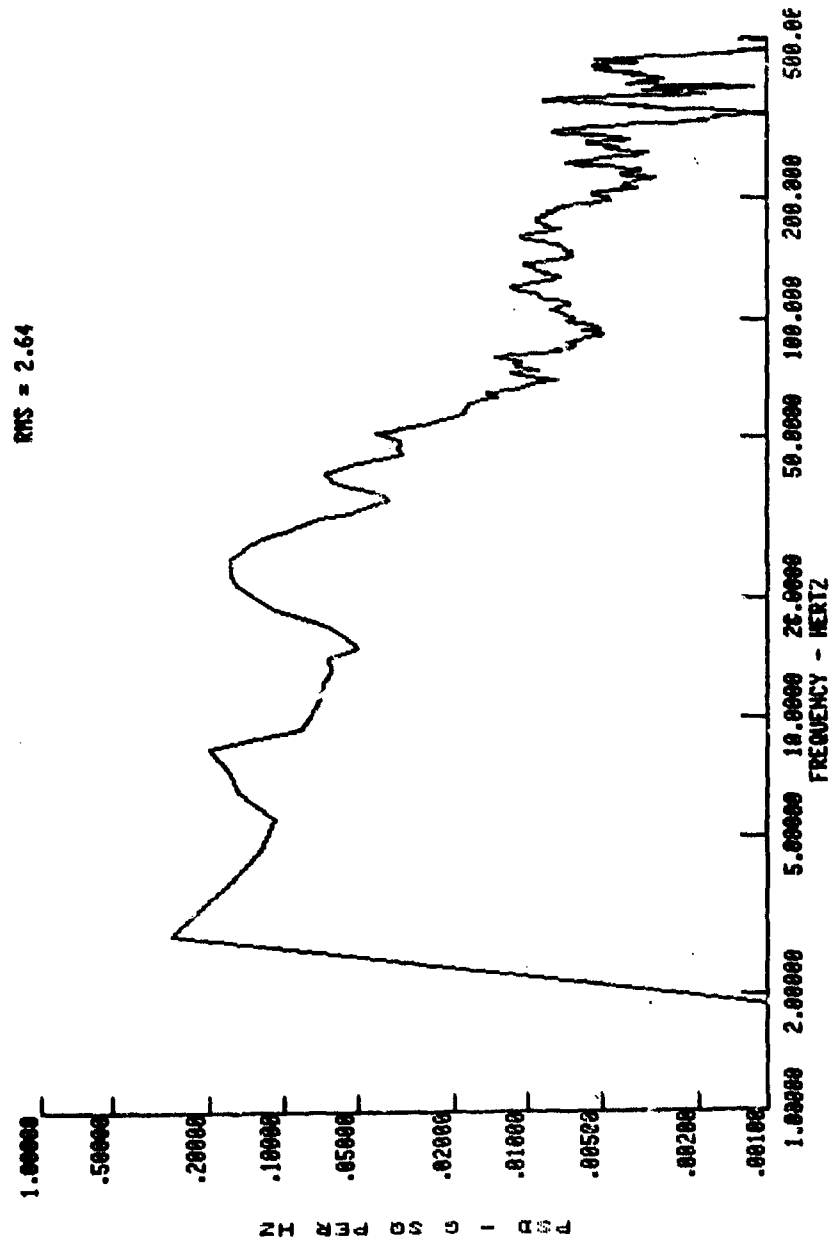


Figure 2

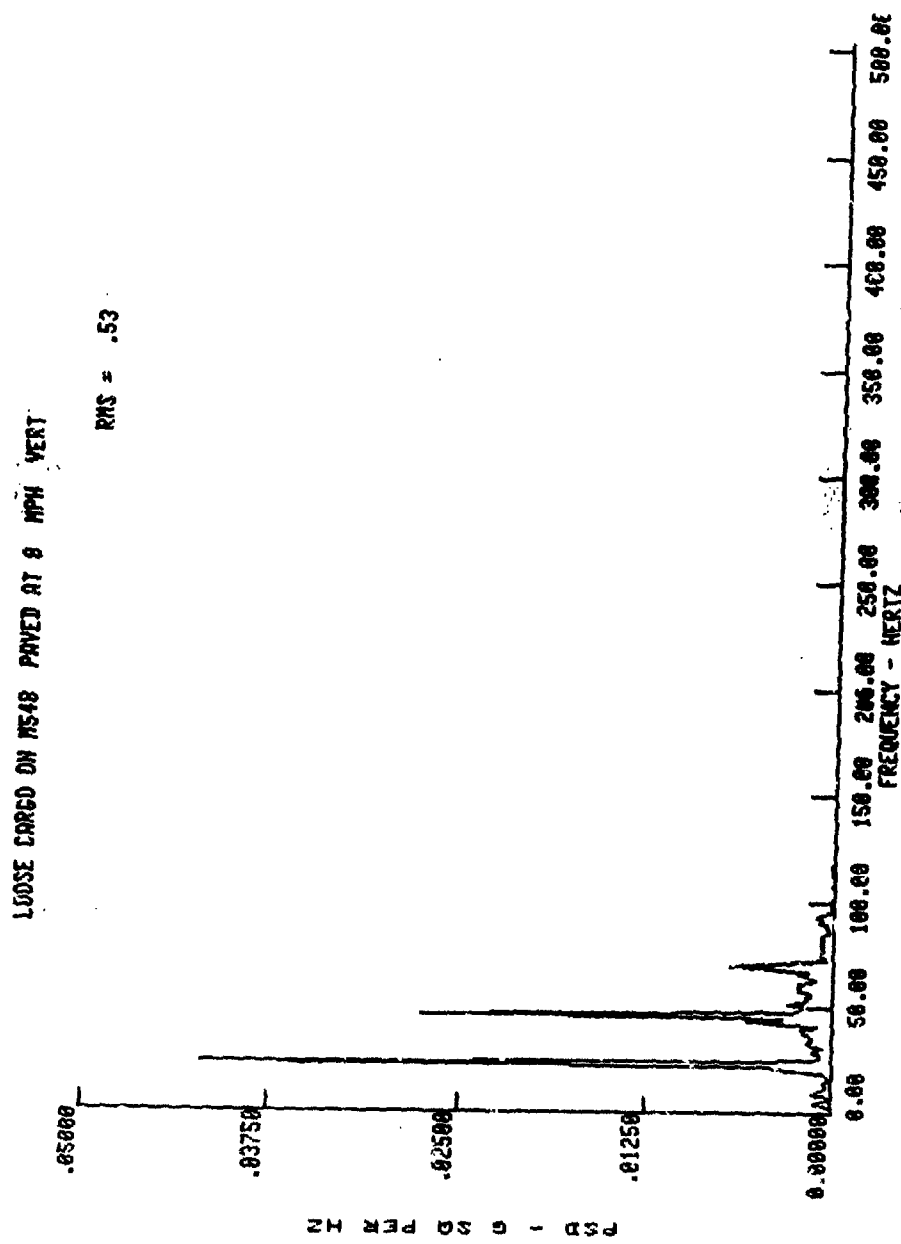


Figure 3

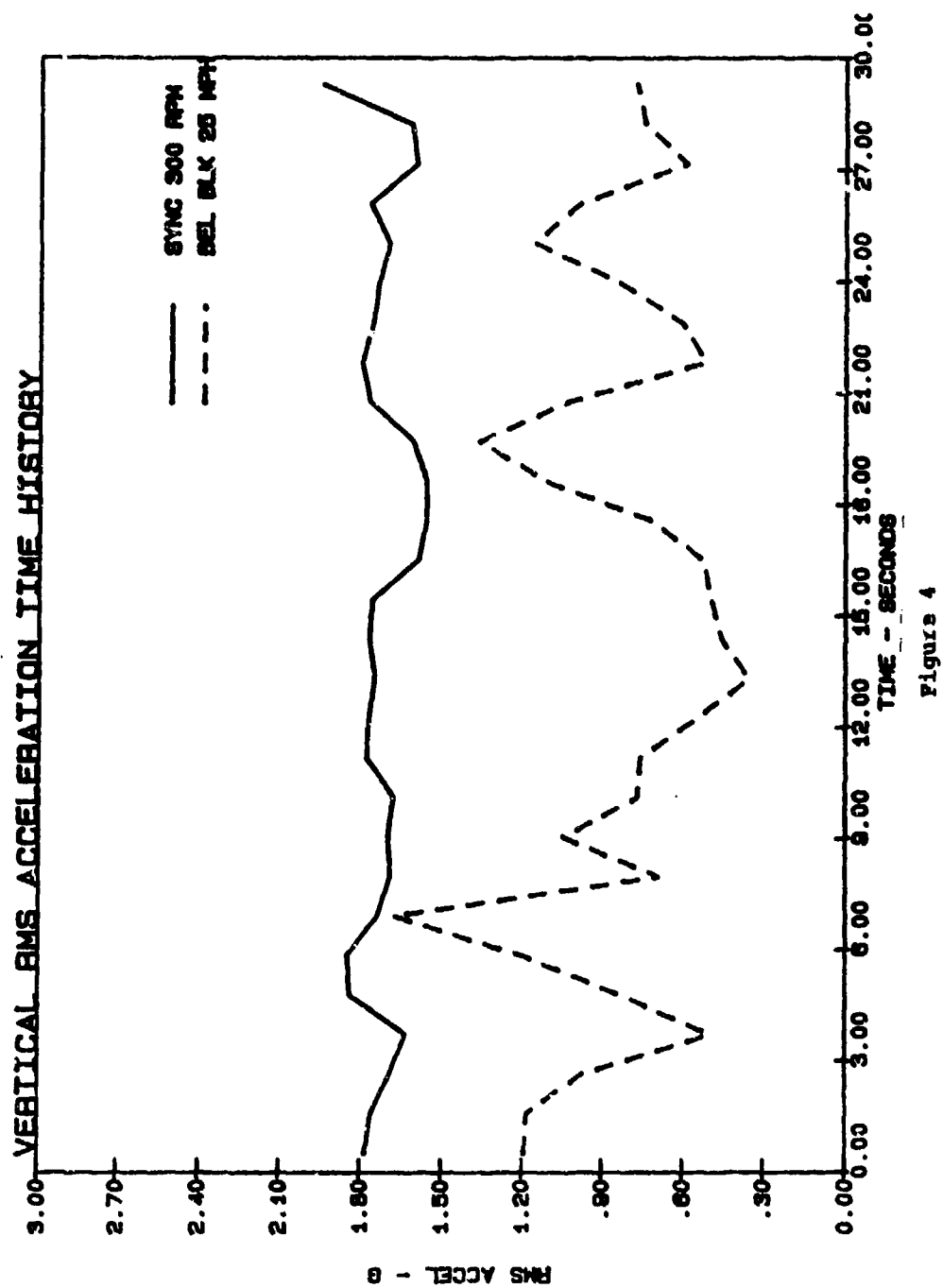


Figure 4

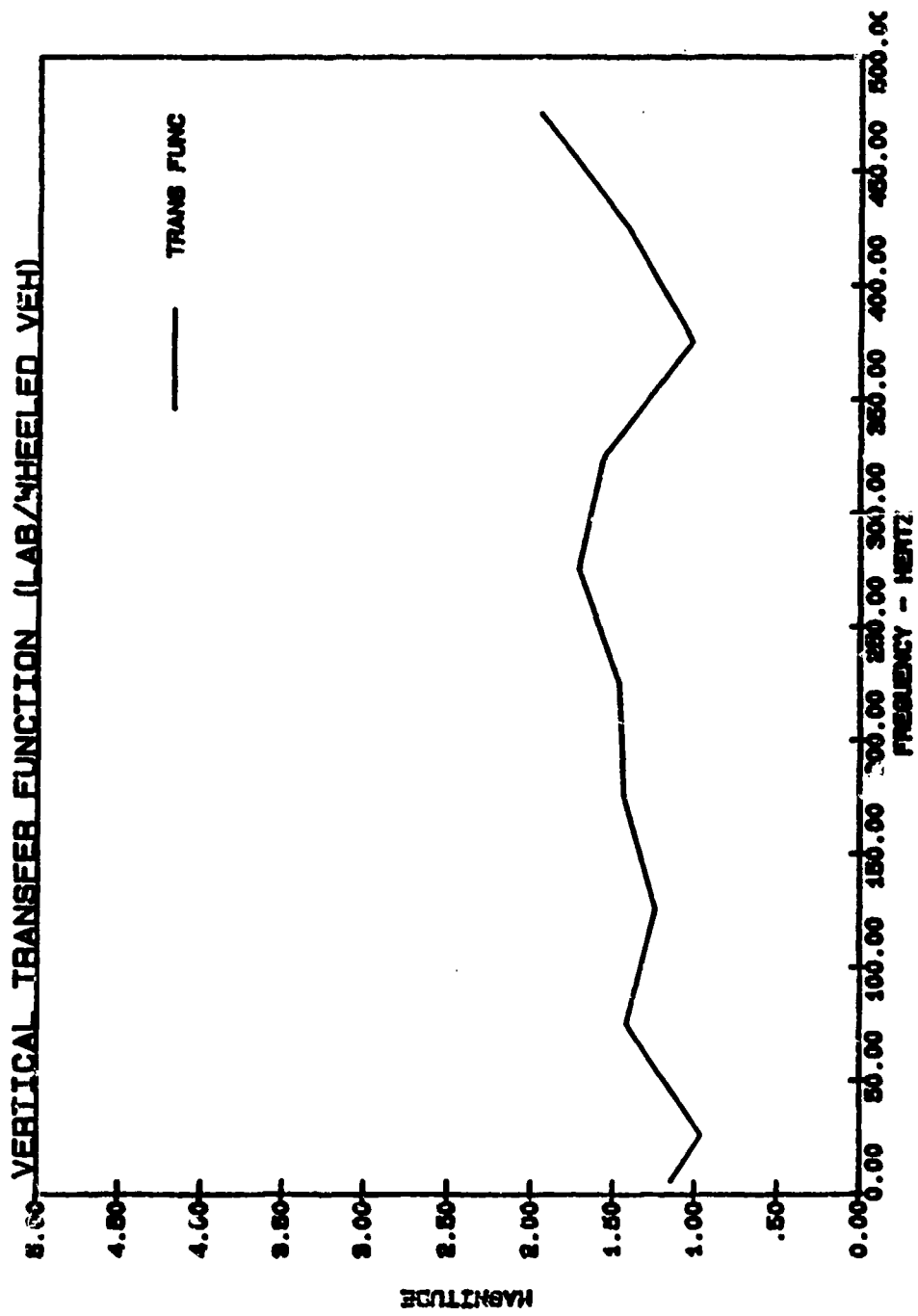


Figure 5

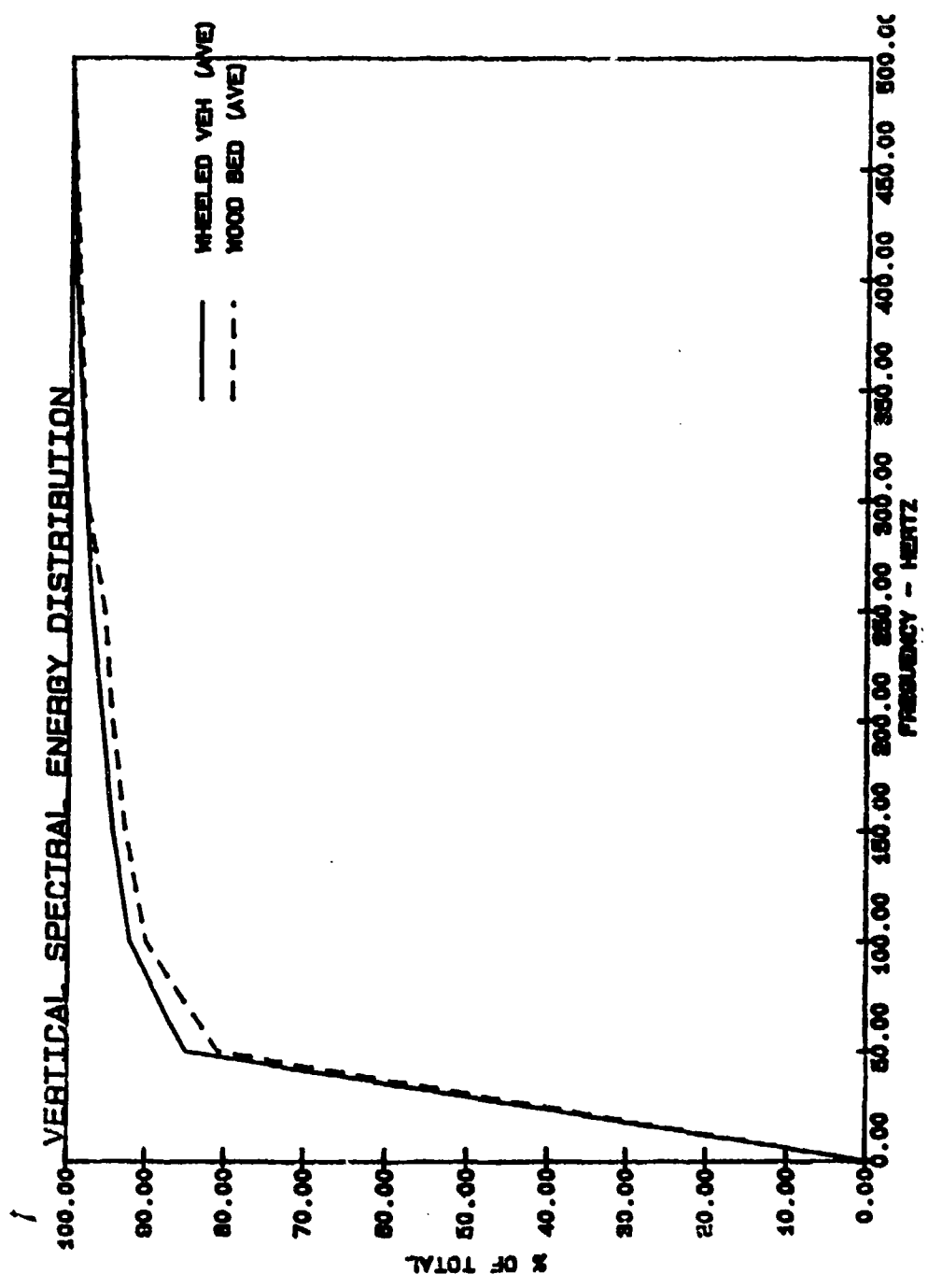


Figure 6

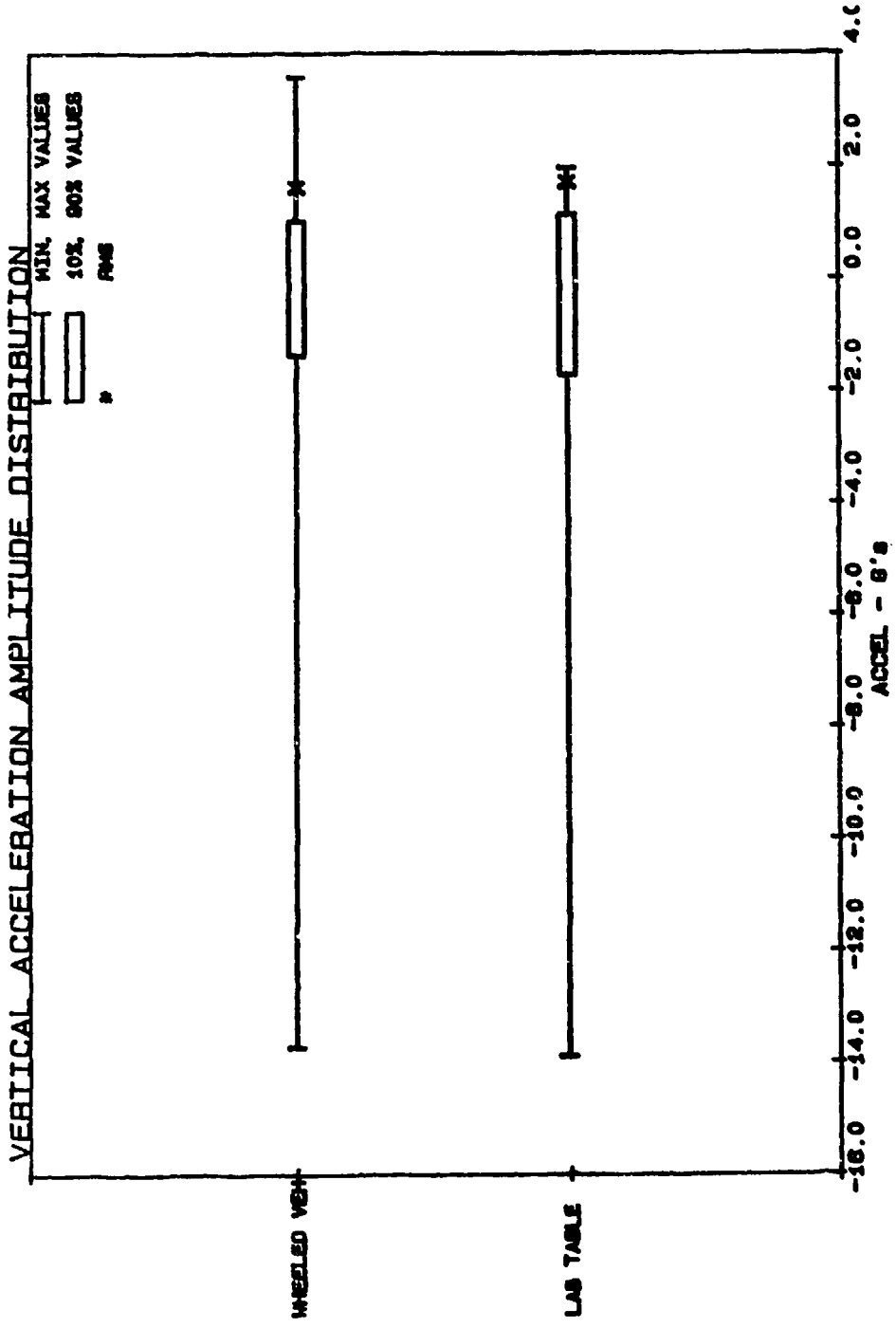


Figure 7

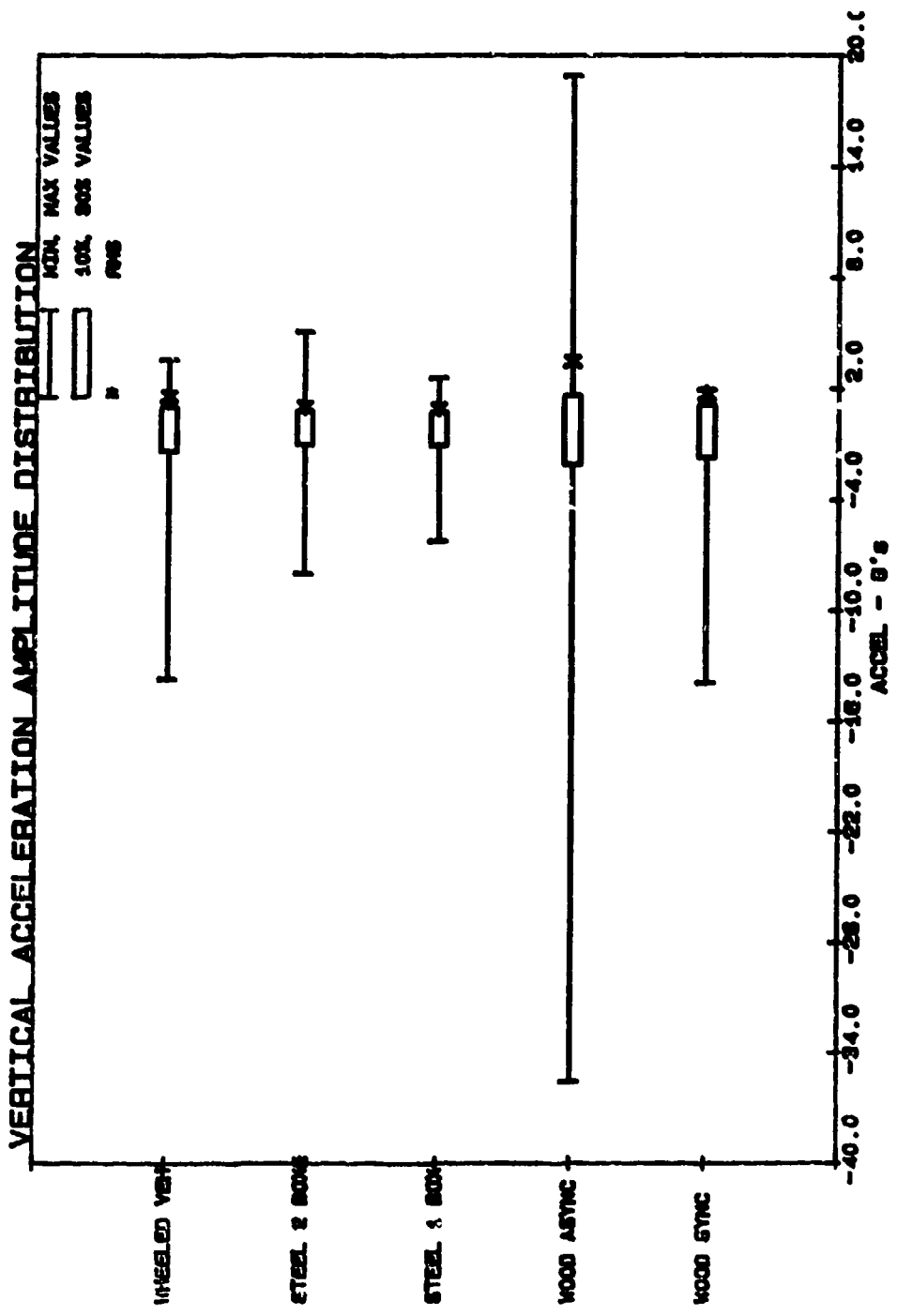


Figure 8

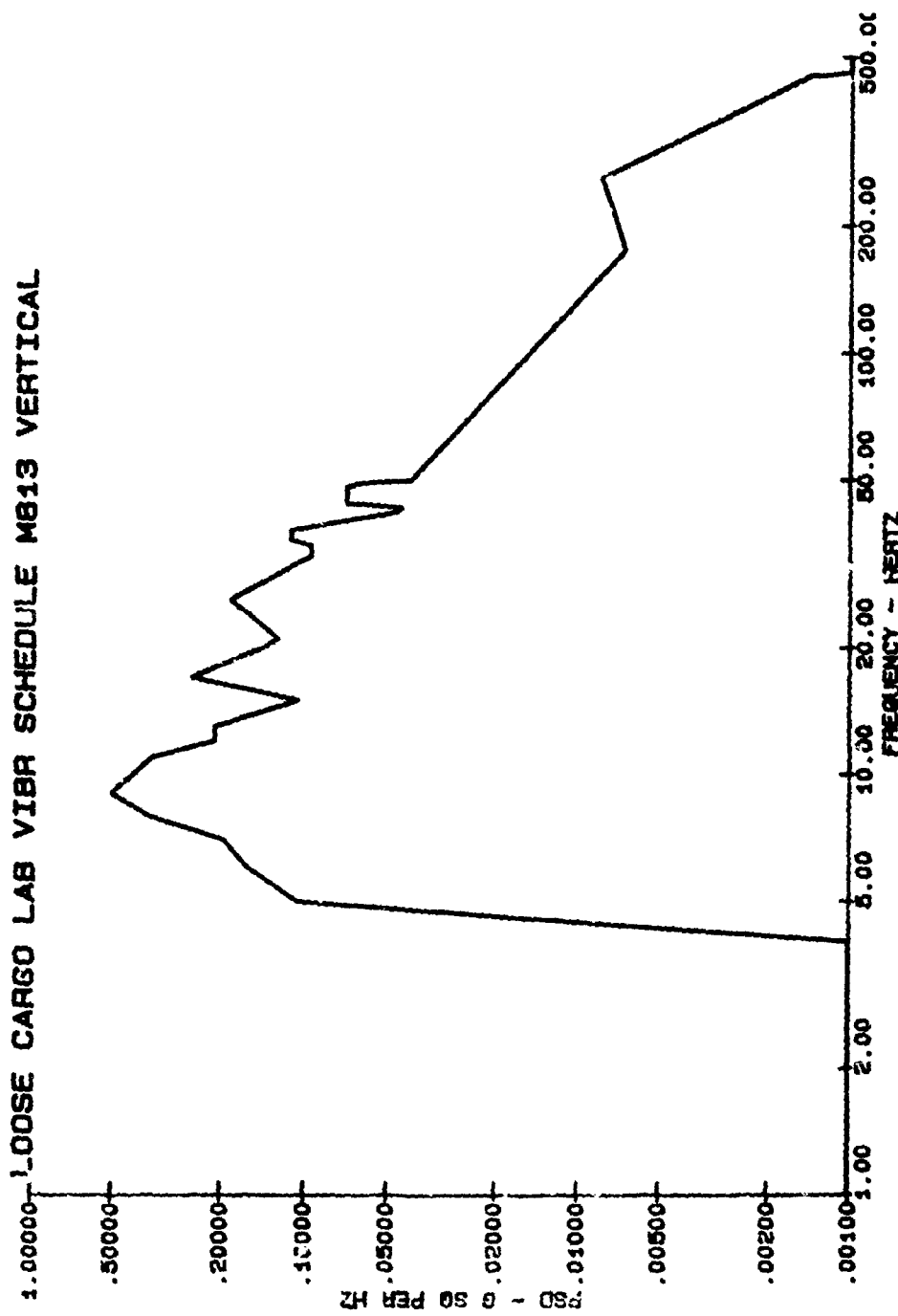


Figure 9

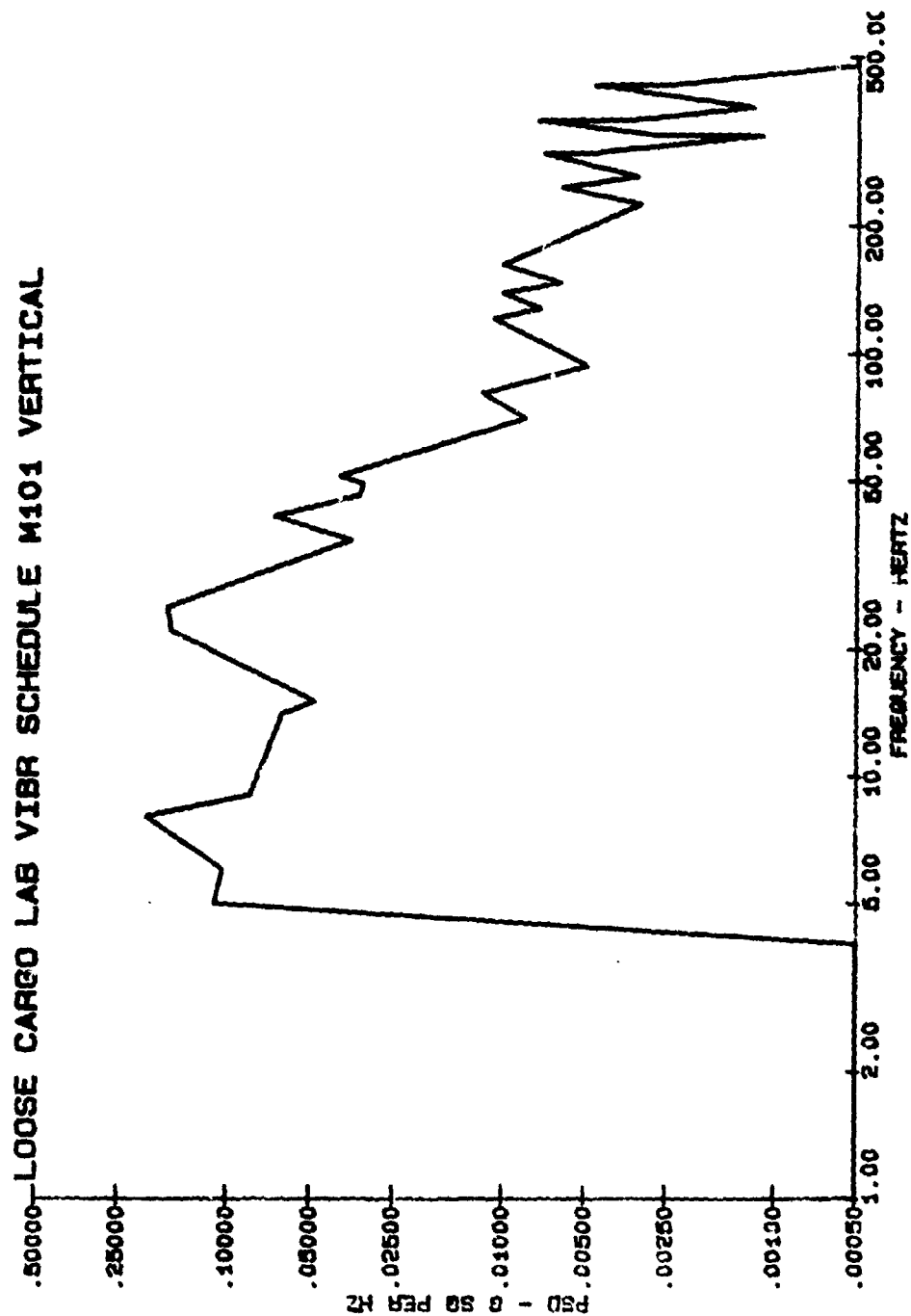


Figure 10

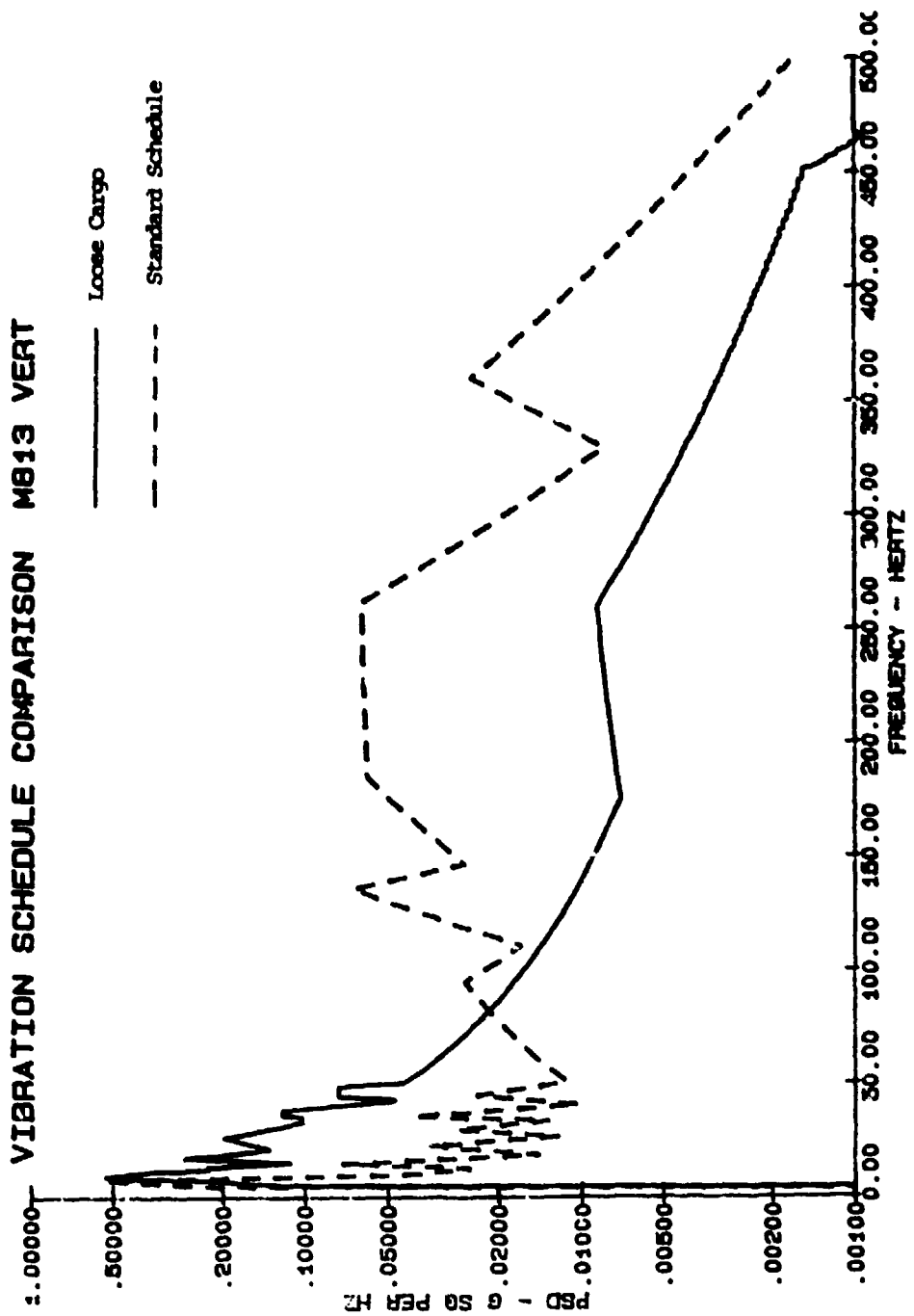


Figure 11

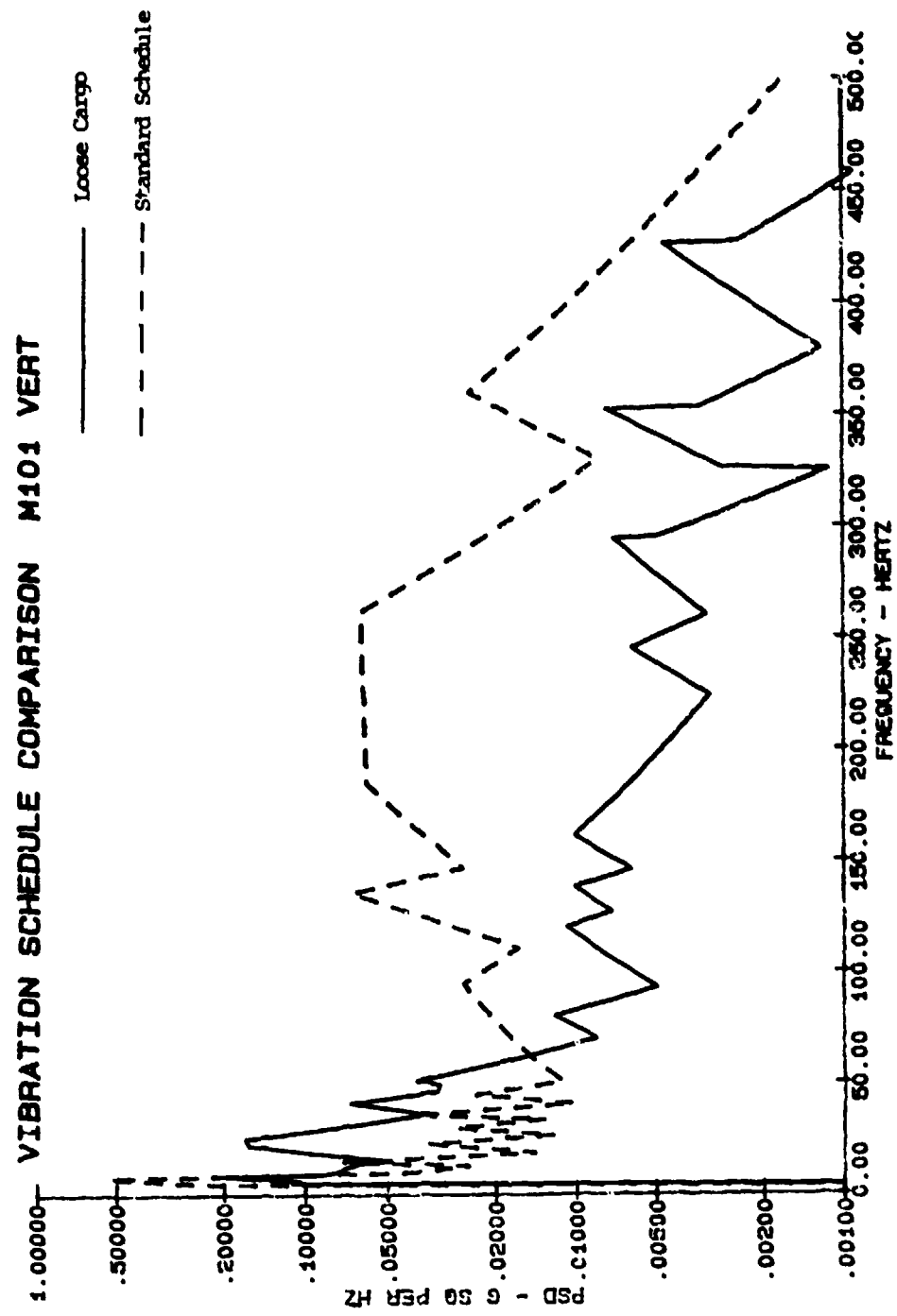


Figure 12

ANALYSIS OF SHOCK AND VIBRATION ENVIRONMENTS
FOR CARGO ON C9B TRANSPORT AIRCRAFT*

Thomas J. Baia
James W. Doggett
Clarence A. Davidson

Sandia National Laboratories
Albuquerque, New Mexico

The definition of shock and vibration environments on the floor of cargo aircraft is of prime interest to designers of hardware which must be transported on these planes and helicopters. The DOE/DOD Environmental Data Bank at Sandia National Laboratories maintains an extensive collection of environmental definitions for aircraft. This paper describes the process involved in acquiring and analyzing shock and vibration data, on the cargo floor of a C9B turbojet aircraft for incorporation into the DOE/DOD Environmental Data Bank. The dual objectives of this paper are to show the procedure by which the environmental definition is created and to compare the results with existing definitions of shock and vibration environments on fixed wing aircraft. Special emphasis is placed on instrumentation considerations which help ensure data integrity. The use of both piezoelectric and piezoresistive accelerometers at each monitor location, for example, reflects the requirement to select the proper transducer to measure either the shock or random vibration events of interest. Computerized data analysis techniques are described which greatly expedite the analysis of voluminous amounts of shock and vibration data stored on a computer data base system. Included in these analyses are auto-spectral density estimates, shock response spectra, and a relatively new shock characterization called the shock intensity spectrum. The resulting environmental definition for cargo transport on the C9B aircraft was significant because it revealed frequency ranges in which the C9B shock and vibration environments exceeded levels seen on other military transport aircraft. The techniques utilized in this analysis will be of great value to other engineers responsible for quantifying shock and vibration environments on cargo vehicles of all types.

INTRODUCTION

Definition of environmental loading conditions has always challenged engineers responsible for developing load-resistant structures. One type of dynamic environment of great practical concern results from the shock and vibration excitations imparted to cargo on military transport vehicles. Quantification of these dynamic loads can first be used by analysts to assess the effects of these inputs to a particular structure which is carried as cargo. The severity of the environment might even necessitate the development of a mechanical isolation system to protect the cargo from

damage. The definition of shock and vibration environments is also used to define dynamic test inputs to the cargo structure. Response measurements made on, or within, the structure serve to verify that the structure's dynamic response capability will not be exceeded in the operational environment. This paper describes the process of defining shock and vibration environments which is critical to adequate design and meaningful dynamic testing of structures. A description of the measurement, analysis, and interpretation of random vibration and shock dynamic field data will be given in the context of the study of shock and vibration environments on the cargo bay floor of the C9B turbojet aircraft.

* This work was performed at Sandia National Laboratories and supported by the U. S. Department of Energy under Contract Number DE-AC04-76DP00789.

DOE/DOD ENVIRONMENTAL DATA BANK

The analysis of shock and vibration environments on transport vehicles is carried out at Sandia National Laboratories as part of development engineering on equipment which must be qualified for transport on these carriers. The transport environment is only one of many environments for which Sandia has collected data. The data base is maintained in the DOE/DOD Environmental Data Bank (References 1 and 2). Measured data from both simulated and actual service conditions are continually being summarized and added to the Data Bank. A substantial amount of shock and vibration data from transport aircraft has been measured and analyzed by Sandia and others (References 3-6), and stored in the Data Bank. Since no shock or vibration data had previously been collected for the Data Bank on the C9B turbojet transport, Sandia undertook this effort with the cooperation of the U.S. Navy.

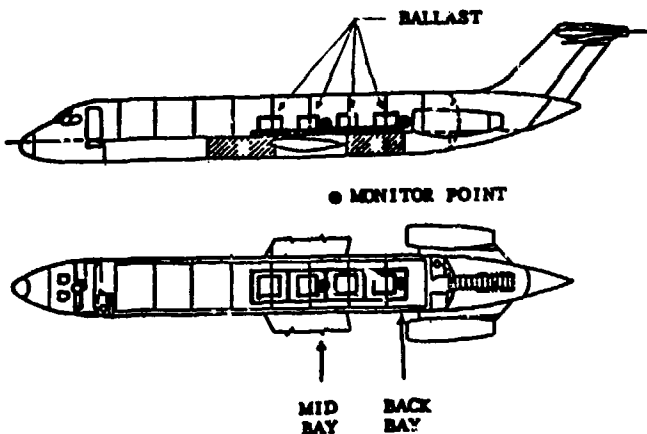


Figure 2. Instrumentation Locations on C9B Aircraft.

C9B DESCRIPTION

The C9B (Figure 1), manufactured by Douglas Aircraft Company, is a Model 200CF DC-9 Jet Transport designed for transportation of passengers or cargo. The aircraft is powered by two Pratt and Whitney JT8D-9 engines, each of which is capable of generating 14,500 pounds of thrust. The C9B utilizes the "Douglas" cargo loading system to permit easy loading and unloading of palletized cargo. Cargo is loaded in the main cabin on pallets and moved into position on belt and roller conveyors which are attached to the deck tracks. Restraint fittings and chains secured to the deck tracks hold the palletized cargo in place.



Figure 1
C9B Transport Aircraft

TEST PREPARATIONS

Careful planning of the C9B flight test measurements was undertaken by addressing the following topics:

1. OBJECTIVE
2. INSTRUMENTATION
3. DATA INTEGRITY
4. FLIGHT PLAN
5. TEST LOGISTICS

Significant details of these subjects are presented in the following discussion.

OBJECTIVE: The objective of the flight tests was to make acceleration measurements on the cargo floor of the C9B during taxi, takeoff, climb, cruise, and landing. Once the data were collected, the data would be analyzed to define shock and random vibration environments for cargo carried on the C9B.

INSTRUMENTATION: Figure 3 shows a schematic diagram of the measurement system. Knowledge that 60 Hz, 115 V AC power was available on the aircraft allowed the selection of a conventional 14 track FM instrumentation magnetic tape recorder for data gathering.

Since both shock and vibration data were desired, two different types of accelerometers were used to make the measurements. Vibration was measured with piezoelectric (PE) accelerometers. Piezoresistive (PR) gauges were used for shock measurements. The PE gauges allow measurement of random vibration data in the frequency range of interest, 10-2000 Hz. The insensitivity of a PE gauge to frequency content below 2 Hz is advantageous for random data spectral analysis where DC components of a random signal are normally removed. The PR gauges respond to frequencies from 0 Hz to 750 Hz, and are required to adequately transduce the low frequency content of the landing shock.

Three PR and three PE gauges were mounted at the mid and back cargo bay locations (see Figure 2). The accelerometers were oriented in the vertical (perpendicular to the cargo floor), longitudinal (along the axis of the fuselage), and transverse (perpendicular to the axis of the fuselage) axes of the aircraft.

Transducers were mounted on three faces of aluminum cubes which were attached with dental cement at the monitor points on the cargo bay

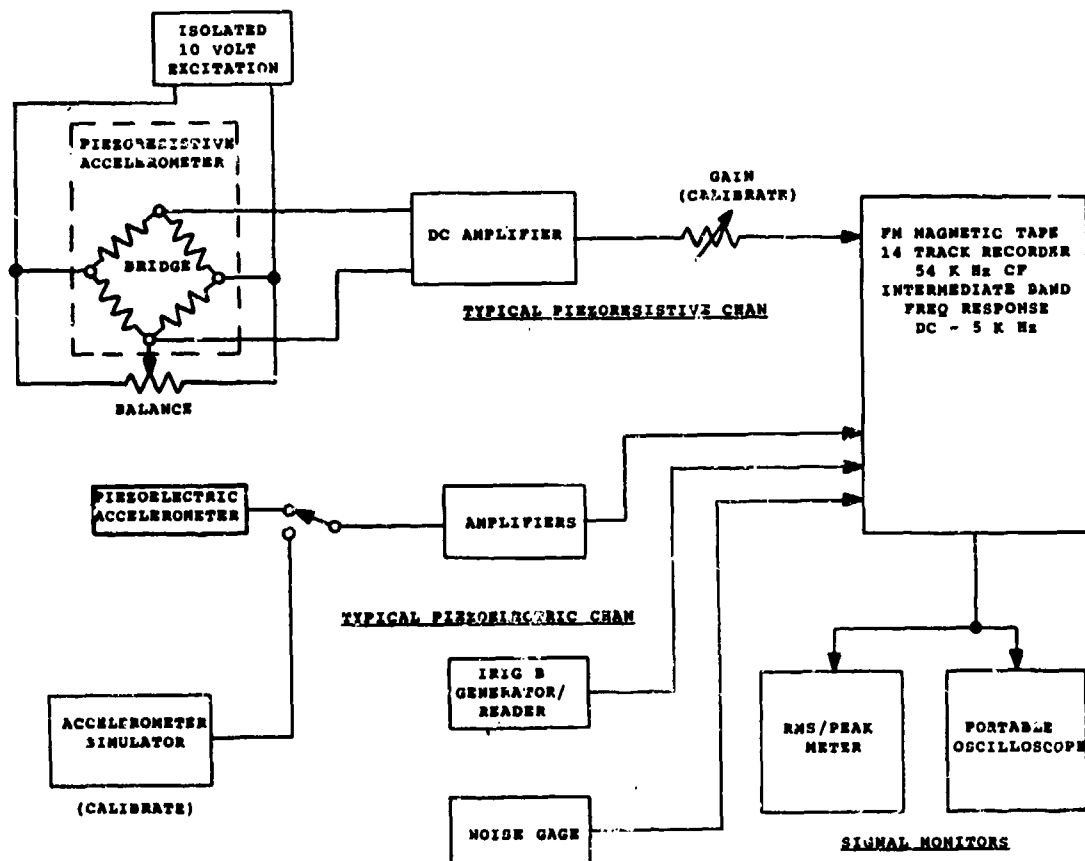


Figure 3. Measurement System Schematic Diagram.

floor. Bridge excitation for the piezoresistive elements and power for their complimentary amplifiers were supplied from a 28 V nickel-cadmium battery bank packaged in a metal case which also contained DC amplifiers and the IRIG generator/reader. The piezoelectric signal conditioners were conventional charge amplifiers with low impedance, normalized voltage outputs. Estimates of channel bandedge settings were made on the basis of flight tests on other aircraft. The entire measurement system was checked out prior to the flight by making accelerometer measurements of known inputs to an electro-dynamic shaker.

DATA INTEGRITY: Achieving data integrity entails practicing normal proficiency in setting up a measurement system, and also requires making a conscientious effort to recognize noise sources in the measurement system. In an effort to accomplish this noise characterization, two steps were taken. First, a noise gauge was included in the instrumentation system. (The noise gauge has a desensitized piezoelectric crystal so it does not transduce acceleration, but experiences the same sources of electrical noise as the active PE accelerometers.) In another effort to describe the noise sources on the active accelerometer channels in the measurement system, the output of the accelerometers was recorded while the plane was powered down and stationary. This set of measurements was useful in verifying that the signals recorded during flight were actually the result of the shock and vibration environments generated on the cargo floor of the C9B aircraft. The portable playback capability was included to allow immediate post-flight review of data to assure adequate signal strength and no clipping of output signals. If the data were not found to be satisfactory, the flight test could be repeated. The IRIG time generator was an important consideration since it allowed accurate recording of event times which would be needed to analyze and interpret the data.

FLIGHT PLAN: A flight test plan was developed to make sure that the flight included the same types of flight events which had been recorded during flight tests on other aircraft. The following data points were defined for the benefit of the pilot during the flight test and for data identification purposes during post test data analysis:

1. Taxi prior to takeoff
2. Full power engine runup prior to takeoff
3. Takeoff - prior to liftoff
4. Climb - gear down, flaps down
5. Climb - gear up, flaps down
6. Climb - gear up, flaps up
7. Climb - turbulence (if any)
8. Climb - to cruise altitude
9. Cruise
10. Descent - buffeting, spoilers down
11. Descent - landing gear down
12. Descent - gear down, flap down
13. Descent - touchdown

14. Touchdown, nose gear down
15. Landing - engines reverse thrust
16. Post-Landing Roll-out
17. Quiet Time

TEST LOGISTICS: Arrangements were made for the U.S. Navy to provide the crew and the C9B aircraft. All of the instrumentation was shipped to the test site. Approximately 1500 kg of ballast was prepared for palletized loading on the aircraft during the test.

TEST DESCRIPTION

The C9B aircraft was loaded with ~1500 kg of ballast which was divided between four standard plywood pallets and chained in place. The tape recorder, instruments, and signal cables were strapped or taped securely to the floor of the aircraft. Accelerometers were mounted at mid (above the landing gear) and aft cargo bay locations, adjacent to the base of the cargo (see Figure 2). All channels and instruments were interconnected and calibrated before packing and shipment to the site of flight operation, and calibrations were again verified just prior to flight takeoff. Just prior to a flight event change, the crew announced the upcoming change so the instruments could be made ready and the IRIG reading noted. To preserve tape time, the event was recorded only long enough to insure time for complete data analysis. Data channels were monitored during the recording using a portable oscilloscope.

Data were recorded during three flights of the C9B aircraft as indicated in more detail in Table 1. Quick-look data were reviewed after the first flight to verify that the data recording system was working properly. The second and third flights were primarily intended to give data on the landing shock. Transition from the second to the third flight consisted of landing and then takeoff without coming to a stop. The human sensation of shock and vibration seemed no different than that experienced on a normal commercial passenger flight.

TABLE 1.

Summary of Data Recorded During
C9B Flight Events.

EVENT	FLIGHT NUMBER		
	#1	#2	#3
LOW SPEED TAXI TO RUNWAY [1]*	YES	NO	NO
FULL POWER RUNUP [2]	YES	NO	NO
TAKOFF RUN PRIOR TO LIFTOFF [3]	YES	YES	NO
CLIMB [4-6]	YES	YES	YES
CRUISE [9] (30,000 FT)	YES	NO	NO
DESCENT [10-13]	YES	YES	YES
LANDING SHOCK [14]	YES	YES	YES
THRUST REVERSAL [15]	YES	NO	YES
POST LANDING ROLLOUT [16]	NO	NO	YES
QUIET TIME [17] (AIRCRAFT POWERED DOWN)	NO	NO	YES

* Number in brackets [] is data point designation.

DATA ANALYSIS

The C9B flight data were analyzed by first creating oscillograph records of the analog data tape. Since IRIG time was displayed on the strip charts, all of the flight events could have their start and stop times identified precisely. The data periods of interest were then digitized in preparation for analysis. It was at this point that loss of the noise channel (due to an intermittent cable connection) was noted and a decision was made to rely on the quiet time data for an indication of the noise baseline of the measurement system. Overall, excellent data return was obtained from the flight test.

RANDOM VIBRATION: Auto-spectral density (ASD) estimates (Reference 7) were made for each piezoelectric accelerometer during each vibration flight event shown in Table 1. An indication of the relative severity of these events is given in Table 2 where overall root-mean-square acceleration (grms) values are listed for the vertical axis accelerometers at the back and mid cargo bay locations. Thrust reversal immediately after landing and the takeoff run prior to liftoff dominate. The back bay monitor point experiences slightly higher response levels than the mid bay location. All of the ASD estimates were placed in a computerized GRAFAID data base (Reference 8). Manipulation of the data was performed with GRAFAID. Envelopes of the ASD estimates were made by dividing the vibration environments into two separate categories, one for cruise vibration and one for the rest of the

TABLE 2.

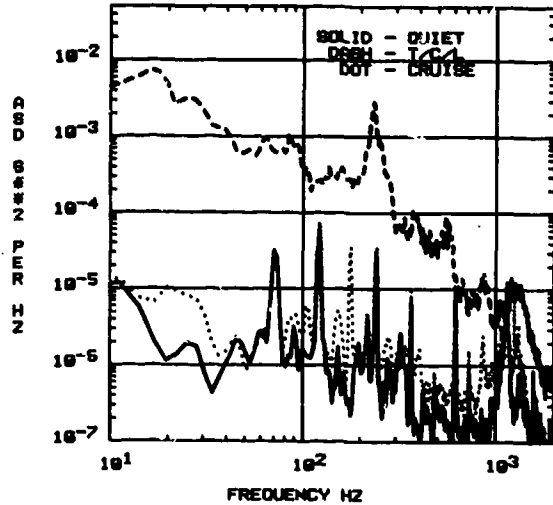
Summary of GRMS of Random Vibration
Measured During C9B Flight Events.

EVENT	GRMS	
	BACK BAY VERTICAL	MID BAY VERTICAL
LOW SPEED TAXI TO RUNWAY [1]*	0.10	0.083
FULL POWER RUNUP [2]	0.049	0.043
TAKOFF RUN PRIOR TO LIFTOFF [3]	0.26	0.19
CLIMB [4-6]	0.13	0.097
CRUISE [9] (30,000 FT)	0.056	0.054
DESCENT [10-13]	0.17	0.17
THRUST REVERSAL [15]	0.54	0.33
POST LANDING ROLLOUT [16]	0.12	0.084
QUIET TIME [17] (AIRCRAFT POWERED DOWN)	0.048	0.041

* Number in brackets [] is data point designation.

environments which will be called T/C/L (Takeoff/Climb/Landing). This classification of the data allows comparison with existing aircraft transport random vibration test specifications. It is a logical division of the environments because the cruise environment exists for an extended period of time, while the other environments are much shorter in duration during long distance air transport. Figure 4 shows an example of one set of envelopes which were made for the vertical axis environment at the back cargo bay location. This plot is indicative of the higher vibration levels experienced during T/C/L in comparison to cruise. This plot also includes an envelope of the quiet period where the aircraft is powered down and stationary. Note that the cruise environment is only slightly higher than the quiescent measurement, indicating that the cruise environment only slightly exceeds the noise level of the measurement system. (Transverse and longitudinal axes measurements exhibited the same relationship between the quiet time and cruise measurements.) This type of enveloping procedure was further expanded to include both the back and mid cargo bay monitor locations in each axis.

Figure 4. Comparison of Vertical Axis (Back Monitor Point) Random Vibration Envelopes for Three Different Periods of the C9B Flight Profile.



The resulting C9B random vibration environment envelopes are presented in Figures 5-10. For purposes of comparison, the C9B data are plotted along with current aircraft transport vibration test specification levels which have been derived at Sandia National Laboratories on the basis of CBA, C141, NC136, C180, and C183 data given in References 1-6. Note that only the vertical axis T/C/L data (Figure 5) exceeds the test specification. The C9B data are greater than the test specification in the 10 to 50 Hz frequency range. Table 3 provides a

summary of the g rms levels of the C9B data in comparison with the g rms level of existing Sandia air transport test specifications. The low g rms levels, particularly in the cruise mode, support an overall assessment that the random vibration levels in the cargo bay of the C9B aircraft are quite low.

Figure 5. Comparison of Vertical Axis Aircraft Takeoff/Climb/Landing Test Specification and C9B Vertical Axis Random Vibration Envelope.

TEST SPEC SRMS = 3.63
C9B VERTICAL SRMS = 8.523

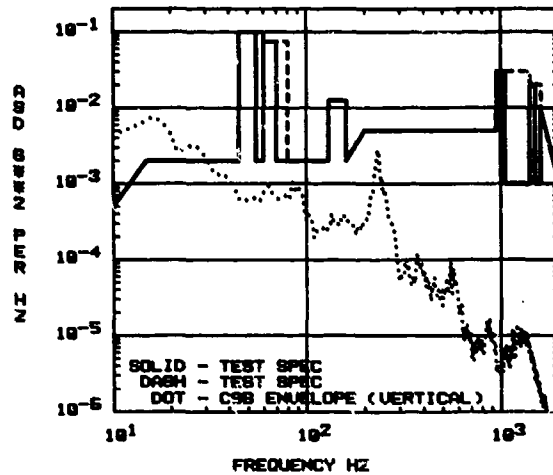


Figure 6. Comparison of Horizontal Axis Aircraft Takeoff/Climb/Landing Test Specification and C9B Transverse Axis Random Vibration Envelope.

TEST SPEC SRMS = 2.31
C9B TRANVERSE SRMS = 8.167

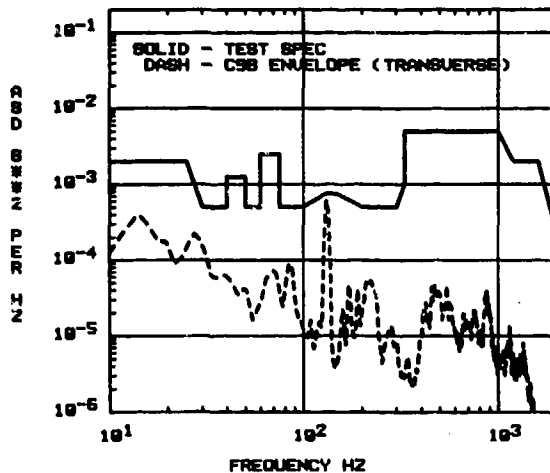


Figure 7. Comparison of Horizontal Axis Aircraft Takeoff/Climb/Landing Test Specification and C9B Longitudinal Axis Random Vibration Envelope.

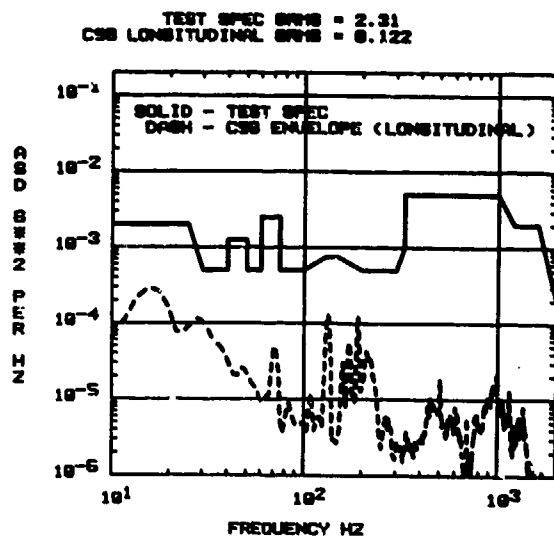


Figure 9. Comparison of Horizontal Axis Aircraft Cruise Test Specification and C9B Transverse Axis Random Vibration Envelope.

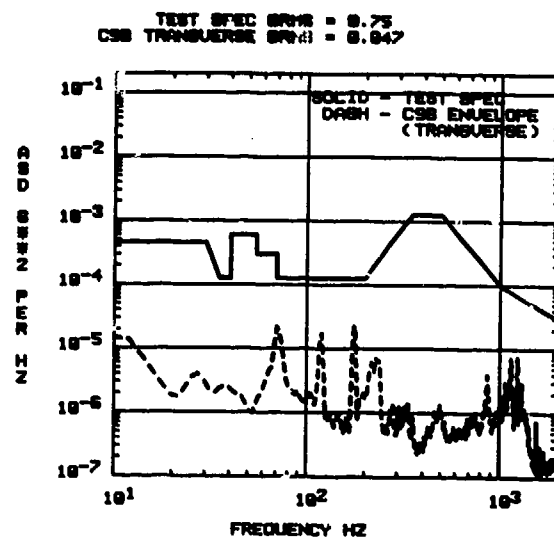


Figure 8. Comparison of Vertical Axis Aircraft Cruise Test Specification and C9B Vertical Axis Random Vibration Envelope.

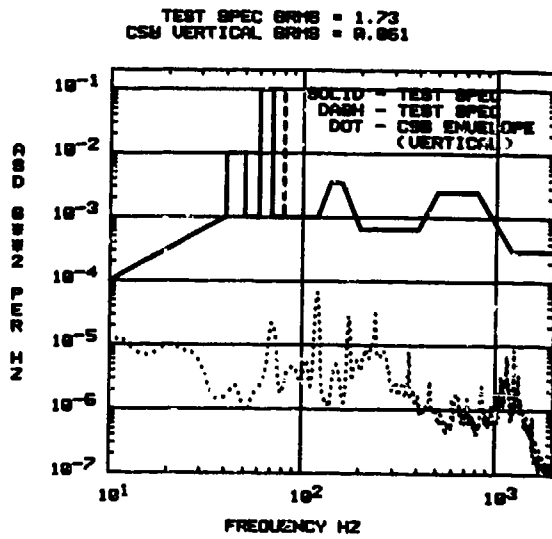
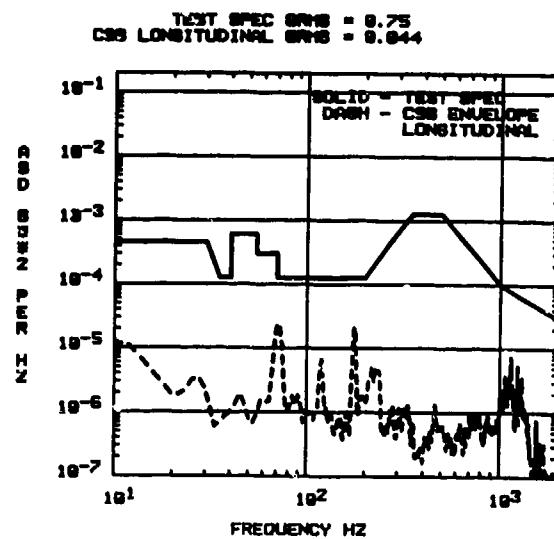


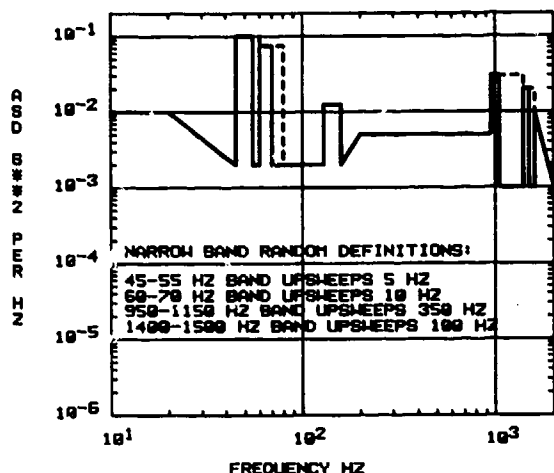
Figure 10. Comparison of Horizontal Axis Aircraft Cruise Test Specification and C9B Longitudinal Axis Random Vibration Envelope.



Figures 11a-11d show the complete set of test specifications which now include the C98 data. The T/C/L test specifications contain bands of narrow-band random vibration which are superimposed on the background spectrum (Reference 9). The vertical axis T/C/L random vibration test specification has been revised to envelop the C98 flight data. Note that the grms in the revised vertical axis test specification shown in Figure 11a has only risen from 3.63 grms to 3.65 grms, indicating that the increased low frequency content in the C98 data is of little significance to the overall test input. It should be mentioned that the test durations stated in the Figures 11a-11d should be altered to reflect specific air

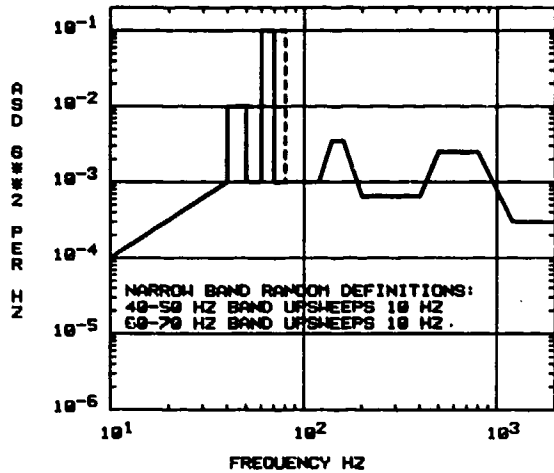
transportation scenarios. The stated times reflect a total cruise duration of three hours (one hour per axis) and thirty minutes (ten minutes per axis) for takeoff, climb, descent, and landing. Only one minute per flight (thirty seconds for takeoff taxi and thirty seconds for landing thrust reversal) accounts for the vibration levels which control the T/C/L test specification. The duration aspect of the test specification, along with the fact that each test specification could be reduced if it was applied to a single model of aircraft instead of the composite of five different aircraft, must both be addressed prior to the implementation of these transport aircraft random vibration test specifications.

Figure 11a



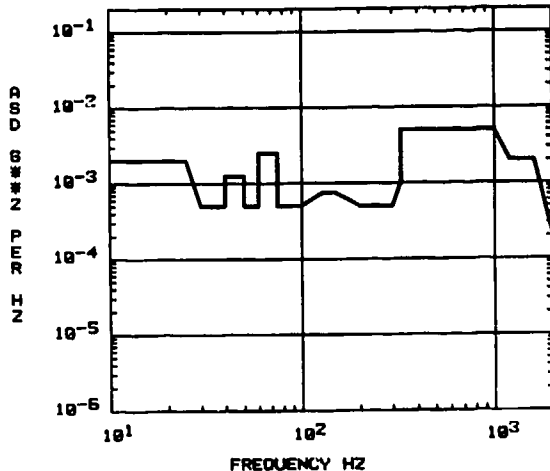
AIRCRAFT CARGO VIBRATION - TEST SPECIFICATION
CARGO FLOOR - TAKEOFF/CLIMB/LANDING - VERTICAL
SHEET RANDOM VIBRATION - 10 MIN DURATION - GRMS=3.65
TURBO-JET (C98, CSA, C141, NC135) AND
TURBO-PROP (C138, C133)

Figure 11c



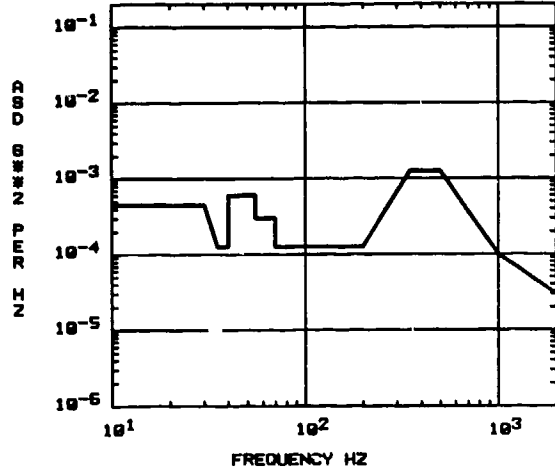
AIRCRAFT CARGO VIBRATION - TEST SPECIFICATION
CARGO FLOOR - CRUISE - VERTICAL
SHEET RANDOM VIBRATION - 1 HR DURATION - GRMS=1.73
TURBO-JET (C98, CSA, C141, NC135) AND
TURBO-PROP (C138, C133)

Figure 11b



AIRCRAFT CARGO VIBRATION - TEST SPECIFICATION
CARGO FLOOR - TAKEOFF/CLIMB/LANDING - HORIZONTAL
RANDOM VIBRATION - 10 MIN PER AXIS - GRMS=2.31
TURBO-JET (C98, CSA, C141, NC135) AND
TURBO-PROP (C138, C133)

Figure 11d



AIRCRAFT CARGO VIBRATION - TEST SPECIFICATION
CARGO FLOOR - CRUISE HORIZONTAL
RANDOM VIBRATION - 1 HR PER AXIS - GRMS=0.75
TURBO-JET (C98, CSA, C141, NC135) AND
TURBO-PROP (C138, C133)

SHOCK: The analyzed shock data included seven different shock events. A landing shock was measured on each of the three flights. Two shocks were analyzed during taxi prior to the takeoff taxi. Two shocks were also selected from takeoff taxi for study. Table 4 shows the peak accelerations from these shocks for all three axes and monitor locations. The landing shock clearly dominates.

Table 3.

Summary of RMS Levels from C9B Random Vibration.

	VIBRATION ENVIRONMENT			
	T/C/L		CRUISE	
AXIS	SPEC*	C9B	SPEC*	C9B
VERTICAL	3.63	0.523	1.73	0.061
TRANSVERSE	2.31	0.167	0.75	0.047
LONGITUDINAL	2.31	0.122	0.75	0.044

* See Figures 5-10

Table 4.

Summary of Peak G Levels from C9B Shock Data. *

AXIS	SHOCK ENVIRONMENT		
	LANDING	TAKEOFF TAXI	LOWSPEED TAXI
VERTICAL	3.72	2.10	0.70
TRANSVERSE	0.0	0.53	0.26
LONGITUDINAL	1.73	0.61	0.84

* Lowpass Filtered at 500 Hz

The shock data analysis procedure involved using a data analysis program called SHARPE (Reference 10). This program computes different types of shock characterizations and then computes extrema and statistics for each ensemble of shock characterizations. Absolute acceleration shock spectra (SAA) and shock intensity spectra (SIS) (Reference 11) were the two characterizations of prime interest to this study. Figures 12a-14b show the time histories and shock spectra of the landing shocks in each axis having the highest peak accelerations. Also shown for comparison on the SAA plots are the shock spectra of the landing shocks for the C5A which show that the C9B landing shocks are of the same magnitude.

Figure 12a.

Time History for C9B Vertical Axis Landing Shock with Highest Peak Acceleration (3.72 g).

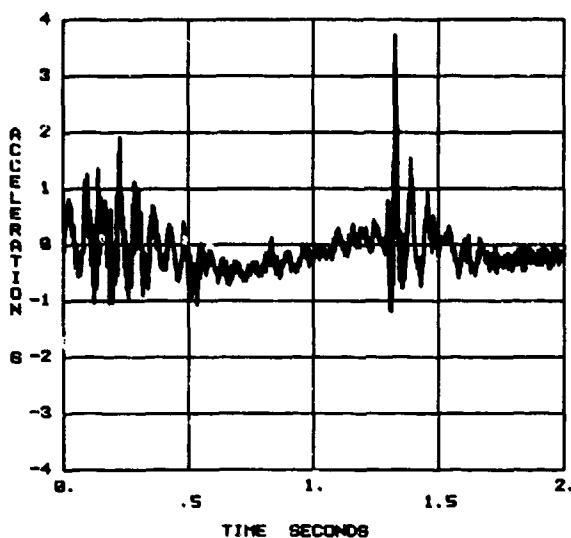


Figure 12b.

Shock Spectrum (SAA) Plot for C9B Vertical Axis Landing Shock Compared to Corresponding C5A Data.

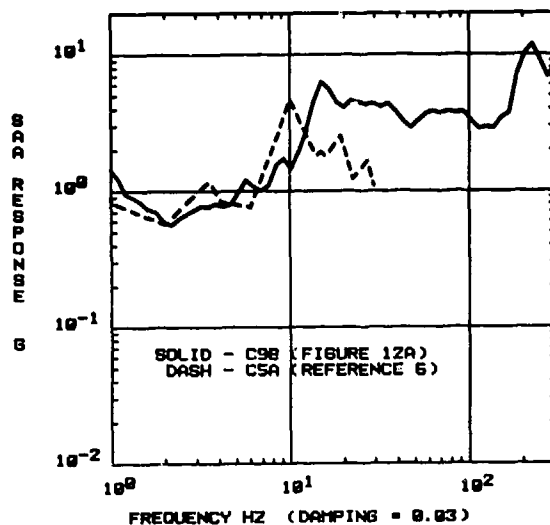


Figure 13a.

Time History for C9B Transverse Axis Landing Shock with Highest Peak Acceleration (0.75 g).

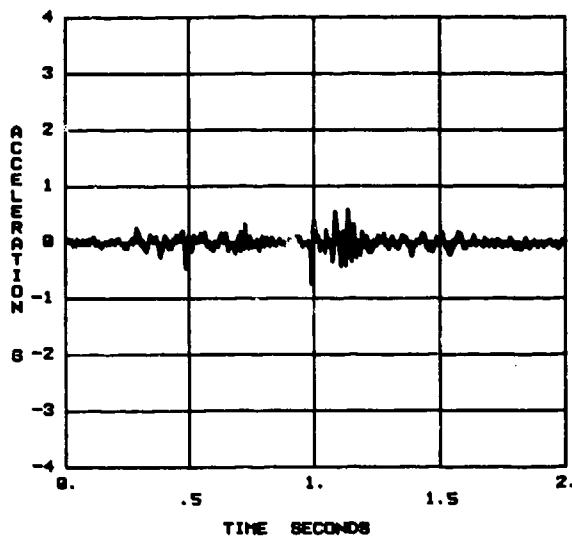


Figure 14a.

Time History for C9B Longitudinal Axis Landing Shock with Highest Peak Acceleration (1.73 g).

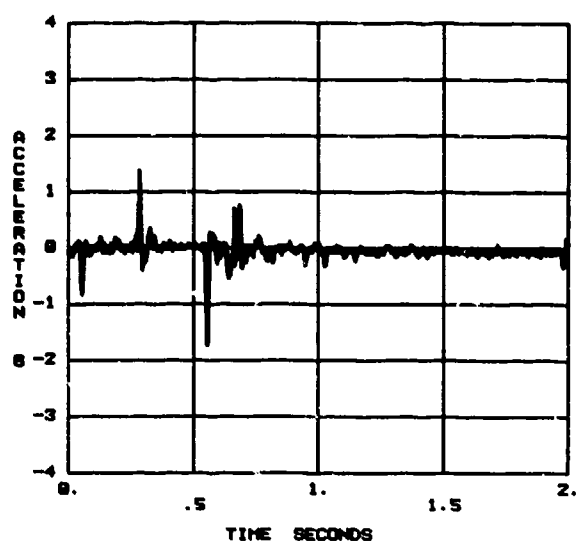


Figure 13b.

Shock Spectrum (SAA) Plot for C9B Transverse Axis Landing Shock Compared to Corresponding CSA Data.

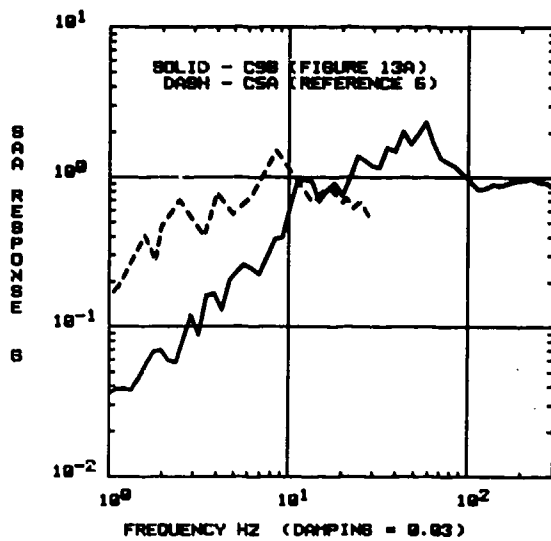
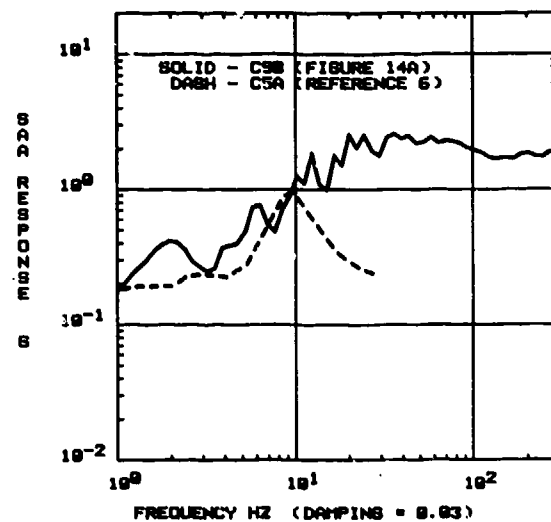


Figure 14b.

Shock Spectrum (SAA) Plot for C9B Longitudinal Axis Landing Shock Compared to Corresponding CSA Data.



The plots of maximum, minimum, and mean SAA and SIS are shown in Figures 15 and 16, respectively. This presentation of the shock spectrum plots indicates the degree of spread in the data. The SIS data analysis is important because it is a direct reflection of the frequency content of the shock transients, while the SAA plots reflect the effect of the measured shocks on single-degree-of-freedom oscillators whose natural frequency is stated on the abscissa of the shock spectrum plot. From the standpoint of test specification, both shock characterizations could be used to define a set of shock pulses to simulate the C9B flight shock environment on an electro-hydraulic shaker.

Figures 17a-c show a comparison of the C9B shock spectrum envelopes and corresponding envelopes for forklift shock (Reference 12) which is another common transportation environment. The fact that the forklift shock envelopes the aircraft shock has led to a general conclusion that a separate set of simulated aircraft shocks does not need to be done if the structure being qualified for aircraft transport has already been qualified for forklift transport. In comparison to forklift shocks, C9B aircraft shocks are low.

Figure 15a.

Summary of C9B Vertical Shock Analysis - Absolute Acceleration Shock Spectra (SAA). Maximum/Minimum/Mean of Seven Taxi and Landing Shocks at Middle and Back Cargo Bay Locations.

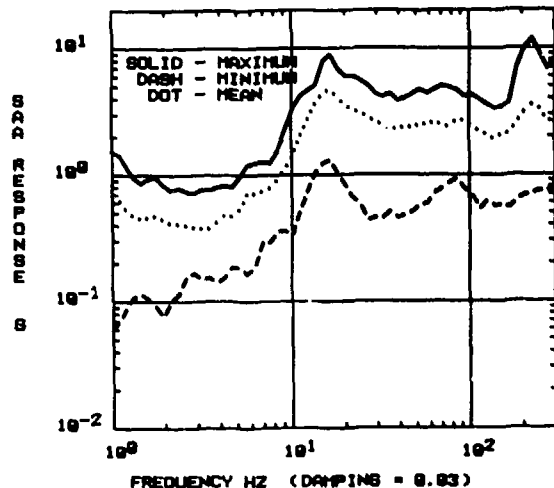


Figure 15b.

Summary of C9B Transverse Shock Analysis - Absolute Acceleration Shock Spectra (SAA). Maximum/Minimum/Mean of Seven Taxi and Landing Shocks at Middle and Back Cargo Bay Locations.

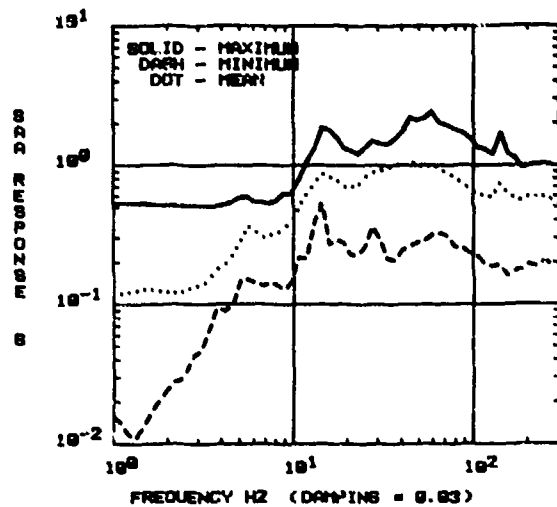


Figure 15c.

Summary of C9B Longitudinal Shock Analysis - Absolute Acceleration Shock Spectra (SAA). Maximum/Minimum/Mean of Seven Taxi and Landing Shocks at Middle and Back Cargo Bay Locations

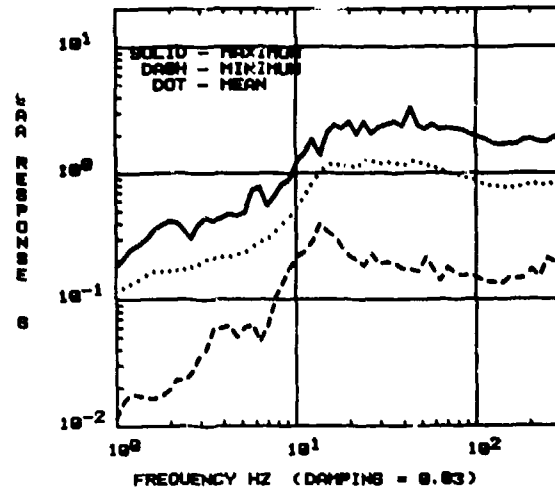


Figure 16a.

Summary of C9B Vertical Shock Analysis - Shock Intensity Spectra (SIS). Maximum/Minimum/Mean of Seven Taxi and Landing Shocks at Middle and Back Cargo Bay Locations.

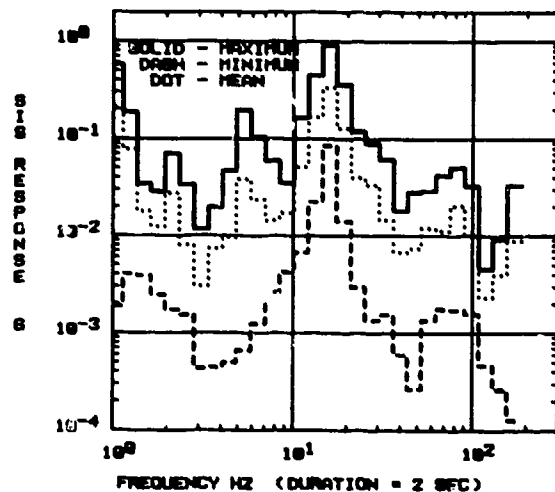


Figure 16c.

Summary of C9B Longitudinal Shock Analysis - Shock Intensity Spectra (SIS). Maximum/Minimum/Mean of Seven Taxi and Landing Shocks at Middle and Back Cargo Bay Locations.

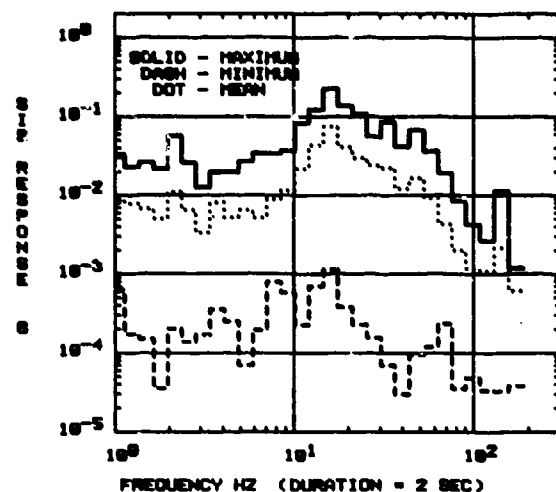


Figure 16b.

Summary of C9B Transverse Shock Analysis - Shock Intensity Spectra (SIS). Maximum/Minimum/Mean of Seven Taxi and Landing Shocks at Middle and Back Cargo Bay Locations.

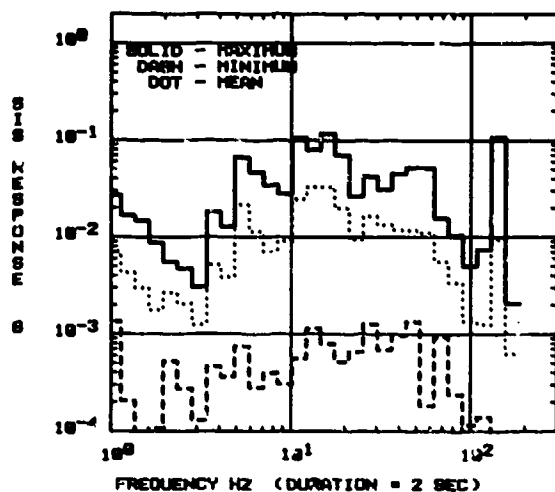


Figure 17a.

Comparison of Shock Spectra (SAA) between C9B Vertical Axis Shock Envelope (Figure 15a) and Forklift Vertical Axis Shock Envelope (Reference 4).

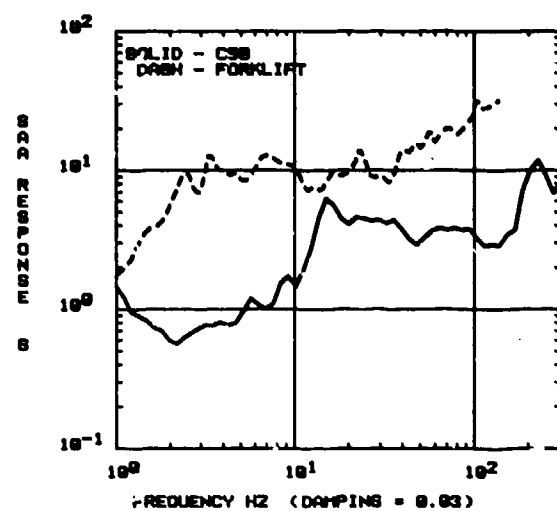


Figure 17b.

Comparison of Shock Spectra (SAA) between C9B Transverse Axis Shock Envelope (Figure 15b) and Forklift Transverse Axis Shock Envelope (Reference 4).

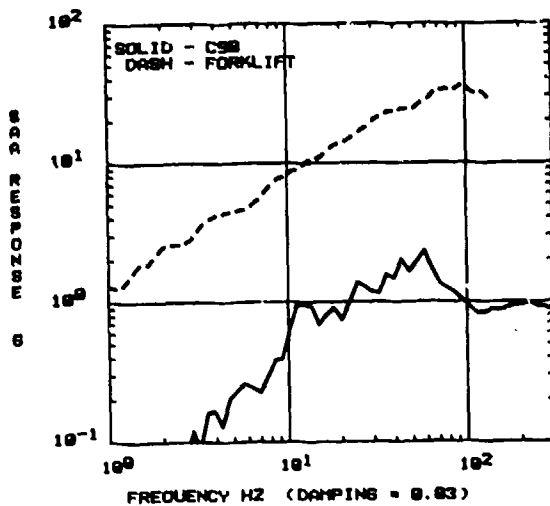
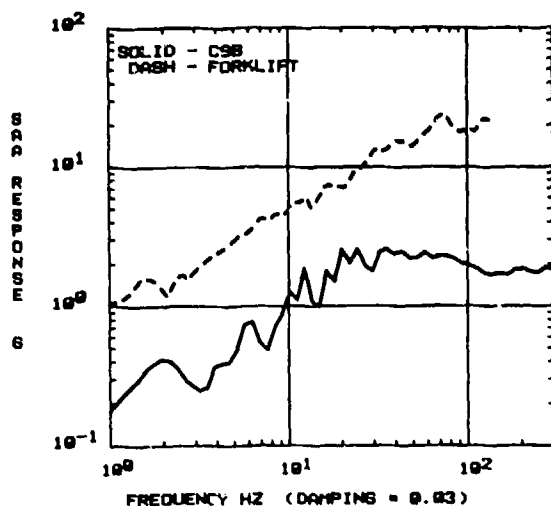


Figure 17c.

Comparison of Shock Spectra (SAA) between C9B Longitudinal Axis Shock Envelope (Figure 15b) and Forklift Longitudinal Axis Shock Envelope (Reference 4).



CONCLUSION

The field test measurement and analysis of C9B random vibration and shock data has produced a set of data which will be an important addition to the DOE/DOD Environmental Data Bank. The C9B shock and vibration environments were generally benign. A modification to the existing aircraft random vibration test specification resulted from the measurements made on the C9B. The measurement and data analysis techniques used in this paper should be of use in future endeavors to measure operational transport environments. Computerized data analysis and manipulation were a fundamental part of the C9B data analysis in that they allowed the synthesis of over 300 data curves into the data presented in this data summary. High regard for data integrity was maintained during the C9B flight tests and needs to be monitored in all future data which are destined for an environmental data bank such as the one at Sandia. It is hoped that the C9B random vibration data as well as the general cargo aircraft random vibration test specifications and techniques detailed in this paper will be of use to other engineers responsible for evaluating the capability of structures carried as cargo on military aircraft.

ACKNOWLEDGMENT

The authors gratefully acknowledge the contributions made to the acquisition and publication of the C9B data by the following individuals: T. G. Priddy, R. C. Reuter, R. D. Christopher, L. L. Keller, C. G. Sain, F. Shelly, and C. D. D'Spain, and T. F. Laney of Sandia; and D. Fisher and M. R. Klingler of the Naval Weapons Evaluation Facility.

REFERENCES

1. Davidson, C. A., J. T. Foley, and C. A. Scott, "DOE/DOD Environmental Index," SAND86-0155, Sandia National Laboratories, May 1986.
2. Davidson, C. A. and J. T. Foley, "Transportation Technical Environmental Information Center Index," SAND82-1200, Sandia National Laboratories, June 1982.
3. Thaller, R. and J. Pearson, "Narrow Band Time History Analysis of Transport Aircraft Vibration Data," Shock and Vibration Bulletin, Vol. 44, Part 4, August 1974, pp. 79-87.

4. Cook, F. E., "Dynamic Load Design Criteria for Cargo Transported by C-5A Aircraft," TOR-0076(C403-01)2, The Aerospace Corporation, December 1975.
5. Magnuson, C. F., "Dynamic Environment Study of Turbojet Cargo Aircraft," Proceedings of the Institute of Environmental Sciences, 16th Annual Technical Meeting, May 1972, pp. 420-425.
6. Crevonnis, E. B., "C-5A Program, C-5A Cargo Floor Vibration Data," DDC/DOD Environmental Data Bank Entry No. 1402, July 1978.
7. Downey, T. L. and R. N. Tomlinson, "Vibration Data Analysis System for SRLA Area III: Reference Manual," SAND84-0380, June 1984.
8. Adams, C. R., "GRAFAID Code User Manual Version 2.0," SAND84-1726, Sandia National Laboratories, September 1985.
9. Tekks, J. D., and D. O. Smallwood, "Extension of Control Techniques for Digital Control of Random Vibration Tests," Shock and Vibration Bulletin, Vol. 45, Part 2, June 1975, pp. 101-109.
10. Baas, T. J., "Characterization of Conservatism in Mechanical Shock Testing of Structures," SAND82-2186, Sandia National Laboratories, May 1983.
11. Baas, T. J., and T. D. Glacker, "Relative Conservatism of Drop Table and Shaker Shock Tests," Shock and Vibration Bulletin, Vol. 56, 1986. (To be published)
12. Gens, M. B., "The Dynamic Environment on Four Industrial Forklift Trucks," Shock and Vibration Bulletin, Vol. 45, Part 4, June 1975, pp. 59-67.

COMPREHENSIVE INFLIGHT VIBRATION AND ACOUSTIC TESTING

Phyllis G. Bolds

Air Force Wright Aeronautical Laboratories
Wright-Patterson Air Force Base, Ohio 45433-6553

The Air Force Flight Dynamics Laboratory has obtained inflight vibration and acoustic data on a series of operational aircraft for the upgrading of environmental design criteria and verification of dynamic prediction techniques. The many uses of this data from the most recent comprehensive inflight survey, the F-111E aircraft, are presented in this paper. In addition to acquiring the dynamics data in a timely manner, cost effectiveness, analysis techniques derived, instrumentation developed, and the expertise gained make a survey of this type most attractive to the Air Force.

INTRODUCTION

In the past the Air Force has conducted comprehensive inflight vibration and acoustic tests on current and experimental vehicles to determine their dynamic environment. These dynamics data have been used in the areas of human comfort, equipment installations and structural dynamics. These data are readily available for use in solving problems that occur in the operation of military aircraft. Since many Air Force vehicles remain in the inventory for decades and undergo numerous changes in purpose and design, this information is invaluable to the aircraft manufacturers and the Department of Defense. The dynamics data gained from inflight testing, can also be used to help make commercial applications of similar aircraft more safe.

The objective of this paper is to take a look at the many ways these dynamics data have been used in the past and comment on the potential savings in time and dollars gained by conducting these surveys on dedicated aircraft. As a result of this potential cost savings, it is recommended that weapon systems be made available by the Air Force to conduct similar comprehensive studies. The Flight Dynamics Laboratory's Vibration and Acoustic Branch has the capability for acquiring, analyzing and interpreting inflight dynamics measurements.

The utilization of these data has been very beneficial to the Air Force. These data have been used in various ways such as; to verify empirical vibration prediction methods, define vibration transmission paths

within the aircraft, fine-tune laser control, define the aero-acoustic environment in the internal weapons bay, establish airframe identification using the vibration signature of the aircraft, update vibration test methods for equipment, Mil-Std-810, and many more.

The results of this program were documented in Ref. 1 in three-parts, AFWAL-TR-81-3182, "F-111E Flight Vibration and Acoustic Test Program," Part I, Test Instrumentation, Test Procedure and Data Reduction, April 1982; Part II, Statistical Analysis of Overall RMS Measurements; and Part III, Spectral Data Presentation.

The Vibration and Acoustic Branch of the Air Force Wright Aeronautical Laboratories is used for recording and analyzing dynamics data. New instrumentation systems have made possible a significant increase in the quality of measurements which can be acquired to define the dynamic environment in various aircraft, missiles, and ground support equipment.

The Branch has developed over the years sensors, tape recorders, amplifiers and other signal conditioning equipment to acquire inflight dynamics data. They have studied packaging and miniaturization for the design of onboard instrumentation while increasing the accuracy and dynamic range of this equipment by using pulse code modulation (PCM) encoding and recording techniques. An example of the research and

development conducted by the laboratory, is the miniaturizing of the signal conditioning equipment as shown in Figure 1. We have included in the endeavor to optimize our capability, the implementation of the latest analysis techniques used to define the dynamic environment and to solve potential problems. These analysis and statistical techniques are contained in Ref. 2, "Compendium of Methods for Applying Measured Data to Vibration and Acoustic Problems," May 1986.

The acquisition equipment includes a wide selection of modern dynamics transducers, signal conditioners, and tape recorders. Figure 2 is a picture of the onboard/portable tape recorder system. In addition, the Branch has available two mobile data acquisition and analysis vans which are completely self-contained. They are used for on-site data acquisition such as related wind tunnel tests, flyover acoustic tests, runway roughness measurements, etc. The pictures of the vans are shown in Figures 3 and 4.

The process of obtaining dynamics data and storing it for subsequent retrieval and processing can be summarized into five major tasks: transduction, signal conditioning, recording, data verification and record keeping.

To reduce the large quantities of data to a usable form, processing techniques based upon the use of spectrum analyzers and mini-max computers are employed. Figure 5 shows the computer system used to process these measured data. The processes for data analysis are retrieval and editing, analog-to-digital conversion (if required), spectral and statistical analysis, and graphic presentation. A discussion of the measurement and analysis capabilities are contained in Reference 3.

TEST DESIGN

Test Vehicle Description. The F-111E aircraft is a two-place, all-weather, high or low altitude, supersonic, tactical fighter/bomber. The aircraft has dual controls and requires a crew of two seated side-by-side. It provides the pilot with the inflight capability to select any angle of wing sweep between 16 and 72.5 degrees respectively. The aircraft has full span Fowler action, double slotted trailing edge flaps, and is powered by two TF30 jet after-burning engines internally mounted in the fuselage. The aircraft has a conventional tricycle gear with the main one as a single assembly. It has a large vertical stabilizer and a conventional rudder plus ventral strakes located on the lower portion of the engine access doors approximately 30 degrees from the vertical.

Test Instrumentation. In the airborne acquisition system, 104 accelerometers and 29 microphones were used for measuring the vibration and acoustic environment throughout the aircraft. The signal conditioning and recording instrumentation consisted of a 12 position switch box, a tape recorder, a portable data acquisition system, a time code generator, voice from the aircraft intercom system, six-channel automatic gain changing amplifier boxes, an in-house fabricated programmable transfer box, a pair of frequency multiplexers each consisting of two voltage control oscillators and one mixer amplifier.

Data Acquisition. Dynamics data were recorded for test conditions which included ground run-up, take-off, climb, level acceleration and deceleration runs, sideslip, turns, stabilized flight, gunfiring passes, landing, and standard maneuvers. The data were recorded during preplanned conditions for up to 3 to 5 minutes.

Data Analysis and Presentation. Analog tapes recorded during the flights were analyzed by the Structural Vibration and Acoustic Branch at WPAFB, Ohio. Root-Mean-Square time histories indicated whether these data were reasonable and stationary. The power spectral density of these vibration data was computed using standard Fast Fourier Transform (FFT) techniques. The amplitudes of the acoustic data were presented in sound pressure levels and the frequencies in one-third octave bands.

The feedback from the users of these data assists in the design of future comprehensive studies. It provides information such as location, frequency-range selection, the analysis to be accomplished and data presentation.

USERS OF F-111E DYNAMICS TEST DATA

The test data were used in AFWAL to support the in-house program "Dynamics Environment on Current and Future Air Force Vehicles," to enhance the vibration analysis and testing technology by verifying the empirical vibration prediction methods and the vibration transmission study. The acoustic measurements were used in a similar manner to validate prediction methods in the design of spoilers to be installed to control the internal weapons-bay aero-acoustic environment. The measured fluctuating pressures were sensitive to Mach number, flight altitude, test configuration and location. The results of this study were published in AFWAL-TM-81-69-FIBE, "Full Scale Flight Evaluation of Suppression Concepts for Flow-Induced Fluctuating Pressures in Cavities," Ref. 4.



Figure 1. Miniaturized Auto Gain Ranging Amplifier and Lowpass Filter



Figure 2. Onboard/Portable Data Acquisition Package



Figure 3. Twenty-Six Foot Mobile Experimental Laboratory

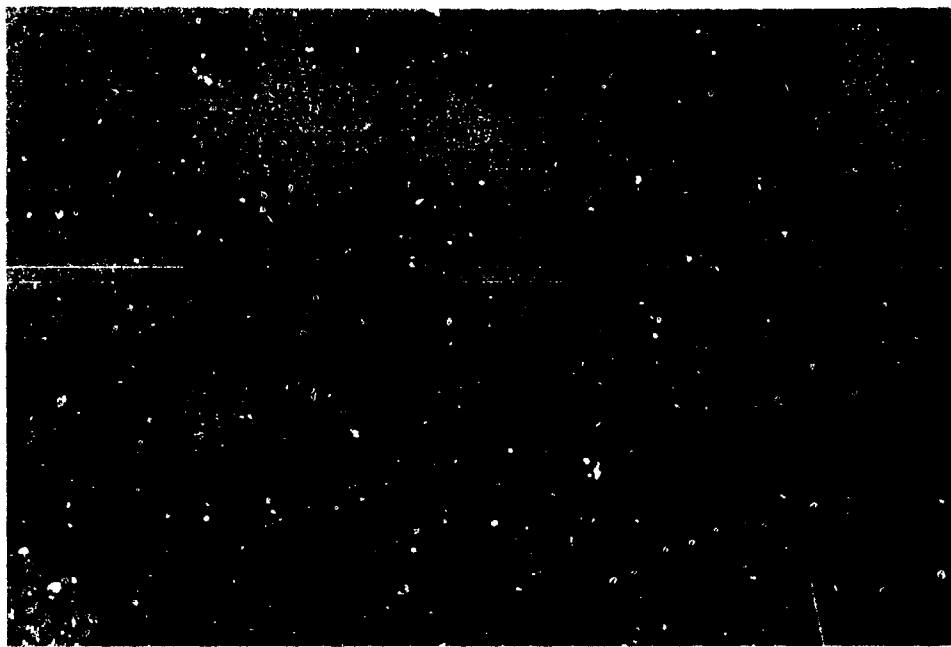


Figure 4. Data Acquisition Van

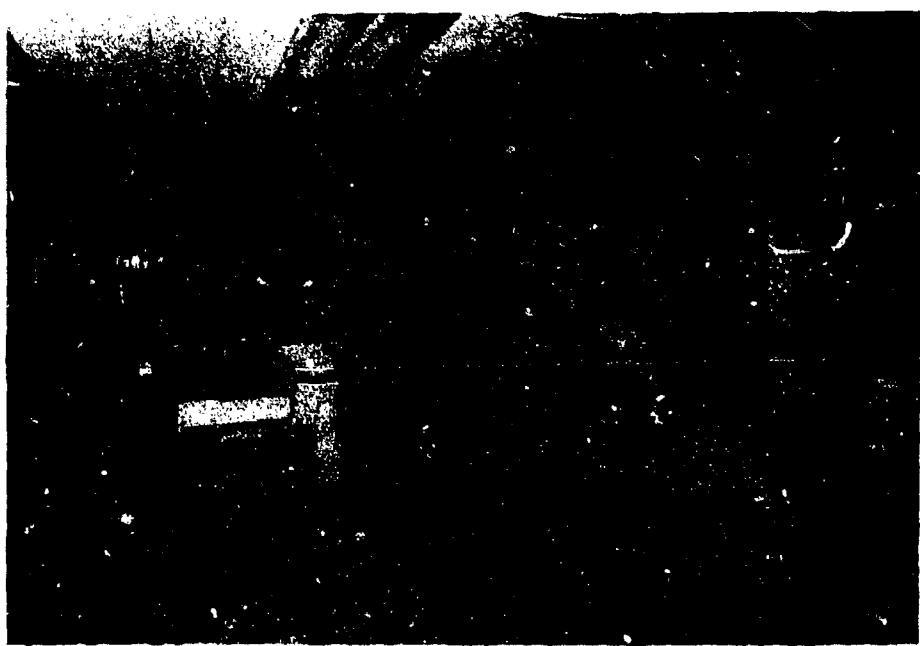


Figure 5. Mini-Max 32-Bit Computer with 7.5 Megabytes of Memory

The contractual program to identify aircraft type from their vibration characteristics by the use of radar return signals, utilized these data to launch their feasibility study. Not only did the F-111E data play a major part in this program by representing the fighter/bomber class, other data from the dynamics data bank maintained by the Flight Dynamics Laboratory from previous comprehensive studies were used to represent other classes of aircraft.

These data were used to develop a computer simulation program as a design tool for an airborne laser transmission system. This program investigated the possibility of designing a system to establish the specifications for each component that will insure desired output performance. The results of this study is documented in AFWAL-TR-85-3008, "Computer Simulation For Vibration Control of Laser Transmission," Ref. 5.

Numerous requirements were received by those responsible for the installation of vibration sensitive equipment such as: camera mounts, radar units, and other avionic instrumentation. The measured data to customize the vibration specification test were supplied.

Aeronautical Systems Division utilized these dynamics data to a large degree. All of the data were used to update the dynamics qualification test criteria and techniques publication. They were also used to re-define and augment the dynamics test methods of Mil-Std-810. Because the data were measured during gunfire and non-gunsire, they were used to evaluate gunfire vibration prediction methods. This program provided low-altitude high-speed vibration data for the development of specifications for the new terrain-following radar unit.

These data were used by the contractor responsible for the verification of the predicted specification for the F-111 Tail Warning System to be installed in the vertical tail pod assembly. The results from this study were presented at the 52nd Shock and Vibration Symposium and published in the proceedings, "Determination of the Dynamic Environment of the F/FB-111 Tail Pod Assembly," Ref. 6. From the analysis of this study, the vibration data exceeded the requirements specified by ASD in the 300 to 500 Hz range. The data did not allow a sufficient cushion for endurance testing for many of the transient conditions. The recommendation was made to shock mount the equipment in the low frequency range or find another location within the aircraft to install this vibration sensitive electronic equipment.

COMPARATIVE INFLIGHT TESTING COST

The total cost for test and evaluation for an aircraft in the F-111E class has more than doubled since these measurements were made. If each test that this dynamics data satisfied had been conducted individually, it would have cost the Air Force approximately fifteen times the initial resources, not including the expertise, instrumentation and equipment to acquire, analyze and interpret these measurements.

These data were utilized to complete many programs that could not otherwise obtain flight test data; therefore, these programs would probably never have been accomplished or empirically verified. Less than 20% of these programs would have been completed and this technology would not be available now.

CONCLUSIONS

The many uses of these data have been mentioned here to give the reader some idea of the importance of having vibration and acoustics data available in an Air Force maintained data bank to support the numerous quick turn-around customized tests required on operational and future flight vehicles.

It appears, in the best interest from a technical and economical viewpoint, that the Air Force should continue to conduct comprehensive vibration and acoustic surveys on dedicated aircraft.

REFERENCES

1. Ach, J. T., et al, "F-111E Flight Vibration and Acoustic Test Program," AFWAL-TR-81-3182, April 1982.
2. Cambridge Collaborative, "Compendium of Methods for Applying Measured Data to Vibration and Acoustic Problems," AFWAL-TR-85-3080, October 1985.
3. Bolds, P. G., "Vibration and Aeroelastic Facility," AFWAL-TR-82-3054, December 1982.
4. Shaw, L. L., Jr., "Full Scale Flight Evaluation of Suppression Concepts for Flow Induced Fluctuating Pressures in Cavities," AFWAL-TM-81-69-FIBE, March 1981.
5. Chen, J., et al, "Computer Simulation for Vibration Control Laser Transmission," AFWAL-TR-85-3008, May 1985.
6. Chinn, J. and P. Bolds, Determination of the Dynamic Environment of the F/FB-111 Tail Pod Assembly," Shock and Vibration Bulletin 52, May 1982.

VIBRATION ANALYSIS AND TEST

EVALUATION OF VIBRATION SPECIFICATIONS FOR ACOUSTIC ENVIRONMENTS

L. T. Nguyen and G. J. Zeronian
Northrop Corporation, Electronics Division
Hawthorne, California

To properly design any structure, it is necessary to determine the effects of various environments, vibration, shock, etc., on that structure. Usually the environment which has the worst effect will be used as the design criteria for comparison with the static (yield or ultimate) material allowables. Analyzing the same structure under all of the various environments can be time consuming and costly. A method has been devised previously to allow for various environments to be compared to each other to select the highest load or acceleration producing environment. The proposed paper introduces a technique which extends the above method and allows an additional environment, acoustic vibration, to be compared with sine, random vibration and shock environments. Furthermore, these techniques enable all dynamic environments to be added together so only a single stress analysis of the structure is needed for combined environments.

INTRODUCTION

The typical approach to decide the design environment for a structure is to perform complete analyses based on several environments, such as sine vibration, shock and random vibration. Once this is done, the resulting stresses and deflections are compared to the yield strength of the material to determine the resulting margins of safety for all environments. This can become both time consuming and costly. Ref. 3 describes a method whereby these three specific environments can be initially compared to each other and the most severe determined prior to any detailed structural analysis. This approach allows for a structural analysis to be completed for the worst environment without having to perform similar analyses for all the other less severe conditions. Another advantage to this method is the ability to add environments together, if required, to do only one stress analysis for the structure under all combined environments.

The "Quick Look" method, described in Ref. 3, is the basis for this comparison. Sine vibration, shock and random vibration spectra are each expressed in different units. This method shows how to convert each of these environments into common units of g response versus hr. Once this conversion has been performed, the different environments can then be plotted on a single graph. For any desired frequency range, the highest curve on the graph will represent the worst environment for that range. This particular spectrum can then be used for the final structural analysis.

The purpose of this paper is to provide for the inclusion of the acoustic vibration environment along with the other previously mentioned environments. Using the proposed method, it is possible to quickly

determine, for sine, shock, random and now acoustic excitation, which one will be the most important to consider for the structural design.

GENERAL APPROACH

There are three main conversions involved to change the acoustic spectrum of decibels versus frequency into g response versus frequency:

- 1) Conversion from sound pressure level (SPL) in decibels (db) to power spectral density (PSD) in terms of psi^2/hz :

This entails calculation of the pressure for each bandwidth in the spectrum, based on one octave or one-third octave divisions. From Ref. 4, the SPL of the center frequency F_c of each bandwidth is defined as:

$$\text{SPL}_{F_c} = 20 \log_{10} \frac{P_{F_c}}{P_R}$$

where P_{F_c} = pressure at F_c

P_R = reference standard sound pressure at 2.9×10^{-9} psi

$$\text{giving } P_{F_c} = P_R \left(10 \frac{\text{SPL}_{F_c}}{20} \right)$$

With P_{F_c} known, the PSD in terms of psi^2/hz can be computed using $\text{PSD} = \frac{(P_{F_c})^2}{B}$ where B is the bandwidth (hz). From Fig. 1, B is the difference between the end frequencies of the bandwidth (i.e. $B = F_2 - F_1$).

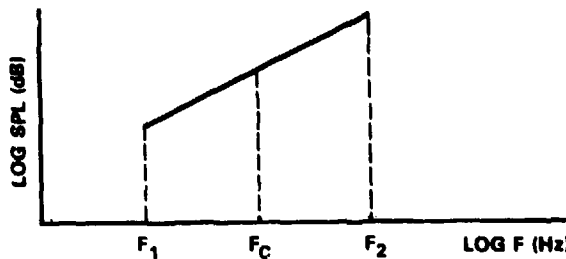


Fig. 1 - Bandwidth

From Ref. 2:

$$F_2 = 2^n F_1 \text{ where } n = \frac{1}{3}, \text{ or } 1 \text{ depending on the band divisions}$$

$$F_c = \sqrt{F_1 F_2} = \sqrt{2^n F_1^2} = 2^{n/2} F_1$$

$$\text{Therefore } F_1 = \frac{F_c}{2^{n/2}} \text{ and}$$

$$F_2 = 2^n \frac{F_c}{2^{n/2}} = 2^{n/2} F_c$$

$$\text{giving } B = F_c (2^{n/2} - 2^{-n/2})$$

2) Conversion from PSD (psi²/hz) to PSD (g²/hz):

The acoustic pressure is dependent on the sound velocity and the thickness of the medium the sound is passing through. With this relationship, it is possible to perform this particular step in the conversion.

By using $F = ma$ and $F = PA$,

where F = force (lbs)

m = mass of the structure (lb sec²/in)

a = acceleration felt by the structure (in/sec²)

P = acoustic pressure acting on the structure (lb/in²)

A = surface area of the structure (in²)

$$ma = PA \quad (1)$$

Since m is defined as the product of the volume v of the structure and the density ρ of the material, m can be rewritten as:

$$m = \frac{tA\rho}{386.4} \quad (2)$$

where t = thickness of the structure (in)

ρ = density of the material (lb/in³)

$$386.4 \text{ in/sec}^2 = \text{gravity}$$

Substitute eq. (2) for m into Eq. (1):

$$\frac{tA\rho}{386.4} a = PA$$

$$\frac{a}{386.4} = \frac{P}{t\rho} \quad (3)$$

$\frac{a}{386.4}$ is known as "g". Therefore Eq. (3) becomes

$$g = \frac{P}{t\rho} \quad (4)$$

With PSD in terms of psi²/hz from conversion (1) and Eq. (4), PSD in units of g²/hz can be calculated

$$\frac{P^2}{\text{hz}} = \frac{(t\rho)^2}{\text{hz}}$$

$$\text{or } \frac{g^2}{\text{hz}} = \frac{P^2}{(t\rho)^2 \text{hz}}$$

This conversion procedure, although simple, is dependent on the thickness and density of the structure. For cases of structures with non-uniform thickness and/or density, only worst case acoustic environment can be evaluated for g response using the smallest thickness and/or density.

3) Conversion from PSD (g²/hz) to g response:

Using the procedure explained in Ref. 3 for random vibration, PSD in g²/hz can be converted to g response.

$$\text{g response} = 3\sqrt{\frac{\pi}{2} f g_{in} Q}$$

where f = frequency (hz) of the spectrum

g_{in} = PSD (g²/hz) at f

Q = amplification factor

$$= \frac{1}{2\zeta}; \zeta = \text{ratio of assumed to critical damping}$$

After these three conversions have been performed, the new acoustic spectrum can be plotted along with the other environments in common units of g response versus frequency.

PROCEDURE

The following example demonstrates how this method is utilised.

An Al-7075 plate clamped as shown in Fig. 2 is subjected to four dynamic environments in the z direction with $Q = 50$.

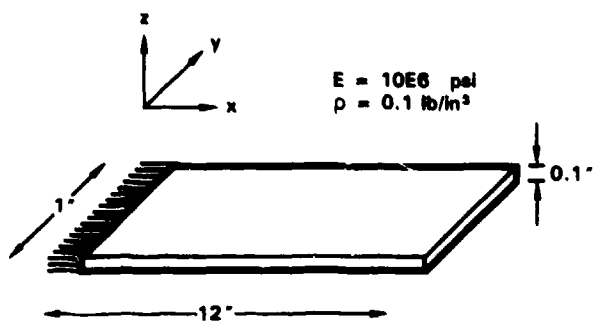


Fig. 2 - Clamped Plate

1) Acoustic field - 144 db overall, 1/3 octave band divisions

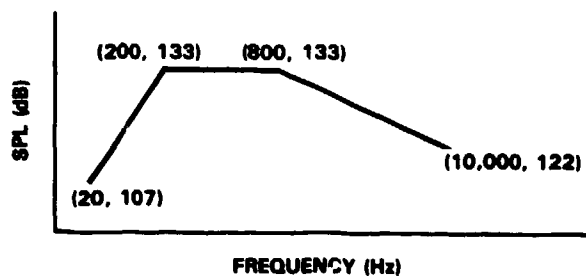


Fig. 3 - Acoustic Spectrum

2) Random Vibration - 13g_{RMS}

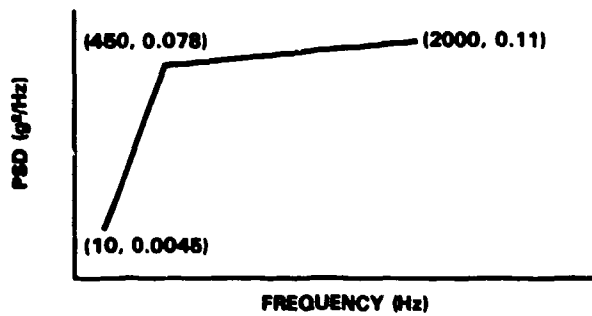


Fig. 4 - Random Vibration Spectrum

3) Shock

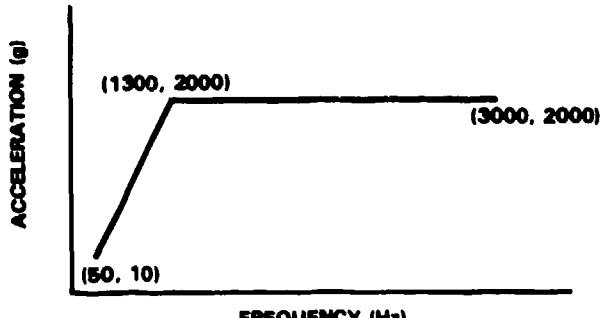


Fig. 5 - Shock Spectrum

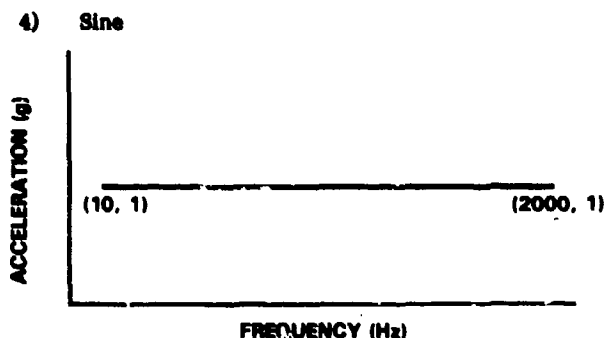


Fig. 6 - Sine Environment

From Ref. 3, environments (2) to (4) can be converted to g response versus frequency.

For environment (1), first use conversion (1) to find PSD in psi²/hz.

TABLE 1
Conversion of SPL to PSD (psi²/hz)

F _c (hz)	SPL (db)	P (lb/in ²)	B (hz)	PSD (psi ² /hz)
20	107	6.492E - 4	4.6	9.101E - 8
200	133	1.295E - 2	46.3	3.623E - 6
800	133	1.295E - 2	185.2	9.058E - 7
10000	122	3.651E - 3	2315.6	5.756E - 9

Change from psi²/hz to g²/hz using $t = 0.1$ in,
 $\rho = .1$ lb/in³

TABLE 2
Conversion of PSD to g²/hz unit

F _c (hz)	PSD (psi ² /hz)	PSD (g ² /hz)
20	9.101E - 8	9.101E - 4
200	3.623E - 6	3.623E - 2
800	9.058E - 7	9.058E - 3
10000	5.756E - 9	5.756E - 5

Finally from g²/hz to g response

TABLE 3
Conversion of g²/hz to g response

F _c (hz)	PSD (g ² /hz)	g response
20	9.101E - 4	4
200	3.623E - 2	72
800	9.058E - 3	72
10000	5.756E - 5	20

Fig. 7 shows all four environments plotted in common units of g response versus frequency. If the combined environments are required for the structural analysis, the spectrum (represented by the dash line --- in Fig. 7) can be used instead of analysing every separate load case and then adding the stresses from each load case. This spectrum is a result from adding all four environments shock, acoustic field, sine and random vibration which the plate is subjected to.

It can be seen that the shock environment is dominant for frequencies above 150 Hz while the sine environment is the worst environment for frequencies below 150 Hz. Another advantage to this analysis approach is the ability to add environments together, if required, to do only one stress analysis for the structure under all combined environments since all environments now have common units.

The results of a structural analysis are usually compared to the static material allowables. While this usually produces satisfactory results, it does not take into account the effects of fatigue. Ref. 1 describes a method which allows for this lower dynamic allowable to be used for comparison. This method is applicable for random vibration environments. Acoustic vibration is a form of random vibration, and thus this method applies as well to vibration analysis involving an acoustic spectrum.

This allows for a more comprehensive analysis, especially when fatigue becomes an important consideration.

CONCLUSION

By using the proposed method along with those described in the two references, (1) and (3) it is now possible to quickly determine which environment, of a broader range of environments, will have the worst effect on a structure. This environment can then be used for the final analysis, with the net result being a great savings in analysis time and cost.

REFERENCES

1. S. P. Bhatia and J. H. Schmidt, "Evaluation of Vibration Specifications for Static and Dynamic Material Allowables", the Shock and Vibration Bulletin, Bulletin 56, 1985.
2. George M. Diehl, "Machinery Acoustics", pp. 7-39, Wiley Interscience, 1973.
3. J. H. Schmidt, "Quick Look Assessment and Comparison of Vibration Specifications", the Shock and Vibration Bulletin, Bulletin 51, pp. 73-79, 1981.
4. William W. Seto, "Schaum's Outline Series - Theory and Problems of Acoustics", pp. 37-43, McGraw-Hill, 1971.

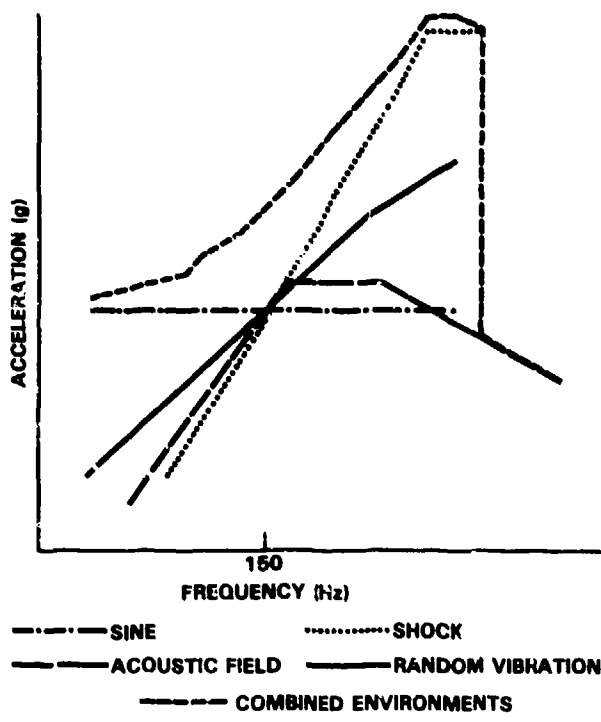


Fig. 7 - Comparison of Environments

FATIGUE EFFECTS OF A SWEPT SINE TEST

A. E. GALEF
TRW ELECTRONICS AND DEFENSE
REDONDO BEACH, CALIFORNIA

There is considerable equipment in the field that was procured before the superiority of a random test over a sinusoidal test was generally acknowledged. This paper develops a procedure which (based upon the usual simplifying assumptions) can be used in some cases to estimate the capability of equipment which has been tested only by an exponential sine sweep to withstand more realistic environments.

Symbols

C	Constant defined in text
D _a	fatigue damage in one cycle of vibration
D _d	fatigue damage done in a sinusoidal dwell at resonance
D _r	fatigue damage done in a random test
D _s	fatigue damage done in a sine sweep
F	Frequency of mode of major response
f	instantaneous frequency
f ₀ , f _f	initial and final frequency of sine sweep
Q	amplification at resonance (frequency F); $Q = 1/(2\zeta)$
R	sweep rate, in octaves/second
R̄	R/number of sweeps (from f ₀ to f _f) in a sweep test
S	sinusoidal excitation amplitude
T _d	time of a sinusoidal dwell test
T _r	time of a random test
W	excitation spectral density at frequencies in the neighborhood of F
Y	exponent of stress in material fatigue expression
ζ	damping in mode of major response, as fraction of critical damping.

INTRODUCTION

In one of my earliest papers (Reference 1) it was claimed that "It is no longer controversial to state that the bulk of vibration which is measured on trucks, aircraft and missiles is random vibration---". Given hindsight, we must recognize that that claim was premature at best; it was not until 23 years after presentation of Reference 1 that the current (D) revision of MIL-STD-810 reflected the acceptance of that verdict, and considerable equipment is still being procured to environmental documents whose vibration tests are limited to sine sweeps.

The question of the ability of equipment in the field, procured under earlier versions of MIL-STD-810 or other equivalent documents, to withstand the more rational vibration tests currently being prescribed is now frequently being asked. Answers are readily constructed, using References 2, 3, subject to the usual simplifying assumptions that-

- The equipment of concern has only one significant (major stress-causing) resonance within the test frequency band. Stress is very nearly proportional to the acceleration response in that mode.
- The equipment is linear and viscously damped; the damping in the major mode is known within reasonable limits.
- The failure mechanism of concern is peak (instantaneous) stress levels. A probabilistic conclusion is acceptable.

If the sinusoidal test that had been performed included dwell at resonance, or if the sine sweep was sufficiently slow and/or the damping was sufficiently high to approach or reach the limiting case (peak response proportional to Q) of the Lewis (Reference 2) study, the procedures involved in comparing the peak response levels of the sinusoidal and random test are shortened slightly, but in this case both the random dwell and the sinusoidal sweep may have sufficient fatigue impact that the "peak level" criteria would, very likely, be insufficient. In this case the third of the "usual simplifying assumptions" cited above would be replaced by the further simplifications:

- The failure mechanism of concern is fatigue.

- The (single-level) fatigue characteristics of all materials of the equipment can be reasonably approximated by straight-line plots of stress vs. number of cycles, on log-log grid. The slopes of these lines are known within reasonable limits.
- Miner's law for cumulative fatigue damage (Reference 4) holds.

For the case of the resonant dwell the comparison of severities is easily derived given the above assumptions. The results, as presented in Reference 5* among others, conclude that equivalent fatigue damage will occur in the same amount of time provided the following relationship between the sinusoidal excitation S and the random spectral density W holds-

$$S = (\pi FW/Q)^{\frac{1}{2}} \quad r\left(\frac{\gamma}{2} + 1\right)^{\frac{1}{\gamma}} \quad (1)$$

If the sinusoidal dwell time, T_d , differs from the random duration T_r , Eq. 1 is modified-

$$S = (\pi FW/Q)^{\frac{1}{2}} \quad \left[\frac{T_r}{T_d} \quad r\left(\frac{\gamma}{2} + 1\right) \right]^{\frac{1}{\gamma}} \quad (2)$$

In response to the practical difficulties in identifying internal resonances the "dwell" portion of sinusoidal tests had been increasingly often deleted from vibration tests. As an example, the "B" (1967) revision of MIL-STD-810 contained a 30 minute dwell at each resonance (up to 4 such resonances) for common carrier transported equipment but the "C" (1975) edition deleted any dwell while retaining 84 minutes/axis of slow sine sweeps. In order to compare the sine sweep of the "C" edition to either the purely random test of the "D" version or the dwell of the "B" version of MIL-STD-810 it is necessary to have an assessment of the damage done by a sweep. While attempting to fulfill the tasks of a recent project I had occasion to search for such an assessment and was surprised by my inability to find in the expected sources the solution to this common and often important problem.

LITERATURE SURVEY

An approach to the problem was provided by Gertel, in Reference 6. He generalized from a sample calculation using low damping (which made stress cycles removed from the peak

[resonant] response cycles have negligible fatigue imprint) and a particular value of γ ($\gamma = 6.5$) to conclude that the sine sweep at a rate sufficiently slow to permit essentially complete resonant build-up, causes approximately one-half as much damage as a sine dwell, at the resonant frequency, for a dwell time equal to the time during the sweep spent within the frequency range ($1 \pm \epsilon$) f_r . He further hypothesized that, because of the interaction between low and high (up to twice as high) levels of stress, the low stress cycles would have more fatigue impact than would be predicted by a direct application of the Miner theory so that it would be reasonable to assume that the damage is as much, instead of one-half as much, in the sweep as in the dwell.

Spence and Luhrs employed the Gertel hypothesis along with assumptions on the interaction of random and swept sinusoidal vibration to develop an approach to "Structural Fatigue under Combined Random and Swept Sinusoidal Vibration", (Reference 7) and, consequently, a reasonable approach to the simpler problem of the sine sweep alone; however, they did not consider a critical examination of the Gertel conjecture necessary in their work, the results of which must be recognized to have uncertain generality.

Morrow (Reference 8) developed the expressions for comparison between the energy dissipated in a sine sweep and the energy* dissipated in a random test. His results are seductive because the "Q" (which is rarely known with precision) has the same weight for energy dissipation in both sine sweep and a random test so that it is not necessary to know the Q. Equivalently, the " γ " does not appear explicitly because the particular value, $\gamma = 2$, is implicit in his solution. However, his results are not applicable to fatigue except for the inordinately low value of $\gamma = 2$ (γ is rarely lower than 6 and, for high cycle fatigue is often more than 10).

Additional and more general results were not found, and it was elected to undertake the study reported on following.

ANALYSIS

Application of the simplifying assumptions cited in the Introduction permit writing the following expression for the fatigue damage caused by a cycle of steady-state response to excitation at frequency f , amplitude A :

* There are changes in notation from that employed by Miles and Thomson in Reference 5.

* It should be appreciated that the Morrow results are for energy and not for power; the sine sweep which develops equal energy in the same time period as a random test would be more likely to cause overheating and failure of isolators.

$$D_a = \frac{C(SQ)^Y}{\left[Q^2 \left(1 - \frac{f^2}{F^2} \right)^2 + \frac{f^2}{F^2} \right]^{Y/2}} \quad (3)$$

The constant "C", depends upon the stress-acceleration transfer function and on the "one cycle" intercept of the linearized (stress - No. cycles) fatigue curve. The definition of the remaining symbols should be sufficiently clear from the notation provided at the beginning of the paper.

For a swept frequency test, it is clear that the time spent while sweeping from f to $f + df$ is

$$dt = df/f \quad (4)$$

and the number of cycles applied during that interval is

$$n(f) = f df/f \quad (5)$$

for an exponential sweep ($f = f_0 * 2^{**} (Rt)$) the operations above lead to

$$n(f) = df/(R \ln 2) \quad (6)$$

The continued application of Miner's Hypothesis permits combining Equation 3, 6 to yield the fraction of damage generated by an exponential sweep.

$$D_s = \sum \frac{n(f)}{N(f)} = \frac{C(SQ)^Y}{R \ln 2} \int_{f_0}^{f_r} \frac{df}{\left[Q^2 \left(1 - \frac{f^2}{F^2} \right)^2 + \frac{f^2}{F^2} \right]^{Y/2}} \quad (7)$$

(If the test under investigation involves several sweeps, Equation 7 should be multiplied by the number of sweeps to yield the total damage done by the test. It will be convenient to do the equivalent by replacing R with R , where $R = R/\text{number of sweeps}$).

It will be apparent that, when $Y = 2$ and when $f_0 < F < f_r$, the integrand of Equation 7 is exactly that involved in evaluating the (rms) response of an oscillator to wide band random excitation. The integration can plainly be performed, and the results are those used by Morrow (Reference 8) in developing his "energy equivalence".

For higher (and therefore more applicable to fatigue) values of Y , attempts to perform the

integration analytically were not successful. A program was written for numerical integration and the integration was performed over the ranges:

$$3 \leq Q \leq 25$$

$$4 \leq Y \leq 16$$

It was found that the results of the integration could be well approximated* by:

$$D_s = \frac{2.27 C (SQ)^Y F}{R Q (1.031 - .127/Y^2) (Y - 1)^{54}} \quad (8)$$

It is seen that the exponent of "Q" in the denominator of Equation 8 differs only slightly from on (1). This is in accordance with the expectations of Gertel, in Reference 6. The additional information added by this work is in the "Y" dependency ($Y - 1.54$) in the denominator.

COMPARISON OF SWEEP TO OTHER TESTS

The damage caused by a sine dwell at the resonant frequency for T_d seconds may be written easily; the damage/cycle is that of Equation 3, for $f = F$. Since the total number of cycles is FT_d , the damage is-

$$D_d = C (SQ)^Y F T_d \quad (9)$$

The damage caused by a random test with acceleration spectral density in the neighborhood of the resonance of W , applied for T_r seconds was developed in Reference 5 in the course of deriving Equation 2.

$$D_r = D F T_r \Gamma(\frac{Y}{2} + 1) (\pi W F Q)^{Y/2} \quad (10)$$

("C" in Equation 3, 7, 8, 9, 10 is the same, since all assumed the validity of Miner's Law which makes no allowance for the interaction between low and high levels of stress. In truth, some allowance should be made for interaction in Equation 8 and a larger allowance should be made in Equation 10. Quantitative recommendations on this line are beyond the scope of this present work).

Equation 8 may be compared to Equation 9 to quantify the relative severity of, for example, the B and C versions of MIL-STD-810. An equivalent evaluation can be made between the

* As with any empirical equation fitting data achieved over a finite range, there is some danger in using the expression for Y or Q much greater than the values of 16, 25, respectively used for numerical integration. For such applications the user should perform his own numerical integration of Equation 7. For high values of "Q", one should be careful that the assumption of essentially full resonant response (Reference 2) is not violated.

effects of the C and D version of that standard if Equation 8 is compared to

Equation 10. In the example following the "normal transport" procedure will be used. This is-

MIL-STD-810-B	MIL-STD-810-C	MIL-STD-810-D
$\pm 1.3g$, 5-27 Hz 0.36 in peak-peak, $27-52$ Hz $\pm 5g$, 52 to 500^*Hz Sweep, plus $1/2$ hour dwell at each resonance (up to four)	$\pm 1.5g$, 5-200 Hz 7 sweeps, 135 sec/octave/sweep $(R = 1/(135*7) = .0010582$	$.015g^2/Hz$ 10-40 Hz 5.5 db/octave roll-off 40-500 Hz 60 Minutes/1000 miles of transport

(In one of the manners in which the "D" version is more rational than its predecessors, the test time is related to the life cycle [60 minutes/1000 miles]. This makes the desired comparison more tenuous, since the test time in the "B", "C" versions is arbitrary. For the present purposes we will let the "D" test time be 2 hours).

Dividing Equation 9 by Equation 8 permits relating the damage caused by a .5 hour dwell (MIL-STD-810-B) to the 84 minutes of sweeping of MIL-STD-810-C. (The pre-dwell sweeping involved in "B" is ignored).

$$\frac{D_d}{D_s} = .84 \left(\frac{1.3}{1.5} \right)^\gamma Q \left(1.031 - \frac{.127}{\gamma^2} \right) (\gamma - 1)^{54}$$

$f < 27Hz$ 11-a

$$= .84 \left(\frac{.00184F^2}{1.5} \right)^\gamma Q \left(1.031 - \frac{.127}{\gamma^2} \right) (\gamma - 1)^{54}$$

$27 < f < 52$ 11-b

$$= .84 \left(\frac{5}{1.5} \right)^\gamma Q \left(1.031 - \frac{.127}{\gamma^2} \right) (\gamma - 1)^{54}$$

$f > 52Hz$ 11-c

It should be clear that, for typical high values of Q , γ , the fatigue damage done by the dwell of MIL-STD-810-B was much greater than that done by the later, C version of the same standard.

The equivalent comparison between the sweep of "C" (Equation 8) and the random test (Equation 10) of the current, "D" version yields-

$$\frac{D_r}{D_s} = \frac{3.36 \Gamma(\frac{\gamma}{2} + 1) (\gamma - 1)^{54} (.047 F)^{\gamma/2}}{1.5^\gamma Q^{(\gamma/2-1.031 + .127/\gamma^2)}}$$

$F < 40$ 12-a

$$= \frac{3.36 \Gamma(\frac{\gamma}{2} + 1) (\gamma - 1)^{54} (40.27/F^3)^{\gamma/2}}{1.5^\gamma Q^{(\gamma/2-1.031 + .127/\gamma^2)}}$$

$F > 40$ 12-b

Conclusions regarding the relative severity are not obvious from inspection of Equation 12. The comparison may be readily evaluated, however, for specific values of Q , γ . To that end, the evaluation will be made for the cases of $Q=5$ and 10 , γ of 8 and 16 . The results are:

Relative Severity of Random & Sine-Sweep Tests

γ	Q		$F < 40$
	5	10	
8	2.7 E-7 F4	4.7 E-8 F4	
16	2.8 E-13 F8	2.3 E-15 F8	
8	2 E5/F3.3	2.5 E4/F3.3	
16	8 3 E10/F6.6	6.6 E8/F6.6	

$F > 40$

It may be seen that, for a low F (typical of a shipping container suspension, for example) the random test of MIL-STD-810-D is much less severe than the sweeps of MIL-STD-810-C. For frequencies in the neighborhood of 40-50 Hz (typical of electronic assembly without vibration mounts) the random test and the sine sweep are comparable in damage potential,

* Upper frequency reduced for heavy items.

while for high frequencies the random test is again relatively benign. But the most important message of Equation 12 and the table is the clear emphasis that it is not possible to make an evaluation regarding relative severity unless the usual assumptions are justified and Q , γ , F are all reasonably known; the hope implicit in the "Energy Equivalence" of Reference 8 and the partial hope of Reference 6 has been dashed!

CONCLUSIONS

The task of comparing the severity of qualitatively different vibration excitations has been confirmed to be neither more rigorous nor simpler when one of the forms of vibration considered is a slow sine sweep. As in the case of a resonant dwell it remains necessary to make "the usual assumptions" (a single response mode of importance; linear and viscously damped response; no damping-coupling of modes; the damage mechanism of concern is known; if fatigue is the likely damage mechanism damage accumulates linearly; fatigue characteristics of all materials are reasonably known and representable by a monomial exponential function; damping in response mode of concern is reasonably known). If there is question about the validity of those assumptions (and there usually is!) or if the assumptions regarding quantitative knowledge of damping (contained in the "Q" of the text) or the fatigue behavior (contained in the " γ " of the text) can not be replaced with conservative assumptions without yielding an excessively pessimistic conclusion regarding the capabilities of the equipment of concern then there appears no recourse other than performing a test to the "new" environment.

REFERENCES

1. Galef, A. E. "Application of Modulated Sinusoids in Vibration Testing". Paper A-1, 59 Meeting of Acoustical Society of America, June 1960.
2. Lewis, F. M. "Vibration During Acceleration Through A Critical Speed". Trans. ASME 54:253 (1932).
3. Morrow, C. T. and R. B. Muchmore. "Shortcomings of Present Methods of Measuring and Simulating Vibration Environments". J. Applied Mechanics, Volume 22 Number 3. (1955)
4. Miner, M.A. "Cumulative Damage in Fatigue". J. Applied Mechanics, Volume 12 Number 3. (1945).
5. Miles, J. W. and W. T. Thomson. "Statistical Concepts in Vibration". Page 11-15. Shock and Vibration Handbook. (Harris and Crede, Editors). McGraw Hill Book Company, 1961.
6. Gertel M. "Specifications of Laboratory Tests". Page 24-17, 24-18. Shock and Vibration Handbook (Harris and Crede, Editors). McGraw Hill Book Company, 1961.
7. Spence, H. R. and H. N. Luhrs. "Structural Fatigue under Combined Random and Swept Sinusoidal Vibration". J. Acoustical Society of America, Volume 34 Number 8, August 1962.
8. Morrow, C. T. "Environmental Specifications and Testing". Page 24-10, Shock and Vibration Handbook. (Harris and Crede, Editors). McGraw Hill Book Company. Second Edition, 1976.

STATISTICAL MEASURES OF CLIPPED RANDOM SIGNALS

Thomas L. Paes
David O. Smallwood

Experimental Mechanics Department
Sandia National Laboratories
Albuquerque, New Mexico

Abstract

It is shown that substantial and yet difficult to detect errors may occur if random data are clipped and then filtered. For stationary random processes formulas are presented for the spectral density (power spectrum) of the clipped and filtered random process in terms of the spectral density of the original random process, the clipping level, and the gain characteristics of the filter. A nonstationary random process that is formed by summing components, each of which is a stationary, band-limited random process modulated by a deterministic function of time, is also analyzed. Estimates of the mean square output (the clipped and filtered input) are given. Examples are given that illustrate the problem of difficult to detect errors for both stationary and nonstationary cases. An overload detector is suggested which could significantly reduce the probability of this error.

1. Introduction

The output of transducers used to measure structural response is seldom directly used. More typically the transducer output is conditioned before recording. The signal conditioning typically involves several stages of conversion, amplification, filtering, and transmission (not necessarily in that order) before the data are recorded.

The structural response being measured is often random in nature. In these cases useful statistical measures of the data, like spectral densities, probability densities, root-mean-square (rms), and time history realizations are estimated to characterize the response.

For example, the response measured could be the acceleration of a point on the structure. The transducer could be a piezoelectric accelerometer. The output of the transducer is charge. The charge is converted to voltage,

amplified, filtered (either with a low pass filter or by the bandwidth characteristics of the amplifiers) to limit the bandwidth, transmitted either by wire or by telemetry, and then recorded. The recorded data are then analyzed.

It has recently been pointed out by Nelson [1] that substantial and yet difficult to detect errors may occur if the data are clipped prior to being filtered. These errors can be detected if the data are observed before any filtering, but the data systems often exclude this observation. Examples include, transducers with internal electronics preventing the user from observing the unconditioned data, and transducers on unmanned flight vehicles where distance and telemetry systems prevent the user from observing the unconditioned data. The resulting statistical measures of the clipped and filtered data can appear plausible and yet be inaccurate. For example, the estimated spectral density can have approximately the correct shape, but the

magnitudes can be seriously underestimated. The data can appear nearly Gaussian, but in fact be severely clipped. Nonstationary data can appear nonstationary in a plausible way, but in fact be in serious error.

The related problem of distortion induced errors has been considered by several authors. See, for example, References 2 through 4. The objective of this investigation is to quantify errors due to clipping and filtering, and discuss the conditions under which the errors can occur. It is shown that while clipping before filtering can lead to plausible but inaccurate results, clues often exist which, with careful examination, will suggest the data are in error. However, the risk of erroneous data is large enough that some simple data system features are suggested that would substantially reduce the chances of accepting inaccurate data and response measures.

2. Preliminary Examples

In order to illustrate the potential problem, some specific situations are considered. Vibration response in mechanical structures is measured using a linear characteristic acceleration transducer. The charge generated by the accelerometer is first converted to a voltage. This stage is usually designed very conservatively because if this section is overloaded the amplifier recovers slowly. The charge converter is usually followed by one or more stages of amplification. If these stages are overdriven they usually hard clip. The result is a charge converter and amplifier with the characteristics shown in Figure 1. The amplifier output is then typically low pass filtered either by a separate filter or by the

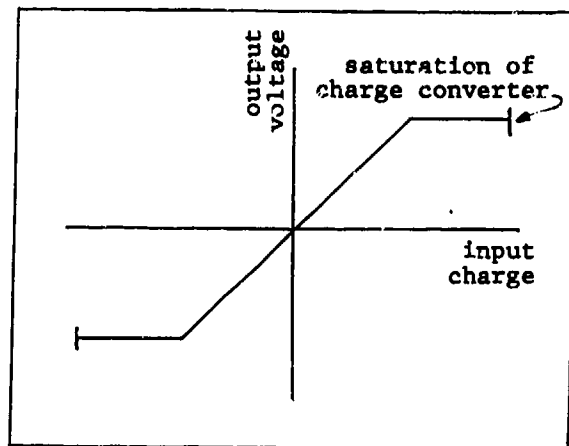


Figure 1. Gain characteristics of a typical charge amplifier.

bandwidth characteristics of the transmission system or recording system, and then recorded. Figure 2 is a simplified diagram of a typical system.

Several problems can occur in the process of measurement, transmission and recording of acceleration signals. The one to be considered in this investigation is what happens when the acceleration signal to be measured has amplitude peaks that are far beyond the values for which the instrumentation is ranged. In this situation the accelerometer generates charge that is far beyond the linear range of the charge amplifier. The result is a clipped signal, and experiments have shown that when this happens typical charge amplifiers yield a cleanly clipped signal. Clean clipping (i.e. clipping that leaves no jagged edges) is assumed in this study.

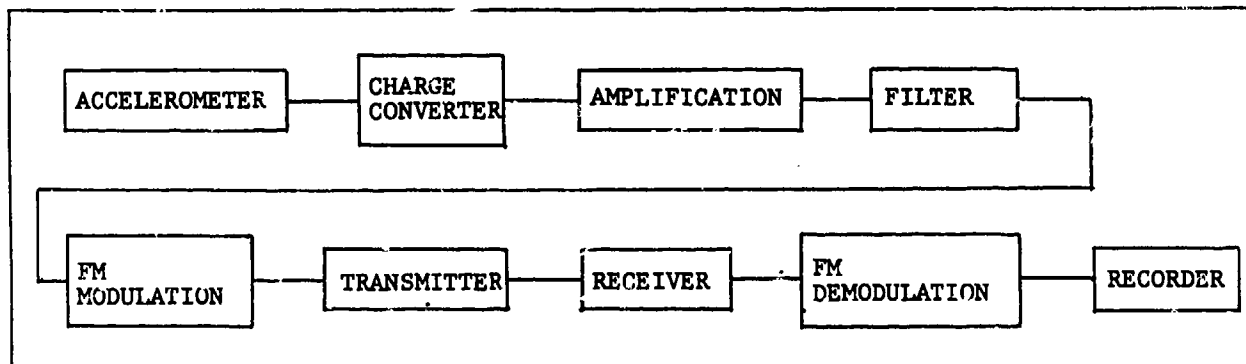


Figure 2. Simplified diagram of typical telemetry data channel.

In the first example a weakly stationary, normal random process is considered. The source has mean zero and the spectral density shown in Figure 3. (This is the spectral density of absolute acceleration response to acceleration excitation of a single-degree-of-freedom (SDF) system.) The rms value of the random process is 6.31, and the clipping level is chosen as 0.63 times the rms value. (In this paper the signals are unitless, but the signals, spectral densities, etc., could be taken as having any consistent set of units.) It can be shown that the spectral density of the clipped and filtered random process is that shown in Figure 4. If one is simply interested in knowing the spectral density of a random process and expects to see the characteristic peak related to SDF system response, then the spectral density shown in Figure 4 may appear plausible even though its rms value is only 3.29 and an extra peak occurs at triple the natural frequency of the SDF system. (The reason for appearance of this peak will be addressed later.) Figure 4 characterizes a signal that is substantially less severe than the actual environment characterized by Figure 3.

It may seem that clipping should be readily apparent in the time history, but it may not be apparent because of the filtering operation. For example, a clipped and filtered realization of the random process whose spectral density is shown in Figure 3, is shown in Figure 5. No clipping is obvious.

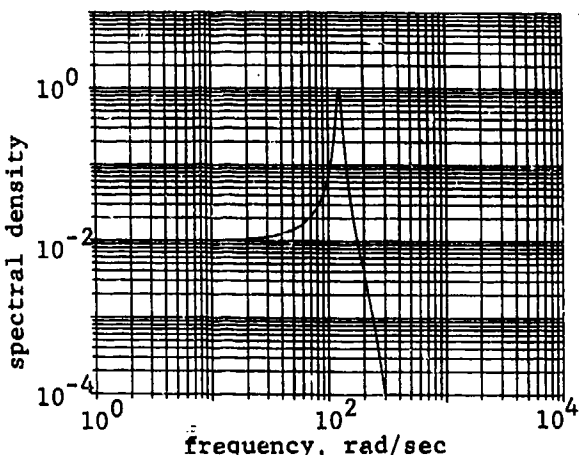


Figure 3. Spectral density of a normal random process.

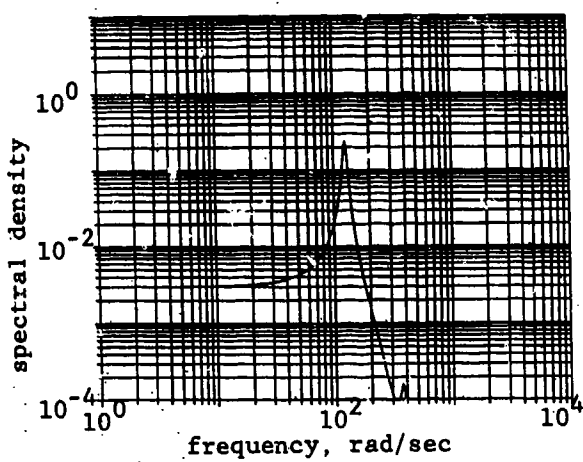


Figure 4. Spectral density of the clipped and filtered random process. Spectral density of the underlying source is shown in Figure 3. Clipping level = 4. Filter: four stage Butterworth with cutoff frequency of 251 rad/sec. (40 Hz)

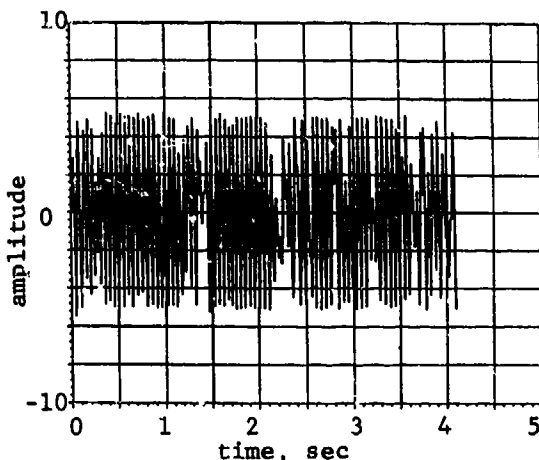


Figure 5. Time history of a clipped and filtered version of the source whose spectral density is Figure 3. Clipping level = 4. Filter: four stage Butterworth with cutoff frequency of 251 rad/sec (40 Hz).

During certain portions of some responses a nonstationary random process realization is expected. Consider now the way in which a realization of a nonstationary random process is affected by clipping and filtering. Figure 6 shows a realization of an oscillatory nonstationary random process. This comes from a source that has a nonstationary low frequency component and a stationary high frequency component.

The low frequency component consists of subcomponents in the frequency range from 6 through 1257 rad/sec (1 through 200 Hz). The high frequency component consists of subcomponents in the frequency range from 1257 through 2513 rad/sec (200 through 400 Hz). The rms value of the low frequency component is a pulse superimposed atop a constant. The high frequency component has a constant rms value. When this signal is clipped and filtered using a clipping level of 10000, the result is the signal shown in Figure 7. Though the signals shown in Figures 6 and 7 do not appear to have precisely the same nonstationary character, it is certainly conceivable that the signal in Figure 7 could be accepted as a plausible representation of the environment affecting the system if the true level of the response were unknown.

The above two examples show cases where a modest amount of energy above the filter cut off frequency exists in the original signal. As a result peaks exist in the clipped and filtered signal which are near or even above the clipping level. This could lead one to conclude that peaks near the clipping level in the final data would indicate clipping. But other examples could be given, which had more original high frequency energy, where the peaks of the clipped and filtered signal are well below the clipping level. This further increases the plausibility of the data.

The examples presented above show that under some circumstances (not defined at this point) random process realizations that are clipped and filtered can be mistaken for plausible representations of random process sources. The objective of this investigation is to quantitatively characterize what conditions are required to make this mistake a possibility.

3. Analysis of Clipped and Filtered Stationary Random Processes

3.1 Preliminary Discussion

Given the spectral density or autocorrelation function of an underlying random process and the clipping level and filter characteristics (when the random process is filtered), it is possible to approximate the spectral density and autocorrelation function of the clipped and filtered random process. This is done by (1) approximating the autocorrelation function of the clipped random process as a function of the autocorrelation function of the underlying random process, (2) Fourier

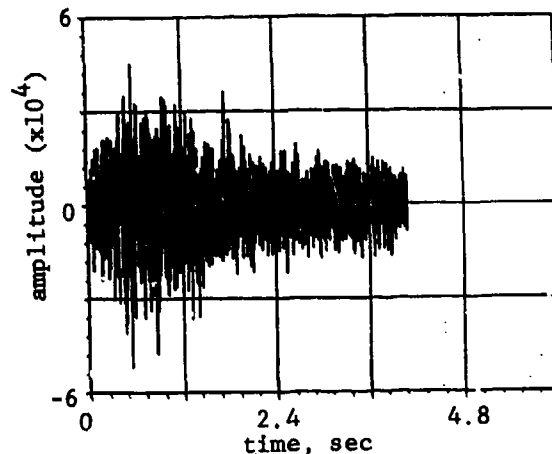


Figure 6. Time history of a nonstationary random process.

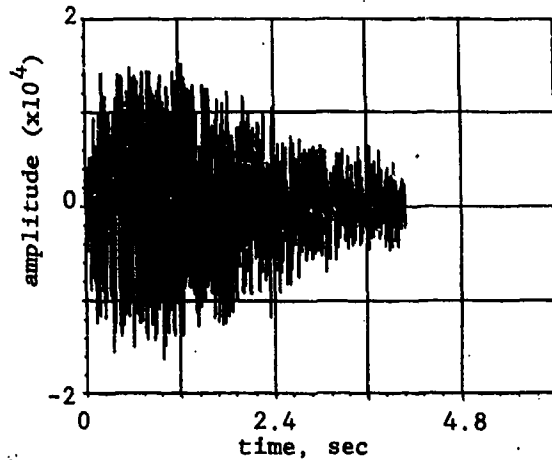


Figure 7. Time history of a clipped and filtered version of the signal in Figure 6. Clipping level = 10000. Filter: four stage Butterworth with cutoff frequency of 1257 rad/sec (200 Hz)

transforming the autocorrelation function to obtain the spectral density of the clipped random process, (3) multiplying the resulting spectral density by the filter gain to obtain the spectral density of the clipped and filtered random process (when the random process is filtered), and (4) inverse Fourier transforming the result to obtain the autocorrelation function of the clipped and filtered random process.

The first step in the above process, approximating the autocorrelation function of the clipped and filtered random process in terms of the autocorrelation function of the underly-

ing random process, yields two formulas; each formula is applicable under different circumstances. One formula for the approximation of the autocorrelation function of a clipped random process is known as the arcsine formula. It is available in the literature (Reference 5) and is applicable in situations where the underlying signal is hard-clipped. (Hard-clipping refers to clipping that occurs at a level that is a fraction of the standard deviation of the original signal.) The other formula involves writing the autocorrelation function of a clipped random process as a cubic function of the autocorrelation function of the underlying random process. This latter formula is derived in this section with additional development in the Appendix.

After development and presentation of the formulas described above some examples that show the spectral density of some clipped and filtered random processes are presented.

3.2 Analysis

The problem to be investigated in this portion of the study is the characterization of stationary signals that have been clipped and then filtered. Consider a stationary random process $\{X(t)\}$ that is normally distributed, has mean zero, autocorrelation function $R_{xx}(\tau)$, spectral density $S_{xx}(\omega)$, and standard deviation σ . A clipped version $\{Y(t)\}$ of the original random process can be established by operating on the original random process as follows.

$$Y(t) = X(t) - H(X(t)-a)[X(t)-a] - H(-X(t)-a)[X(t)+a] \quad (1)$$

where $H(\cdot)$ is the Heaviside unit step function and a is the clipping level. The second term on the right clips the positive peaks. The third term on the right clips the negative peaks. The mean of the random process $\{Y(t)\}$ is zero because the underlying random process has zero mean and normal distribution and $Y(t)$ is an odd function of $X(t)$.

The autocorrelation function of the random process $\{Y(t)\}$ can be obtained by multiplying $Y(t)$ by $Y(t+\tau)$ and taking the expected value. $\{Y(t)\}$ is a stationary random process because $\{X(t)\}$ is a stationary random process and $\{Y(t)\}$ simply clips the peaks on $\{X(t)\}$; therefore, its autocorrelation function is simply a function of τ . The autocorrelation function is, by definition,

$$R_{yy}(\tau) = E[Y(t)Y(t+\tau)] \quad (2)$$

When (1) is used in (2) along with the fact that $\{X(t)\}$ is a normal random process, it can be shown that the autocorrelation function of $\{Y(t)\}$ is approximately

$$R_{yy}(\tau) \approx [1 + 4(a_1 - b_1)]R_{xx}(\tau) + \frac{4a_3}{\sigma^4} R_{xx}^3(\tau) \quad (3)$$

The coefficients of $R_{xx}(\tau)$ and $\sigma^{-4}R_{xx}^3(\tau)$ in the above equation are functions of the ratio of clipping to rms input level, a/σ , and are plotted in Figure 8. The mathematics that link (2) to (3) are given in the Appendix. The autocorrelation function, $R_{yy}(\tau)$, has the desirable characteristics that as the ratio a/σ approaches zero, the autocorrelation function approaches zero, and as the ratio approaches infinity, the autocorrelation function approaches $R_{xx}(\tau)$.

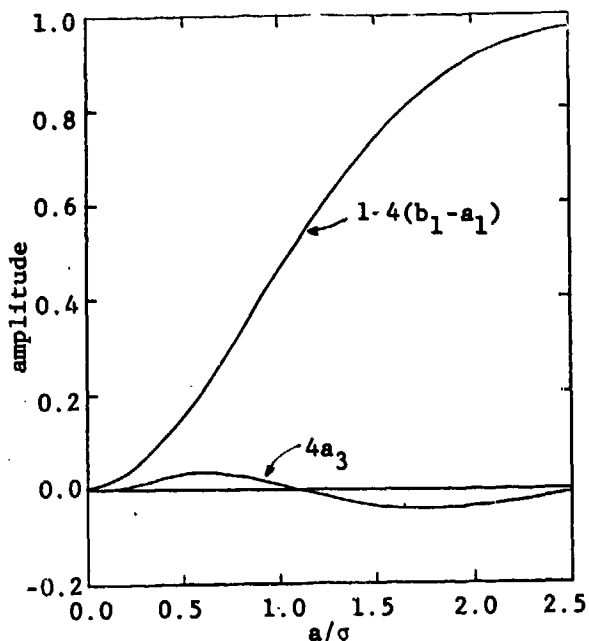


Figure 8. Coefficients of the terms in (9).

The spectral density of the clipped random process can be obtained directly by Fourier transforming the result given in (3). The spectral density is

$$S_{yy}(\omega) = [1 - 4(b_1 - a_1)]S_{xx}(\omega) + \frac{4a_3}{\sigma^4} \frac{1}{2\pi} \int_{-\infty}^{\infty} R_{xx}^3(\tau) e^{-i\omega\tau} d\tau . \quad (4)$$

The second term on the right-hand side is the Fourier transform of the cube of the autocorrelation function of the underlying random process. This operation must usually be executed numerically, though, under some circumstances, it may be performed in closed form. The second term can also be written as a double convolution of the spectral density terms.

We can make a few general comments about the shape of the spectral density of the second term in (4). If the autocorrelation function, $R_{xx}(\tau)$, can be written as a Fourier series we can see that the cubing operation will generate third harmonic and sum-and-difference frequencies. The net result will be a spectral density that is broader-band and more-white than $S_{xx}(\omega)$. The same result can be noted by observing that $R_{xx}^3(\tau)$ will tend to be of shorter duration than $R_{xx}(\tau)$. This also implies that $R_{xx}^3(\tau)$ will have a broader bandwidth than $R_{xx}(\tau)$. The means by which and degree to which the bandwidth is broadened becomes apparent when it is noted that the second term in (4) is the convolution of $S_{xx}(\omega)$ with itself, and the convolution of the result with $S_{xx}(\omega)$. Each convolution yields a broader band result.

The formulas developed above are only applicable when the clipping level is greater than one fourth the standard deviation of the underlying random process source. However, when the clipping level is lower than one fourth the standard deviation of the underlying source, an approximation for the statistics of the clipped signal can still be obtained by use of the arcsine formula. It is assumed that a clipped signal, $Y(t)$, can be modeled as

$$Y(t) = a[H(X(t)) - H(-X(t))] \quad (5)$$

where $X(t)$ is the underlying signal, $H(\cdot)$ is the Heaviside unit step function, and a is the clipping level. When

a random process $\{Y(t)\}$ is formed by clipping a random process $\{X(t)\}$ as in the above formula, the autocorrelation function of the clipped random process, $\{Y(t)\}$, is

$$R_{yy}(\tau) = \frac{2a^2}{\pi} \sin^{-1} \left(\frac{R_{xx}(\tau)}{\sigma^2} \right) \quad (6)$$

where, as before, $R_{xx}(\tau)$ is the autocorrelation function of the underlying random process. Reference 5 provides the derivation of this formula.

This is a random telegraph signal whose sign is determined by the sign of the underlying signal, $X(t)$. The approximation lacks perfect accuracy because the model does not allow for the finiteness of the slopes of the realizations of $\{X(t)\}$ for $-a < X(t) < a$. However, when the clipping level, a , is much smaller than the rms value, σ , of the random process $\{X(t)\}$, little information is lost in using the approximation. Note that the Taylor series expansion for $\sin^{-1}(x)$ is a sum involving the odd powered terms of x , therefore, when (6) is written in series form it resembles the expression for $R_{yy}(\tau)$ in (3).

The spectral density of the clipped random process can be obtained directly by Fourier transforming the autocorrelation function in (6). The spectral density is

$$S_{yy}(\omega) = \frac{a^2}{\pi^2} \int_{-\infty}^{\infty} \sin^{-1} \left(\frac{R_{xx}(\tau)}{\sigma^2} \right) e^{-i\omega\tau} d\tau . \quad (7)$$

For most underlying random processes the autocorrelation function will be complicated, therefore, the spectral density cannot be evaluated in closed form.

As mentioned previously, the situation of interest in this analysis concerns a signal that is both clipped and then filtered. The formulas describing the approximate spectral density of a clipped, stationary random process are given in (4) and (7). To consider the effects of filtering on the spectral density of the random process, let $\{Z(t)\}$ be a random process that is the filtered version of $\{Y(t)\}$. Let $H(\omega)$, $-\infty < \omega < \infty$, denote the frequency response function of the filter and $|H(\omega)|^2$ its magnitude squared. Then the spectral density of $\{Z(t)\}$ is

$$S_{zz}(\omega) = |H(\omega)|^2 S_{yy}(\omega) . \quad (8)$$

The autocorrelation function of the clipped and filtered random process, $\{z(t)\}$, can be obtained by Fourier transforming its spectral density.

In summary, to find the effects of clipping and filtering on a stationary, mean zero, normal random process, one must first approximate the autocorrelation function of the clipped random process using (3) or (6), depending on the clipping level. Next, the Fourier transform of the autocorrelation function must be taken to obtain the spectral density as in (4) and (7). Finally, the effect of filtering must be established using (8).

3.3 Discussion and Example

The expressions for the spectral density of a clipped and filtered random process are developed in the previous section. The spectral density is given by (8) and, depending on the clipping level, this formula uses (4) or (7) to express the spectral density of a clipped random process. These expressions, in turn, rely upon (3) and (6) for their character. The functions in (3) and (6) express the autocorrelation function of a clipped random process in terms of the autocorrelation function of an underlying normal random process. The functions in (3) and (6) are similar in character; their effect is to distort the values of

$R_{xx}(\tau)$ to yield values of $R_{yy}(\tau)$. In both (3) and (6) the functions on the right hand side have a strong linear component followed by a weaker cubic component. (The arcsine formula includes all odd-powered components; as the degree of the component increases, its contribution diminishes.) A scale factor on each function causes the root-mean-square of the clipped signal to be equal to or lower than the clipping level.

The form of the functions in (3) and (6), the autocorrelation function of the clipped random process, has a strong influence on the spectral density of the clipped signal. For simplicity, consider (3). If $R_{xx}(\tau)$ can be expressed as a Fourier series, then each harmonic term in $R_{xx}(\tau)$ is affected by the operation on the right hand side in (3). The first operation on the right hand side in (3) simply scales the value of the underlying harmonic term. The second operation in (3) cubes the underlying harmonic term producing, in the process, a component with triple the frequency of the original, then it scales this result. When the entire Fourier series

representing $R_{xx}(\tau)$ is cubed, the overall effect of each term producing a component with triple its frequency is maintained. Beyond this, components with many other frequencies are produced by the interaction between terms. Yet the production of "triple-frequency" terms is a strong effect and will frequently be noted. In (6) the influence of the cubic term is also strong and the production of higher harmonic terms as described above can also be noted.

An example that expands on the preliminary example in Section 2 will demonstrate the point described above. Recall that Figure 3 shows the spectral density of a mean zero, weakly stationary, normal random process. The spectral density is sharply peaked, therefore, the appearance of higher order harmonics upon clipping of the underlying random process should be plainly apparent. In fact, when (3) and (4) are used to establish the spectral density of the clipped random process, Figure 9 results. The contribution to the spectral density of the clipped random process at triple the frequency of the fundamental contribution is present as predicted. The ratio between the spectral density ordinates of the fundamental and harmonic contributions is about 50 to one indicating a ratio of contributions to the clipped random process rms of about seven to one.

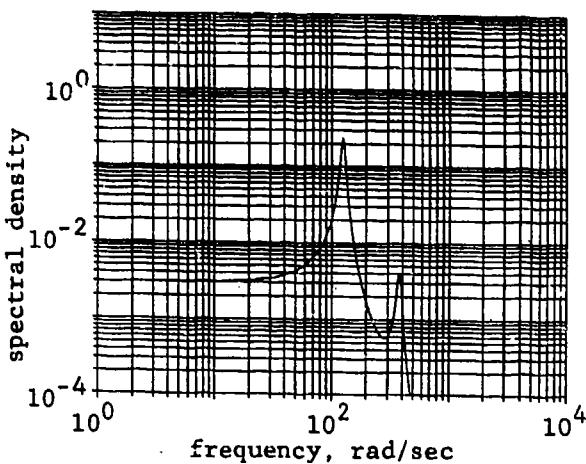


Figure 9. Spectral density of a clipped random process. The spectral density of the underlying random process is shown in Figure 3. Clipping level = 4.

When the clipped random process is filtered using a four-stage Butterworth filter with cutoff frequency of 251 rad/sec (40 Hz) Figure 4 results. The presence of the peak at 377 rad/sec (60 Hz) goes almost unnoticed even in this simple, idealized example. This is always a potential effect with filtering. In a more complicated situation where contributions to the mean square occur at many frequencies, the production of mean square contributions at harmonic frequencies can go unnoticed much more easily. Even if it is recognized that mean square contributions are occurring at frequencies exactly triple the frequencies where more substantial contributions are occurring, the data analyst cannot judge whether this effect is caused by clipping of the measured data or true nonlinearity in structural response. (Structural response nonlinearity can certainly cause this effect.) Therefore, a means is required for judging whether or not clipping of measured data has occurred. This will be discussed later in the paper.

4.0 Clipped and Filtered Nonstationary Random Processes

4.1 Preliminary Discussion

The problem of predicting the behavior of a clipped and filtered, nonstationary random process is more difficult than analysis of a stationary random process. However, there are nonstationary random process models which include a high degree of generality and which can be operated on, that lead to conclusions useful in assessing the practical behavior of clipped and filtered, nonstationary random processes. Such a model is specified in the following section along with the equations necessary to approximately evaluate the mean square of a clipped and filtered version of the random process. It is rather difficult to establish specific behavior directly from the equations as written, therefore, two specific cases are considered. Finally, discussion and an example are presented.

As stated in the Introduction, the present problem is to establish the conditions under which the realization of a clipped and filtered, nonstationary random process might reasonably be mistaken for a realization of the underlying random process. It is clear that, if the clipping level is of the same order of magnitude as the highest values in the realization of the underlying random process, some confusion might easily occur. The highest values in the realization of the clipped and filtered

random process would simply be somewhat lower than the highest values in the realization of the underlying random process, and the low values in both random processes would be the same. A more difficult problem exists when the clipping level is low compared to all values in the realization of the underlying random process. In this case it is not obvious how the realization of the clipped and filtered random process could exhibit any nonstationary trend. This is the problem investigated in these sections.

4.2 Analysis

The problem to be investigated in this portion of the study is the characterization of nonstationary random signals that have been clipped and then filtered. Consider a mean zero, nonstationary random process $\{X(t)\}$ that has normal distribution and the component form

$$X(t) = \sum_{k=1}^M A_k(t)W_k(t) \quad -\infty < t < \infty . \quad (9)$$

The random process is formed from M component random processes. The $A_k(t)$, $-\infty < t < \infty$, $k=1, \dots, M$, are deterministic functions of time defined for all times, and the $\{W_k(t)\}$, $-\infty < t < \infty$, $k=1, \dots, M$, are mean zero, normal, stationary random processes with spectral densities, $S_k(\omega)$, $k=1, \dots, M$. The spectral densities are defined to be nonzero for $\omega_{1k} \leq |\omega| \leq \omega_{2k}$, $k=1, \dots, M$, where $\omega_{2k} = \omega_{1,k+1}$, $k=1, \dots, M$; that is, the component random processes do not overlap in the frequency domain. Furthermore, the component random processes $\{W_k(t)\}$ and $\{W_l(t)\}$ are statistically independent for $k \neq l$. Each function $A_k(t)$ is defined to be "slowly varying" with respect to the time scale $2\pi/\omega_{1k}$. The mean square of the component random process $\{W_k(t)\}$ is denoted σ_k^2 , $k=1, \dots, M$, and is defined

$$\sigma_k^2 = \int_{-\infty}^{\infty} S_k(\omega) d\omega , \quad k=1, \dots, M . \quad (10)$$

At time t a spectral representation of the random process $\{X(t)\}$ is available and is given by

$$S_{xx}(\omega, t) = \sum_{k=1}^M A_k^2(t) S_k(\omega) . \quad (11)$$

This is obtained by Fourier transforming the expected value of $X(t)$ times $X(t+\tau)$ with respect to τ , and noting that $A_k(t)$ varies slowly. This can be interpreted as the spectral density of $\{X(t)\}$ at time t . The mean square of the random process at time t is

$$\sigma_x^2(t) = \sum_{k=1}^M A_k^2(t) \sigma_k^2 \quad (12)$$

Based on (4), a spectral description for $\{Y(t)\}$, the clipped form of $\{X(t)\}$, can be established at time t . It is

$$\begin{aligned} S_{yy}(\omega, t) &= Q_1 \left(\frac{a}{\sigma_x(t)} \right) S_{xx}(\omega, t) \\ &+ Q_2 \left(\frac{a}{\sigma_x(t)} \right) S_{xx}^{(3)}(\omega, t) \\ &- \infty < \omega < \infty, -\infty < t < \infty \end{aligned} \quad (13)$$

The clipping level is a , which is small compared to the rms of $\{X(t)\}$, $\sigma_x(t)$. The function $Q_1(a/\sigma_x(t))$ represents the coefficient of the first term on the right hand side in (4). The function $Q_2(a/\sigma_x(t))$ represents the coefficient of the second term on the right hand side in (4). Based on the expressions given in the Appendix, b_1 , a_1 , and a_3 can be evaluated for small values of $a/\sigma_x(t)$, yielding expressions for $Q_1(a/\sigma_x(t))$ and $Q_2(a/\sigma_x(t))$, as

$$Q_1(a/\sigma_x(t)) \approx \frac{2}{\pi} \left(\frac{a}{\sigma_x(t)} \right)^2$$

$$a \ll \sigma_x(t) \quad (14a)$$

$$Q_2(a/\sigma_x(t)) \approx 0.09 \left(\frac{a}{\sigma_x(t)} \right)^2$$

$$a \ll \sigma_x(t) \quad (14b)$$

Because $Q_2(x)$ is smaller than $Q_1(x)$, and because the second term in (13) is, basically, a producer of higher harmonics, the second term in (13) is dropped to form the following approximation for $S_{yy}(\omega, t)$.

$$S_{yy}(\omega, t) = Q_1 \left(\frac{a}{\sigma_x(t)} \right) S_{xx}(\omega, t),$$

$$-\infty < \omega < \infty$$

$$-\infty < t < \infty \quad (15)$$

The filtered form of the clipped random process is the quantity of interest in this analysis, and the mean square of this quantity provides one measure useful in judging the non-stationarity of the random process. The effect of a low pass filter is to retain low frequency components and to eliminate high frequency components, therefore, a filtered version of $\{Y(t)\}$, denoted $\{Z(t)\}$, might simply eliminate high frequency components in $\{Y(t)\}$ and retain low frequency components. Let ω_c be the cutoff frequency of the filter, and let $\omega_{2M_c} = \omega_c$ be the upper frequency of the band corresponding to the component numbered M_c in $\{X(t)\}$. Then the mean square of $\{Z(t)\}$ at time t is

$$\sigma_z^2(t) = \int_{-\omega_c}^{\omega_c} S_{yy}(\omega, t) d\omega, -\infty < t < \infty \quad (16)$$

From (12), (14a), (15) and (16) the approximate expression for the mean square of the clipped and filtered random process is

$$\sigma_z^2(t) \approx \frac{2}{\pi} \frac{a^2}{\sum_{k=1}^M A_k^2(t) \sigma_k^2} \sum_{k=1}^{M_c} A_k^2(t) \sigma_k^2,$$

$$-\infty < t < \infty \quad (17)$$

This function will not, in general, be a constant, and, in fact, depends on the relationship between the low frequency parameters of $\{X(t)\}$, $A_k(t)$ and σ_k^2 , $k=1, \dots, M_c$, and the high frequency parameters of $\{X(t)\}$, $A_k(t)$ and σ_k^2 , $k=M_c+1, \dots, M$. Further, recall that the second term in (13) was discarded to develop (17). The omitted term would certainly have some effect on the mean square of $\{Z(t)\}$, but it can safely be said that when the right side of (17) is a time varying function, inclusion of the omitted term would rarely, if ever, change this.

Consider some special cases to clarify the behavior of a clipped and filtered random process. First, consider the case where

$$A_k(t) = A(t) \quad k=1, \dots, M \\ -\infty < t < \infty \quad . \quad (18)$$

This is the case where all the coefficient functions causing nonstationarity in $\{X(t)\}$ are identical. Use of (18) in (17) permits the factorization and cancellation of the $A_k(t)$ terms yielding the result

$$\sigma_x^2(t) = \frac{2}{\pi} a^2 \frac{\sum_{k=1}^{M_c} \sigma_k^2}{\sum_{k=1}^M \sigma_k^2}, \quad -\infty < t < \infty \quad . \quad (19)$$

This result is not a function of time. Therefore, based on this approximate analysis, it can be concluded that the mean square of a hard clipped and filtered, nonstationary random process is a constant if every frequency component in the underlying nonstationary random process is modulated with the same function.

As a second special case, let $M=2$ and $M_c=1$. Then the approximate mean square of $\{Z(t)\}$ is

$$\sigma_x^2(t) = \frac{2a^2}{\pi} \frac{1}{1 + \left\{ \left(\frac{A_2(t)}{A_1(t)} \right) \left(\frac{\sigma_2}{\sigma_1} \right)^2 \right\}} \\ -\infty < t < \infty \quad . \quad (20)$$

The mean square is a function of time, but the degree of variation will be quite weak if $A_2(t)$ is much less than $A_1(t)$ and/or σ_2 is much less than σ_1 . In view of this approximate analysis, it can be concluded that when a nonstationary random process consists of two component parts, as defined in (14), the clipped and filtered form of the random process will have a nonconstant mean square if $A_1(t) \neq A_2(t)$. The variation

in $\sigma_x^2(t)$ will be substantial if the term in braces on the right in (20) varies greatly from values less than one to values much greater than one.

4.3 Discussion and Example

The analysis in the previous section showed that the mean square value of a clipped and filtered, nonstationary random process is not necessarily a constant. In fact, the approximate analysis shows that the mean square of a clipped and filtered, nonstationary random process will rarely be a constant. The analysis relied upon the simplification of a spectral expression for the clipped and filtered random process, but it probably does not affect the accuracy of the main conclusion, that is, that a hard clipped and filtered, nonstationary random process can display nonstationary behavior. The reason for this is that the term eliminated in (13) will probably almost never cause an expression like (17) to appear to be a constant; this would require very complicated and restrictive behavior of the elements of (9).

We cannot specify, in general, what behavior is required of the elements of (9) in order to yield a clipped and filtered, nonstationary random process that displays a specific behavior. However, an example is presented that shows, for one specific case, the results that can occur. This is an expansion of the preliminary example in Section 2. In the preliminary example it was stated that Figure 6 represents a realization of a nonstationary random process. In fact, the nonstationary random process has two components; realizations of those component random processes are shown in Figures 10 and 11. Figure 10 is the low frequency component. It is a four second segment of band-limited white noise with signal content in the range 6 rad/sec through 1257 rad/sec (1 Hz through 200 Hz) and spectral density, $400 \text{ (rad/sec)}^{-1}$, multiplied by the modulating function

$$A_1(t) = 1 + 50 e^{-1.5t}, \quad t \geq 20. \quad (21)$$

Figure 11 is the high frequency component. It is a four second segment of band-limited white noise with signal content in the range 1257 rad/sec through 2513 rad/sec (200 Hz through 400 Hz), and spectral density, 10,000.

The components in Figures 10 and 11 are summed to form Figure 6. The result is clipped at a level of 10,000 units and then filtered using a four-stage Butterworth filter with cutoff frequency of 1257 rad/sec (200 Hz). The result is shown in Figure 7. The clear nonstationarity in Figure 7 results from

the fact that component one, in Figure 10, starts near zero, is very small toward the end, and is greater than component two, in Figure 11, between the times 0.2 sec and 1.4 sec.

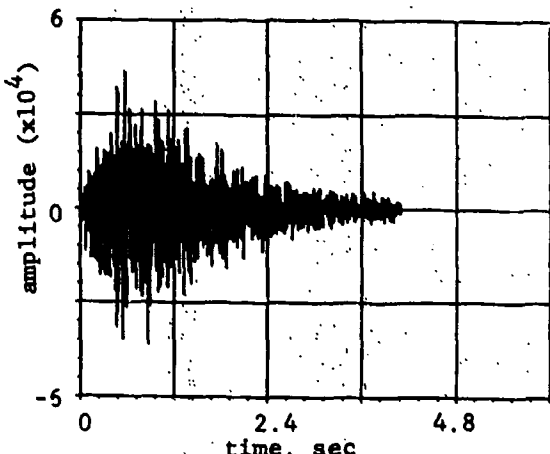


Figure 10. Component number one of the signal in Figure 6.

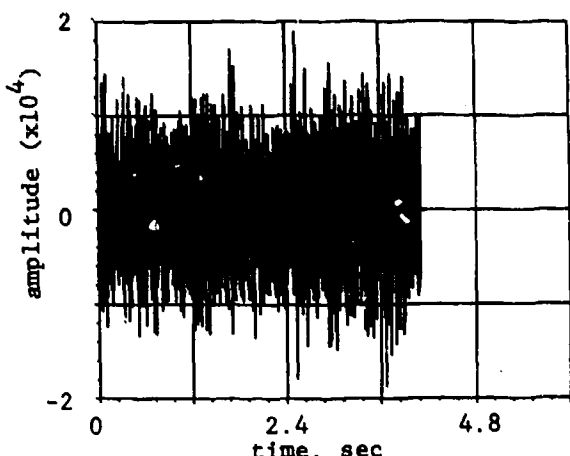


Figure 11. Component number two of the signal in Figure 6.

5.0 Conclusions and Recommendations

We have shown that the real danger of producing erroneous but plausible data can result from the analysis of random data which has been clipped and filtered. While this error probably

occurs infrequently the possibility has serious implications.

It would seem appropriate to add some kind of an overload detector to the instrumentation to avoid this problem. A simple peak overload detector does not seem appropriate because a few clipped peaks will do very little damage to random data. A simple peak detector would detect even a single peak which exceeded the clipping level. A better idea is to measure the rectified average of the data before any filtering. For a severely clipped signal this average will approach the clipping level. Unclipped data will have an average much less than the clipping level. For normally distributed random data the

average will be $\sqrt{2/\pi}$ times the standard deviation. The time constant of the averaging circuit would be set by the bandwidth of the input data to give an acceptable error in the estimate of the rectified average, and the duration of the event to be detected. The rectified average is compared with a predetermined voltage level which represents a fraction of the clipping level. When the rectified average exceeds the reference level an overload detector is turned on. The overload detector could be sampled and reset at a low rate. This simple method would eliminate the possibility of undetected errors addressed in this paper.

Appendix -- Development of Autocorrelation of Clipped Random Process

The mathematics connecting (2) to (3) in the text are presented in this section. When (1) is used in (2) the result is

$$\begin{aligned}
 R_{yy}(\tau) = & E[(X(t) - E[X(t)-a][X(t)-a] \\
 & - E[-X(t)-a][X(t)+a]) * \\
 & (X(t+\tau) - E[X(t+\tau)-a][X(t+\tau)-a] \\
 & - E[-X(t+\tau)-a][X(t+\tau)+a])] . \quad (A1)
 \end{aligned}$$

When the product on the right is executed the result is the expected value of nine terms. The first is $X(t)X(t+\tau)$, the second is $-X(t)E[X(t+\tau)-a][X(t+\tau)-a]$, etc. The expected value of the first term is $R_{xx}(\tau)$. The expected value of the second term is

$$-\int_{-\infty}^{\infty} dx_1 \int_a^{\infty} dx_2 x_1(x_2-a) p_{X_1 X_2}(x_1, x_2) \quad (A2)$$

where the expected value is written in terms of the joint probability density function (pdf) of two random variables. x_1 identifies with $X(t)$, and x_2 identifies with $X(t+\tau)$. The joint normal pdf is

$$p_{x_1 x_2}(x_1, x_2) = \frac{1}{2\pi\sigma^2\sqrt{1-\rho^2}} \exp\left(-\frac{1}{2(1-\rho^2)\sigma^2}(x_1^2 - 2\rho x_1 x_2 + x_2^2)\right) \quad -\infty < x_1 < \infty, \quad -\infty < x_2 < \infty \quad (A3)$$

The expected values of all the terms in (A1) can be written in a similar fashion, and all can be evaluated by establishing expressions for two integrals; these are

$$I_1(\rho) = \int_{-\infty}^{\infty} dx_1 \int_{-\infty}^{\infty} dx_2 (x_1 - a)(x_2 - a) p_{x_1 x_2}(x_1, x_2) \quad (A4)$$

$$I_2(\rho) = \int_{-\infty}^{\infty} dx_1 \int_{-\infty}^{\infty} dx_2 x_1(x_2 - a) p_{x_1 x_2}(x_1, x_2) \quad (A5)$$

Both these expressions can be accurately approximated.

Consider first $I_2(\rho)$. When (A3) is used in (A5) the x_1 integral can be executed, and the remaining integral is related to the standard normal cumulative distribution function (cdf). The result is

$$I_2(\rho) = \sigma^2 [1 - \Phi(\frac{a}{\sigma})] = b_1 \rho \quad (A6)$$

where $\Phi(\cdot)$ is the standard normal cdf.

The integral $I_1(\rho)$ must be evaluated differently. We do this by evaluating $I_1(\rho)$ at $\rho = -1, 0, +1$, and evaluating $\partial I_1 / \partial \rho$ at $\rho = 0$, then using the results to write a cubic approximation to $I_1(\rho)$, $-1 \leq \rho \leq 1$. Consider $I_1(\rho)$ at $\rho = -1$. In this situation $p_{x_1 x_2}(x_1, x_2)$ is a delta function with non-zero values only above the line $x_2 = -x_1$. Use of this fact in (A4) yields

$$I_1(\rho) = 0, \quad \rho = -1. \quad (A7)$$

Consider next $I_1(\rho)$ at $\rho = 1$. In this situation $x_1 = x_2$ and (A4) is the expected value of $(X-a)^2 H(X-a)$, where X is a mean zero normal random variable with variance σ^2 , and $H(\cdot)$ is the Heaviside function. A straightforward evaluation yields

$$I_1(\rho) = (\sigma^2 + a^2)[1 - \Phi(\frac{a}{\sigma})] - \frac{a\sigma}{\sqrt{2\pi}} \exp\left(-\frac{1}{2}\left(\frac{a}{\sigma}\right)^2\right), \quad \rho = 1. \quad (A8)$$

When $\rho = 0$ the cross terms in (A3) vanish, therefore, (A4) is easy to evaluate. It is

$$I_1(\rho) = \{a[1 - \Phi(\frac{a}{\sigma})] - \frac{a\sigma}{\sqrt{2\pi}} \exp\left(-\frac{1}{2}\left(\frac{a}{\sigma}\right)^2\right)\}^2, \quad \rho = 0. \quad (A9)$$

Finally, $\partial I_1 / \partial \rho$ can be evaluated by knowing $\partial p_{x_1 x_2}(x_1, x_2) / \partial \rho$ and using it in place of $p_{x_1 x_2}(x_1, x_2)$ in (A4).

$$\frac{\partial}{\partial \rho} p_{x_1 x_2}(x_1, x_2) \Big|_{\rho=0} = \frac{x_1 x_2}{\sigma^2} p_{x_1 x_2}(x_1, x_2) \Big|_{\rho=0} \quad (A10)$$

Appropriate use of this expression yields

$$\frac{\partial I_1(\rho)}{\partial \rho} = \sigma^2 [1 - \Phi(\frac{a}{\sigma})]^2, \quad \rho = 0. \quad (A11)$$

Based on (A7), (A8), (A9) and (A10), $I_1(\rho)$ can be approximated

$$I_1(\rho) = \sigma^2 (a_0 + a_1 \rho + a_2 \rho^2 + a_3 \rho^3) \quad (A12)$$

where

$$a_0 = \left(\frac{1}{\sqrt{2\pi}} \exp\left(-\frac{1}{2}\left(\frac{a}{\sigma}\right)^2\right) - \frac{a}{\sigma} [1 - \Phi(\frac{a}{\sigma})]\right)^2$$

$$a_1 = \left[1 - \Phi\left(\frac{a}{\sigma}\right)\right]^2$$

$$\begin{aligned}
 a_2 &= \frac{1}{2} [1 + \left(\frac{a}{\sigma}\right)^2] [1 - \Phi\left(\frac{a}{\sigma}\right)] \\
 &\quad - \frac{a}{2\sigma\sqrt{2\pi}} \exp\left[-\frac{1}{2}\left(\frac{a}{\sigma}\right)^2\right] \\
 &\quad - \left(\frac{1}{\sqrt{2\pi}} \exp\left[-\frac{1}{2}\left(\frac{a}{\sigma}\right)^2\right] - \frac{a}{\sigma}[1 - \Phi\left(\frac{a}{\sigma}\right)]\right)^2 \\
 a_3 &= \frac{1}{2} [1 + \left(\frac{a}{\sigma}\right)^2] [1 - \Phi\left(\frac{a}{\sigma}\right)] \\
 &\quad - \frac{a}{2\sigma\sqrt{2\pi}} \exp\left[-\frac{1}{2}\left(\frac{a}{\sigma}\right)^2\right] - [1 - \Phi\left(\frac{a}{\sigma}\right)]^2.
 \end{aligned}$$

The formulas (A6) and (A12) can now be used to establish the approximation for $R_{yy}(\tau)$. The integrals like (A2) that result from the expansion of (A1) must first be written in terms of $I_1(\rho)$ and $I_2(\rho)$. The result is

$$\begin{aligned}
 R_{yz}(\tau) &= R_{xx}(\tau) + 2(I_1(\rho) - I_1(-\rho)) \\
 &\quad - 2I_2(\rho). \quad (A13)
 \end{aligned}$$

When (A6) and (A12) are used in (A13) the result is (3) in the text. In developing (3) it is recognized that $\rho\sigma^2 = R_{xx}(\tau)$.

To check the accuracy of the formulas in (A6) and (A12), they were substituted into (A13) and compared to the case where (A4) and (A5) were integrated numerically and used in (A13). Figures A1 and A2 show comparisons of $R_{yy}(\tau)/\sigma^2$ as a function of ρ for the approximation (solid line) and the numerical estimate (points). Figure A1 is the case where $a/\sigma = 0.5$; Figure A2 is the case where $a/\sigma = 1.0$. The greatest error appears to be lower than three percent.

References

1. Nelson, D., In oral presentations at Sandia National Laboratories, he raised the issues addressed by this paper in June and July, 1985.
2. Jung, W., Stephens, M., Todd, C., "An Overview of SID and TIM, Part I," Audio, V. 63, June, 1979.
3. Jung, W., Stephens, M., Todd, C., "An Overview of SID and TIM, Part II-Testing," Audio, V. 63, July, 1979.
4. Walter, P., "Problems with Frequency Creation in Nonlinear Measurement Systems," to be published IMEKO XI Proceedings, 11th Triennial World Congress, International Measurement Confederation, Houston, TX, October 1988.
5. Papoulis, A., Probability, Random Variables, and Stochastic Processes, McGraw-Hill, New York, 1965.

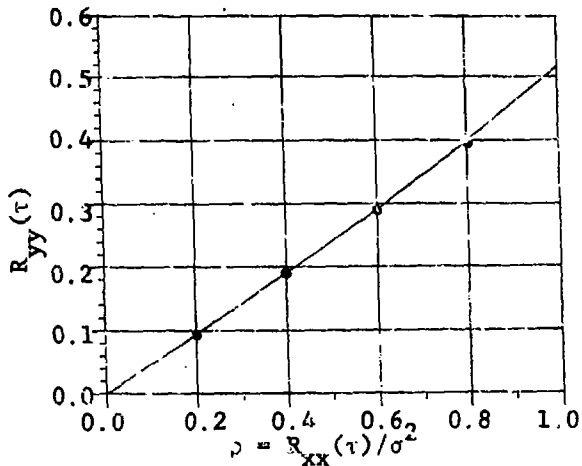


Figure A1. Autocorrelation function of a clipped signal as a function of correlation coefficient of the underlying signal. $a/\sigma=1$.

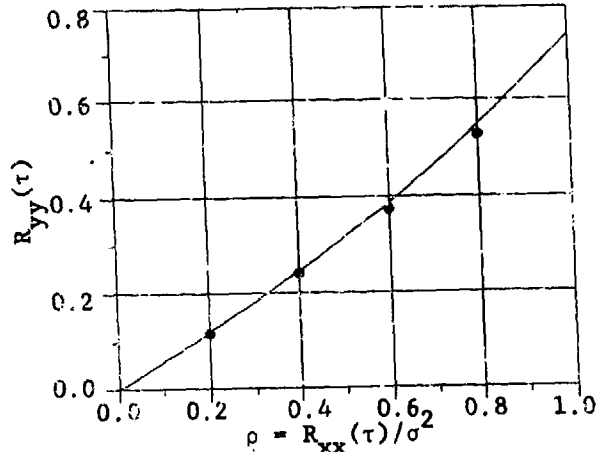


Figure A2. Autocorrelation function of a clipped signal as a function of correlation coefficient of the underlying signal. $a/\sigma=0.5$.

FULLY TURBULENT INTERNAL FLOW EXCITATION OF PIPE SYSTEMS

J.M. Cuschieri, E.J. Richards, S.E. Dunn
CENTER FOR ACOUSTICS AND VIBRATIONS
Department of Ocean Engineering
Florida Atlantic University
Boca Raton, FL 33431

The excitation of pipe systems due to the internal flow turbulence is examined. The response of a pipe structure excited by a fully turbulent internal flow is described in terms of a forcing function dependent on the turbulence pressure spectrum and the corresponding functions of the correlation areas, and the mechanical mobility of the pipe structure. The resulting form of the pipe response is examined for both air and water flows with comparisons being made to previously published analytical and experimental results.

INTRODUCTION

The excitation of pipe systems due to the internal flow can contribute significantly to the total vibrational energy on board naval vessels. There are a number of sources that can excite a typical pipe system and in general these excitation sources can be divided into four types:

- (1) The excitation of the pipe wall due to the internally fully developed turbulent flow.
- (2) The excitation of the pipe wall due to acoustic waves propagating in the internal fluid.
- (3) The excitation of the pipe by external mechanical forces which have a defined point of application.
- (4) The excitation of the pipe wall by enhanced turbulence created by separated flow near pipe fittings, valves, etc.

The excitation from unbalanced acoustic forces near pipe system bends or bifurcations can be included with excitation type (3) since the location of these types of sources is defined. Acoustic waves propagating along a pipe section have to change direction when a pipe bend is encountered. The change in direction and the different areas of pipe wall at the bend over which the acoustic pressures act create unbalanced forces [1].

In developing vibration control solutions for a piping system, it would be required that the above excitation

sources be classified in importance. Thus it would be convenient that if an energy method is used in the analysis, a consistent form of expressing the energy transferred to the pipe section by each source should be developed. The energy transferred from each of the above sources to the pipe system can be expressed in terms of an equivalent forcing function and a structural point response of the pipe. Thus the task of classifying the sources would reduce to obtaining equivalent force terms for each of the sources. In this paper emphasis is placed on the energy input from the fully turbulent flow excitation. However, the results are also useful in the analysis of the energy input from the enhanced turbulence excitation due to separated flow near pipe fittings.

Extensive work has been done on the excitation of pipe sections by the internally fully developed turbulent flow for both air and water systems. The result of previous work is generally in the form of a joint acceptance function initially introduced by Powell [2], which matches the excitation with the response of the pipe structure. This approach is only necessary for low frequency analysis where individual modes have to be studied separately. For medium to high frequency regimes, where the modal density is high, some approximations can be applied to the joint acceptance function to obtain an expression for the vibration level or the input energy

to the pipe structure in terms of the internal turbulence pressure, the associated correlation area and the point response of the pipe structure. The combination of the pressure and correlation area is required since the energy that escapes into the pipe structure depends on the level of force excitation and not simply on the pressure excitation. Thus, axial and circumferential correlation lengths of the pressure fluctuations will be included in the forcing term.

GENERAL PIPE RESPONSE

The response of a pipe structure excited by fully turbulent internal flow can be given in terms of a forcing function, which is dependent on the turbulence pressure spectrum, the mechanical impedance or mobility function of the pipe structure and a joint acceptance function:

$$\langle \phi_d(\omega) \rangle = \sum_{m,n} \frac{a_{mn}^2 (x,y) \phi_p(\omega) A^2 J^2(\omega)}{|Z_{mn}(\omega)|^2} \quad (1)$$

where $\langle \rangle$ denotes spatial averaging, $a_{mn}(x, y)$ are the mode shapes of vibration, $\phi_p(\omega)$ and $\phi_d(\omega)$ are the power spectral density functions of the turbulence pressure and the pipe wall displacement vibrations respectively, A is the surface area of the pipe, $Z_{mn}(\omega)$ is the impedance of the m th mode and $J^2(\omega)$ is the joint acceptance function.

The joint acceptance function is a measure of the effectiveness of the turbulence pressures in exciting specific modes of vibration within a particular frequency range. In general the joint acceptance function is given by [2]:

$$J^2(\omega) = \frac{1}{A^2} \int \int \int \int R_f(x_1, y_1; x_2, y_2; \omega) a_{mn}(x_1, y_1) a_{mn}(x_2, y_2) dx_1 dy_1 dx_2 dy_2 \quad (2)$$

R_f represents the spatial correlation between the pressures at points (x_1, y_1) and (x_2, y_2) in a narrow frequency band $\Delta\omega$ centered on ω ; A is the surface area of the pipe wall and $a_{mn}(x, y)$ are the mode shapes.

For a convected turbulent wall pressure in a longitudinal flow direction, space-time correlation functions have been developed in references [3,4 and 5]. These functions can be substituted in the expression for the joint acceptance

function which if then substituted into Equation (1) a relationship for the pipe response is obtained. Since the derivations of the correlation functions has been done in a number of references, rather than repeating these derivations here, relevant results from selected references that deal with air and water systems separately, will be stated.

WATER FLOW SYSTEMS

Extensive work has been done by Clinch [6] in developing the expression for the joint acceptance function for water flow in pipe systems. The expression for the joint acceptance function is obtained in terms of two components for a pipe with its axis along the x -direction.

$$J^2(\omega) = J_x^2(\omega) \cdot J_y^2(\omega) \quad (3)$$

where $J_x^2(\omega)$ is the axial component, given by

$$J_x^2(\omega) = \frac{L_x}{L} \frac{U_c^2}{U_c^2 + \omega^2 L_x} \quad (4)$$

where L_x is the axial correlation length; and $J_y^2(\omega)$ is the circumferential component given by

$$J_y^2(\omega) = \frac{L_y}{2\pi a} \left[1 - \frac{L_y}{\pi a} \right] \quad (5)$$

where L_y is the circumferential correlation length. Since $L_y \ll a$, where a is the radius of the pipe

$$J_y^2(\omega) \approx \frac{L_y}{2\pi a} \quad (6)$$

Thus

$$J^2(\omega) \approx \frac{L_x L_y}{2\pi a L} \left[\frac{U_c^2}{U_c^2 + \omega^2 L_x^2} \right] \quad (7)$$

which for low frequencies, simplifies to

$$J^2(\omega) = \frac{L_x L_y}{2\pi a L} \quad (8)$$

and for high frequencies

$$J^2(\omega) = \frac{L_y}{L_x} \frac{U_c^2}{\omega^2} \frac{1}{2\pi a L} \quad (9)$$

The low frequency expression for the joint acceptance function assumes that the turbulence pattern travels unaltered downstream at a convection speed of U_c . At low frequencies the correlation area given by $L_x L_y$ is very

small compared to the wave length and thus the excitation can be considered as being equivalent to a point force.

The high frequency expression shows that the excitation is not due to the pressure acting over a small area over which the pressure is correlated. The area represented by $L_x L_y$ becomes too large compared to the wavelength, in which case the high frequencies cannot be excited. This would be the case had the turbulence pattern been stationary, that is nonconvected. However, turbulence eddies are propagating downstream with the convection velocity U_c . Thus each eddy, although of a size which is too large compared with the wavelength, is rolling along the length of the pipe exciting the high frequencies due to this "rolling ball" effect. Thus the input energy expression can still be given in terms of a point force and a point response. That is the input energy into a pipe structure due to the internal fully developed turbulent flow excitation is given by

$$E_{in} = 1/2 [\Phi_p A_c 2\pi aL] \text{ Real } [M(\omega)] \quad (10)$$

where $M(\omega)$ is the point mobility response of the pipe structure and

$A_c = L_x L_y$ at low frequencies, and

$$= \frac{L_y}{L_x} \frac{U_c^2}{2} \text{ at high frequencies} \quad (11)$$

This result can be compared to the analytical and experimental results obtained by Clinch. In his paper Clinch expressed the result in terms of the spatial averaged mean squared value of the displacement for a finite length of pipe isolated from the rest of the pipe system. Therefore in this experiment the energy that escaped into the pipe could only be dissipated or radiated as acoustical energy out of the pipe. Setting up an energy balance for a single isolated pipe section the input energy can only be dissipated due to structural damping and radiation damping. Thus

$$E_{in} = E_{diss} = \omega^3 \rho_e h 2\pi a L \eta \langle W^2 \rangle \quad (12)$$

where ρ_e is the equivalent density taking into account the effect of the water loading, $\langle W^2 \rangle$ is the spatial averaged mean square value of the surface displacement and η is the structural and acoustic damping of the pipe. Also

$$\text{Real } [M(\omega)] = \frac{2\pi}{\rho_e 2\pi a L h} \left(\frac{\Delta N}{\Delta \omega} \right) \quad (13)$$

Thus

$$\langle \tilde{W} \rangle = \frac{2\pi}{\rho_e 2\pi a L h} \cdot \frac{1}{2} \cdot \frac{\Delta N}{\Delta \omega} \cdot \frac{|P(\omega)|^2 A_c 2\pi a L}{2\pi a L h \rho_e \omega^3} \quad (14)$$

where $|P(\omega)|^2$ is the spectrum of the pressure, and

$$\langle \Phi_d \rangle = \frac{2\pi}{2\pi h^2} \Phi_p \frac{A_c}{2\pi a L} \cdot \frac{\Delta N}{\Delta \omega} \cdot \frac{1}{\omega^3} \quad (15)$$

which is similar to the expression given by Clinch.

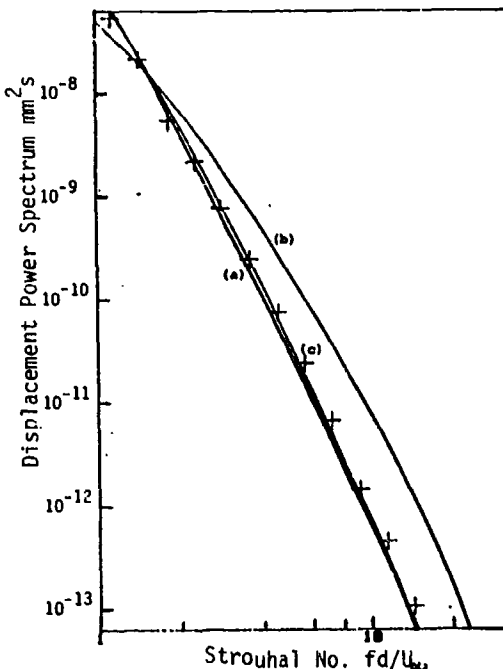


Figure 1.
Comparison between the results obtained by Clinch and the results obtained using equation (15) for the displacement power spectrum of the pipe wall.
(a) Experimental results by Clinch; (b) and (c) low and high frequency asymptotes of equation (15); +---+ Theoretical results obtained by Clinch.

Figure (1) shows a comparison between the experimental results obtained by Clinch and the results obtained by using the above expression for the response. In computing the response the results for the measured correlation areas and the pressure power spectrum from Clinch's work are used which are shown in Figures (2) and (3) respectively. Figure (4) shows the equivalent density term as a function of frequency; note the increase in apparent density at low frequency because of the water added mass effect.

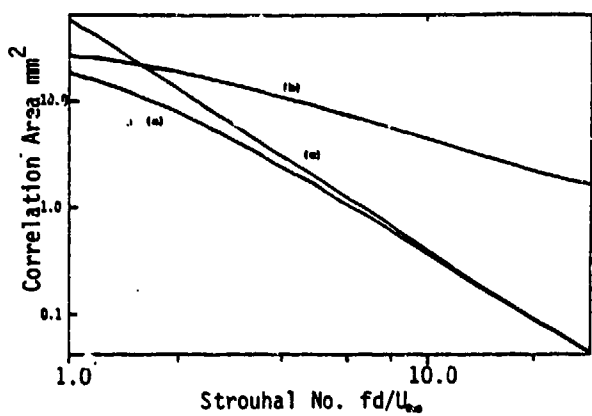


Figure 2.
Low and high frequency asymptotes for the correlation area. (a) Measured correlation area by Clinch; (b) low frequency asymptote; (c) high frequency asymptote. At a flow speed of 1.5 m/s in a 5 cm pipe a Strouhal No. of 1.0 corresponds to 30 Hz, and at a flow rate of 9 m/s it corresponds to 180 Hz.

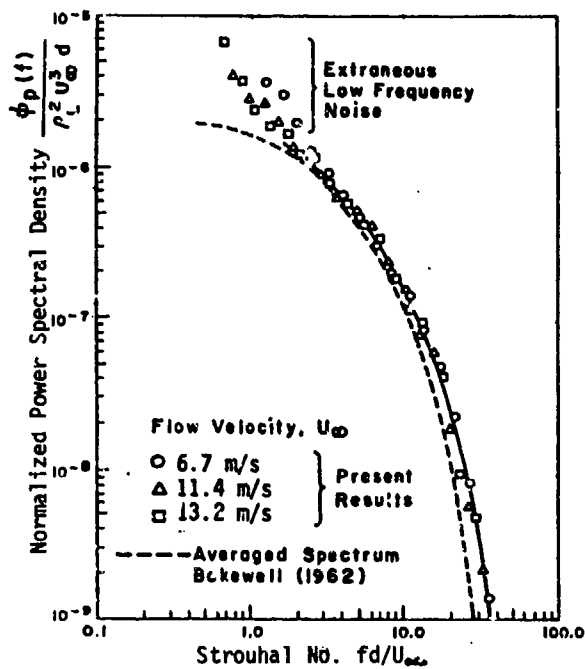


Figure 3.
Internal turbulence pressure spectrum measured by Clinch and used in this analysis for water flow systems.

Figure (5) shows the mean structural response term $\text{Real} [M(u)]$, also modified from the response of a cylindrical shell in a vacuum because of the added mass effect which is included in the ρ_e term.

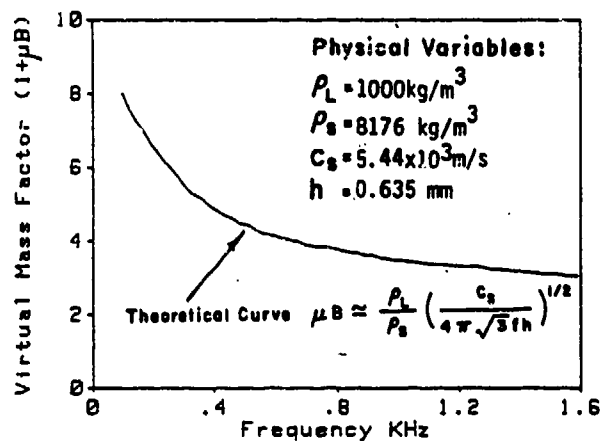


Figure 4.
Change of effective density with frequency for a water flow system due to water loading $\rho_e = \rho_s (1 + \mu B)$

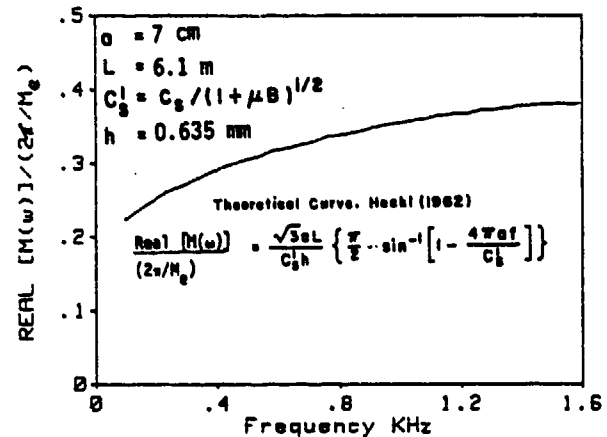


Figure 5.
Mean point mobility response for a water-loaded thin walled cylindrical shell.

AIR FLOW SYSTEMS

Work on the analysis of air flow systems is more extensive than that for water flow systems. Bull and Rennison [7], Bull and Norton [8], Reethof [9], Fagerlund [10], to name just a few, developed relationships which are generally based on the joint acceptance function. Bull [7] from the general result stated in Equation (1) developed an expression for the noise radiated from a straight pipe section due to the excitation from the internal turbulent flow. This expression includes the use of the joint acceptance function, defined similar to Equation (2). Following a similar analysis as for the water flow systems an expression for the input energy can be obtained in terms of the point response of the pipe, the turbulence pressure spectrum and a correlation area expression

obtained from the joint acceptance function. The expression for the energy input thus obtained is as follows:

$$E_{in} = \frac{1}{2} \cdot \phi_p \cdot aL \left(\frac{L_y}{L_x} \cdot \frac{h C_{LP}}{u} \cdot \frac{u^2 M_0^2}{2\pi} \right) \text{ Real } [M(u)] \quad (16)$$

where C_{LP} is defined by

$$C_{LP} = \left[\frac{E}{\rho_e (1-\gamma)^2} \right]^{\frac{1}{2}} \quad (17)$$

u is the ratio of the convection velocity U_c to the mean flow velocity and M_0 is the flow mean Mach number. In obtaining the above expression the following approximations were made: $(1-\gamma^2)^{\frac{1}{2}} \approx 1$ and $4/(\pi/6) \approx 0.5$. In the expression for C_{LP} an equivalent density term is used. However, in the case of an air flow system, the influence of the internal medium is negligible and thus the equivalent density is equal to the density of the material of the pipe structure, ρ_s .

This expression, Equation (16), is for a straight pipe section which can dissipate the energy either through damping losses or through acoustical radiation. Using this expression to obtain the surface vibration level and introducing a radiation efficiency term for the pipe wall ϵ_{rad} , the radiated noise energy in one-third octave frequency bands is given by

$$E_{rad} = \left(\phi_p \frac{\Delta u}{2\pi} \right) \frac{C_{rad} \epsilon_{rad} \omega L}{u h n} \left(\frac{L_y}{L_x} \cdot \frac{h C_{LP}}{u} \cdot \frac{u^2 M_0^2}{2\pi} \right) \text{ Real } [M(u)] \quad (18)$$

This expression is similar to the one developed by Bull for the noise radiated from a straight pipe section excited by fully turbulent flow. The results obtained for the radiated noise in one-third octave frequency bands using Equation (18) are compared to the experimental results obtained by Bull in Figure (6). The agreement in the results is good, especially in the shape of the spectrum for the radiated noise power, also, the estimated levels and sound power levels measured by Bull are in close agreement. There is some discrepancy between the estimated and measured levels in the one-third octave frequency band centered on 630 Hz. Within this frequency band exists the cut-off frequency of the second higher order mode. Because the relative

change in the frequency with increasing axial wavenumber is very slow compared to the structural mode, complete coincidence for this mode occurs close to the cut-off frequency, that is the radiation efficiency should be unity in this frequency band. If this is taken into account good agreement is also achieved in this one-third octave frequency band. Figure (7) shows the frequency averaged point mobility response for the pipe structure which is different from the one shown in Figure (5) because in this case the fluid loading effect is negligible. Figure (8) shows the internal turbulence pressure spectrum measured by Bull. Both results in figures (7) and (8) were used in the above computations of the radiated acoustical power.

DISCUSSION OF THE RESULTS

In the two expressions obtained for the input energy due to excitation from the fully turbulent flow an important requirement is information on the nature and magnitude of the turbulence. A parameter which appears in both the water flow and the air flow expressions is the convection velocity of the turbulence, U_c . This has been measured in a number of references [6, 11], and is typically a constant with frequency, equal to approximately 62% of the mean flow velocity. This value for U_c was used in the above calculations.

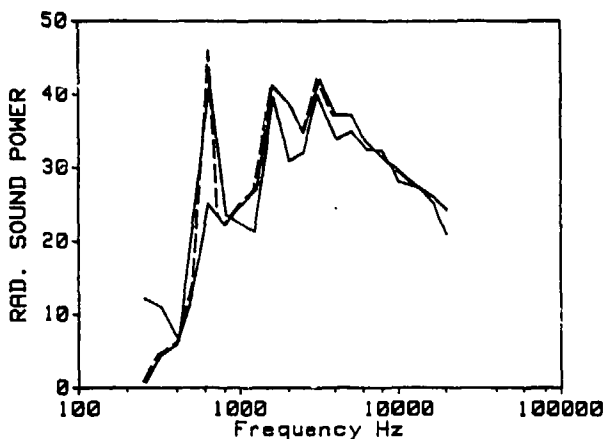


Figure 6.
Comparison of experimental data to estimates obtained using equation (18) for an air flow system with Mach No. 0.22. —: estimated data; —: estimated data with modified radiation efficiency; - - -: experimental data by Bull.

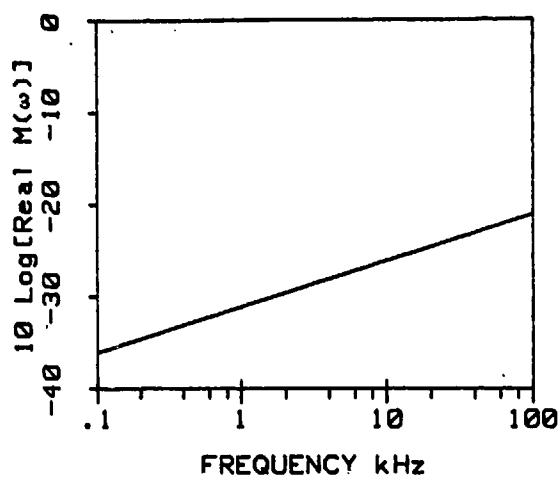


Figure 7.
Point mobility response for a cylindrical shell below the ring frequency, diameter of shell 0.363 cm and thickness 1.4mm.

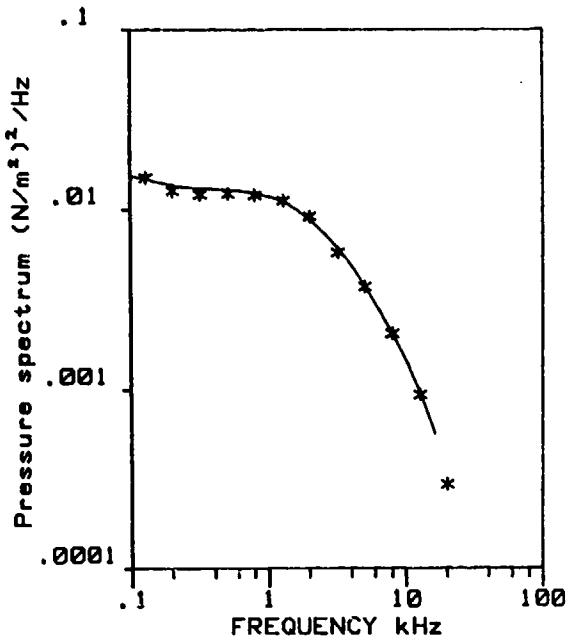


Figure 8.
Pressure spectrum as measured by Bull for air flow systems. * experimental results; —, best fit curve. The flow mach number is 0.22

Two other important parameters are the correlation lengths in the axial (L_x) and circumferential (L_y) directions. The absolute value of these two parameters is only necessary in the case of water flow systems at low frequencies where the value of the joint acceptance function is dependent on the product of these two correlation

lengths, Equation (8). For a 5cm diameter pipe and a flow speed of 1.5 m/s, low frequencies would be less than approximately 50Hz, while for a 9 m/s flow rate, low frequencies would be less than approximately 200 Hz, Figure (2). Thus for most of the frequency range of interest, in the audible frequency range, both for air and water flow systems only a ratio of these two correlation lengths is required. The value of this ratio can also be found in a number of references and in general it is a constant and independent of frequency with L_y/L_x being equal to approximately 0.2. This implies that the only turbulence information required is the amplitude and frequency content of the internal turbulence pressure.

Comparing the two results for the air flow systems and water flow systems the input energy is, in the case of air flow, dependent on the flow Mach number. The reasons for this flow velocity dependence in the case of air systems, are, the cut-on frequencies of the high order modes decreases with increasing mach number and the speed of propagation of these spiralling modes is a function of the flow velocity. Thus, as the flow mach number increases there will be more propagating modes and more of these modes become coincident with the structural modes at lower frequencies. This will result in more vibrational energy being transmitted into the pipe structure, and hence the transmission loss of the pipe wall will decrease with increasing flow speeds. In the case of water systems the flow mach number is negligibly small and thus there is no effect on the higher order modes compared with the no flow condition. In this case coincidence between the structural and acoustical modes does not occur within the audible frequency range for general piping systems and the water inside the pipe act as a reactive medium. Thus for water systems the energy input into the pipe structure is independent of the flow speed. This dependency on the flow mach number to the power of two for air systems explains the 6 dB change per doubling of flow speed for the transmission loss of the pipe obtained by Holmer and Heymann [12].

Another observation is that the input energy expressions are independent of the size of the turbulence (especially at high frequencies), they are only dependent on the ratio of L_y/L_x . Therefore these expressions can also be used to obtain the energy input near a pipe bend or

fitting where separation of flow or enhanced turbulence exists. In regions of separated flow with enhanced turbulence the increase in size of the turbulence will be similar in both the circumferential and the axial directions, thus the ratio L_y/L_x will remain constant at 0.2. The only requirement will be the different pressure spectrum which, depending on the pipe fitting creating the separated flow, may change both in frequency content and magnitude.

The rest of the parameters in the equations are pipe structure parameters including the total surface area of the pipe ($2\pi aL$). The length of the pipe L can be eliminated from the expression if the input energy is expressed per unit length. This modification has to be included in dealing with the excitation from separated flow since in this case the excitation is only over five to ten diameters from the pipe fitting and not over the whole length of the pipe section.

CONCLUSION

From the expressions that have been presented and the comparison with experimental results, it can be concluded that it is possible to express the vibrational energy input from turbulent flow excitation in the form of a forcing function and a point mobility expression. This form of representing the energy input is common to other forms of excitation thus allowing for the direct comparison of the sources exciting a piping system. These expressions for the input energy can be used in an energy accountancy approach to obtain the vibrational level of the pipe section or the radiated noise energy from the pipe. The results obtained with this method compare favorably with the results obtained through the evaluation of the joint acceptance function and with experimental results obtained for both water and air flow systems. Because of the form of the results these can also be used to estimate the energy input near pipe fitting due to the separated flow in the vicinity of pipe fittings. However no experimental results are yet available which can be used to verify this conclusion.

In using the above results use was made of measured turbulence pressure power spectra. This is a limiting factor on all forms of predictive methods whether using the above method or the joint acceptance function method. Work is currently in progress to set up a series of nomograms based

on experimental data which can be used to predict the amplitude and frequency content of the turbulence pressure spectrum for undisturbed fully turbulent flow and also for regions of separated flow.

REFERENCES

1. CUMMINGS, A. (1974) Journal of Sound and Vibration 35 (4), 451-477, "Sound Transmission in Curved Duct Bends".
2. POWELL, A. (1958) "On the Response of Structures to Random Pressures", Chapter 8, Random Vibrations, S.H. Crandall Ed., Technology Press, Cambridge, Mass.
3. BULL, M.K. and WILLIS, J.L. (1961) University of Southampton AASU Report Number 199, "Some Results of Experimental Investigations of the Surface Pressure Field Due to a Turbulent Boundary Layer".
4. CORCOS, G.M. (1962) University of California Inst. of Engineering Res. Report No. 183, "Pressure Fluctuations in Shear Flows".
5. DYER, I. (1958) "Estimation of Sound-Induced Missile Vibration", Chapter 9, Random Vibrations, S.H. Crandall Ed., Technology Press, Cambridge Mass.
6. CLINCH, J.M. (1965) NASA report number NAS 8-11248 "Study of vibrations induced in thin walled pipes by fluid flow".
7. BULL, M. K. and RENNISON, D.C. (1974) Noise Shock and Vibration Conference Proceedings, "Acoustic Radiation from Pipes with Internal Turbulent Gas Flows".
8. NORTON, M.P. and BULL, M.K. (1984) Journal of Sound and Vibration 94 (1), 105-146, "Mechanisms of the Generation of External Acoustic Radiation from Pipes due to Internal Flow Disturbances".
9. REETHOF, G. (1978) Ann. Rev. Fluid Mechanics 10, 333-367, "Turbulence-Generated Noise in Pipe Flow".
10. FAGERLUND, A.C. (1973) ASME Paper number 73-WA/PID, "Transmission of Sound through Cylindrical Pipe Walls".
11. BULL, M.K. (1963) University of Southampton AASU Report number 234, "Properties of the Fluctuating Wall-Pressure Field of a Turbulent Boundary Layer".
12. HOLMER, C.I. and HEYMANN, F.J. (1980) Journal of Sound and Vibration 70(2), 275-301, "Transmission of Sound through Pipe Walls in the Presence of Flow".

THE EFFECTS OF ROTOR UNBALANCE ON THE VERTICAL RESPONSE OF A SOFT-MOUNTED BLOCK

B. M. Antkowiak
The Charles Stark Draper Laboratory
Cambridge, MA 02139

and

F. C. Nelson
College of Engineering
Tufts University
Medford, MA 02155

and

M. Nabavi-Noori
Department of Mechanical Engineering
Worcester Polytechnic Institute
Worcester, MA 01609

Lagrangian dynamics is used to derive the equations of motion for two, overhung, unbalanced rotors attached to a rigid, soft-mounted block. Solution methods are established for the associated eigenvalue problem and for steady-state response. For a particular set of parameters, predictions are made for the critical speeds, the steady-state vertical block motion, the cross-talk between rotors, and the effect of rotor speed detuning.

INTRODUCTION

Rotating unbalance is a common source of vibration excitation. Electric motors, turbines, automobile engines, and gyroscope wheels are examples of such sources. Often these rotating elements are mounted on block-like structures that are separated from a foundation by vibration isolators. The block is then actively excited by the rotating unbalance and responds by oscillating on the low-impedance mounts. This paper considers such response for the special case of two overhung rotors. The rotors are allowed to have different spin speeds, different angular orientation in a vertical plane, and different amounts of unbalance.

MODEL OF THE ROTOR

The rotor model is shown in Figure 1. A rigid, circular disk of mass m is mounted on a massless shaft. The shaft is modeled as two rigid links connected by a hinge of rotary stiffness k . The hinge is assumed rigid against translation. The inner link of the shaft is supported by rolling-element bearings that are mounted concentric with the spin axis y . The outer link, of length s , supports the overhung disk whose mass center is offset from the spin axis by a radial distance e . The rotor, links, and hinge all rotate about the y -axis with angular speed Ω .

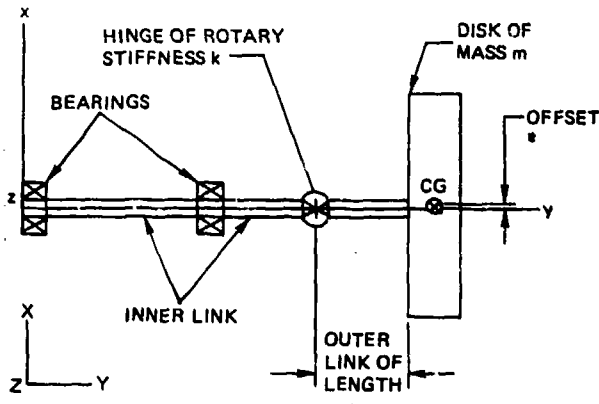


Figure 1

Although the above hinge model is appropriate for some applications, other applications are better served by a shaft with distributed elasticity. This modification would not change the method used below but would change the various energy expressions and the form of the equations of motion.

If the translations of the rotor center are denoted by u_R and w_R , see Figure 2, and if $u_R, w_R \ll s$, the strain energy in the rotary hinge can be written

$$U_R = \frac{1}{2}(k/s^2)u_R^2 + \frac{1}{2}(k/s^2)w_R^2 \quad (1)$$

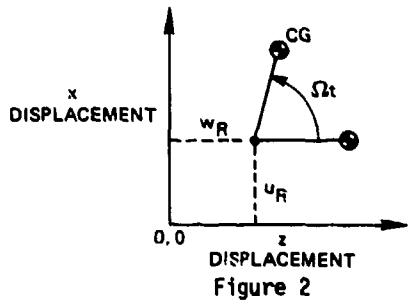


Figure 2

The coordinates of the rotor center of gravity are

$$\begin{aligned} u_R + esin\omega t \\ w_R + ecos\omega t \end{aligned} \quad (2)$$

so that the translational kinetic energy of the rotor is

$$\begin{aligned} T_1 = \frac{1}{2} m \left[\frac{d}{dt} (u_R + esin\omega t) \right]^2 \\ + \frac{1}{2} m \left[\frac{d}{dt} (w_R + ecos\omega t) \right]^2 \end{aligned} \quad (3)$$

which becomes

$$\begin{aligned} T_1 = \frac{1}{2} m \dot{u}_R^2 + \frac{1}{2} m \dot{w}_R^2 + m u_R e \omega \cos\omega t \\ - m \dot{w}_R e \sin\omega t + \frac{1}{2} m (e\omega)^2 \end{aligned} \quad (4)$$

The expression of rotational kinetic of the rotor is more complicated but may be shown to be [1, appendix A]

$$T_2 = \frac{1}{2} \frac{I_x}{s^2} (\dot{u}_R^2 + \dot{w}_R^2) + \frac{1}{2} I_y \left(\omega^2 - \frac{2\dot{u}_R \dot{w}_R}{s^2} \right) \quad (5)$$

where, by symmetry, $I_z = I_x$.

The terms $\frac{1}{2} m (e\omega)^2$ in (4) and $\frac{1}{2} I_y \omega^2$ in (5) represent the kinetic energy of the undeflected rotor. As such, they will disappear from any subsequent equations of motion and will be dropped at this point.

MODEL OF THE BLOCK

A block with two overhung rotors and three vibration isolators is shown in Figure 3. The rotors are oriented as shown with angular speeds ω_1 and ω_2 about y_1 and y_2 . The block is assumed to be rigid with mass M and to translate in the vertical (x_B) direction without rotation. The strain energy of the block is

$$U_B = \frac{1}{2} K_B x_B^2 \quad (6)$$

where $K_B = C_1 + C_2 + C_3$. The kinetic energy of the block is

$$T_B = \frac{1}{2} M \dot{x}_B^2 \quad (7)$$

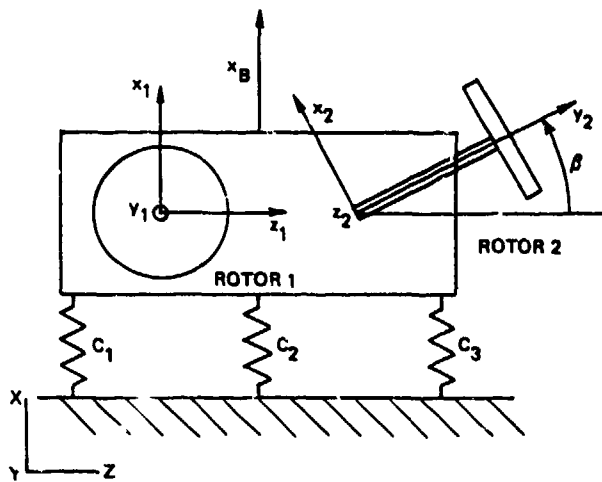


Figure 3

ROTORS AND BLOCK

The strain energy for rotor 1 is

$$U_{R1} = \frac{1}{2} \frac{(k)}{s^2} u_{R1}^2 + \frac{1}{2} \frac{(k)}{s^2} w_{R1}^2 \quad (8)$$

and the kinetic energy is

$$\begin{aligned} T_{R1} = & \frac{1}{2} m (\dot{u}_1^2 + \dot{w}_1^2) + \frac{1}{2} \frac{I_x}{s^2} (\dot{u}_{R1}^2 + \dot{w}_{R1}^2) \\ & - \frac{I_x \omega_1}{s^2} (\dot{u}_{R1} w_{R1}) + m \dot{u}_1 e_1 \omega_1 \cos\omega_1 t \\ & - m \dot{w}_1 e_1 \omega_1 \sin\omega_1 t \end{aligned} \quad (9)$$

$$\text{where } u_1 = u_{R1} + x_B$$

$$w_1 = w_{R1}$$

Similarly for rotor 2

$$U_{R2} = \frac{1}{2} \frac{(k)}{s^2} u_{R2}^2 + \frac{1}{2} \frac{(k)}{s^2} w_{R2}^2 \quad (10)$$

$$\begin{aligned} T_{R2} = & \frac{1}{2} m (\dot{u}_2^2 + \dot{v}_2^2 + \dot{w}_2^2) \\ & + \frac{1}{2} \frac{I_x}{s^2} (\dot{u}_{R2}^2 + \dot{w}_{R2}^2) \\ & - \frac{I_x \omega_2}{s^2} (\dot{u}_{R2} w_{R2}) + m \dot{u}_2 e_2 \omega_2 \cos\omega_2 t \\ & - m \dot{w}_2 e_2 \omega_2 \sin\omega_2 t \end{aligned} \quad (11)$$

$$\text{where } u_2 = u_{R2} + x_B \cos\beta$$

$$w_2 = w_{R2}$$

$$v_2 = x_B \sin\beta$$

It can be noted that the only distinctions maintained between rotors 1 and 2 are the terms Ω_1, e_1 and Ω_2, e_2 .

The strain energy and kinetic energy of the combined rotors and blocks are

$$U = U_{R1} + U_{R2} + U_B \quad (12)$$

$$T = T_{R1} + T_{R2} + T_B \quad (13)$$

EQUATIONS OF MOTION

The expressions for U and T given in (12) and (13) can be used in Lagrange's equations to give [1, appendix B]

$$[M]\{\ddot{\delta}\} + [G]\{\dot{\delta}\} + [K]\{\delta\} = \{F\} \quad (14)$$

where

$$[M] = \begin{bmatrix} M_2 & 0 & 0 & 0 & M_1 \\ 0 & M_2 & 0 & 0 & 0 \\ 0 & 0 & M_2 & 0 & M_3 \\ 0 & 0 & 0 & M_2 & 0 \\ M_1 & 0 & M_3 & 0 & M_4 \end{bmatrix}$$

$$M_1 = m$$

$$M_2 = m + I_x/s^2$$

$$M_3 = mc\cos\beta$$

$$M_4 = 2m+M$$

$$[G] = \begin{bmatrix} 0 & -G_1 & 0 & 0 & 0 \\ G_1 & 0 & 0 & 0 & 0 \\ 0 & 0 & 0 & -G_2 & 0 \\ 0 & 0 & G_2 & 0 & 0 \\ 0 & 0 & 0 & 0 & 0 \end{bmatrix}$$

$$G_1 = I_y\Omega_1/s^2$$

$$G_2 = I_y\Omega_2/s^2$$

$$[K] = \begin{bmatrix} K_1 & 0 & 0 & 0 & 0 \\ 0 & K_1 & 0 & 0 & 0 \\ 0 & 0 & K_1 & 0 & 0 \\ 0 & 0 & 0 & K_1 & 0 \\ 0 & 0 & 0 & 0 & K_2 \end{bmatrix}$$

$$K_1 = k/s^2$$

$$K_2 = K_B$$

$$\{F\}^T = \{me_1\Omega_1^2 \sin\Omega_1 t, me_1\Omega_1^2 \cos\Omega_1 t, \\ me_2\Omega_2^2 \sin\Omega_2 t, me_2\Omega_2^2 \cos\Omega_2 t, \\ me_1\Omega_1^2 \sin\Omega_1 t + me_2\Omega_2^2 \cos\Omega_2 t\}$$

$$\{\delta\}^T = \{u_{R1}, w_{R1}, u_{R2}, w_{R2}, x_B\}$$

EIGENVALUE SOLUTION

Consider equation (14) with $\{F\} = \{0\}$. Define

$$\{\gamma\} = \{\delta, \dot{\delta}\}^T$$

and use this change of variable in (14) together with the identity

$$[M]\{0\} \{\dot{\gamma}\} + [0] \ {- [M]\} \{\gamma\} = \{0\} \quad (15)$$

This gives

$$[A]\{\dot{\gamma}\} + [B]\{\gamma\} = \{0\} \quad (16)$$

where

$$[A] = \begin{bmatrix} [G] & [M] \\ [M] & [0] \end{bmatrix}$$

$$[B] = \begin{bmatrix} [K] & [0] \\ [0] & [M] \end{bmatrix}$$

If a trial solution is assumed in the form

$$\{\gamma\} = \{r\} e^{\lambda t}$$

equation (16) becomes

$$\lambda[A]\{r\} = [B]\{r\} \quad (17)$$

Equation (17) can be solved with a standard eigenvalue-solver and the eigenvalues λ_i related back to those of (14). Note that the resulting eigenvalues will be functions of Ω_1 and Ω_2 .

STEADY STATE SOLUTION

Rewrite equation (14) in phasor form. For example, let

$$u_{R1} = u_{R1,1} \exp(i\Omega_1 t) + u_{R1,2} \exp(i\Omega_2 t)$$

where $u_{R1,1}$ and $u_{R1,2}$ are complex quantities with real, $(\)_R$, and imaginary, $(\)_I$, parts, i.e.

$$u_{R1,1} = (u_{R1,1})_R + i(u_{R1,1})_I$$

$$u_{R1,2} = (u_{R1,2})_R + i(u_{R1,2})_I$$

This converts the first of equation (14); namely,

$$M_2 \ddot{u}_{R1} + M_1 \ddot{x}_B - G_1 \dot{w}_{R1} + K_1 u_{R1} = m \epsilon_1 \omega_1^2 \sin \omega_1 t$$

into four equations

$$-M_2 \omega_1^2 (u_{R1,1})_R - M_1 \omega_1^2 (x_{B,1})_R + \omega_1 G_1 (w_{R1,1})_I \\ + K_1 (u_{R1,1})_R = 0$$

$$-M_2 \omega_1^2 (u_{R1,1})_I - M_1 \omega_1^2 (x_{B,1})_I - \omega_1 G_1 (w_{R1,1})_R \\ + K_1 (u_{R1,1})_I = -m \epsilon_1 \omega_1^2$$

$$-M_2 \omega_2^2 (u_{R1,2})_R - M_1 \omega_2^2 (x_{B,2})_R + \omega_2 G_1 (w_{R1,2})_I \\ + K_1 (u_{R1,2})_R = 0$$

$$-M_2 \omega_2^2 (u_{R1,2})_I - M_1 \omega_2^2 (x_{B,2})_I - \omega_2 G_1 (w_{R1,2})_R \\ + K_1 (u_{R1,2})_I = 0$$

and hence the 5x5 system of (14) is converted into the 20x20 system

$$[c]\{x\} = \{b\} \quad (18)$$

The structure of $[c]$, $\{x\}$ and $\{b\}$ are given in [1].

Given the small size of (18), an accurate solution is possible via a standard matrix inversion algorithm. The vector $\{\delta\}$ may then be constructed from the resulting $\{x\}$.

A complete FORTRAN source program for separately or jointly solving the eigenvalue and steady state problems is given in [1].

SAMPLE PROBLEM

A sample solution to equations (17) and (18) has been carried out for the data of Table 1.

TABLE 1: Model Parameters

$\omega_1 = \omega_2 = \omega$	variable, rad/sec
ϵ_1	2.4×10^{-5} in
ϵ_2	2.4×10^{-5} in
m	7.42×10^{-5} lbf-sec ² /in
I_x	2.6×10^{-6} in-lbf-sec ²
I_y	5.2×10^{-6} in-lbf-sec ²
M	4.27×10^{-3} lbf-sec ² /in
k	400 in-lbf/rad
K_B	27000 lbf/in
s	0.1 in
θ	0.48 rad

The resulting eigenvalues vs. rotor speed are shown in Figure 4 in the format of a Campbell Diagram. There are five eigenvalues: two identical forward rotor whirls, two identical backward rotor whirls, and a vertical vibration of the block. The intercepts A & B with the frequency equals rotor speed line are critical speeds; in this case at 394 Hz (23,640 RPM) and 1100 Hz (66,000 RPM). The steady state operating speed of this sample system was 200 Hz (12,000 Hz), which is well below the first critical speed.

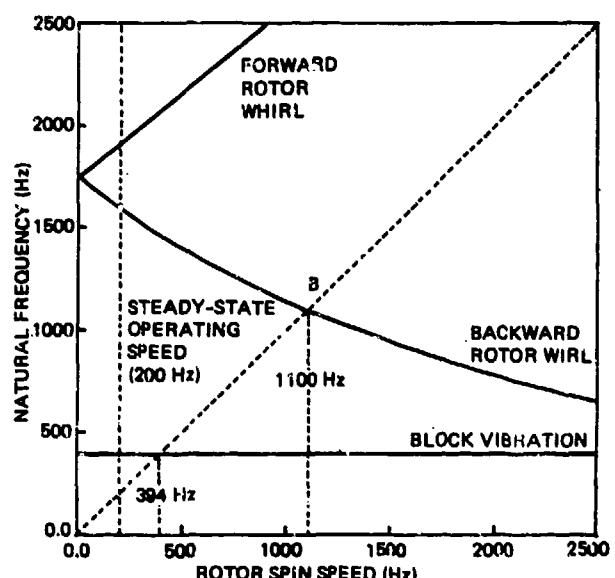


Figure 4

The steady state solution is first investigated for the case of both rotors at the same operating speed, i.e. $\Omega_1 = \Omega_2 = \Omega = 1257$ rad/sec (200 Hz). Figure 5 shows the time history of the vertical motion of the block $X_B(t)$.

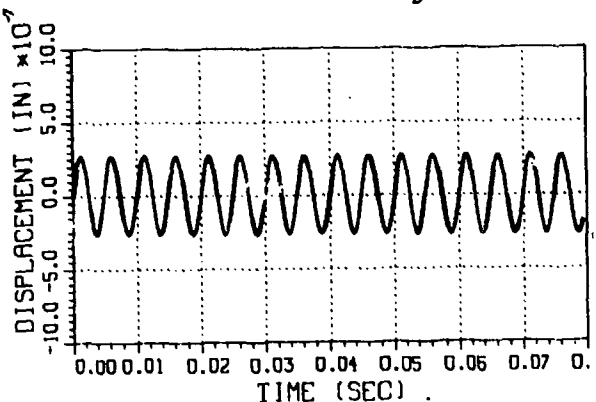


Figure 5

Figures 6 and 7 show $u_{R1,1}(t)$ and $u_{R2,2}(t)$, which are components of the motion respectively of rotor 1 and rotor 2 from their own unbalances.

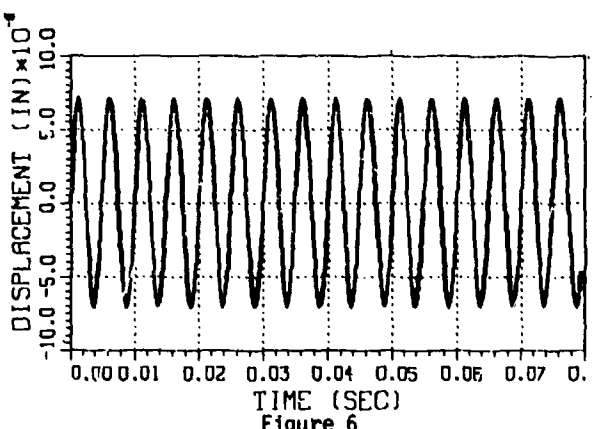


Figure 6

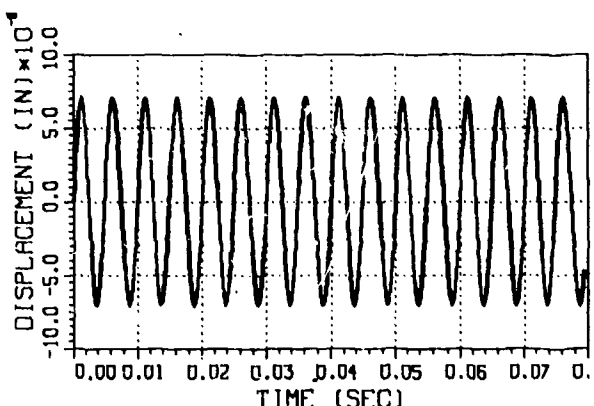


Figure 7

Figures 8 and 9 show $u_{R1,2}(t)$ and $u_{R2,1}(t)$, which are rotor 1 and rotor 2 motion components induced by the opposite rotor unbalance. For the example considered, the magnitude of this cross-talk is less than 1% of the self-induced rotor motion.

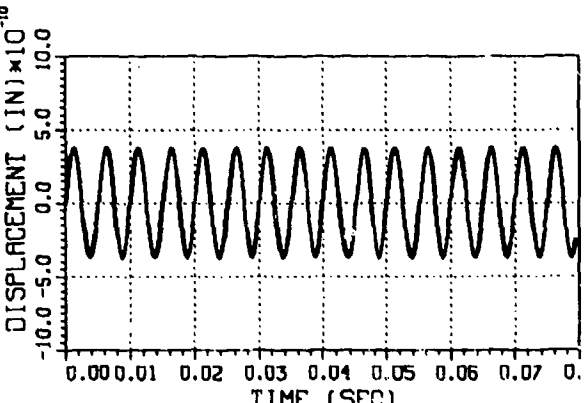


Figure 8

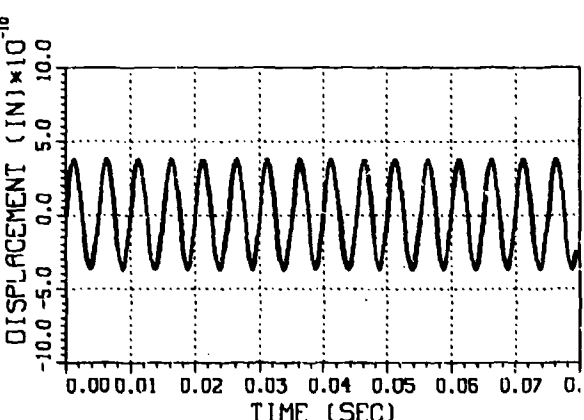


Figure 9

Lastly, consider the same case except that the two rotors speeds are slightly detuned

$$\Omega_1 = 1194 \text{ rad/sec (190 Hz)}$$

$$\Omega_2 = 1319 \text{ rad/sec (210 Hz)}$$

Figure 10 shows $X_B(t)$ for this case.

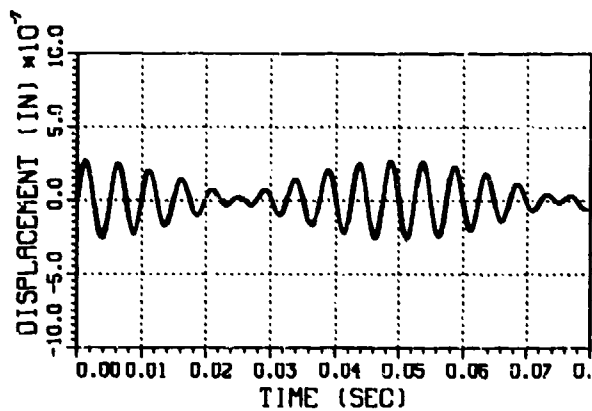


Figure 10

Comparison of Figures 5 and 10 show that for the sample problem under consideration the above detuning (10% of the operating speed) has little effect on the maximum value of block motion. However, as expected, Figure 10 shows a beating phenomenon at 20 Hz.

REFERENCES

- [1] B.M. Antkowiak, "The Effects of Rotor Unbalance on the Vertical Motion of a Soft-mounted Block," M.S. Thesis, Department of Mechanical Engineering, Worcester Polytechnic Institute, Dec. 1985.

INVESTIGATION OF VIBRATION PROBLEMS WITH
HETERODYNE HOLOGRAPHIC INTERFEROMETER

Robert A. McLauchlan, P. E.
Associate Professor
Civil and Mechanical Engineering Department
Texas A and I University
Kingsville, Texas 78363

Consistently large mechanical/acoustic vibration induced RMS deviations ($\lambda/35$) in 10 in. beam wavefronts were measured with the AFWL/ARAA heterodyne holographic interferometer, wavefront sensor (HET) system. These large wavefront surface measurement errors motivated an investigation of the sources of these mechanical/acoustic vibrations and work to eliminate/minimize their impact on HET wavefront sensor performance. Measurements were made of the RMS acceleration level spectra at several locations on the floor in the HET lab and on the HET optical table with the acoustic/wind screen in place - i.e., mechanically attached to the table. These spectra showed two very significant local peaks in the vibration levels at nominal frequencies of 30 and 40 Hz. Independent spectral decompositions of the vertical and horizontal, two-point relative phase measurements made with the HET system indicate that these 30 and 40 Hz frequencies correspond to pitch and yaw vibratory modulations, respectively, of the HET (reference and object) optical beams. A simple analysis (using nominal mass and stiffness values) made of the motion of the top member of the acoustic/wind screen with respect to the optical table gave translational (corresponding to pitch, roll optical beam modulations) and yaw natural resonance frequencies of 29.03 Hz and 40.81 Hz, respectively. The close agreement between the analysis and measured RMS spectra results indicated that the acoustic/wind screen, when attached to the optical table, is a significant local "source" of vibratory motion and hence of relative optical beam modulations which degrade the wavefront sensor performance of the HET system. Removal of the acoustic/wind screen gave significant reduction of these 30, 40 Hz vibration noise components for seismometer locations on the optical table. Use of a system of floor to ceiling curtains reduced the largescale ($\lambda/4$) random, low-frequency (0 to 2.5 Hz) oscillations -- induced by random air movements and turbulence -- which degraded HET system performance without the wind screen in place. Here ten-inch beam RMS wavefront surface errors were reduced to $\lambda/60$ with the curtains. In support of the above described measurement and analysis program, work was also done in three areas: (1) Rigid-body, time-domain analysis of the motion of the HET optical table, etc; (2) Tabulation of normalized, approximate-flexural and torsional frequencies for various free, pinned-corner and intermediate support leg conditions; (3) Impact of vibratory motion on differential hologram fringe modulation function. Based upon this work and the results of the measurement and analysis program, recommendations were made to further reduce or eliminate mechanical/acoustic vibration induced problems with the HET system.

ACKNOWLEDGMENTS

The author wishes to thank the Air Force Systems Command, the Air Force Office of Scientific Research, the South-eastern Center for Electrical Engineering Education and the Advanced Beam Control Branch/Air Force Weapons Laboratory, Kirtland AFB, NM for the opportunity to participate in the 1983 AFOSR/SCEE Summer Faculty Research Program. Thanks are given to Dr. John R. Kenemuth for suggesting this area of research and to Captain Joseph T. Evans, USAF Project Officer for the HET System for his collaboration and help in the performance of the author's research work.

INTRODUCTION

Interactions with the vibration environment (mechanical/structural, acoustic, etc.) can severely degrade sensitive optical sensor performance. The resulting degradation can cause loss of the sensor-observability and via the feedback path, the control-systems functions. The problem is especially important with respect to the use of large optical beam wavefront sensors.

As confirmed in 1983/1984, the AFWL/ARAA heterodyne holographic interferometer (referred to subsequently in this paper as the HET) system was an extremely sensitive optical wavefront sensor system. Figure 1 gives a block diagram of this heterodyne interferometer configuration. This version of the HET can operate in either a conventional hologram-interferometer or a heterodyning hologram-interferometer mode. In the conventional mode both the reference and object optical beams are at the same frequency. In the heterodyning mode the HET uses a constant 625 KHz frequency difference between the reference and the object beams in a heterodyning, frequency-modulation sense. Here the optical result is used to define the differential holographic fringes (difference between specified reference and desired wavefront surfaces) characterizing the spatial distortion of a nominal 10 in. diameter wavefront image of the transverse distortion of a static or a vibrating surface. The 10 in. diameter wavefront size is a nominal design value for the HET system. It can be varied from 1 in. to 16 in. by suitable choice of the beam expander lenses in the optical path components comprising the HET wavefront sensor system.

The HET system is mounted on an optical bench which is presently supported by six vibration isolation support mounts or legs. It originally (through 1 August 1983) was covered by an attached

acoustic/wind screen to minimize the effects of random air movements and turbulence upon performance of the HET system. Figure 2 depicts this configuration.

Significant mechanical and/or acoustic vibration level problems have been observed with the HET configuration in its 1983/1984 laboratory location in the center of the first floor of a building at AFWL/ARAA. This location may have been at a vibration antinode in what was originally an office building which was neither structurally nor acoustically designed to house high precision optical measurement laboratories.

The mechanical and acoustic vibration problems referred to above manifest themselves in real time as vibrating differential hologram, interferometer fringe patterns in the image formed of the transverse distortion of an illuminated object/wavefront surface. That is, the vibrations can cause modulations in the relative phase between the object and reference beams. After electronic detection at spatially discrete sampling locations and Zernike orthogonal-modal-basis-function, least squares fit to the deformed surface, consistently large RMS deviations ($\lambda/35$, $\lambda=5145 \text{ \AA}$) have been found in the 10 in. optical beam wavefronts through late Spring 1983. These large wavefront surface measurement errors as compared to an apparently obtainable ($\lambda/200$ to $\lambda/75$), have motivated the measurement and analysis work described in this paper. This primary effort in this work consisted of an investigation of the sources of unwanted mechanical/acoustic vibrations and of system modifications to eliminate/minimize their impact on HET wavefront sensor performance. In support of the primary effort, work was also accomplished in the following three areas:

- Rigid-body, undamped resonant frequency and time-domain analyses of the motion of the HET optical table, etc.
- Calculation of normalized, approximate-flexural and torsional frequencies of optical table for various free, pinned-corner and intermediate support leg conditions
- Impact of vibrating motion on differential hologram fringe modulation function.

The remainder of this paper is organized as follows. First the HET system is reviewed and all known potential sources of unwanted noise in the system

are summarized. Next the experimental and analytical investigations of the sources of mechanical, etc. vibration are described and their results discussed. This is followed by sections describing modifications to the HET optical table configuration and the results of these modifications. Next the work in the three supporting areas are described. Their supporting

analyses and results can be found in the Appendices of Reference 21. Conclusions are then made regarding the investigation of vibration sources and modifications tried to improve HET system performance, as well as the related support area work. Recommendations are made to further improve HET wavefront sensor performance at the end of this paper.

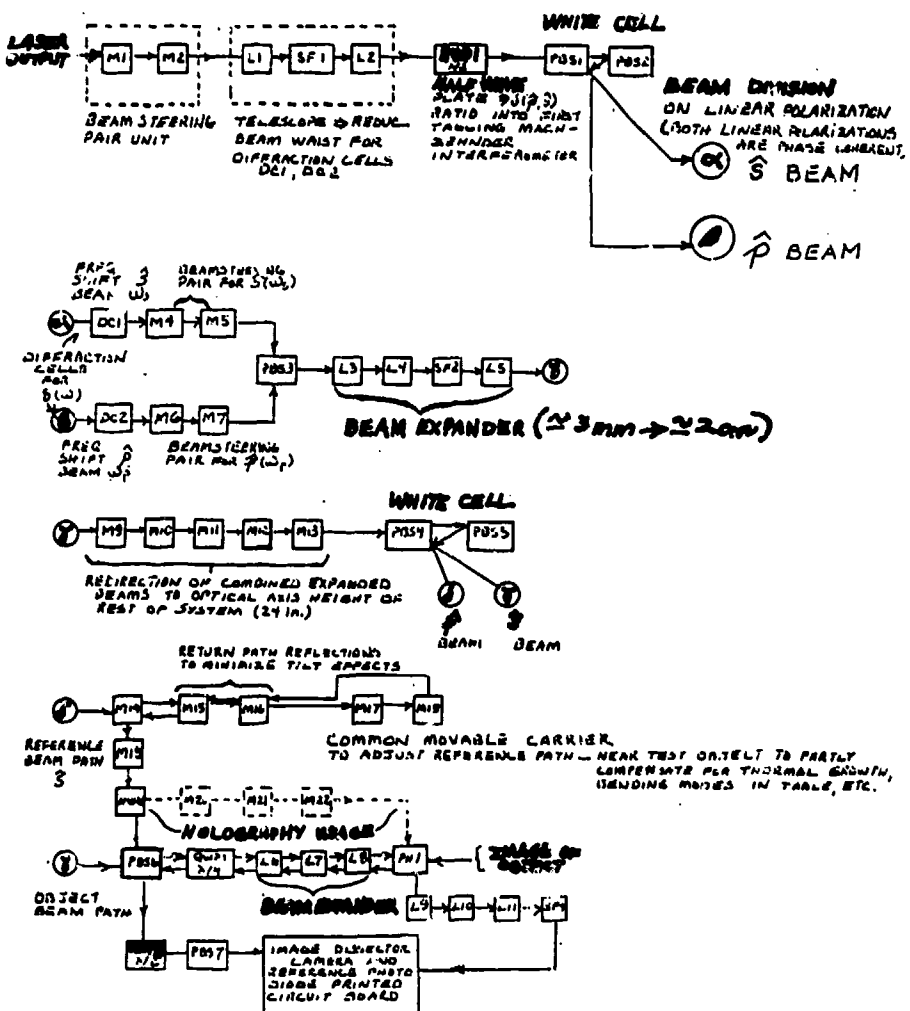


FIGURE 1
BLOCK DIAGRAM OF HETERODYNE INTERFEROMETER

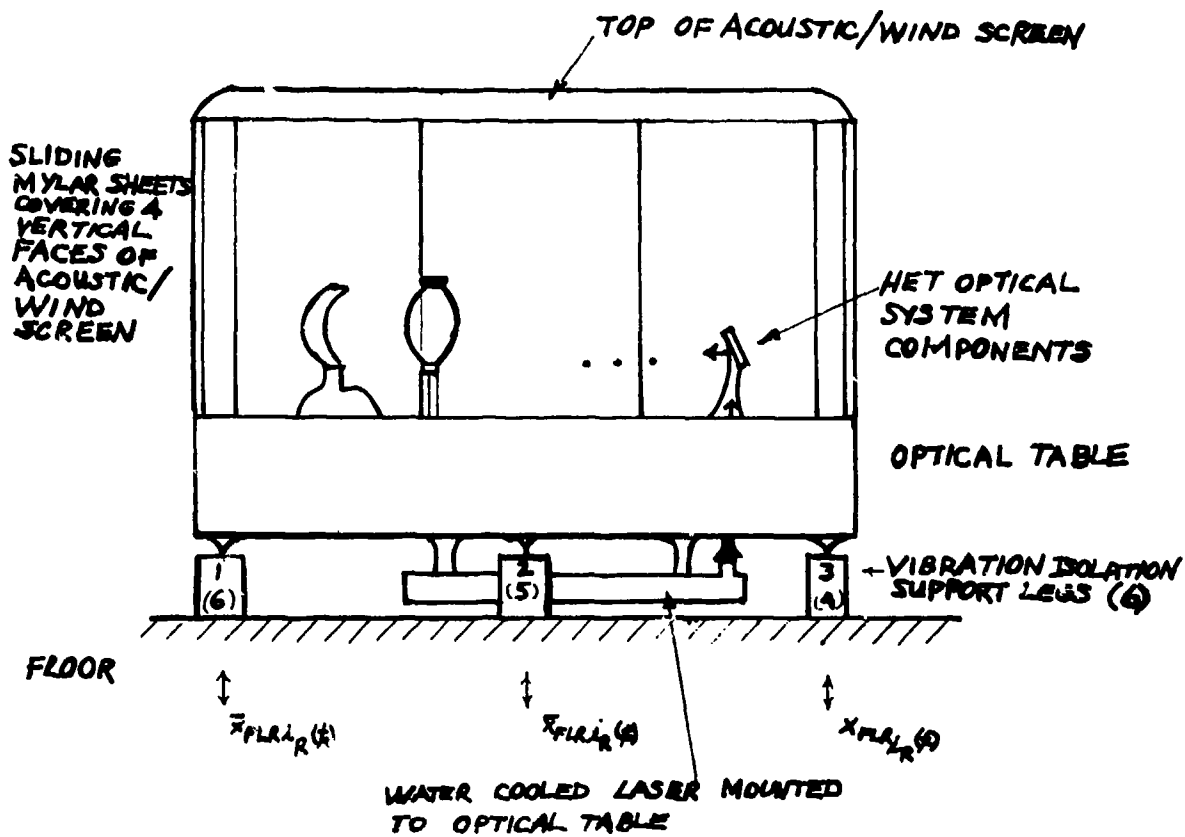


FIGURE 2
HET OPTICAL TABLE PLUS ATTACHED ACOUSTIC/WIND SCREEN, LASER SUPPORT TABLE,
VIBRATION ISOLATION SUPPORT LEGS, ETC. SYSTEM CONFIGURATION

FAMILIARIZATION WITH HET SYSTEM

A review was made of the relevant optics and of the laser and optical path system components comprising the HET system (Refs. 1-8). As indicated in the introduction, Figure 1 schematically depicts the component lineup and the optical path signal flow in the present HET system. In addition, the data collection electronics system and the heterodyning holographic interferometry/signal processing principles upon which the HET system is based were also reviewed (Refs. 4,9-12).

All relevant aspects of noise degrading HET wavefront sensor performance, the optical bench or table, etc. plus the vibration isolation legs and the complete optical path/optical, etc. component lineup in the HET were considered. This was done to place the

mechanical/acoustic vibration problems in context with respect to other noise sources and to obtain an indication of the potential noise floor--i.e., best wavefront sensor performance possible with the HET system. Table I summarizes the five mechanical/acoustic and the three-laser/optical polarization/detector -- potential sources or mechanisms of unwanted noise which were identified.

Newport Research Corporation was contacted relevant the design and dynamic mechanical response details of the optical bench, the attached acoustic screen, the bottom mounted laser bench, and the vibration isolation leg support system (Refs. 13,14). This was done to gain further insight from the equipment manufacturer into the mechanical/acoustic vibration frequencies and mode shapes possible in the HET

optical table design. NRC indicated that the first free-free flexural bending and torsional resonance frequencies should be approximately 100 and 170 Hz, respectively for the HET's 12 ft x 4 ft x 1.5 ft optical table in an unloaded condition. Nominal vertical and transverse stiffnesses of 64 lbf/in and 125 to 150 lbf/in were indicated for each of the six pneumatic, vibration isolation mount support legs for frequencies around 1 Hz.

It was also indicated these stiffnesses are frequency dependent. That is, above 1 Hz these stiffnesses are somewhat less than (nominal 50 to 60% of) the 1 Hz values. Vertical and transverse damping values were unavailable. They can, however, be inferred from the frequency response results given in the equipment catalog (Ref. 13).

TABLE 1
SOURCES OF UNWANTED NOISE

- Seismic/Structural Floor Vibration
- Acoustic Pressure Radiation Via Air Path (Fluidborne; Fluidborne; Structureborne)
- Acousto-optical Interaction Coupling
- Flow Induced Vibration Using Water Cooling for Laser (Monitor Transition, Mid and Laser Output Beam Sections of Flow-Line on Laser)
- Flow Induced Plasma Fluctuation and Beam Modal Drift
- Optical Separation of p,s Polarization Beams
- Electrical Line/Electronic Recording Processing and Radiation
- Laser-Detector Shot Noise - System Optical Gain Figures.

HET INTERFEROMETER PLUS ACCELERATION, ETC. SENSOR MEASUREMENTS

The author used three ENDEVCO 2262C-25 piezoresistive accelerometers plus corresponding amplifier/signal condition cards (AFWL/NTDE) and three Geo Space HS-10-1 seismometers (AFWL/NTDE) (Refs. 15,16). In addition, two PCB 303A02 piezotronics accelerometers and amplifier/signal conditioning systems were borrowed from the M.E. Department of Texas Tech University (Ref. 17).

Velocity and acceleration measurements have been made using the three Geo Space seismometers (direct measurement of velocity) and the two PCB accelerometers. The seismometers have been the sensors most extensively used

to

(a) Measure acceleration, velocity, and motion levels at three locations across the mid-length plane on the optical table and at three locations near the 10-inch beam expander and mirror components (east end of optical table in HET lab).

(b) Measure acceleration, velocity and motion levels at three locations on the floor under the optical table and at a location south of and away from (4 ft) the optical table.

In addition, the seismometers were also used to survey the acceleration, etc. levels in three other ARAA labs. Here measurements were made at locations under and on the optical tables in the (1) Phasar lab, (2) Deformable Mirror Lab and (3) Adaptive Optics Lab. It should be noted that the optical table in the Phasar Lab also has an attached (somewhat shorter vertically) wind screen enclosure. The deformable mirror and adaptive optics labs also each have a 6+ ft long trench running lengthwise (east-west) along their floors. The optical tables in these three labs are somewhat longer (15 to 18 ft) than the nominal 12 ft table long HET Lab table.

Vertical and horizontal, two-point relative phase modulation measurements and RMS wavefront surface error measurements were made using HET system detector signal conditioning A/D conversion hardware and its Data General signal processing software. It should be noted that the vertical and horizontal, two-point relative phase measurements correspond to pitch and yaw vibratory motion modulations, respectively, of the reference and object beams in the HET system.

DATA PROCESSING/ANALYSIS

The results discussed in this report were based on (a) Nicolet 660A digital oscilloscope RMS spectral analysis, differentiation and integration processing and plotting system and (b) HET system relative phase measurement, FFT processing and plotting capability using Data General Eclipse S/200 computer system (Refs. 18-20). The latter was developed during Summer 1983 by Miss Geraldine Cordova under the direction of Captain Joseph T. Evans.

IDENTIFICATION OF VIBRATION NOISE SOURCES IMPACTING SYSTEM PERFORMANCE

As indicated previously a survey/

comparison was made of the velocity and acceleration levels in the ARAA-HET, PHASAR, Deformable Mirror and Adaptive Optics Labs. RMS floor velocity, etc. level results in these four labs indicated that the Deformable Mirror Lab is quietest at 20 to 50 Hz closely followed by the Adaptive Optics Lab. The Phasar and HET Labs seemed to be noisier (nominal 5 to 10 dB) in terms of peak velocity and acceleration levels in this 20 to 50 Hz frequency range with the HET Lab the noisiest of these two. This may be correlated with the fact that the HET Lab is near the center of the first floor of its AFWL Building location which can be a vibration antinode. This AFWL Building is an office building which was not structurally and acoustically designed for precision optical measurements.

Comparison of the differences between the RMS acceleration, etc. spectra levels for the table and the floor for each of the four above-mentioned labs indicates nominal 25 to 35 dB differences (level reductions) for the Deformable Mirror and Adaptive Optics Labs and 20 to 25 dB level reductions for the HET (nominal 20 dB) and PHASAR (nominal 25 dB) Labs in the 25 to 45 Hz

frequency range. The relevance of the peak levels observed at nominal 30, 40 Hz frequencies will be discussed later. Here it should be noted that the optical tables in the HET and PHASAR Labs both have attached acoustic/wind screen enclosures while the optical tables in the Deformable Mirror and Adaptive Optics Labs do not.

Figures 3a and 3b give representative plots of the RMS spectral decompositions of the velocity levels under and on the HET system optical table with the attached wind screen enclosure. These results show very significant peaks at nominal frequencies of 30 and 40 Hz. Examination of these figures indicates that the floor minus table differences in the 30, 40 Hz levels are 19.8, 21.4 dB, respectively, or a nominal 20 dB. These reductions are somewhat less than the vibration isolation to be expected at the NRC indicated 12 dB/octave fall off above 1 Hz with the six NRC vibration isolation mount support legs. Since comparable NRC vibration isolation legs seem to perform well in corresponding leg configurations in the Deformable Mirror and Adaptive Optics Labs, these results indicate that additional vibration noise sources as, e.g., acoustic are exciting the system via the acoustic/wind screen enclosure.

-3.9 dBV VLG
C

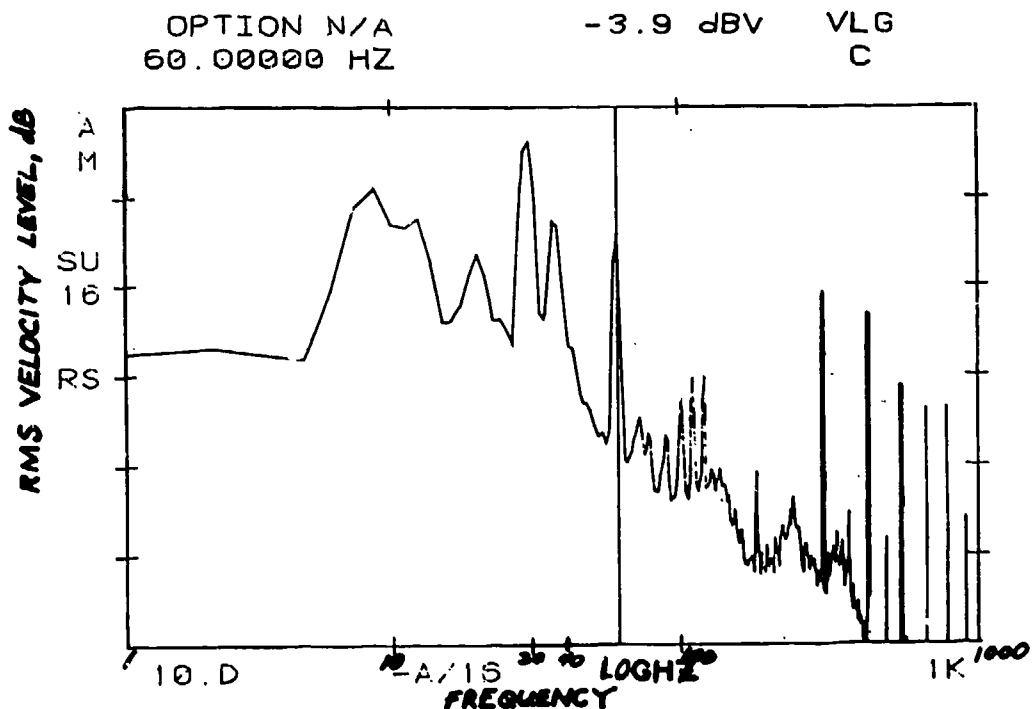


FIGURE 3a RMS SPECTRAL DECOMPOSITION OF VELOCITY LEVEL UNDER HET OPTICAL TABLE

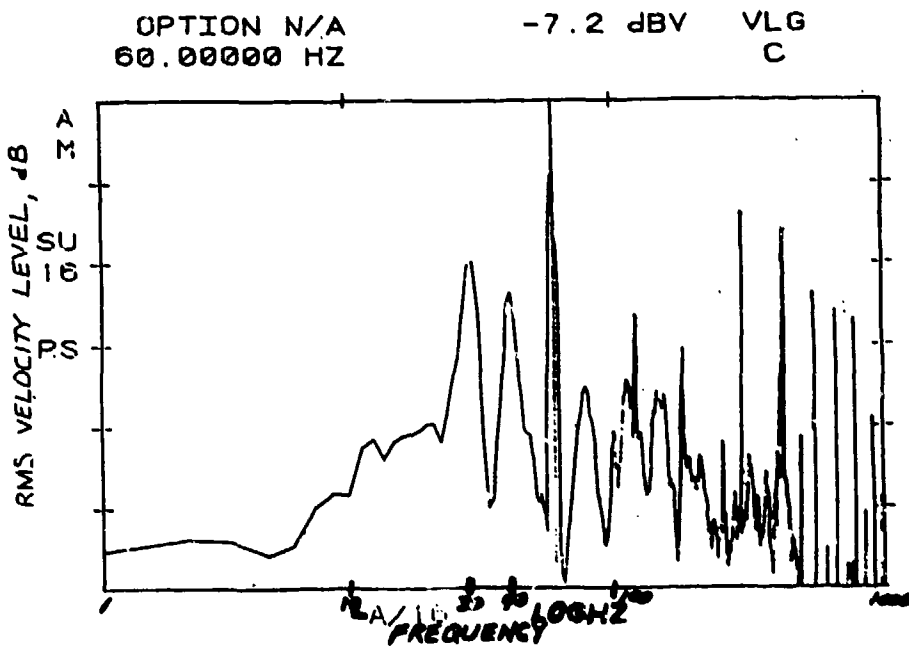


FIGURE 3b RMS SPECTRAL DECOMPOSITION OF VELOCITY LEVEL ON HET OPTICAL TABLE

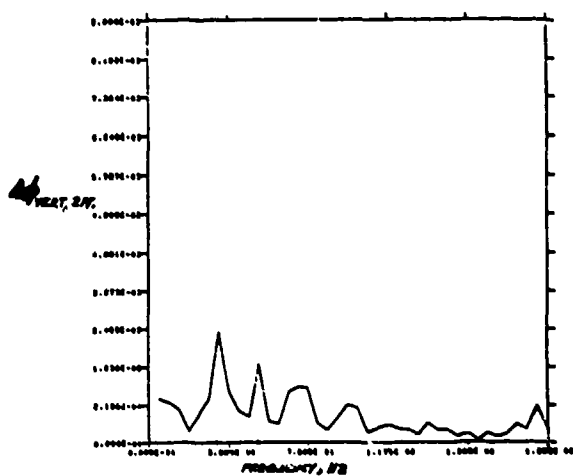


FIGURE 4a SPECTRAL DECOMPOSITION OF VERTICAL, 2 POINT RELATIVE PHASE MEASUREMENT FROM HET SYSTEM

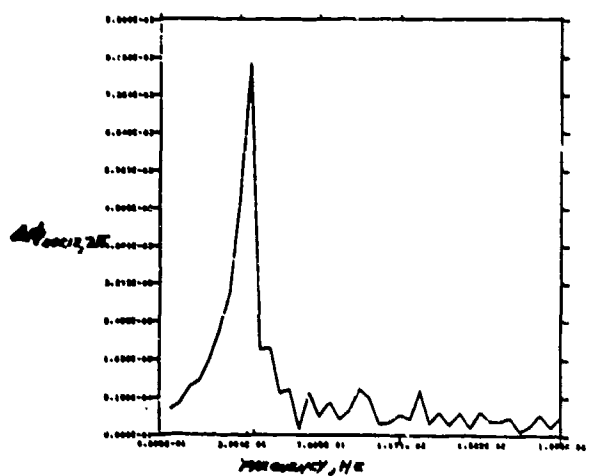


FIGURE 4b SPECTRAL DECOMPOSITION OF HORIZONTAL, 2 POINT RELATIVE PHASE MEASUREMENT FROM HET SYSTEM

Figures 4a and 4b respectively plot spectral decompositions of the vertical and horizontal, two-point relative phase measurements which were made with the HET system. It should be noted that an independent sensor (HET system) using a different physical process--as compared to the seismometers--was used to obtain these results. Figure 4a shows a relatively large RMS motion/relative phase modulation peak at a nominal 30 Hz. This is for the two vertical points configuration in the HET detector array and corresponds therefore to a pitch vibratory modulation of the HET reference and object optical beams. Figure 4b similarly gives a large RMS motion/relative phase modulation peak at a frequency of 42 to 43 Hz. In this case two horizontal points were sampled in the HET detector array. Thus it corresponds to a yaw vibratory modulation of the reference and object optical beams in the HET system.

SIMPLE ANALYSIS OF SCREEN ENCLOSURE, LASER TABLE MOTIONS WITH RESPECT TO OPTICAL TABLE

Simple spring-mass analyses were made of the translational and yaw motions of

- (a) Top member of the acoustic/wind screen with fixed end attachment to the top of the optical table.
- (b) Bottom member/ledge of laser bench with fixed end attachment to the bottom of the optical table.

Figure 2 depicts the location of the wind screen and laser bench structures. Figures 5 and 6 give more detailed representations of these structures.

Nominal mass, stiffness values were used in the analyses of these motions with respect to the optical table. Here it is assumed that the rigid body motion natural frequencies of the optical table (as indicated by experimental results and by analysis and time domain computer model results) are in the low frequency range 0 to 5 Hz while the wind screen and laser bench resonant frequencies are in the range 25 to 55 Hz. That is, they are somewhat separated in frequency and thus the wind screen and laser bench can be considered (each separately) as moving with respect to a fixed table. Thus uncoupled, single-degree-of-freedom representations can be used for each of the x,y translation and yaw (with respect to the z axis) motions. Details of the analysis calculations are

given in Appendix A of Reference 21.

TABLE II
TRANSLATIONAL MODE AND YAW
MODE NATURAL RESONANT FREQUENCY
RESULTS FOR MOTION OF TOP
MEMBER OF ACOUSTIC/WIND SCREEN
WITH RESPECT TO OPTICAL TABLE

	$f_{NAT\ RES}$ (Hz)
x_{TRANS} (along table length)	29.03
y_{TRANS} (along table width)	29.03
yaw (angular motion with respect to vertical z axis)	40.81

TABLE III
TRANSLATIONAL MODE AND YAW
MODE NATURAL RESONANT FREQUENCY
RESULTS FOR MOTION OF BOTTOM
LEDGE OF LASER SUPPORT BENCH
WITH RESPECT TO OPTICAL TABLE

	$f_{NAT\ RES}$ (Hz)
x_{TRANS} (along table length)	48.09
y_{TRANS} (along table width)	48.09
yaw (angular motion with respect to vertical z axis)	39.88

Table II gives the natural frequency results, 29.03 Hz and 40.81 Hz calculated for the translational

and yaw motions, respectively, of the top member of the wind screen. Table III summarizes corresponding transla-

tional and yaw resonant frequency results, 48.09 Hz and 39.88 Hz, respectively, for the laser support bench.

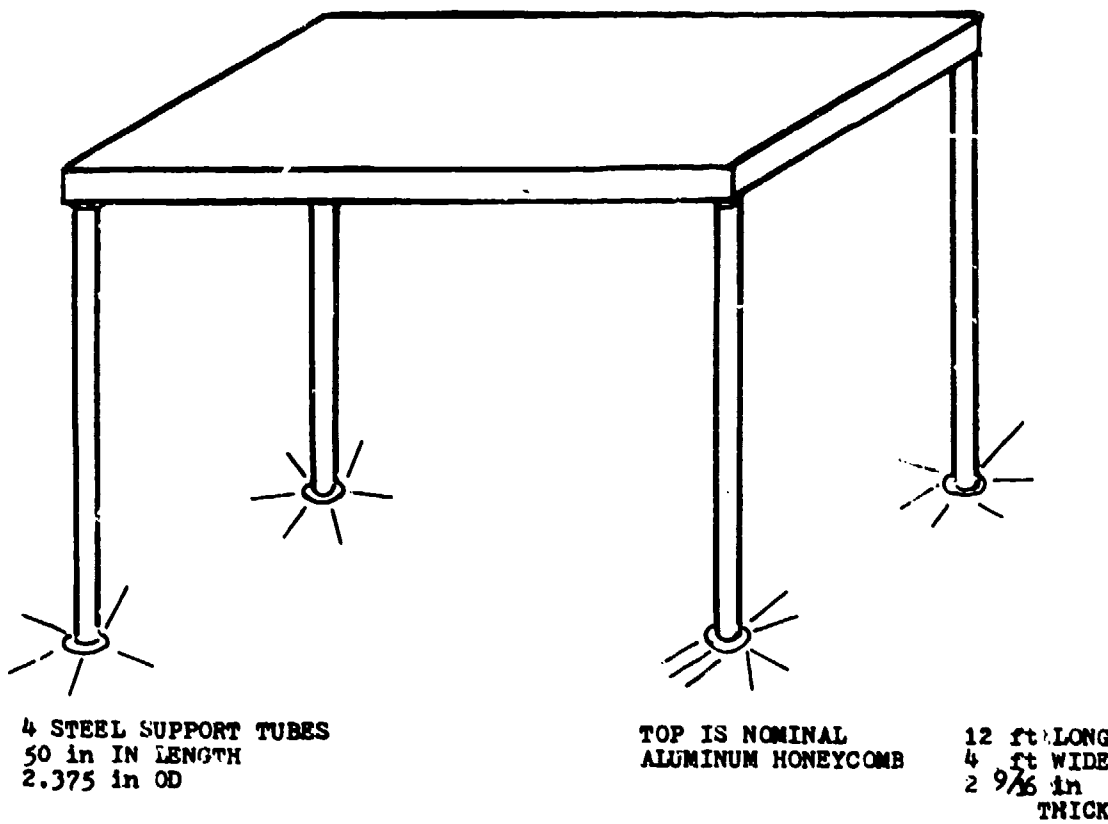


FIGURE 5
ACOUSTIC/WIND SCREEN SUPPORT STRUCTURE

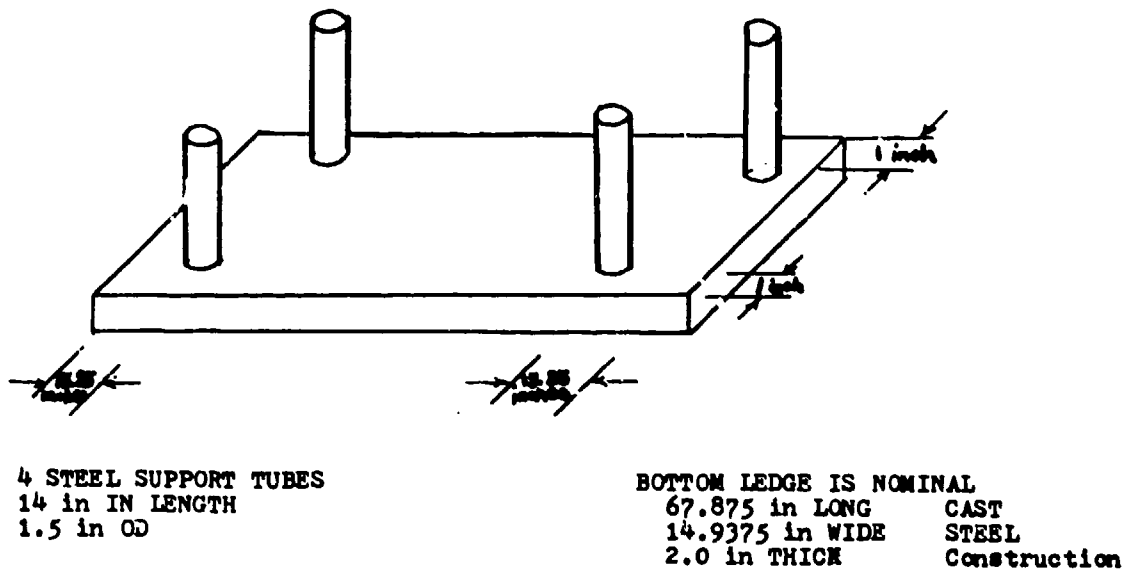


FIGURE 6
LASER BENCH AND SUPPORT STRUCTURE

These resonant frequency analysis results taken together indicate that there are translational motion resonant frequencies at nominal values of 29 and 48 Hz. In addition, there are two closely placed yaw motion resonant frequencies at nominal values of 40 and 41 Hz. These results are in close agreement with the significant peaks observed in the RMS seismometer velocity level spectra at nominal ranges of 29-31 Hz, 40-42 Hz and on occasion 50-52 Hz with both wind screen and laser bench structures in place. These results are also in agreement with observed peaks in the independent spectral decompositions of the vertical and horizontal, two-point relative phase measurements made with the HET system (with both the wind screen and the laser bench attached to the optical table).

Specifically, the 29 Hz and 48 Hz natural resonant frequencies are for relative (x,y) translational motions which correspond to roll and pitch optical beam modulations. They correspond to the 32 to 33 Hz and 53 Hz spectral peaks found in the vertical, two-point relative phase measurements directly giving the pitch motion component of the modulation of the HET system optical beams. Similarly, the calculated 40 Hz and 41 Hz yaw natural resonance frequencies correspond to the 43 Hz spectral peak found in the horizontal, two-point relative phase measurements. These measurements directly give the yaw motion component of the modulation of the optical beams in the HET system.

In summary, these results indicate that both the acoustic/wind screen and the laser support bench are important local "sources" of mechanical vibration in the HET system. Together they can cause nominal 25 to 55 Hz frequency modulations of the phase difference between the reference and the object beams. Thus they are apparently significant local sources or causes of the consistently large $\lambda/35$ -RMS wavefront surface deviation errors measured with the HET system.

DESIGN MODIFICATION STUDY AND RESULTS

It was decided to remove the attached acoustic/wind screen--a non-trivial, though relatively easy task-- and investigate the impact of this change upon measured acceleration, velocity, etc. levels and upon HET system wavefront sensor performance. The laser support bench, etc. was not also removed because its removal is relatively difficult and would require long

term separate mounting modifications to suitably reconfigure the laser to optically drive the HET system. It should be noted that the ideal modification plan here would be to remove only one of these two structures then, replacing that one, only remove the other, and then remove both.

Removal of the acoustic/wind screen was found to give significant reduction of the nominal 29-31 Hz (10 to 15 dB reduction) and 40-43 Hz (15 to 20 dB reduction) vibration noise components for seismometer locations on top of the optical table. However, when the

- (a) Differential hologram optical fringes were visually observed for the 10 in. beam wavefronts in the HET system,
- and
- (b) Corresponding relative phase between the reference and object optical beams was visually observed on the system oscilloscope,

it was seen that removal of the wind screen gave large-scale ($\gtrsim \lambda/4$ and hence quadrant errors), random oscillations in the low frequency range 0.0 to 2.5 Hz.

Subsequent investigations showed that these oscillations were due to random air movements and turbulence as, e.g., generated by oscilloscope and computer, etc. equipment fans and blowers in the HET Lab. These air movements, etc. severely degraded HET system wavefront sensor performance without some form of a wind screen surrounding the optical table and system components.

A system of floor to ceiling curtains with a rudimentary ceiling of plastic film sheeting which completely surrounds, but is not physically attached to, the HET optical table was used as a near term solution to reduce the effects of the random air movements and turbulence. It was found that 10 in. beam RMS wavefront deviation errors can be reduced to $\lambda/60$ with the curtains and ceiling in place.

SUPPORTING STUDIES

UNDAMPED NATURAL RESONANT FREQUENCY ANALYSIS OF RIGID BODY MOTION OF OPTICAL TABLE

An undamped natural resonant frequency analysis was made of the rigid body motion (RBM) of the HET optical table (Refs. 22-26). Figure 7 depicts

the idealized six degree-of-freedom representation used in the analysis. The six degrees of freedom are:

- x or x_F^1 = Translational motion along the table length
- y or x_F^2 = Translational motion transverse to the table length, i.e., along table width.
- z or x_F^3 = Translational motion in the vertical direction.
- ϕ = Roll angular motion about the x axis.
- θ = Pitch angular motion about the y axis.
- ψ = Yaw angular motion about the z axis.

Hence x, y, z (or x_F^1, x_F^2, x_F^3) form a right-handed, fixed inertial coordinate system. Positive x, y, z are in the directions indicated in Figure 7. Positive ϕ, θ, ψ are defined as positive if they are counter-clock-wise with respect to the positive x, y, z axes, respectively. Figure 7 also shows the six vibration isolation mount support legs, which are represented as three-dimensional linear springs. In this analysis the motions are assumed to be small such that the resulting dynamic system is linear. It is further assumed that the (x, θ) motions and the (y, ϕ) motions are coupled each pair together, while the z and ψ motions are each uncoupled.

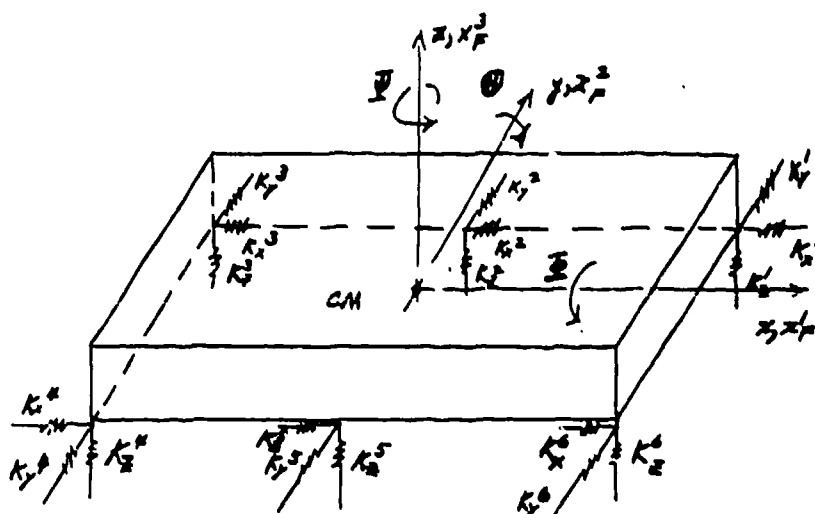


FIGURE 7
IDEALIZED SIX DEGREE OF FREEDOM REPRESENTATION FOR RIGID BODY MOTION
ANALYSIS OF MET OPTICAL TABLE SYSTEM

NOTE THAT (A) FOR THE VIBRATION ISOLATION MOUNT DAMPING EXTENSION, EACH SPRING ELEMENT IS REPLACED BY A SPRING AND DAMPER ELEMENT IN PARALLEL FOR EXAMPLE,



IS REPLACED BY



(B) ADDITIONAL NONSYMMETRICALLY PLACED MASSES ARE CONSIDERED WITH RESPECT TO THE CENTER OF MASS OF THE OPTICAL TABLE. THUS,

$$I_{11}^{cm}(\text{OPT.TAB}) = I_{11}^{cm}(\text{ARB.MASS}) + M(\text{ARB.MASS}) (R^2 \delta_{ij} - R_{ij})$$

FOR THE INERTIA TENSOR COMPONENTS IN WHICH

$$\bar{R} = R_1 \bar{U}_1 + R_2 \bar{U}_2 + R_3 \bar{U}_3, \quad R = |\bar{R}|$$

$$\delta_{ij} = \text{Kronecker Delta}$$

TABLE IV
SUMMARY OF UNDAMPED NATURAL
RESONANT FREQUENCIES OF HET
OPTICAL TABLE WITH SIX LEGS

$f_{NAT\ RES}$ (Hz)		
x_{TRANS}	Mode 1	0.27
θ_{PITCH}		
x_{TRANS}	Mode 2	2.34
θ_{PITCH}		
y_{TRANS}	Mode 1	0.66
θ_{ROLL}		
y_{TRANS}	Mode 2	2.61
θ_{ROLL}		
z_{TRANS}		1.12
θ_{YAW}		2.49

Note that the six legs are assumed to be placed one at each corner and one at the midpoint of each nominal 12 ft length-side.

Table IV summarizes the results of this undamped natural resonant frequency analysis. These RBM frequencies range from 0.27 Hz to 2.61 Hz. They are in basic agreement with relative/load peaks which have been observed in the measured acceleration, velocity and motion level spectra for non-zero initial conditions in each of the six degrees of freedom. Appendix B of Ref. 21 gives details of the analysis. This includes a summary of the equations used to calculate the resonant frequencies given in Table IV.

12 STATE VARIABLE, TIME-DOMAIN ANALYSIS OF RIGID-BODY-MOTION OF OPTICAL TABLE, ETC. DESIGNS

A 12 state-variable, nonlinear, time-domain model analysis was made of the rigid-body-motion (RBM) of the HET optical table, etc. system design. The dynamic systems model considers x_i , $i = 1, 2, 3$ -- translational motion of the center of mass and θ, θ, θ -- roll.

pitch and yaw degrees of freedom (fixed inertial vector components). The dynamic systems model can handle an arbitrary number (4) of vibration isolation mount support legs arbitrarily placed under the table. Figure 7, as discussed previously, gives an idealized representation of the system under consideration. Details of the HET RBM model can be found in Ref. 21. See also Refs. 27, 28 for background regarding development of the state variable equations.

This dynamic systems model was implemented in the Fortran IV computer software package HETRBM09, which consists of a driver plus 21 subroutines and 2 function subprograms. This software has been thoroughly checked out. Complete listings of HETRBM09 and of an example input data set file HETRBMIN are given in Appendix C of Ref. 21.

HETRBM09 runs have been made which show the coupling of the

- (1) x_p = x translation and θ pitch
- (2) $y = x_p^2$ translation and θ roll

degrees of freedom. The $z = x_p^3$ vertical translation and θ yaw degrees of freedom are each essentially uncoupled from all others. The undamped resonant frequency behavior observed with HETRBM09 for non-zero initial condition runs with zero motion input at the floor is in good agreement with the results discussed in the previous section of this paper.

CONTINUOUS BEAM APPROXIMATE RESONANT FREQUENCY ANALYSIS

A normalized, approximate frequency analysis was made of the flexural and torsional vibration modes of the optical table. Here the free/pinned boundary, pinned intermediate support results given in Blevins (ref. 29) for the resonant frequencies of the multi-span elastic beam configuration were used. Tables V, VI, and VII present these undamped natural resonant frequency results which have been normalized to a first free-free unloaded, single span flexural frequency of 100 Hz and a corresponding torsional frequency of 170 Hz. These values were given by Newport Research Corporation (Ref. 14) as reasonable approximations for a nominal 12 ft x 4 ft x 1.5 ft HET system optical table.

These results indicate that significant changes in the resonant frequencies and hence mode shapes excited at a given excitation frequency can be effected by a judicious or more optimal placement of the vibration

isolation mount support legs. Indeed, Whaley and Pearson (Ref. 30) have shown (via model predictions) that reductions of 10 to 30 dB can be obtained in the RMS angular motion of the optical table. This means that since the velocity modulation of an optical component is given by an equation of the form:

$$\bar{v}_{\text{OPT. COMP.}} = (v_T - \bar{v}_I) \quad (15)$$

in which (refer to Fig. 8)

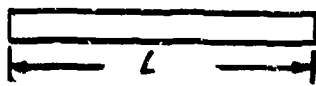
$$\bar{v}_{\text{OPT. COMP.}} = v_T \bar{x} + \bar{\omega} \times \text{Loc} \bar{x} \quad (16)$$

$$\bar{\omega} = \left(\frac{\partial v_T}{\partial x} \bar{i} - \frac{\partial v_T}{\partial y} \bar{j} \right) x_{\text{oc}}, y_{\text{oc}} \quad (17)$$

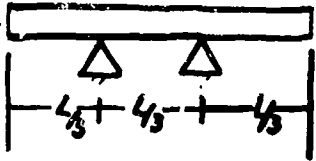
TABLE V
RESONANT OR NATURAL FREQUENCIES
FOR OPTICAL TABLE MODELED AS A
FREE-FREE BEAM WITH PINNED
INTERMEDIATE SUPPORTS
 $L \approx 12.0$ ft.

i	f_i (Hz) Single span	f_i (Hz) Triple Span 2 Supports	f_i (Hz) Quadruple Span (4 Legs)
1	100.0	80.2	162.2
2	275.6	109.3	176.5
3	540.8	515.6	833.0
4	893.7	734.5	1103.4
5	1334.6	891.3	1408.6
6	1863.8	1809.5	1588.5

FREE-FREE
SINGLE SPAN



FREE-FREE
TRIPLE SPAN



FREE-FREE
QUADRUPLE
SPAN

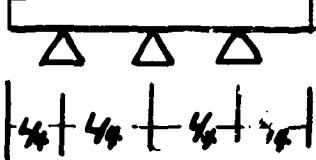
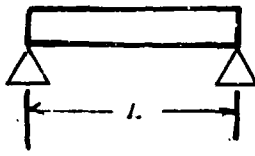


TABLE VI
RESONANT OR NATURAL FREQUENCIES
FOR OPTICAL TABLE MODELED AS A
PINNED-PINNED BEAM WITH PINNED
INTERMEDIATE SUPPORTS
 $L \approx 12$ ft.

i	f_i (Hz) Single Span 2 Supports (4 Legs)	f_i (Hz) Double Span 3 Supports (6 Legs)
1	44.1	176.5
2	176.5	275.7
3	397.0	705.8
4	706.8	893.2
5	1103.1	1587.8
6	1588.2	1863.8

PINNED-PINNED
SINGLE SPAN



PINNED-PINNED
DOUBLE SPAN

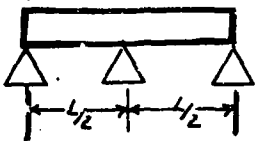
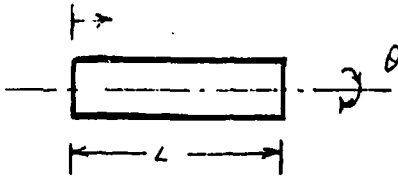


TABLE VII
RESONANT OR NATURAL FREQUENCIES
FOR OPTICAL BENCH REPRESENTED AS
A FREE-FREE STRAIGHT BEAM UNDER-
GOING TORSIONAL VIBRATION

i	f_i (Hz)
1	170
2	340
3	510
4	680
5	850
6	1020

FREE-FREE
SINGLE SPAN



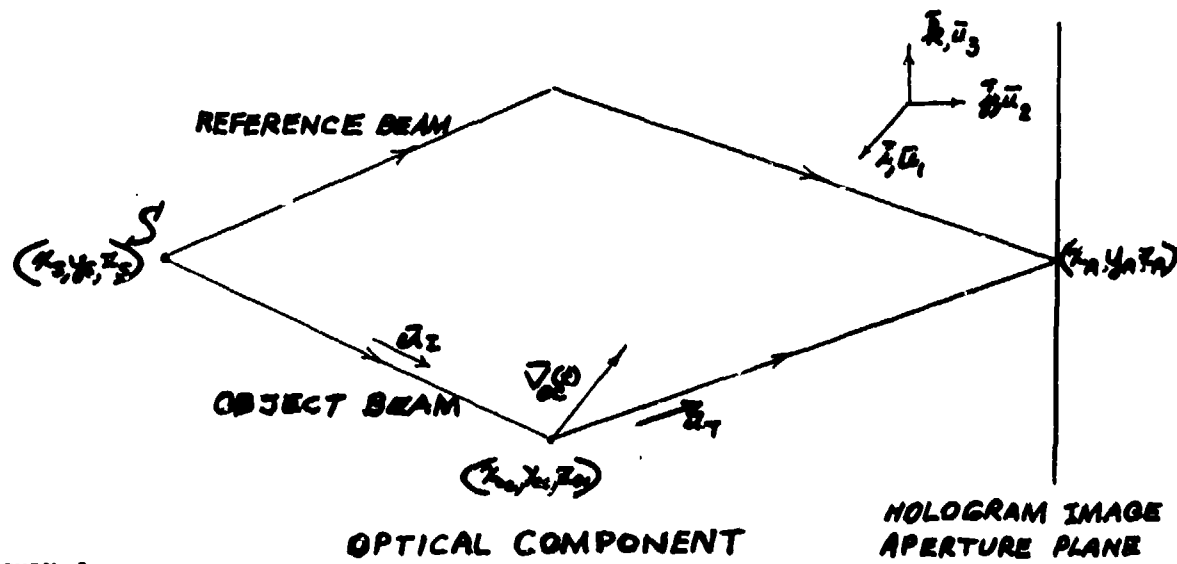


FIGURE 8

REPRESENTATIVE LINE DRAWING SHOWING VIBRATORY MOTION GEOMETRY FOR AN OPTICAL COMPONENT IN OBJECT BEAM PATH. NOTE THAT \vec{u}_I , \vec{u}_T ARE THREE-DIMENSIONAL UNIT VECTORS FOR INCIDENT, TRANSMITTED OPTICAL BEAMS AT OPTICAL COMPONENT

v_T = Transverse velocity of table surface at optical component table location (x_{oc}, y_{oc}).

$\frac{\partial v_T, \partial v_T}{\partial x, \partial y}$ = Angular velocity of table surface at optical component table location (x_{oc}, y_{oc}).

\vec{u}_I, \vec{u}_T = Unit vectors defining directions of incident, transmitted optical beams at optical component location (x_{oc}, y_{oc}, z_{oc}).

L_{oc} = Length of lever arm (assumed vertical) of the optical component

that significant reductions can be systematically obtained in the relative phase modulation of the reference, object beams in the HET system. This would follow as, e.g., via

$$\text{Min} \left[\frac{1}{\text{OPT. COMP.}} \cdot (\vec{u}_T - \vec{u}_I) \right]^2 \quad (18)$$

Over

Leg Placement Designs

Table Physical Parameters

Table Placement, etc. of Optical

Components

VIBRATORY/AcouSTIC MOTION-IMPACT ON FRINGE MODULATION

A review was made of the survey work by Smith (Ref. 31) relevant the impact of motion upon holograms and the fringe modulation function. Smith's consideration is based upon the temporal filtering of holograms formulation introduced by Goodman (Ref. 32). Powell and Stetson also considered the related problem of interferometric vibration analysis and derived equivalent results from a somewhat more complicated point of view (Ref. 33). The related areas of FM modulation (straight line FM slide, constant frequency sinusoidal modulation, etc.) as considered by Nitta (Ref. 34) and the impact of noise on phase-lock-loop, heterodyne system performance as examined by Gardner (Ref. 35), Lindsey (Ref. 36) and Van Trees (Ref. 37) were also reviewed.

Reference 21 gives a detailed summary of the analysis for sinusoidally vibrating motion. This reference also discusses a preliminary FORTRAN IV software package TFVMHF02 developed by the author to evaluate the fringe modulation as a function of HET sampling time, translational or angular sinusoidal vibration amplitude as a function of frequency, and planar direction of motion with respect to the optical beam. Aper-

ture size effects can also be investigated using a checked-out version of TFVMHF02. The idea here is that TFVMHF02 should allow the investigation of meaningful amplitude levels for both mechanical and acoustic vibration source mechanisms.

CONCLUSIONS

An investigation has been made of mechanical vibration/acoustic sources of the consistently large ($\lambda/35$) RMS deviation errors in 10 in. beam wavefront surfaces measured with the AFWL/ARAA heterodyne holographic interferometer, wavefront sensor (HET) system as it was configured in 1983/1984. Spectral decompositions of vibration level measurements made with seismometer sensors and independent spectral decomposition measurements made with the HET system of pitch, yaw modulations of HET (reference and object) optical beams -- showed significant peaks at nominal frequencies of 30 and 40 Hz. Additional seismometer and HET beam modulation peak responses (albeit at somewhat lower levels) have also been seen at nominal frequencies of 50-52 Hz.

Simple undamped resonant frequency analyses of the relative motions with respect to the optical table of the

- (a) Top mounted acoustic/ wind screen structure
- (b) Bottom mounted laser support bench structure

have been made using nominal mass, stiffness values. These analyses gave translational (x,y) and yaw angular motion resonant frequencies corresponding to (roll, pitch) and yaw optical beam modulations of (29.03, 40.81) Hz for the wind screen and (48.09, 39.88) Hz for the laser support table. These results plus the attachment of the wind screen to the top of the optical table indicate that the wind screen is a significant local source (or antenna/amplifier as opposed to absorber) of mechanical/acoustic vibratory motion.

Removal of the acoustic/wind screen enclosure resulted in reduction of the nominal 30 Hz pitch and 40 Hz yaw vibration levels and optical beam modulation components. However, large amplitude, low frequency random motion induced modulations caused quadrant errors ($\lambda/4$) in (a) the two-point relative phase observed as a function of time on the HET system oscilloscope and (b) the wavefront sensor

surface error results indicated in using the HET system detection plus A/D conversion hardware and Zernike polynomial surface fitting software. These large amplitude, low frequency (0.0 to 2.5 Hz) random modulations were found to be caused by low level, random air movement and turbulence. The use of a system of floor to ceiling curtains and plastic sheeting ceiling as a near term/interim fix to this problem was found to improve HET system performance to the extent that 10 in. beam RMS wavefront surface errors of $\leq \lambda/60$ could be obtained.

Four supporting studies were also performed and reported in this paper. These studies were:

- (1) Resonant frequency analysis for linearized rigid body motion of HET optical table system.
- (2) 12 state variable, time-domain analysis of the nonlinear rigid body motion of HET optical table, etc. system designs.
- (3) Approximate beam resonant frequency analysis of flexible motion response of optical table system designs.
- (4) Impact of mechanical vibration/acoustic motion on relative phase modulation of HET system optical beams and hence on fringe modulation.

Limited work in supporting studies (1), (2) above gave good rigid body motion resonant frequency and time-domain predictions as compared to a limited amount of sensor time function measurements. These good comparison results indicate that the 12 state-variable, nonlinear time-domain model and the linearized resonant frequency model, when extended to include such effects as vibration isolation support leg damping and realistic nonsymmetric mass distributions can be used to investigate the number and placement of the support legs to minimize the effect on the rigid body motion of the HET optical table system.

The limited results and formulations presented in supporting studies (3), (4) indicate that computer model analytical calculation results (and corresponding modal analysis measurements) can be used to directly investigate the impact of HET system vibratory motion upon its relative phase modulation and aperture-plane fringe modulation response behavior. Therefore,

these computer model analytical, etc. studies can be used to optimize or at least improve upon the design of HET and similar optical, large-beam (as, e.g., ≥ 10 in.) wavefront sensor systems.

RECOMMENDATIONS

Based upon the results of the research work reported herein, the following recommendations are made:

- (1) That an unattached "rigid" member wind screen enclosure (4 sides and top) be constructed and used for the HET optical table and components mounted to its top surface. This structure should be separately supported on its own set of vibration isolation-rubber or similar material pads. It should minimize the effect of random air movements, etc. on HET wavefront/sensor performance.
- (2) That usage be investigated of additional local wind screen enclosures at the location of the large-beam expander and mirror, etc. optical components as well as at the table location where the laser beam enters the HET optical system.
- (3) Consideration should also be given to the design and use of off-the-shelf components to provide a positive pressure, clean room system environment in the interior of the large wind screen enclosure surrounding the HET optical table.
- (4) An investigation should be made of designs employing separate mounting of the driving laser and the use of fibre-optic or comparable means for light input to the HET system. Alternatively, placement of the laser on top of the optical table should be considered.
- (5) An investigation should be made of the optimization/ improvement of water input for laser cooling to reduce low frequency vibration inputs to HET system.
- (6) Consideration should be given to the design, construction and use of a 1 or 2 mass plus damper, spring elements tuned vibration absorber (yielding 10 to 30+ dB notch at specified design frequency) to reduce the still high 30 Hz, etc. line vertical motion component ob-

served at the top of the HET optical table.

- (7) That detailed modal analysis and acoustic sensor measurements be performed. These measurements can be used to define present optical component vibration mode sensitivities and to suggest changes/perturbations to the HET system resulting in improved wavefront sensor performance. This modal analysis and acoustic sensor work can also be used to head-off potential future wavefront sensor problems relevant the calibration, testing and use of flexible mirror and subaperture-to-full wavefront-reconstruction components.

REFERENCES

1. Baldwin, George C., An Introduction to Nonlinear Optics, Plenum, N.Y., 1969.
2. Born, Max and Wolf, Emil, Principles of Optics: Electromagnetic Theory of Propagation, Interference and Diffraction of Light, Sixth (Corrected) Edition, Pergamon Press, N.Y., 1980.
3. Hecht, Eugene and Zajac, Alfred, Optics, Addison Wesley, Reading, Mass., 1974.
4. Malacara, Daniel (Editor), Optical Shop Testing, John Wiley, N.Y., 1978.
5. Wyant, James C., Optical Testing, Optical Sciences Center, University of Arizona, Tucson, Arizona, June 1976.
6. Verdeyen, Joseph T., Laser Electronics, Prentice-Hall, Englewood Cliffs, N.J., 1981.
7. Calendar, Al, "Optics Overview/Summary for Heterodyne Holographic Interferometer Wavefront Sensor System," Unpublished Notes, AFWL/ARAA, Spring 1983.
8. Heterodyne Set-Up Drawing, AFWL/ARAA, Spring 1983.
9. Calendar, Al, "Heterodyne Interferometer-Data Collection Electronics System," Unpublished Notes, AFWL/ARAA, Spring 1983.
10. Gardner, Floyd M., Phaselock Techniques, Second Edition, Wiley-Interscience, N. Y., 1979, Chapters 1-4, 9.

11. Perina, Jan, Coherence of Light, Van Nostrand Reinhold, N.Y., 1971.
12. Steel, W. H., Interferometry, Cambridge University Press, England, 1967.
13. "Newport Corporation 1983-1984 Catalog," Newport Research Corporation, Mountain Valley, Calif., pp. 3-29.
14. Telephone conversations with Dennis Siegel, John Turechek, Newport Research Corporation -- Relevant (a) Vibration Isolation Mount Support Legs; (b) Rigid Body and Flexural and Torsional Modes of Vibration of HET system Optical Table; (c) Design of Attached Acoustic/Wind Screen, June, July 1983.
15. "HS-10-1 Seismometer: Operational and Frequency Calibration Procedures," Version 1, Revision A, Geo Space Corporation, Houston, Tx., 19 January 1976.
16. "Instruction Manual for ENDEVCO Piezoresistive Accelerometers," Endevco Dynamic Instruments Division, Division of Becton, Dickinson and Company, Copyright 1968 ENDEVCO, Revised January 1972.
17. "PCB Piezotronics Catalog 375," PCB Piezotronics, Inc., Depew, N.Y., Summer 1983.
18. Bendat, Julius S. and Piersol, Allan G., Random Data: Analysis and Measurement Procedures, John Wiley-Interscience, N.Y., 1971.
19. Bendat, Julius S. and Piersol, Allan G., Engineering Applications of Correlation and Spectral Analysis, John Wiley-Interscience, N.Y., 1980.
20. Enochson, Loren D. and Otnes, Robert K., Programming and Analysis for Digital Time Series Data, Shock and Vibration Information Center, Naval Research Laboratory, United States Department of Defense, Washington, D.C., 1968.
21. McLauchlan, Robert A., "Investigation of Vibration Problems with Heterodyne Holographic Interferometer," Final Report, 1983 USAF-SCEEE Summer Faculty Research Program, Department of Mechanical Engineering, Texas Tech University, 1 September 1983.
22. Meirvitch, Leonard, Analytical Methods in Vibrations, MacMillan, N.Y., 1967, Chapters 7,9,10,11.
23. Meirovitch, Leonard, Elements of Vibration Analysis, McGraw-Hill, N.Y., 1975, Chapters 7, 9, 11.
24. Thomson, William T., Theory of Vibrations with Applications, Prentice-Hall, Englewood Cliffs, N.J., 1972, Chapters 5-8, 10, 11.
25. Timoshenko, S., Young, D.H., and Weaver, W., Jr., Vibration Problems in Engineering, Fourth Edition, John Wiley, N.Y., 1974.
26. Warburton, G.B., The Dynamical Behavior of Structures, Second Edition, Pergamon Press, N.Y., 1976.
27. Lipscombe, J.M., "Aerospace Systems," Chapter 5 of Modeling of Dynamical Systems, Vol 1 (Edited by H. Nicholson), Peter Peregrinus Ltd. on Behalf of the Institution of Electrical Engineers, London and N.Y., 1980.
28. McKuer, D., Ashkenas, I., and Graham, D., Aircraft Dynamics and Automatic Control, Princeton University Press, Princeton, N.J., 1973.
29. Blevins, Robert D., Formulas for Natural Frequency and Mode Shape, Van Nostrand Reinhold, N.Y., 1979, Chapters 5,6,8,11.
30. Whaley, P.W. and Pearson, J. "Computer Aided Design of Passive Vibration Isolators for Airborne Optical Systems," Shock and Vibration Bulletin, No. 49, Pt. 2, September 1979, pp. 81-86.
31. Smith, Howard M., Principles of Holography, J. Wiley-Interscience, N.Y., 1969, Chapters 6,8.
32. Goodman, J. W., "Temporal Filtering Properties of Holograms," Applied Optics, Volume 6, 857 (1967).
33. Powell, R.L. and Stetson, K.A., "Interferometric Vibration Analysis by Wavefront Reconstruction," Journal of the Optical Society of America, Volume 55, 1593 (1965).
34. Nitta, G.H., "Frequency-Modulated Signals and Their Power Spectra," Tech Memo No. TM-74-208, Naval Ordnance Laboratory-Corona, Corona, California, February 1964.

35. Gardner, Floyd M., Phaselock Techniques, Second Edition, John Wiley-Interscience, N.Y., 1979, Chapters 1-4,9,10.
36. Lindsey, W.C., Synchronization Systems in Communications and Control, Prentice-Hall, Englewood Cliffs, N.J., 1972, Chapter 9.
37. Van Trees, Harry L., Detection Estimation and Modulation Theory, Part II: Nonlinear Modulation Theory, John Wiley, N. Y., 1971, Chapters 3,4.

This work was sponsored under contract No. F49620-82-C-0035.